Heavy metal opacity and line blanketing in hot DA white dwarf stars

Thesis submitted for the degree of
Doctor of Philosophy
at the University of Leicester

by
Simon P Preval
Department of Physics & Astronomy
University of Leicester

November 2014

Declaration

I hereby declare that no part of this thesis has been previously submitted to this or any other University as part of the requirement for a higher degree. The work described herein was conducted by the undersigned except for contributions from colleagues as acknowledged in the text.

Simon P Preval

24th November 2014

Heavy metal opacity and line blanketing in hot DA white dwarf stars

Simon Preval

Abstract

This thesis concerns atomic data, and it's impact upon white dwarf model atmosphere calculations, and consequentially, the measurements made using such models. The thesis begins with a brief introduction to the history and properties of white dwarfs, the theory of radiative transfer, and the uses of white dwarfs in astronomy.

A detailed spectroscopic survey of WD0501+524 (G191-B2B) is presented. 976 absorption features were detected, 947 of which have been successfully identified. $\sim 60\%$ of the identified features were found to pertain to Fe and Ni IV-VI transitions. The potential consequences of using a limited atomic data set in model atmospheres are discussed, and other possible identifications to the unknown absorption features are queried.

The Kurucz (1992) (Ku92) atomic database (containing $\sim 9,000,000$ transitions) is supplemented by photoionisation (PI) cross section data from the Opacity Project for use in stellar atmosphere calculations. The more recent Kurucz (2011) (Ku11) database (containing $\sim 160,000,000$ transitions) is not accompanied by PI cross section data. Calculations performed to create this data are described, and their effects on model atmosphere calculations are discussed.

The Lyman/Balmer line problem, a discrepancy between the measured effective temperatures (T_{eff}) from the Lyman/Balmer line series is considered. T_{eff} and surface gravity ($\log g$) measurements are made of 24 DA white dwarfs using model atmosphere grids utilising two atmospheric compositions, two Stark broadening tables, and the Ku92 and Ku11 atomic data sets. It is shown that the average opacity contributed by all metal species in the atmosphere drives the discrepancy between the measured Lyman/Balmer T_{eff}.

Analysis of Extreme Ultraviolet Explorer (EUVE) data for seven metal rich white dwarf stars is presented. Four model atmosphere grids were calculated using two atmospheric compositions (Preval et al. 2013; Barstow et al. 2003) and the Ku92 and Ku11 atomic datasets. Improved fits for wavelengths shortward of 230Å are obtained for all stars except WD0501+524, where significant discrepancies remain.

Acknowledgements

One thing I have learnt whilst embarking on a PhD is how important communication can be. It is not just our experiences that shape us, but also the people we talk to and work with. I would not have been able to get to where I am today where it not for the love, friendship, and support my family, friends, and colleagues have given me over the years. The acknowledgements listed here is by no means exhaustive, so to those of you not listed here, know that I appreciate everything you have done to support me.

Several members of my family deserve honourable mentions, such as my mother and father Mark Preval, and Pamela Preval. With their encouragement and advice, I have always strived to better myself, and be the best I can be. My siblings have also been invaluable in this venture. My sister, Jaime-Leigh, has provided endless advice and support, whilst my brother, Aidan, has shown me how to wind down and relax at the end of a rough day. Thank you guys! A very well deserved thanks goes to Katie Boulger, who put up with my various bad moods whilst trying to type this document, as well as providing emotional support when I needed it the most.

Growing up, I was taught by some fantastic people. Without the support of one of these people, however, I would not be in physics today. I met Lynn Morgan when I was 11 years old. At a time when my specific learning difficulties were not well known about, Lynn was the only one that treated me as a normal person, and inspired me to pursue my ambitions to their fullest. Thank you so much.

David Lomer was another excellent educator, whose enthusiasm for physics was contagious! He also helped me to mature as a person. In 2006, David arrange for me and several other participants to go to Russia to attend the Space Olympics. This trip was life changing for me, and allowed me to pin down what I wanted to do in my future ventures.

Whilst at the University of Leicester, I have met some very talented physicists such as Sarah Casewell, Matt Burleigh, Dick Willingale. Thank you for helping me to become a better scientist, and for answering the numerous questions I had.

Mark Mahabir was a form of deity whilst I was doing my PhD, as he maintained, updated, and repaired my work desktop. Thank you for keeping everything working smoothly, and also for converting me to the dark side (Macs are the best!)!

Ivan Hubeny taught me the inner workings of TLUSTY, and without him, I would not have been able to perform the necessary upgrades to do this project.

Nigel Badnell deserves a hefty mention, as the atomic physics part of this thesis (roughly 70%) would not exist were it not for his expertise! He eluded a lot of questions I had about his signature program AUTOSTRUCTURE, and has even taken me on for my first post doctorate job.

Finally, my sincerest gratitude goes to Martin Barstow. You knew that health issues I had been battling for quite some time might have compromised my ability to complete my thesis. Despite this, you chose me to be your PhD student. Every step of the way, you have offered guidance and support. You also allowed me a lot of freedom in exploring other areas of Astronomy, as well as areas outside, including atomic physics. Thank you sir.

Dedicated to the memory of Grandma and Granddad Skinner

Publications

A large portion of this thesis has been, or will be, published in the following works:

- "A possible solution to the Lyman/Balmer line problem in hot DA white dwarfs." - Preval S. P., Barstow M. A., Badnell N. R., Holberg J. B., Hubeny I., 2014, arXiv:1410.0811 (To appear in the proceedings of the "19th European White Dwarf Workshop" in Montreal, Canada, 2014)
- "A comprehensive near and far ultraviolet spectroscopic study of the hot DA white dwarf G191-B2B." - Preval S. P., Barstow M. A., Holberg J. B., Dickinson N. J., 2013, MNRAS, 436, 659
- "Towards a standardized line list for G191-B2B and other DA type objects." - Preval S. P., Barstow M. A., Holberg J. B., Dickinson N. J., 2013, ASPC, 469, 193

I have also collaborated in the following works:

- "Do the constants of nature couple to strong gravitational fields?", Preval S. P., Barstow M. A., Holberg J. B., Barrow J. D., Berengut J. C., Webb J. K., Dougan D., Hu J., 2014, arXiv:1410.0809 (To appear in the proceedings of the "19th European White Dwarf Workshop" in Montreal, Canada, 2014)
- "Limits on a gravitational field dependence of the proton-electron mass ratio from H_2 in white dwarf stars.", Bagdonaite J., Salumbides E. J., Preval S. P., Barstow M. A., Barrow J. D., Murphy M. T., Ubachs W., Phys. Rev. Lett, 2014, 113, 12
- "Limits on variations of the fine structure constant with gravitational potential from white dwarf spectra." - Berengut J. C., Flambaum V. V., Ong A., Webb J. K., Barrow J. D., Barstow M. A., Preval S. P., Holberg J. B., Phys. Rev Lett, 2013, 111, 1
- "O VI in the Local Interstellar Medium" - Barstow M. A., Boyce D. D., Welsh B. Y., Lallement R., Barstow J. K., Forbes A. E., Preval S., ApJ, 723, 1762
- "Post Iron Group Elements in DO Stars" - Boyce D. D., Barstow M. A., Dobbie P. D., Aston J. H., Booles B. C., Preval S. P., Laird R. J. M., James F. A., Barstow J. K., Forbes A. E., ASPC, 391, 235

Contents

Declaration **i**

Abstract **ii**

Acknowledgments **iii**

Publications **v**

List of Figures **xiii**

List of Tables **xv**

1 Introduction **1**

1.1 Introduction 1

1.2 The first white dwarfs 1

1.3 White dwarf structure 1

1.4 The white dwarf cooling curve 3

1.5 White dwarf characterisation 4

1.6 Radiative Levitation 4

1.7 Absorption features 5

1.7.1 Line Profiles 5

1.7.2 Broadening convolution 6

1.8 Stellar Atmospheric Modelling 7

1.8.1 Radiative transfer 7

1.8.2 Local and non-local thermodynamic equilibrium 8

1.8.3 Solution of the radiative transfer equation 9

1.8.4 Acceleration methods 10

1.8.5 Model atmosphere packages 11

1.9 White dwarfs in other areas 11

1.9.1 Interstellar Physics 11

1.9.2 Circumstellar Physics 12

1.9.3 White dwarfs as tests of fundamental physics 14

1.10 The story to come 14

2 The prototypical White Dwarf G191-B2B (WD0501+527) **16**

2.1 Introduction 16

2.2 Observations 16

2.2.1 FUSE 16

2.2.2 STIS 18

2.3 Line survey 20

2.3.1 Atomic data 20
2.3.2 Parameterisation of absorption features 24
2.3.3 Detections and identification 24
2.4 Model atmospheres and abundance determinations 26
2.4.1 Carbon 28
2.4.2 Nitrogen 31
2.4.3 Oxygen 31
2.4.4 Aluminium 33
2.4.5 Silicon 33
2.4.6 Phosphorus 33
2.4.7 Sulphur 33
2.4.8 Iron 35
2.4.9 Nickel 35
2.5 Discussion 35
2.5.1 Circumstellar absorption 37
2.5.2 General abundance discussion 37
2.5.3 Trans-Iron metals and other possible identifications 38
2.5.4 Opacity considerations 40
2.6 Conclusion 41
2.7 Summary 41

3 Atomic data calculations for NLTE model atmospheres **43**
3.1 Introduction 43
3.2 Calculations 44
3.2.1 Atomic Data 44
3.2.2 AUTOSTRUCTURE 45
3.2.3 Model atoms 53
3.2.4 Model atmospheres 54
3.3 Results & Discussion 55
3.3.1 Abundance variations 55
3.3.2 SED variations 57
3.3.3 Structure variations 59
3.3.4 $T_{\rm eff}$ and $\log g$ dependency 59
3.3.5 Effective flux redistribution 61
3.4 Conclusion 61
3.5 Summary 64

4 The Lyman-Balmer line problem **65**
4.1 Introduction 65
4.2 Observations 66

4.2.1 Ultraviolet . . . 67
4.2.2 Optical . . . 67
4.3 Possible contributing factors . . . 67
4.3.1 Model atmosphere composition . . . 67
4.3.2 Stark broadening tables . . . 72
4.3.3 Atomic data completeness . . . 72
4.4 Model Atmospheres . . . 73
4.5 Method . . . 74
4.6 Results - Pure H . . . 74
4.7 Results - Preval et al. (2013) model grids . . . 85
4.8 Results - Barstow et al. (2003) model grids . . . 87
4.9 Discussion . . . 89
4.9.1 Grid comparisons - Pure H/Prevold . . . 91
4.9.2 Grid Comparisons - Lemke/Tremblay . . . 91
4.9.3 Grid Comparisons - Prevold/Barsold . . . 94
4.9.4 Origin of the Lyman/Balmer line problem . . . 95
4.10 Conclusions . . . 95
4.11 Summary . . . 96

5 Extreme ultraviolet physics with white dwarfs **98**
5.1 Introduction . . . 98
5.2 Observations . . . 99
5.3 Model atmospheres . . . 100
5.4 Method . . . 100
5.5 Results . . . 101
5.5.1 WD0232+035 . . . 106
5.5.2 WD0455-282 . . . 106
5.5.3 WD0501+524 . . . 106
5.5.4 WD0621-376 . . . 106
5.5.5 WD2211-495 . . . 106
5.5.6 WD2331-475 . . . 108
5.5.7 WD2350-706 . . . 108
5.6 Discussion . . . 108
5.6.1 The role of P and S in white dwarfs . . . 108
5.6.2 Atomic data . . . 113
5.7 Conclusion . . . 113
5.8 Summary . . . 114

6 Concluding remarks **115**
6.1 Introduction . . . 115
6.2 Summaries and future work . . . 115

6.3 Final remarks . . . 118

A WD0501+524 line list **120**

Bibliography **156**

List of Figures

1.1 Optical image of Sirius A and B taken with the Hubble Space Telescope, using the Wide Field Planetary Camera 2 (WFPC2). Sirius A is the bright object in the centre, and Sirius B is the smaller object, bottom left. Image Credit: NASA, ESA, H. Bond (STScI) and M. Barstow (University of Leicester). 2

1.2 Calculated cooling curves from Salaris et al. (1997) for white dwarf stars with a C-O core and different masses. The x axis is the luminosity of the white dwarf in units of solar luminosities, and the y axis is the cooling time in Gyr. The curves from right to left correspond to white dwarf masses of 0.54, 0.55, 0.61, 0.68, 0.77, 0.87, and $1.00M_{\odot}$. 3

1.3 Table of NLTE correction vectors from Napiwotzki et al. (1999). The vector lengths have been multiplied by a factor of three for clarity. 9

1.4 C II 1334Å absorption feature as observed in G191-B2B. The feature is a combination of two blended ISM components, one from the Local Interstellar Cloud (LIC), and the other from the Hyades Cloud. 12

1.5 Diagrammatic representation of the formation of 'circumstellar' lines. A cold interstellar cloud falls within reach of a white dwarf's Strömgren Sphere, and species in this region are highly ionised. 13

2.1 Co-added spectrum of WD0501+524 using 47 *FUSE* observations from LWRS, MDRS, and HIRS apertures. 18

2.2 The final coadded spectra for the E140H (blue line) and the E230H spectra (red line). Most of the features falling below the continuum are identified absorption features. 20

2.3 The dependence of signal to noise with wavelength. The wavelength ranges are the same as for Figure 2.2. 23

2.4 A comparison of the predicted synthetic (upper line) spectrum to the observed spectrum (bottom line). In the top plot, the spectrum has been synthesised using only the 1992 Kurucz data release and some lines from NIST (described in text), whereas in the bottom plot, the spectrum has been synthesised using lines from the 1992 Kurucz data, and the Kentucky database. The synthetic spectrum has been offset for clarity. 24

2.5 Addition of a Gaussian component (red solid line) to the photospheric (blue dashed line) component of C IV 1548Å. The left subplot shows the individual contributions to the absorption feature, while the right subplot shows the combined contribution from both lines. C IV/H=2.13×10^{-7}. The discrepancy is explained in text. 31

2.6 The same as Figure 2.5, but for the C IV 1550Å line. 32

2.7 Comparison between the model and observed spectra for the C III sextuplet spanning 1174-1177Å with C III/H=1.72×10^{-7}. 32

2.8 Addition of a Gaussian component (red solid line) to the photospheric (blue dashed line) Si III 1206Å. The left subplot shows the individual contributions to the absorption feature, while the right subplot shows the combined contribution from both lines. Si III/H=3.16×10^{-7}. . . 34

2.9 Same as Figure 2.8, but for the Si IV 1393Å line with Si IV/H=3.68×10^{-7}. 34
2.10 Same as Figure 2.9, but for the Si IV 1402Å line. 35
2.11 Comparison between the model (top line) and observed (bottom line) spectra for several Fe V lines, with Fe V/H=5.00×10^{-6}. The synthetic spectrum is offset for clarity. 36
2.12 Comparison between the model (top line) and observed (bottom line) spectra for several Ni V lines, with Ni V/H=1.01×10^{-6}. The synthetic spectrum is offset for clarity. The large absorption feature near 1239Å is from N V. 36
2.13 A comparison of abundances with respect to H for solar abundance (Asplund et al., 2009) (dotted line), atmospheric abundance as predicted from radiative levitation (dashed line) (Chayer et al. 1994, 1995a,b), and the atmospheric abundances determined in this study (solid line). The error bars are omitted for clarity. 38

3.1 Variation of temperature with mass column (increasing depth) in a WD with $T_{\rm eff}$=52500K and log g=7.53. The solid curve is for a pure H model atmosphere, while the dashed curve is for a fully line blanketed model atmosphere with WD0501+524 abundances. 44
3.2 Number of available transitions from the Kurucz (1992) data release for Fe and Ni IV-VI. . . . 45
3.3 Number of available transitions from the Kurucz (2011) data release for Fe and Ni IV-VI. . . . 46
3.4 Comparison of energy levels determined in this work to that of Ku11. The dashed line is for equal Ku11 and AUTOSTRUCTURE energies. 51
3.5 Residual between calculated energy levels (AUTOSTRUCTURE) and Ku11. 52
3.6 Plot of measure abundances for a model atmosphere calculated with the Ku92 data (triangles) and the Ku11 data (squares). 57
3.7 A comparison between synthesised EUV spectra calculated with the Ku92 data (red), and the Ku11 data (blue). The residual between the two models is plotted below. 58
3.8 The same as Figure 3.7, but for the near and far ultraviolet region. 59
3.9 The same as Figure 3.7, but for the optical region. 60
3.10 A comparison between the variation of temperature with column mass (deeper into the atmosphere). The solid curve is the Ku92 model, while the dashed curve is the Ku11 model. 60
3.11 Plot of Lyman region residuals for the Ku92 and Ku11 models. From the bottom to the top, $T_{\rm eff}$ increases from 35000-100000K in steps of 2500K. From the left to the right, log g increases from 7.0 to 9.0 in steps of 1.0. Every spectrum above the lowest is offset by 0.01. 62
3.12 The same as Figure 3.11, but for the optical region. The spectrum closest to zero is offset by 0.008, while every spectrum above is offset by 0.008. 63

4.1 Plot of calculated $T_{\rm eff}$ using a pure H model grid. The left plot shows the results obtained for spectra synthesised with the Lemke tables, and the right plot is for results obtained with spectra synthesised with the Tremblay tables. The dashed line is for equal Lyman and Balmer line $T_{\rm eff}$. The far outlier on the top right of the plots is WD1738+669. 85

4.2 Plot of calculated log g using a pure H model grid. The left plot shows the results obtained for spectra synthesised with the Lemke tables, and the right plot is for results obtained with spectra synthesised with the Tremblay tables. The dashed line is for equal Lyman and Balmer line $T_{\rm eff}$. The outlier near log $g > 9$ is the heavy white dwarf WD0346-011. 86

4.3 Plot of calculated $T_{\rm eff}$ using a Prevold model grid. The left plot shows the results obtained for spectra synthesised with the Lemke tables, and the right plot is for results obtained with spectra synthesised with the Tremblay tables. The dashed line is for equal Lyman and Balmer line $T_{\rm eff}$. The far outlier on the top right of the plots is WD1738+669. 86

4.4 Plot of calculated log g using a Prevold model grid. The left plot shows the results obtained for spectra synthesised with the Lemke tables, and the right plot is for results obtained with spectra synthesised with the Tremblay tables. The dashed line is for equal Lyman and Balmer line $T_{\rm eff}$. The outlier near log $g > 9$ is the heavy white dwarf WD0346-011. 87

4.5 Differences between calculated Lyman Prevold $T_{\rm eff}$ and Lyman Prevnew $T_{\rm eff}$, plotted against their respective stars. 87

4.6 Differences between calculated Balmer Prevold $T_{\rm eff}$ and Balmer Prevnew $T_{\rm eff}$, plotted against their respective stars. 88

4.7 Plot of calculated $T_{\rm eff}$ using a Barsold model grid. The left plot shows the results obtained for spectra synthesised with the Lemke tables, and the right plot is for results obtained with spectra synthesised with the Tremblay tables. The dashed line is for equal Lyman and Balmer line $T_{\rm eff}$. The far outlier on the top right of the plots is WD1738+669. 88

4.8 Plot of calculated log g using a Barsold model grid. The left plot shows the results obtained for spectra synthesised with the Lemke tables, and the right plot is for results obtained with spectra synthesised with the Tremblay tables. The dashed line is for equal Lyman and Balmer line $T_{\rm eff}$. The outlier near log $g > 9$ is the massive white dwarf WD0346-011. 89

4.9 Differences between calculated Lyman Barsold $T_{\rm eff}$ and Lyman Barsnew $T_{\rm eff}$, plotted against their respective stars. 89

4.10 Differences between calculated Balmer Barsold $T_{\rm eff}$ and Balmer Barsnew $T_{\rm eff}$, plotted against their respective stars. 90

4.11 Differences between calculated Lyman Pure H $T_{\rm eff}$ and Lyman Prevold $T_{\rm eff}$, plotted against their respective stars. 91

4.12 Differences between calculated Balmer Pure H $T_{\rm eff}$ and Balmer Prevold $T_{\rm eff}$, plotted against their respective stars. 92

4.13 Plot of determined $T_{\rm eff}$ using the Lyman lines synthesised with the Lemke tables (x axis) and the Tremblay tables (y axis) with a pure H model atmosphere grid. The dashed line is the straight line best fit to the data (see text). 93

4.14 Same as Figure 4.13, but for log g. 93

4.15 Plot of the temperature difference between values determined using the Prevold and Barsold grid for the Lyman series. 94

4.16 Same as Figure 4.15, but for the Balmer series. 94

5.1 Plot of effective cross section of the ISM versus the wavelength of light being absorbed by the cloud. Credit: Cruddace et al. (1974). 99
5.2 Plot of the measured H column density values using either the Barsold grid (solid line, + pointers), the Barsnew grid (dotted line, * markers), the Prevold grid (dashed line, diamond markers), and the Prevnew grid (dot-dash line, triangle markers). 101
5.3 Same as Figure 5.2, but for the He I column density values. 101
5.4 Same as Figure 5.2, but for the He II column density values. 104
5.5 Same as Figure 5.2, but for the He I Doppler parameter (b) values. 104
5.6 Same as Figure 5.2, but for the He II doppler parameter (b) values. 104
5.7 Same as Figure 5.2, but for the Z values. 105
5.8 Same as Figure 5.2, but for the T_{eff} values. 105
5.9 Same as Figure 5.2, but for the log g values. 105
5.10 Plot of the EUVE spectrum of WD0232+035. The red curve is for the LW spectrum, the blue curve is for the MW spectrum, and the black curve is the best fitting model using the Barsold grid. 106
5.11 Plot of the EUVE spectrum of WD0455-282. The red curve is for the LW spectrum, the blue curve is for the MW spectrum, and the black curve is the best fitting model using the Barsold grid. 107
5.12 Plot of the EUVE spectrum of WD0501+524. The red curve is for the LW spectrum, the blue curve is for the MW spectrum, and the black curve is the best fitting model using the Barsold grid. 107
5.13 Plot of the EUVE spectrum of WD0621-376. The red curve is for the LW spectrum, the blue curve is for the MW spectrum, and the black curve is the best fitting model using the Barsnew grid. 108
5.14 Plot of the EUVE spectrum of WD2211-495. The red curve is for the LW spectrum, the blue curve is for the MW spectrum, and the black curve is the best fitting model using the Barsnew grid. 109
5.15 Plot of the EUVE spectrum of WD2331-475. The red curve is for the MW spectrum, and the black curve is the best fitting model using the Prevold grid. 109
5.16 Plot of the EUVE spectrum of WD2350-706. The red curve is for the MW spectrum, and the black curve is the best fitting model using the Prevold grid. 110
5.17 Plot of the EUVE spectrum of WD0501+524 (red curve) in the region 320-370Å. The black curve is the best fitting model using the Barsold model grid. 111
5.18 The same as Figure 5.17, but the black curve is now the best fitting model using the Prevold model grid. 111
5.19 Plot of the EUVE spectrum of WD0232+035 (red curve) in the region 320-370Å. The black curve is the best fitting model using the Barsold model grid. 112
5.20 The same as Figure 5.19, but the black curve is now the best fitting model using the Prevold model grid. 112

List of Tables

1.1 Summary of white dwarf types currently known of. 4

2.1 A summary of the physical parameters of WD0501+524. The velocities v_{LIC} and v_{Hyades} are calculated along the line of sight to the star. 17
2.2 List of detector segments aboard FUSE, and the wavelength range covered by each. 17
2.3 The *FUSE* datasets obtained from MAST. 19
2.4 A list of exposures used in the STIS spectrum coaddition. Where λ_c is the central wavelength of the exposure, P is the primary setting, and S is the secondary setting. 21
2.5 A list of absorption features that could not be identified, where λ_{Obs} is the observed wavelength with accompanying error $\delta\lambda_{\mathrm{Obs}}$, and W_λ is the equivalent width, with error δW_λ. 25
2.6 A summary of the velocity components identified in the spectrum. Each velocity was calculated using the weighted mean of the various line velocities measured in the STIS data. The calculated photospheric velocity is compared to the value found by Vennes & Lanz (2001), and the ISM velocities with that of Redfield & Linsky (2008). 26
2.7 Model atoms used in calculating the initial model atmosphere. 27
2.8 The grid of abundances used in fitting the metal absorption features. T_{eff} and log g were fixed at 52500K and 7.53 respectively. 28
2.9 The list of lines examined to determine the abundances of the photospheric metals, and the spectral window extracted to perform the analysis. 29
2.10 Summary of the abundances determined in this work, along with 1σ errors. 30
2.11 The best fitting XSPEC Gaussian model parameters for a given transition, where λ_{lab} is the lab wavelength, λ_{obs} is the observed wavelength as calculated from E_l, and v is the corresponding velocity of the absorber. All parameters have been calculated to 1σ confidence. 30
2.12 The number of lines present in the Kurucz linelist in 1992 and 2011 for Fe and Ni IV-VII. . . . 41

3.1 Configurations used in AUTOSTRUCTURE calculations. Configurations in bold typeset represent the ground state configuration. 47
3.2 Calculated scaling parameters from AUTOSTRUCTURE in IC. 50
3.3 PI Configurations used in AUTOSTRUCTURE calculations. 53
3.4 Metal abundances used in calculating the Ku11 line blanketed model atmosphere as a fraction of H. These abundances originate from Table 2.10, where the values with the lowest statistical uncertainty were used. 55
3.5 Model ions used to calculate the Ku92 and Ku11 model atmosphere grid spanning 35000-100000K, and log g spanning 7.00-9.00. The first three columns correspond to the ions used in the Ku92 calculations, and the last three columns to the ions in the Ku11 calculations. A '-' symbol in the 6th column means the same model ion was used as in the Ku92 calculation. Ions with a * next to the element name signify ions that were treated approximately by TLUSTY as a single level ion. 56

3.6 Summary of the abundances determined using a model atmosphere calculated with the Ku11 atomic data. The difference between these and the abundances determined in Chapter 2 are also given. 58

4.1 FUSE observations used in this analysis. 68
4.2 STIS observations used in this analysis. All datasets were obtained using the G430L grating. 71
4.3 Abundances used in calculating the models. 73
4.4 List of measured $T_{\rm eff}$ and log g values for the pure H, Prevold, Prevnew, Barsold, and Barsnew grids using the Lemke broadening tables. The Lyman values are given by columns with "Ly", while the Balmer values are given by "Bal". $\Delta T_{\rm eff}$ is the difference between the Lyman and Balmer $T_{\rm eff}$, and Δlog g is the difference between the measured Lyman and Balmer log g values. 75
4.5 Same as Table 4.4, but for the Tremblay broadening tables. 80
4.6 Straight line coefficients to translate Lemke $T_{\rm eff}$ to Tremblay $T_{\rm eff}$. 92
4.7 Straight line coefficients to translate Lemke log g to Tremblay log g. 92

5.1 EUVE data sets from the EUVE spectral atlas Craig et al. (1997) 99
5.2 Abundances used in calculating the models. 100
5.3 List of measured parameters from fitting the EUVE spectra of seven white dwarfs using the Barsold, Barsnew, Prevold, and Prevnew model grids. The column densities are in units of 10^{22} cm^{-2}, and the Doppler widths are in units of km s^{-1}. Quantities marked with a * mean the hard limit of the grid was reached. 102

A.1 List of detected absorption features from *FUSE*. Wavelengths (λ's) are given in Å, wavelength uncertainties ($\delta\lambda$) in mÅ, equivalent widths and uncertainties (W_λ and δW_λ respectively) in mÅ, and velocities and uncertainties (v and δv respectively) in km s^{-1}. The Origin column indicates the determined origin of the line, where PHOT=Photosphere, ISM1=LIC, and ISM2=Hyades. The List column indicates the atomic database referencing the transition, where 1=Kentucky database, 2=Kurucz (1992),3=NIST, and 4=Verner et al. (1994). 121

Chapter 1

Introduction

1.1 Introduction

Astronomy is a unique science, in that, it is the most readily communicable to the general public. It is also the most accesible of the sciences, as the most basic instrument required to practice astronomy is an eye, or in the case of the optically challenged, an eye and a pair of glasses. It is difficult to look at the night sky, and not wonder where humanity fits into the grand scheme of things, where it came from, and where it is going. It has only recently transpired that the material used to create the solar system was formed in the fiery crucible of a supernovae explosion. In this Chapter, a brief introduction is provided into the history and physics of white dwarf stars, and the foundations for the rest of the thesis are laid.

1.2 The first white dwarfs

Relatively speaking, the first observations of white dwarf stars have occurred only recently. Eridani 40, a triple star system located in the Eridanus Constellation, hosted the first white dwarf discovered, namely Eridani 40 B. An actual observation of this star, however, did not occur until 1783, where it was observed as a pair with Eridani 40 C (a red dwarf) by Herschel (1785). It wasn't until 1910 that Eridani 40 B was reported to have a spectral class of "A" by Henry Norris Russell, Edward Charles Pickering, and Williamina Fleming (a much more detailed account than is afforded here can be found in Holberg 2007). Parodoxically, Eridani 40 B was much fainter than it's host star, Eridani 40 A. This was the first identified white dwarf.

Perhaps a more popular white dwarf, Sirius B, a companion to the A star Sirius A, was the second such white dwarf to be discovered. Bessel (1844) inferred the existence of Sirius B by taking precise measurements of the position of Sirius A on the night sky. Observations by Alvan Graham Clark in 1862 showed this prediction to be true, discovering a companion to Sirius A (Flammarion, 1877).

Third in line was the discovery of Van Maanen's star by van Maanen (1917). Observations of this star showed that it had a very high proper motion, implying it was relatively close to the Earth. The discovery of Van Maanen's star also signalled the first detection of an isolated white dwarf.

Eridani B, Sirius B, and Van Maanen's star are collectively known as Classical White Dwarfs, and have been studied extensively. In particular, Sirius B has garnered a lot of attention from the white dwarf community due to it's proximity to the Earth ($\sim 2.64 \pm 0.01$pc). Figure 1.1 shows an optical image of the Sirius system taken by the Hubble Space Telescope using the Wide Field Planetary Camera 2.

1.3 White dwarf structure

A white dwarf has a very curious structure, and is fundamentally a quantum mechanical object. Simply, it is the remains of a star that has shed it's outer layers to leave behind a hot, dense core, surrounded

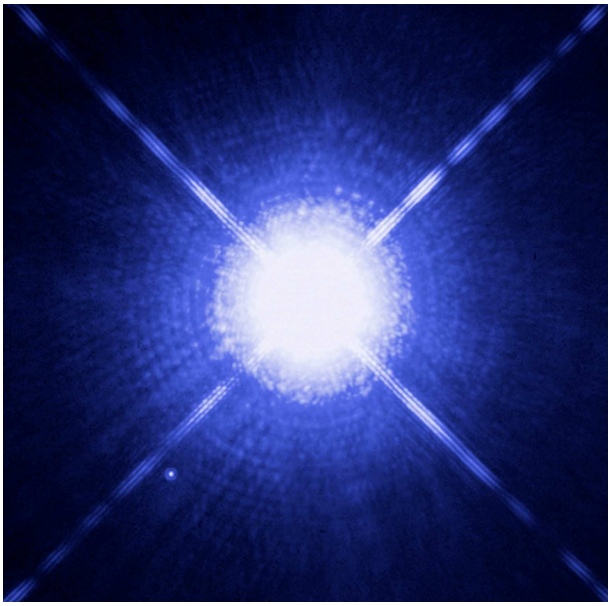

Figure 1.1: Optical image of Sirius A and B taken with the Hubble Space Telescope, using the Wide Field Planetary Camera 2 (WFPC2). Sirius A is the bright object in the centre, and Sirius B is the smaller object, bottom left. Image Credit: NASA, ESA, H. Bond (STScI) and M. Barstow (University of Leicester).

by a thin atmosphere. A main sequence star in hydrostatic equilibrium is prevented from collapse under gravity because of the thermal pressure of the hot gas in the inner layers of the star, supplemented by the thermal energy generated from nuclear fusion. In a white dwarf star, nuclear fusion has ceased, meaning the inner layers of gas are no longer being heated by this reaction. This results in the core being compressed to such an extent, that the electrons contained within become degenerate. This effect arises due to the Pauli exclusion principle, which states that no two fermions may occupy the same quantum state in a bound system. The degeneracy results in the electrons repelling each other as to not violate the Pauli exclusion principle, producing an outward force that counteracts the effects of gravitational contraction, preventing the collapse of the core. The strength of the degeneracy pressure is dependent upon the mass of the white dwarf. As more mass is added, the radius of the star decreases. The radius of the star can be related to the mass via the mass-radius relationship. In the non-relativistic limit (low mass), this relationship takes the form:

$$r \propto \frac{1}{M^{\frac{1}{3}}}, \tag{1.1}$$

where M and r are the mass and radius of the white dwarf respectively. When relativistic effects are taken into account, however, this relationship begins to break down. At a certain mass, the radius of the white dwarf goes to zero. At this mass, known as the Chandrasekhar limit, the degeneracy pressure supplied by the electrons is no longer adequate to counteract the gravitational contraction of the star. At this point, carbon fusion is initiated, burning through the core in a matter of seconds, resulting in a cataclysmic explosion, forming a type 1a supernova.

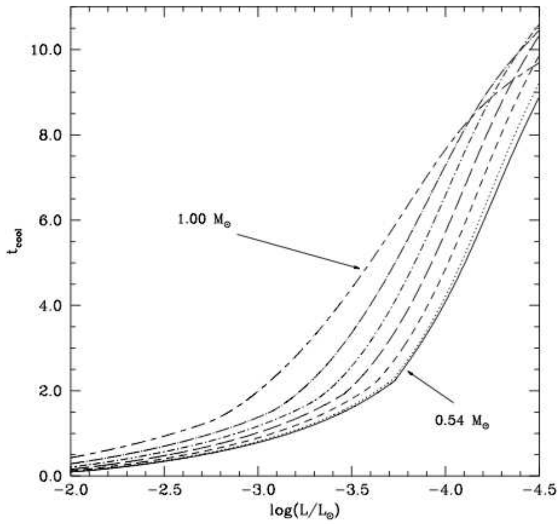

Figure 1.2: Calculated cooling curves from Salaris et al. (1997) for white dwarf stars with a C-O core and different masses. The x axis is the luminosity of the white dwarf in units of solar luminosities, and the y axis is the cooling time in Gyr. The curves from right to left correspond to white dwarf masses of 0.54, 0.55, 0.61, 0.68, 0.77, 0.87, and $1.00M_{\odot}$.

1.4 The white dwarf cooling curve

A model that predicts the luminosity of a white dwarf that cools over a period of time is known as a cooling curve. An example of a cooling curve calculated for several white dwarf masses from Salaris et al. (1997) is given in Figure 1.2. A famous example of a cooling curve comes from Mestel (1952), who derived the relation:

$$t_{\mathrm{cool}} \propto A^{-1}\mu^{-2/7}M^{5/7}L^{-5/7}, \tag{1.2}$$

where t_{cool} is the cooling time, A is the atomic weight of the core material, μ is the mean molecular weight of the gas-fluid envelope of the white dwarf atmosphere, and M and L are the mass and luminosity of the object respectively. As $L \propto T_{\mathrm{eff}}$, it is possible to use the measured T_{eff} to predict how far along the white dwarf is along the cooling curve. If the white dwarf is in a cluster of stars, the ages of members of the group can also constrain the total age of the white dwarf (Claver et al., 2001; Casewell et al., 2009). This also has an interesting consequence. A white dwarf cannot be older than the cluster in which it formed. By extension, the cluster of stars cannot be older than the galaxy in which it formed. As the cooling curve for a white dwarf has a direct relationship between T_{eff} and the time spent cooling, the coolest white dwarf can be used to put a lower limit on the age of the milky way

It is hypothesised that a white dwarf will eventually become a black dwarf after cooling to ambient temperature, however, models predict that the time it would take for a white dwarf to cool to this temperature would be longer than the age of the observable universe, meaning that no black dwarfs will have yet had sufficient time to form.

Table 1.1: Summary of white dwarf types currently known of.

Spectral Type	Characteristic
DA	Balmer lines only, no He or metals.
DB	He I lines, no H or metals.
DC	Continuous spectrum, no lines deeper than 5% in any part of the spectrum.
DO	He II rich, He I or H present.
DZ	Metal lines only, no H or He.
DQ	Carbon features, atomic or molecular, in any part of the spectrum.

1.5 White dwarf characterisation

White dwarf stars are classified by the content of their spectra and their effective temperature. All classifications begin with the letter "D", standing for degenerate. This is followed by another letter that indicates the spectral type. This classification scheme was devised by Sion et al. (1983), and is summarised in Table 1.1. These letters can be combined in the case of white dwarfs displaying characteristics of more than one type. For example, a white dwarf with both H and He II would be a DAO. Furthermore, there are symbols to indicate whether the star has a magnetic field and displays polarisation (P), has a magnetic field and does not display polarisation, or is a cataclysmic variable (v). If the white dwarf cannot be classified, it is classed as a type DX.

A number may also be added to the letter classification to indicate the temperature of the white dwarf, starting from 0 for the hottest, up to 9 for the coolest objects. This is calculated using T_{eff}:

$$\mathrm{Index} = \frac{50400}{T_{\mathrm{eff}}}. \tag{1.3}$$

Therefore, a hydrogen rich white dwarf with $T_{\mathrm{eff}} = 100000\mathrm{K}$ would have the classification DA0.5.

1.6 Radiative Levitation

The presence of metals in white dwarf stars was a conundrum until the work of Chayer et al. (1994, 1995a,b) (C3 hereafter), which laid the foundations for radiative levitation theory. In a high gravity object such as a white dwarf, any material other than H that finds itself in the atmosphere would be expected to sink to the core of the object. For hot white dwarfs, however, the radiation flux is sufficient to levitate material to the top of the atmosphere, preventing it from reaching the core. Qualitatively, an atom or ion in the atmosphere will absorb a photon from the hotter layers of the white dwarf below. This excites an electron to a higher energy level, which then decays, causing a photon to be emitted. To conserve momentum, the atom or ion is propelled in the opposite direction to the photon emission towards the top of the atmosphere.

C3 were able to use their theory to calculate the amount of material one should expect to see in a photospheric spectrum of a white dwarf dependent on T_{eff} and $\log g$ (see Figure 19 in C3). It has been shown, however, that the predictions of radiative levitation do not always match observation.Barstow et al. (2003) presented a spectral analysis of several DA white dwarf stars with T_{eff} ranging from 20000-100000K.

The authors found that white dwarfs with $T_{\rm eff}$ >50000K were polluted with metals, whereas objects below this temperature had pure H atmospheres. An exception to this observation was the Si rich white dwarf GD394 with $T_{\rm eff}$=39290K, however, this star has been reported as being "out of the ordinary" (Barstow et al., 1996; Chayer et al., 2000; Dupuis et al., 2000). The major assumption of C3's theory is that there is a sufficient reservoir of material available in the star without reference to the origin of the material. It hasn't been until recently that evidence was presented that metals in hot white dwarf stars may come from accreted materials (Barstow et al., 2014).

1.7 Absorption features

The primary diagnostic in characterising white dwarf atmospheres is that of spectroscopy. Detailed measurements of absorption profiles can yield information on the temperature of the star, the pressure conditions, and the abundances of metal species present. All absorption features can be expressed generally as

$$F_\lambda = F_0 \exp\left[-\tau_\lambda\right], \tag{1.4}$$

where F_λ is the observed flux, F_0 is the continuum flux, and τ_λ is the optical depth of the absorption feature. The exact form of τ_λ is dependent upon the conditions in which the absorption feature formed, however, it is linearly dependent upon the absorption profile ϕ, the number of absorbers N, and the type of absorber:

$$\tau_\lambda = N a_0 \phi. \tag{1.5}$$

a_0 is a constant dependent on the transition, calculated as:

$$a_0 = \frac{\lambda_0^4}{8\pi c}\frac{g_k}{g_i}a_{ki}, \tag{1.6}$$

where g_i and g_k are the initial and final statistical weights of the levels involved in the transition, and a_{ki} is the transition rate given in s^{-1}. The transition rate can be recast in terms of the oscillator strength f_{ik} with the relation:

$$a_{ki} = \frac{8\pi^2 e^2}{m_e c \lambda_0^2}\frac{g_i}{g_k}f_{ik}. \tag{1.7}$$

a_0 then becomes:

$$a_0 = \frac{\lambda_0^2 \pi e^2}{m_e c^2}f_{ik}. \tag{1.8}$$

The absorption profile ϕ can take many forms dependent upon the medium in which the absorber resides. What follows is a description of the three most commonly encountered absorption features in DA white dwarf spectra, and their formation mechanisms.

1.7.1 Line Profiles

The shape, or profile, of an absorption feature, is dependent upon the medium in which an absorber resides. Proper parameterisation of an absorption feature is vital for extracting information about the star being observed. What follows is a description of the various profiles, and the media in which they arise.

Gaussian Profile

The Gaussian profile arises in low density, low pressure media where a set of absorbers exhibit a distribution of velocities. A classic example of where this occurs is the interstellar medium. The Gaussian profile ϕ_G can be written as

$$\phi_G = \frac{1}{\sigma\sqrt{2\pi}} \exp\left[-\frac{(\lambda - \lambda_0)^2}{2\sigma^2}\right], \tag{1.9}$$

where λ_0 is the rest wavelength of the absorption feature (also referred to as the wavelength centroid), and σ is the line width, dependent upon the ion mass m, and the temperature of the medium in which it resides, T:

$$\sigma = \sqrt{\frac{k_B T}{m}} \lambda_0, \tag{1.10}$$

where k_B is Boltzmann's constant.

Lorentzian/Cauchy Profile

The Lorentzian profile is formed in media where there is high density/pressure. The Lorentzian profile ϕ_L is written as

$$\phi_L = \frac{1}{\pi} \frac{1}{(\lambda - \lambda_0)^2 + \gamma^2}, \tag{1.11}$$

where γ is the transition rate, which is also written as A_{ik}. A Lorentzian profile is also formed in the case of natural broadening, which is a property of all atoms. This can be visualised by considering the energy-time Heisenberg uncertainty relation:

$$\Delta E \Delta t \geq \hbar. \tag{1.12}$$

In this case, ΔE can be thought of as an analog to the width of the profile, and Δt as the half life of a particular transition. For transitions with small half lives, this means ΔE will become large resulting in a broad absorption feature, whereas transitions with large half lives will have a smaller ΔE resulting in a sharp absorption feature.

1.7.2 Broadening convolution

The Voigt profile is a convolution of the Gaussian and the Cauchy/Lorentzian profiles. It is formed in media with high density/pressure, and in which the absorbers have a distribution of velocities. A typical example of this case is in a stellar atmosphere. Expressing both profiles in terms of frequency ν, and a Doppler width $\Delta\nu$, the Voigt profile can be expressed as:

$$H(a, u) = \phi_G \otimes \phi_L = \frac{a}{\pi} \int_0^\infty \frac{e^{-y^2}}{a^2 + (u - y)^2} dy, \tag{1.13}$$

where $u = (\nu - \nu_0)/\Delta\nu$ is the frequency offset, ν_0 is the centroid frequency, and $a = \gamma/4\pi\Delta\nu$. The Voigt profile is then written as:

$$\phi_V = \frac{H(a, u)}{\Delta\nu\sqrt{\pi}} \tag{1.14}$$

1.8 Stellar Atmospheric Modelling

Determination of parameters in stars such as T_{eff}, log g, and the abundance of metal species is done by comparing observational data to model calculations. Typically, a grid of model atmospheres is calculated for a range of parameter values. Interpolation, along with chi square minimisation, is used to find the optimum value of the parameter that best represents the data. Below is a brief description of the physics that goes into calculating a model atmosphere.

1.8.1 Radiative transfer

At the very heart of modelling stellar atmospheres is the radiative transfer equation. In three dimensions plus time, it is given as:

$$\left(\frac{d}{ds} + \frac{1}{c}\frac{d}{dt}\right) I_\nu = \eta_\nu - \chi_\nu I_\nu, \tag{1.15}$$

where I_ν is the specific intensity, η_ν and χ_ν are the emission and absorption coefficients respectively, and s is the distance along a ray. The subscript ν is included to denote the frequency dependency of the variables. The derivative along the ray can be re-written in a more convenient form:

$$\frac{d}{ds} = n.\nabla = n_x\frac{\partial}{\partial x} + n_y\frac{\partial}{\partial y} + n_z\frac{\partial}{\partial z}, \tag{1.16}$$

where the n are the direction cosines for each dimension. In this many dimensions, the radiative transfer equation is rather difficult to solve due to the large computational expense required. In the case of white dwarf stars outside the instability strip, heat is transferred to the surface via radiative diffusion rather than convection. It is, therefore, adequate to consider a reduced version of the problem. This approximation, known as the plane-parallel approximation, assumes no time variability in the structure of the atmosphere. Furthermore, the atmosphere is assumed to extend to $\pm\infty$ in the x and y coordinates, allowing variation only in the $\pm z$ direction. Under these assumptions, the time derivative goes to zero, and the spatial derivative can be re-written as:

$$n.\nabla = n_z\frac{\partial}{\partial z} = \cos\theta\frac{\partial}{\partial z}, \tag{1.17}$$

where θ is the angle the ray makes to the x-y plane normal vector. A simplification can be made by making the substitution $\mu = \cos\theta$. The radiative transfer equation now takes the form:

$$\mu\frac{\partial I_\nu}{\partial z} = \eta_\nu - \chi_\nu I_\nu \tag{1.18}$$

It is more convenient to express the radiative transfer equation in terms of the optical depth, τ, the derivative of which is:

$$d\tau = -\chi_\nu dz \tag{1.19}$$

The negative sign is included as τ tends to $-\infty$ towards the $-z$ direction, and zero in the $+z$ direction. The radiative transfer equation becomes:

$$\mu\frac{\partial I_\nu}{\partial \tau} = I_\nu - \frac{\eta_\nu}{\chi_\nu} \tag{1.20}$$

One last simplification to make is the introduction of the source function S_ν, which is the ratio of the emission coefficient to the absorption coefficient:

$$\mu \frac{\partial I_\nu}{\partial \tau} = I_\nu - S_\nu \tag{1.21}$$

What remains is a first-order differential equation, which is in principle simple to solve. The difficulty arises in determining the form of S_ν, which is dependent upon the metals included, the temperature, the surface gravity, and many other variables. Further complicating a possible solution is the coupling of variables to other variables, meaning a change in one may affect the other.

1.8.2 Local and non-local thermodynamic equilibrium

Before commenting on the methods used to determine the source function, it is worth discussing the assumption of local and non-local thermodynamic equilibrium (LTE and NLTE respectively) in model atmosphere calculations. In the case of LTE, the source function is simply the Planck blackbody spectrum:

$$S_\nu = B_\nu = \frac{2h\nu^3}{c^2}\left[\exp\left(\frac{h\nu}{k_B T} - 1\right)\right]^{-1}, \tag{1.22}$$

where B_ν is the intensity of radiation at a specific frequency ν, T is the blackbody temperature, k_B is Boltzmanns constant, h is Plancks constant, and c is the speed of light. In LTE, the rate of emission versus the rate of absorption is exactly matched, vis:

$$g_i A_{ik} = g_k A_{ki}, \tag{1.23}$$

where g is the statistical weight of the level, A is the transition rate, and the indices i and k represent the lower and upper levels of the transition. The velocity distribution of particles assuming LTE is governed by a Maxwellian distribution, and the ionization balance of various atoms can be calculated using the Saha-Boltzmann equation:

$$\frac{n_{i+1}}{n_i} n_e = \frac{2}{\lambda_{\mathrm{db}}^3} \frac{g_{i+1}}{g_i} \exp\left[-\frac{(E_{i+1} - E_i)}{k_B T}\right] \tag{1.24}$$

Where λ_{db} is the thermal de-Broglie wavelength of an electron, given by:

$$\lambda_{\mathrm{db}} = \sqrt{\frac{2\pi\hbar^2}{m_e k_B T}} \tag{1.25}$$

In NLTE, none of the above applies. The validity of LTE or NLTE is determined by whether collisional or radiative excitation is dominant. If the former is true, then LTE is satisfactory, whereas if the latter is dominant, then NLTE effects dominate. Therefore, in deeper regions of stellar atmospheres where the density is greater, LTE conditions are more prominent. Higher up into the atmosphere, the density decreases, meaning photon excitations now dominate, and NLTE effects become prominent. In the case of white dwarf atmospheres, objects with low effective temperatures and high surface gravities are well approximated with LTE models, whereas hotter stars require NLTE models. For objects with pure hydrogen atmospheres, it is possible to define an "NLTE correction vector", which translates a measurement made of the effective temperature and surface gravity in LTE to the correct value in NLTE (see Figure 1.3).

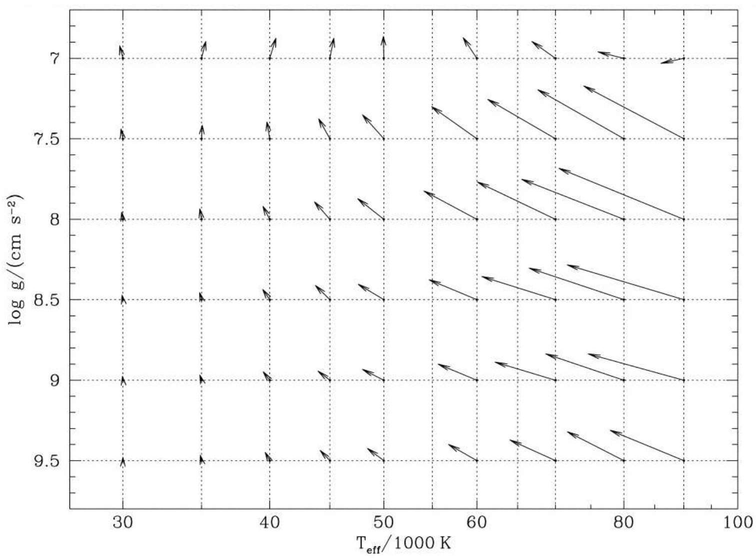

Figure 1.3: Table of NLTE correction vectors from Napiwotzki et al. (1999). The vector lengths have been multiplied by a factor of three for clarity.

1.8.3 Solution of the radiative transfer equation

In the plane parallel approximation, two sets of boundary conditions can be used. The first is for a semi infinite atmosphere, where the upper boundary has an optical depth of zero, and the lower boundary tends towards $\tau = -\infty$. The second set of boundary conditions is for a "finite slab". The solution of the radiative transfer equation under these conditions is discussed, as this underpins the solution of model atmospheres described in this thesis. The atmosphere is divided into N_D slabs, and a set of NF frequencies is defined to solve the equation for.

Each slab is described with a vector ψ_d, where d is the index of the slab, or "depth point". For each depth point, ψ_d contains information about the mean radiation intensity $J_{i=1,...,NF}$, and the atomic/ionic energy level $n_{i=1,...,NL}$, where i is a dummy index, and NL is the number of atomic/ionic energy levels included. In addition, psi_d also includes the total particle density N, the temperature T, and the electron density n_e. ψ_d can then be written:

$$\psi_d = \psi_d(J_1, J_2, ..., J_{NF}, N, T, n_e, n_1, n_2, ..., n_{NL}) \tag{1.26}$$

The "finite slab" boundary conditions are used in two model atmosphere programs, namely TLUSTY (Hubeny, 1988; Hubeny & Lanz, 1995) and the Tubingen Model Atmosphere Package (TMAP, Werner & Dreizler 1999; Werner et al. 2003).

The solution of the radiative transfer equation including multiple ions and energy levels is computationally demanding. There are two methods that can be used to reduce the time taken to compute a solution, known as complete linearisation (CL), and accelerated lambda iteration (ALI). First introduced by Auer & Mihalas (1969), CL discretises the radiative transfer equations, constraint equations, and replaces all integrals with quadrature sums. This yields a set of non-linear equations, which are then linearised in terms of an estimate ψ_d^0 and a correction $\delta\psi_d$ which is found from each iteration of the solution. This method results in convergence being achieved in relatively few iterations, however, a single iteration will solve all equations at once. Therefore, the time required to complete a single iteration will rise very quickly as the number of energy levels increases, making the solution scheme very computationally expensive for models including many metal species.

ALI (Werner et al., 2003; Hubeny, 2003) uses a different approach. The radiation intensity is expressed in terms of some approximate lambda operator acting on the source function, and a correction term found from a previous iteration. This method completes each iteration much faster than CL, but more iterations must be performed to converge upon a solution.

Given both of the advantages of CL and ALI, Hubeny & Lanz (1995) considered the idea of using both methods concurrently. This is known as the hybrid CL/ALI method, and greatly reduces the time required to fully converge a model atmosphere calculation.

1.8.4 Acceleration methods

In the case of LTE models, determining the population of energy levels in each slab is relatively straight forward. Problems arise when attempting to do the same in NLTE, where the statistical balance between the energy levels can differ considerably from their LTE counterparts. The most effective method to determine the NLTE quantities is to iterate towards the solution starting from an LTE model. The next iteration can be obtained by defining a column vector x, which is formed from the state vectors ψ_d. If $P(x)$ is a set of structural equations, then the Newton-Raphson method can be used to write:

$$x^{(n+1)} = x^{(n)} - J(x^{(n)})^{-1} P(x^{(n)}), \tag{1.27}$$

where x^n and x^{n+1} are the current and next iteration, and J is the Jacobian, defined as:

$$J_{ij} = \frac{\partial P_i}{\partial x_j}. \tag{1.28}$$

The process of finding the iteration and working towards the converged result can be accelerated. Typically, the calculation can be sped up by decreasing the size of the matrices that need to be inverted, or by using an acceleration scheme. There are two well known acceleration schemes that are used in TLUSTY and TMAP. These are known as the Ng and Kantorovich acceleration methods. The Ng method (Auer, 1987) uses previous iterations of the column vector x, and linearly combines them to find the accelerated estimate:

$$x_{acc} = \left(1 - \sum_{m=1}^{M} \alpha_m\right) x^{(n)} + \sum_{m=1}^{M} \alpha_m x^{n-m}, \tag{1.29}$$

where x_{acc} is the accelerated estimate, and α are coefficients determined by residual minimization. Usual practice sets M=2, using the current iteration, and the previous two. Hubeny (2003) advises that the Ng acceleration be applied for the first time at the 7th iteration, and thereafter every 4-6 iterations. This is based on trial and error.

The Kantorovich method decreases the computation time by reducing the number of matrix inversions performed during the atmosphere calculation. Also known as the Kantorovich variant, the next iteration is obtained with the equation:

$$x^{(n+1)} = x^{(n)} - J(X)^{-1} P(x^{(n)}), \tag{1.30}$$

where X is a fixed value of the column vector, and $J(X)$ is the Jacobian for a particular iteration. This is then used for a set number of following iterations, at which point the Jacobian is inverted.

1.8.5 Model atmosphere packages

Several packages exist for the purpose of calculating model atmospheres, however, not all packages are capable of calculating model atmospheres for white dwarf stars as they do not contain the correct equation of state. Two packages already mentioned are TLUSTY and TMAP and are very similar to each other, in that they both use the plane-parallel approximation, and also use ALI, and the Ng and Kantorivich acceleration schemes to improve convergence time. Similar abundance measurements for WD0501+524 have also been made using TLUSTY and TMAP (see Preval et al. 2013; Rauch et al. 2013 respectively).

One notable difference, however, is that TLUSTY uses the hybrid CL/ALI method to accelerate model atmosphere calculations. The impact of this can be seen in Rauch et al. (2013). The authors calculated a series of model atmospheres in order to analyse WD0501+524 containing multiple species. In total, (Rauch et al., 2013) included 70 model ions, accounting for 1038 levels in NLTE, and 1614 levels in LTE. The authors stated that a single model atmosphere took TMAP ∼1 week (168 hours) to calculate to completion. The model atmosphere calculated by Preval et al. (2013) included 25 model ions, and accounted for 693 levels in NLTE. This model took ∼16 hours to fully converge using TLUSTY. Neglecting the LTE levels, TMAP used more than double the ions, nearly twice as many NLTE levels, resulting in a calculation time taking a factor ∼10 longer than the TLUSTY calculation. It is for this reason that TLUSTY is used to calculate the model atmospheres discussed in this thesis hereafter.

1.9 White dwarfs in other areas

While interesting in it's own right, characterisation of a white dwarf's photosphere is only one thing that can be done with these objects. White dwarf stars have relatively simple spectra, making them excellent photometric standards. This means they can also be used to calibrate telescopes and provide flux scales for other objects. For the remainder of the Chapter, other applications pertaining to white dwarf observations are discussed. In particular, attention is paid to inferences that can be made about the interstellar medium through observations of white dwarfs. Furthermore, a very recent and upcoming field using white dwarf stars to investigate fundamental physics is also considered.

1.9.1 Interstellar Physics

The high surface brightness of a white dwarf star makes them excellent objects to illuminate the cold, dark interstellar medium (ISM). Absorption features originating from transitions in the ISM are simple to differentiate from those pertaining to the photosphere. The low density of the ISM means collisional excitation rarely occurs due to the large mean free path. Therefore, any excited electrons will quickly decay back to the ground state before being excited to higher levels. This means the only observable transitions of atoms or ions in the ISM will be resonant. A resonant transition is such that an electron is excited from the ground state to a higher excited state, or vice versa. Examples of resonant transitions are C IV 1548Å, N V

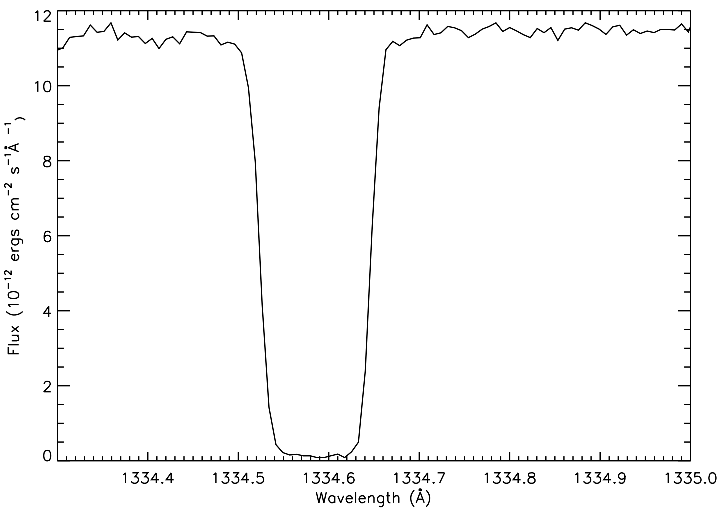

Figure 1.4: C II *1334Å absorption feature as observed in G191-B2B. The feature is a combination of two blended ISM components, one from the Local Interstellar Cloud (LIC), and the other from the Hyades Cloud.*

1238Å, O VI 1032Å, and many others. An example of an ISM absorption feature pertaining to C II 1331.98Å is given in Figure 1.4.

The low density of the ISM also allows transitions to occur that would not normally be possible in denser media such as a stellar atmosphere. These are so called 'forbidden transitions', which involve the excitation of an electron from the ground state to an excited state with a large half-life, also known as a metastable state. The transition is regarded as forbidden, because a de-excitation of an electron back to the ground state would violate the electric dipole (E1) quantum selection rules. Furthermore, as a metastable state has such a long half-life, if an electron were excited to this state in a sufficiently dense medium, then an excitation to another state would be more likely to occur before the forbidden transition happened. As well as the ISM, forbidden transitions are observed in planetary nebulae, and other rarefied plasmas.

1.9.2 Circumstellar Physics

In the context of white dwarf stars, "circumstellar" refers to any absorption features that cannot be associated with the photosphere or the ISM. Such absorption features tend to be highly ionised. The first detection of a circumstellar feature in a white dwarf was performed by Bruhweiler et al. (1999), who upon examining Space Telescope Imaging Spectrometer (STIS) observations of G191-B2B, found that the C IV 1548 and 1550Å photospheric transitions were blended with another component. The term 'circumstellar' was given to this additional component by Vennes & Lanz (2001). The authors also found that the additional component was blue shifted with respect to the photospheric component by 15km s^{-1}. As well as G191-B2B, seven other white dwarfs were found to have circumstellar absorption features by Bannister et al. (2003), who found not only C IV lines, but also N V and Si IV.

A very interesting result to come from Bannister et al. (2003) was the similarity of the circumstellar velocities to that of other ISM features. Indeed, a repeat study by Dickinson et al. (2012) using higher quality, higher resolution data for the same eight white dwarfs concurred that the velocity of detected circumstellar features was very similar to that of other ISM features in the objects 'spectra. Considering

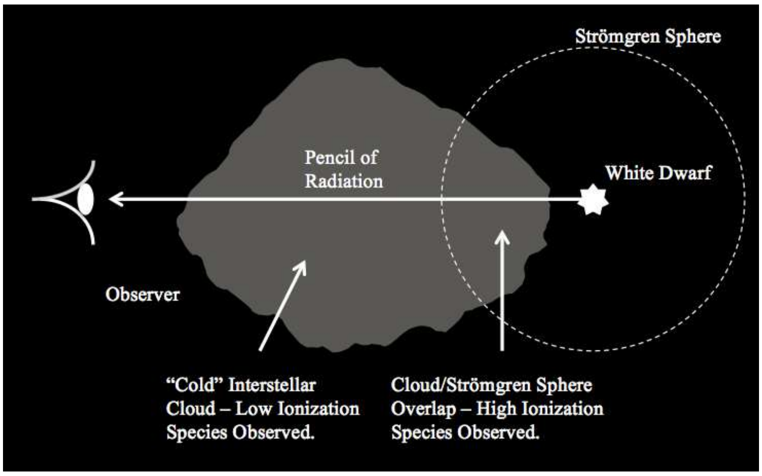

Figure 1.5: Diagrammatic representation of the formation of 'circumstellar' lines. A cold interstellar cloud falls within reach of a white dwarf's Strömgren Sphere, and species in this region are highly ionised.

G191-B2B, there are two ISM components, one from the Local Interstellar Cloud (LIC), and the other from the Hyades Cloud (Redfield & Linsky, 2008). In the LIC, the highest ionisation observed along the line of sight to G191-B2B is C, N, and Si II, whereas in the Hyades Cloud, it is C and S IV (Preval et al., 2013). However, lower ionisation states such as N II are also observed in the Hyades, implying a mixture of low and high ionisation state gas. One way of explaining this is through the overlap of an ISM cloud with a white dwarf's Strömgren sphere.

As a hot white dwarf emits radiation predominantly in the EUV and UV wavebands, the photons are of sufficient energy to ionise any interstellar matter along the line of sight. Out to a certain radius, known as the Strömgren radius, the rate at which an atom/ion is ionised by the white dwarf's radiation is equal to the rate at which the ion recombines with surrounding electrons. This sphere of influence is known as a Strömgren Sphere. The equal rate of ionisation and recombination means that the ionisation balance of highly ionised metals within the Strömgren radius can be maintained. The radius of a Strömgren Sphere is sensitive to the electron density of the medium in which it resides, the temperature of the white dwarf, and the composition of the medium. The Strömgren Sphere radius (r_s) can be calculated as:

$$r_s = \sqrt[3]{\frac{3F}{4\pi n^2 \beta}}, \tag{1.31}$$

where F is the stellar flux, n is the electron density, and β is the recombination rate of the material composing the medium. For a white dwarf such as WD0501+524, the Strömgren Sphere can have radii between 12.5-26 parsecs (Tat & Terzian, 1999).

Because the ISM cloud is not completely contained within the Strömgren Sphere, both low and high ionisation absorption features will be observed. Furthermore, as the absorption features originate from the same cloud, they will also have the same velocity along the line of sight. A diagrammatic representation of the ISM cloud/Strömgren Sphere overlap is given in Figure 1.5.

1.9.3 White dwarfs as tests of fundamental physics

Several fundamental theories of physics allow for the possibility of varying constants such as the fine structure constant (α), the proton to electron mass (μ), and many others. Theories predicting such variation usually concern changes over vast cosmological time scales (Barrow et al., 2002), however, it has also been postulated that fundamental constant variation may occur in the presence of strong gravitational fields (Flambaum & Shuryak, 2008). For an object with mass M, and a radius R, the dimensionless gravitational potential ϕ can be written as:

$$\phi = \frac{GM}{c^2 R}. \tag{1.32}$$

For a fundamental constant X_0 as measured on Earth, and a fundamental constant as measured for a different body, the variation is related to the dimensionless potential for each object as:

$$\frac{\Delta X}{X} = \frac{X - X_0}{X_0} = \kappa_X \Delta\phi = \kappa_X \Delta\left(\frac{GM}{c^2 R}\right), \tag{1.33}$$

where κ_X is the sensitivity parameter for X_0. The Δ is included to indicate the difference in ϕ for the two bodies being considered:

$$\Delta\phi = \frac{GM_1}{c^2 R_1} - \frac{GM_2}{c^2 R_2}. \tag{1.34}$$

For the Earth, $M = 5.97 \times 10^{24}$kg and $R = 6,371$km, giving $\phi = 6.95 \times 10^{-10}$. For the Sun, $M = 1.99 \times 10^{30}$ and $R = 696,342$km, giving $\phi = 2.12 \times 10^{-6}$. These appear quite small, however, in the case of the white dwarf G191-B2B, where $M = 0.52M_\odot$ and $R = 0.02R_\odot$ (Preval et al., 2013), $\phi = 5.51 \times 10^{-5}$. Therefore, any variation in X will potentially be largest for a white dwarf.

Variation of α presents itself as a characteristic shift in the laboratory wavelength of particular transitions. The shift in wavelength is dependent upon the mass of the atom/ion, the ionisation stage, and the transition being considered. Heavy ions that are highly ionised are more susceptible to changes in α. The study of α variation in white dwarf stars is a very new area, and was pioneered by Berengut et al. (2013). The study focused on the hot DA white dwarf G191-B2B, measuring multiple absorption features of Fe and Ni V using a coadded E140H spectrum from the Space Telescope Imaging Spectrometer (STIS), in an attempt to measure any potential variation in α. The measured redshift (velocity) of each feature was then plotted against their respective sensitivity coefficients Q_α, which is a measurement of the sensitivity of a transition to a change in α. The authors were able to derive limits on any potential variation of α, calculating $\Delta\alpha/\alpha = (4.2 \pm 1.6) \times 10^{-5}$ for the Fe V lines, and $\Delta\alpha/\alpha = (-6.1 \pm 5.8) \times 10^{-5}$ for the Ni V lines. It was concluded that the discrepancy arose from two factors. The first was a wavelength dependent distortion in the spectrum, and the second was the quality of the atomic data used in the analysis. Despite these shortcomings, the study showed that it is indeed possible to derive constraints on gravitational variations of α in this way.

1.10 The story to come

As has been seen, current methods used to determine parameters pertaining to white dwarf stars are heavily dependent upon model atmosphere calculations. Any model atmospheres used in parameter determination, therefore, have to account for all contributions to its structure as accurately as possible. As has been seen in previous sections, many variables need to be considered in the calculation of model atmospheres, most notably, the atomic data. It can be surmised that the inclusion of transitions with large oscillator strengths will have a larger effect on the structure of the atmosphere, while transitions with smaller oscillator strengths will have a smaller effect. This implies that after adding a certain amount of transitions, any further additions will have little to no effect on the overall structure of the atmosphere. This is an important factor to consider when calculating model atmospheres, as the number of transitions included dramatically increases the computation time.

In Chapter 2, the case is made for performing detailed model atmosphere calculations using a more complete set of atomic data. This is done through a spectroscopic survey of the hot DA white dwarf G191-B2B. Following on from this, Chapter 3 describes the process of calculating photoionization cross sections for the Kurucz (2011) atomic data set. The accuracy of the AUTOSTRUCTURE energy levels in comparision to those listed by Kurucz (2011) is considered. Using the newly calculated data, model atoms are designed for use with TLUSTY. The difference between the model atmospheres calculated with the Kurucz (1992) and Kurucz (2011) atomic data is then considered. With this new data, model atmospheres are calculated to assess the effects of including more transitions on determined stellar parameters such as $T_{\rm eff}$ and log g. In particular, Chapter 4 considers the Lyman/Balmer line problem of hot DA white dwarfs, which is a disagreement between the determined $T_{\rm eff}$ calculated using either the Lyman or Balmer line series. A final test is then performed by attempting to fit spectroscopic data from the Extreme Ultraviolet Explorer in Chapter 5.

The focus of this thesis is atomic data, and its use in the modelling of white dwarf stars. By using the atomic datasets of Kurucz (1992) and Kurucz (2011), this thesis will aim to address the following questions:

- Can a more complete set of Fe and Ni transitions explain the multitude of absorption features present in the spectrum of WD0501+524?
- How does the atomic data used in calculating a model atmosphere change the output synthetic spectra?
- Does the completeness of an atomic dataset have any bearing on the Lyman/Balmer line problem?
- What is the effect of using different atomic data sets to calculate synthetic spectra for white dwarfs in the EUV region? Again, does this improve the quality of fits over previous work?

Chapter 2

The prototypical White Dwarf G191-B2B (WD0501+527)

2.1 Introduction

G191-B2B (WD0501+527) has long been used both as a photometric standard in calibrating telescopes, and as a spectroscopic standard in the study of metal-polluted DA white dwarfs. Along with the likes of GD153, GD246, and HZ43, WD0501+524 has been used as a flux standard in many parts of the electromagnetic spectrum, as far back as the work done by Oke (1974), to the more recent work of Bohlin & Gilliland (2004), providing an absolute flux scale for the Hubble Space Telescope (HST). Based on work described herein, as well as parameters from other sources, Table 2.1 lists the basic stellar parameters of WD0501+524. Quantities such as the mass, absolute magnitude, and cooling time were calculated by interpolating the photometric tables of Holberg & Bergeron (2006); Kowalski & Saumon (2006); Tremblay et al. (2011); and Bergeron et al. (2011)[1] (hereafter the Montreal photometric tables).

In this Chapter, a detailed spectral survey of WD0501+524 is performed in the ultraviolet wavelengths covering 915-3145Å. One coadded Far Ultraviolet Spectroscopic Explorer (FUSE) spectrum comprising 47 datasets, and two coadded Space Telescope Imaging Spectrometer (STIS, aboard the HST) spectra comprising 32 E140H and 66 E230H observations respectively are used. The S/N of these spectra are exception, exceeding 100 in places. These spectra are analysed, and their absorption features identified using a linelist combining data from Kurucz (1992), the Kentucky database[2], NIST[3], and Verner et al. (1994). Updated metal abundances for C, N, O, Si, P, S, Fe, and Ni are calculated, and an NLTE abundance for Al is determined for WD0501+524 for the first time.

2.2 Observations

All datasets were downloaded from the Mikulski Archive for Space Telescopes (MAST). Described below are the observations used, and the data reduction process utilised.

2.2.1 FUSE

The Far Ultraviolet Spectroscopic Explorer (FUSE) was launched in 1997, producing spectra in the far ultraviolet (FUV) waveband covering 910-1185Å. The primary objective of FUSE was to measure the primordial and local D/H ratio, important for putting constraints on cosmological models. FUSE also observed several targets in the galactic disk, such as AGB stars and white dwarfs. It also found uses in investigating

[1]http://www.astro.umontreal.ca/∼bergeron/CoolingModels
[2]http://www.pa.uky.edu/∼peter/newpage/
[3]http://www.nist.gov/pml/data/asd.cfm

Table 2.1: A summary of the physical parameters of WD0501+524. The velocities v_{LIC} and v_{Hyades} are calculated along the line of sight to the star.

Parameter	Value	Reference
V	11.727 ± 0.016	Holberg & Bergeron (2006)
M_v	8.280 ± 0.164	This work
T_{eff} (K)	52500 ± 900	Barstow et al. (2003)
$\log g$	7.53 ± 0.09	Barstow et al. (2003)
Mass ($M_\odot$)	0.52 ± 0.035	This work
Radius ($R_\odot$)	0.0204 ± 0.0014	This work
Distance (Pc)	48.9 ± 3.7	This work
t_{cool} (Myr)	1.50 ± 0.08	This work
v_{phot} (km s^{-1})	23.8 ± 0.03	This work
v_{LIC} (km s^{-1})	19.4 ± 0.03	This work
v_{Hyades} (km s^{-1})	8.64 ± 0.03	This work

Table 2.2: List of detector segments aboard FUSE, and the wavelength range covered by each.

Channel	Segment A	Segment B
SiC1	1090.9 - 1003.7Å	992.7 - 905.0Å
LiF1	987.1 - 1082.3Å	1094.0 - 1187.7Å
SiC2	916.6 - 1005.5Å	1016.4 - 1103.8Å
LiF2	1181.9 - 1086.7Å	1075 - 979.2Å

the structure of the ISM. On the 11th July 2007, the reaction wheels aboard the spacecraft failed, leading to the observatory being decommissioned on the 7th September the same year. The observatory was based on a Rowland Circle design, consisting of four mirrors, two being LiF, and the other two SiC. In addition, there were two detectors. This setup yielded eight spectra per exposure. In Table 2.2, the wavelength range covered by each mirror and detector is given.

Three different apertures were available to use, namely the low (LWRS), medium (MDRS), and high resolution (HIRS) slits, each having dimensions of 30×30”, 4×20”, and 1.25×20” respectively. In addition, a pinhole aperture was also available, however, this was not widely implemented. Issues with thermal expansion in the spacecraft and pointing meant that the target observation would often drift out of the field of view (FOV). This could be a partial drift, where only some of the target left the FOV, reducing the flux incident on the CCD through the slit and causing discontinuities, or not being contained in the FOV at all. To minimise this problem, the LWRS aperture was used in many observations given it’s large area.

All data utilized were reduced and processed using version 3.2 of CALFUSE (Dixon et al., 2007), comprising 47 observations listed in Table 2.3. These were obtained using the LWRS, MDRS, and HIRS apertures. The coadded spectrum has been used previously in Barstow et al. (2010) to search for absorption features of O VI. Despite their different sizes, the resolutions of the LWRS, MDRS, and HIRS apertures were quite similar, with an FWHM instrumental broadening of ≈ 0.0641Å. This means that exposures from different apertures could be coadded with little effect on the wavelength centroids of the lines. The exposures were interpolated onto a common wavelength scale, and then coadded weighted by exposure time. The segments were then aligned and stitched together to give a single, continuous spectrum covering 910-1185Å. As all three apertures were used in the coadded spectrum, discontinuities in the MDRS and HIRS observations carried over to the final spectrum. Comparison of the coadded spectrum to the flux level of a STIS WD0501+524

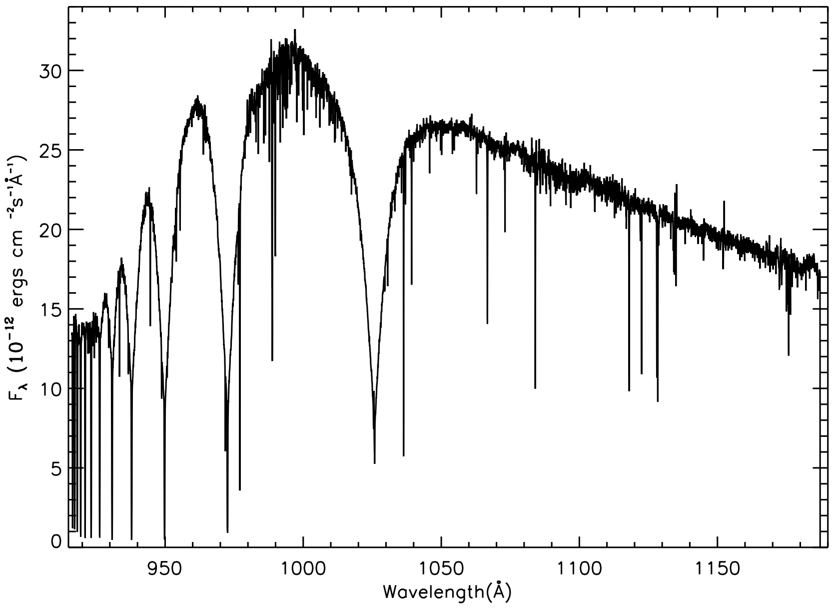

Figure 2.1: Co-added spectrum of WD0501+524 using 47 FUSE observations from LWRS, MDRS, and HIRS apertures.

spectrum (observation ID O57U01030), showed that the flux level longward of 1089Å in the FUSE spectrum was in agreement with the STIS spectrum. As the flux calibration of STIS data is typically of high quality (see Hernandez 2012), the flux shortward of 1089Å in the FUSE spectrum was multiplied by 1.08 to ensure continuity between the FUSE and STIS flux distributions (Figure 2.1).

2.2.2 STIS

STIS was installed aboard the HST during Service Mission 2, and replaced the Goddard High Resolution Spectrometer (GHRS). It operates in the ultraviolet and optical wavebands, covering wavelengths 1140-3200Å and 2000-10300Å respectively. Several apertures are available for use in STIS observations, the largest of which is the 52×2" slit, allowing the highest photometric throughput. For observations requiring exceptional wavelength calibration, the 0.2×0.06"slit may be used, however, this comes at the expense of photometric throughput, requiring longer exposure times to obtain a high signal to noise. STIS is equipped with 14 gratings, 10 of which are used for UV observations, and the remaining four for optical observations. For UV observations, there are four echelle gratings that can be used for high resolution spectroscopy, namely E140M, E140H, E230M, and E230H, with resolutions of 45,000, 114,000, 30,000, and 114,000 respectively. E140M and E140H are used for far UV observations, covering 1140-1729Å and 1140-1699Å, and the E230M and E230H gratings cover the near UV over wavelengths 1605-3110Å and 1620-3150Å respectively.

WD0501+524 has been observed extensively by STIS. Observations used in this analysis were obtained as part of the STIS calibration programs 8067, 8421, and 8915 executed during cycle 8. These programs aimed to provide flux calibrations down to the 1% level for all E140H and E230H primary and secondary echelle grating modes using strong stellar continua sources. These data were obtained during the periods of 17th December 1998, 16th - 19th of March 2000, and the 17th - 19th September 2001 in ACCUM mode, which measures the total number of photons arriving at the detector. This mode does not record the arrival time

Table 2.3: The FUSE datasets obtained from MAST.

Observation ID	Number of exposures	Start time	Exposure time (s)	Aperture
M1010201000	8	13/10/99 01:25	4164	LWRS
M1030502000	1	20/11/99 07:22	900	MDRS
M1030401000	1	20/11/99 09:02	1298	HIRS
M1030603000	5	20/11/99 10:43	3664	LWRS
M1030503000	3	21/11/99 06:43	1709	MDRS
M1030504000	4	21/11/99 10:03	3212	MDRS
M1030602000	5	21/11/99 11:39	2812	LWRS
S3070101000	32	14/01/00 09:40	15456	LWRS
M1010202000	7	17/02/00 06:10	3450	LWRS
M1030604000	1	09/01/01 09:02	503	LWRS
M1030506000	1	09/01/01 09:26	503	MDRS
M1030605000	1	10/01/01 13:20	503	LWRS
M1030507000	1	10/01/01 13:45	503	MDRS
M1030403000	2	10/01/01 15:08	483	HIRS
M1030606000	5	23/01/01 06:08	2190	LWRS
M1030508000	5	23/01/01 07:55	2418	MDRS
M1030404000	5	23/01/01 11:18	1853	HIRS
M1030607000	5	25/01/01 04:46	1926	LWRS
M1030509000	5	25/01/01 06:33	2417	MDRS
M1030405000	5	25/01/01 09:53	2419	HIRS
M1030608000	5	28/09/01 13:50	2728	LWRS
M1030510000	4	28/09/01 15:35	1910	MDRS
M1030406000	5	28/09/01 17:15	1932	HIRS
M1030609000	5	21/11/01 09:54	2703	LWRS
M1030511000	4	21/11/01 11:39	1910	MDRS
M1030407000	5	21/11/01 13:19	1932	HIRS
M1030610000	16	17/02/02 07:27	8639	LWRS
M1030512000	11	17/02/02 12:34	4757	MDRS
M1030408000	5	17/02/02 17:43	1932	HIRS
M1030611000	8	23/02/02 02:05	3645	LWRS
M1030513000	5	23/02/02 06:43	1797	MDRS
M1030409000	5	23/02/02 08:23	1921	HIRS
M1030612000	14	25/02/02 02:17	7004	LWRS
M1030514000	4	25/02/02 06:59	1617	MDRS
M1030613000	5	03/12/02 21:00	2358	LWRS
M1030614000	3	06/12/02 02:30	702	LWRS
M1030515000	4	06/12/02 05:16	2002	MDRS
M1052001000	16	07/12/02 21:46	7061	LWRS
M1030615000	4	08/12/02 22:36	1895	LWRS
M1030516000	4	09/12/02 00:29	1911	MDRS
M1030412000	4	09/12/02 03:53	1880	HIRS
M1030616000	4	05/02/03 19:14	1980	LWRS
M1030517000	4	05/02/03 21:07	1910	MDRS
M1030413000	4	06/02/03 00:36	1932	HIRS
M1030617000	8	23/11/03 20:16	4121	LWRS
M1030519000	4	25/01/04 21:31	1887	MDRS
M1030415000	4	26/01/04 00:51	1902	HIRS

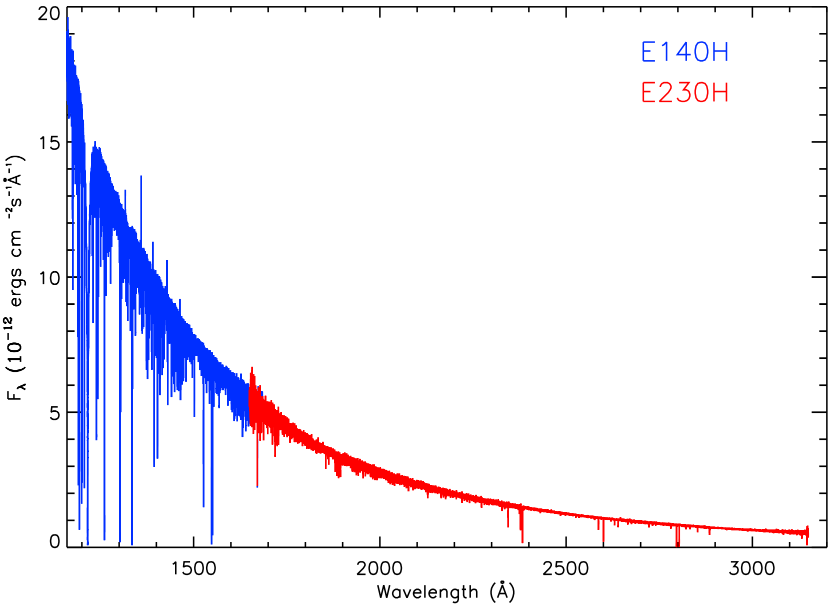

Figure 2.2: The final coadded spectra for the E140H (blue line) and the E230H spectra (red line). Most of the features falling below the continuum are identified absorption features.

of the photons, and is designed for use with bright source observations. WD0501+524 was centered in the 0.2×0.2" slit using standard target acquisition procedures. The wavelength range 1140-3145Å was covered using all nine STIS primary and all 28 secondary grating settings (cf. Chapter 11 of Hernandez (2012)). 39 E140H and 77 E230H spectra are available to use on the MAST database, all of which were examined prior to download. Datasets where the measured flux appeared discontinuous, or where it appeared attentuated relative to other exposures were excluded. 32 E140H and 66 E230H datasets (summarised in Table 2.4) were used to construct the final spectrum, each with a cumulative exposure time of 53318 and 77743s respectively. The individual spectra were interpolated onto a common, linear wavelength scale prior to coaddition, and were then coadded weighted by exposure time. This yielded two continuous spectra plotted in Figure 2.2, covering 1140-1645Å and 1620-3145Å respectively. The variation of S/N with wavelength is also plotted in Figure 2.3.

2.3 Line survey

2.3.1 Atomic data

A comparison of the Kurucz (1992) database with the Kentucky[4] database shows that the latter contains many more transitions for Fe and Ni IV-VI than the former. This difference is illustrated in Figure 2.4, where a region of spectrum has been sythesised for the wavelength range 980-1020Å. In the top plot, the spectrum uses the Kurucz (1992) linelist, while the bottom plot uses a linelist combining the Kurucz (1992) and the Kentucky databases. In the case of the latter, some transitions in the Kentucky database did not possess oscillator strengths. Where this occured, transitions were assigned an oscillator strength of 1×10^{-6}, a typical value for weak Fe and Ni transitions. It should be noted that this was done for the sole purpose of

[4] http://www.pa.uky.edu/peter/newpage/

Table 2.4: A list of exposures used in the STIS spectrum coaddition. Where λ_c is the central wavelength of the exposure, P is the primary setting, and S is the secondary setting.

Observation ID	Date	Prog. ID	Grating	λ_c (Å)	Setting	Exposure time (s)
O57U01020	17/12/1998 08:17	8067	E140H	1416	P	2040
O57U01030	17/12/1998 09:34	8067	E140H	1234	P	2789
O57U01040	17/12/1998 11:14	8067	E140H	1598	P	2703
O5I010010	16/03/2000 23:31	8421	E140H	1234	P	2279
O5I010020	17/03/2000 00:52	8421	E140H	1234	P	3000
O5I010030	17/03/2000 02:29	8421	E140H	1234	P	3000
O5I011010	17/03/2000 04:21	8421	E140H	1598	P	2284
O5I011020	17/03/2000 05:42	8421	E140H	1598	P	3000
O5I011030	17/03/2000 07:18	8421	E140H	1598	P	3000
O5I014010	18/03/2000 02:52	8421	E230H	2513	P	2304
O5I014020	18/03/2000 04:14	8421	E230H	2513	P	3000
O5I014030	18/03/2000 05:50	8421	E230H	2513	P	3000
O5I015010	18/03/2000 22:10	8421	E230H	3012	P	2304
O5I015020	18/03/2000 23:32	8421	E230H	3012	P	3000
O5I015030	19/03/2000 01:09	8421	E230H	3012	P	3000
O5I013010	19/03/2000 03:00	8421	E230H	1763	P	2304
O5I013020	19/03/2000 04:22	8421	E230H	1763	P	3000
O5I013030	19/03/2000 05:59	8421	E230H	1763	P	3000
O6HB40080	12/09/2001 23:09	8915	E230H	2413	S	774
O6HB40090	13/09/2001 00:08	8915	E230H	3012	P	2228
O6HB10010	17/09/2001 13:49	8915	E140H	1234	P	867
O6HB10020	17/09/2001 14:05	8915	E140H	1234	P	867
O6HB10040	17/09/2001 14:54	8915	E140H	1271	S	640
O6HB10050	17/09/2001 15:11	8915	E140H	1307	S	654
O6HB10080	17/09/2001 16:30	8915	E140H	1380	S	719
O6HB10090	17/09/2001 16:48	8915	E140H	1416	P	851
O6HB100A0	17/09/2001 17:09	8915	E140H	1453	S	809
O6HB100B0	17/09/2001 18:07	8915	E140H	1453	S	229
O6HB100C0	17/09/2001 18:17	8915	E140H	1489	S	1263
O6HB100D0	17/09/2001 18:44	8915	E140H	1526	S	887
O6HB100E0	17/09/2001 19:43	8915	E140H	1526	S	749
O6HB100F0	17/09/2001 20:02	8915	E140H	1562	S	1996
O6HB20010	18/09/2001 15:32	8915	E230H	1763	P	1314
O6HB20020	18/09/2001 16:00	8915	E230H	1813	S	654
O6HB20030	18/09/2001 16:35	8915	E230H	1813	S	455
O6HB20040	18/09/2001 16:49	8915	E230H	1863	S	997
O6HB20050	18/09/2001 17:12	8915	E230H	1913	S	907
O6HB20060	18/09/2001 18:11	8915	E230H	1963	S	871
O6HB20070	18/09/2001 18:32	8915	E230H	2013	P	808
O6HB20080	18/09/2001 18:51	8915	E230H	2063	S	718
O6HB20090	18/09/2001 19:47	8915	E230H	2113	S	679
O6HB200A0	18/09/2001 20:05	8915	E230H	2163	S	640
O6HB200B0	18/09/2001 20:21	8915	E230H	2213	S	620
O6HB200C0	18/09/2001 20:38	8915	E230H	2263	P	101
O6HB200D0	18/09/2001 21:24	8915	E230H	2263	P	609.6

Table 2.4: Continued.

Observation ID	Date	Prog. ID	Grating	λ_c (Å)	Setting	Exposure time (s)
O6HB200E0	18/09/2001 21:40	8915	E230H	2313	S	734.3
O6HB200F0	18/09/2001 21:59	8915	E230H	2363	S	748.7
O6HB30010	19/09/2001 15:39	8915	E230H	2463	S	668
O6HB30020	19/09/2001 15:56	8915	E230H	2513	P	696
O6HB30030	19/09/2001 16:13	8915	E230H	2563	S	247
O6HB30040	19/09/2001 16:39	8915	E230H	2563	S	484
O6HB30050	19/09/2001 16:54	8915	E230H	2613	S	769
O6HB30060	19/09/2001 17:13	8915	E230H	2663	S	992.3
O6HB30070	19/09/2001 18:16	8915	E230H	2713	S	900
O6HB30080	19/09/2001 18:37	8915	E230H	2762	P	978
O6HB30090	19/09/2001 18:59	8915	E230H	2812	S	519
O6HB300A0	19/09/2001 19:52	8915	E230H	2812	S	578
O6HB300B0	19/09/2001 20:08	8915	E230H	2862	S	1232
O6HB300C0	19/09/2001 20:35	8915	E230H	2912	S	549
O6HB300D0	19/09/2001 21:28	8915	E230H	2912	S	873
O6HB300E0	19/09/2001 21:49	8915	E230H	2962	S	1862
OBB002010	28/11/2009 08:36	11866	E230H	1863	S	1000
OBB002020	28/11/2009 08:59	11866	E230H	1963	S	870
OBB002030	28/11/2009 09:55	11866	E230H	1913	S	920
OBB002040	28/11/2009 10:16	11866	E230H	2013	P	810
OBB002050	28/11/2009 10:36	11866	E230H	2063	S	740
OBB002060	28/11/2009 11:31	11866	E230H	2263	P	800
OBB002070	28/11/2009 11:50	11866	E230H	2113	S	850
OBB002080	28/11/2009 12:10	11866	E230H	2163	S	800
OBB002090	28/11/2009 13:07	11866	E230H	1763	P	1800
OBB0020A0	28/11/2009 13:43	11866	E230H	2213	S	1000
OBB0020B0	28/11/2009 14:43	11866	E230H	1813	S	1160
OBB0020C0	28/11/2009 15:08	11866	E230H	2313	S	650
OBB0020D0	28/11/2009 15:25	11866	E230H	2363	S	650
OBB004080	29/11/2009 12:12	11866	E230H	2413	S	645
OBB004090	29/11/2009 13:05	11866	E230H	3012	P	2192
OBB001010	30/11/2009 06:58	11866	E140H	1271	S	696
OBB001020	30/11/2009 07:15	11866	E140H	1453	S	1038
OBB001030	30/11/2009 08:16	11866	E140H	1380	S	752
OBB001040	30/11/2009 08:34	11866	E140H	1234	P	867
OBB001050	30/11/2009 08:54	11866	E140H	1416	P	851
OBB001070	30/11/2009 10:09	11866	E140H	1526	S	2100
OBB001080	30/11/2009 11:27	11866	E140H	1562	S	2134
OBB001090	30/11/2009 12:09	11866	E140H	1307	S	654
OBB0010A0	30/11/2009 13:03	11866	E140H	1489	S	1200
OBB005010	01/12/2009 05:12	11866	E140H	1234	P	2200
OBB005020	01/12/2009 06:38	11866	E140H	1234	P	6200
OBB053010	06/01/2010 13:30	11866	E230H	2563	S	900
OBB053020	06/01/2010 13:51	11866	E230H	2613	S	950
OBB053030	06/01/2010 14:43	11866	E230H	2663	S	830

Table 2.4: Continued.

Observation ID	Date	Prog. ID	Grating	λ_c (Å)	Setting	Exposure time (s)
OBB053040	06/01/2010 15:03	11866	E230H	2463	S	670
OBB053050	06/01/2010 15:20	11866	E230H	2713	S	900
OBB053060	06/01/2010 16:19	11866	E230H	2762	P	1197
OBB053070	06/01/2010 16:45	11866	E230H	2862	S	1647
OBB053080	06/01/2010 17:55	11866	E230H	2513	P	1000
OBB053090	06/01/2010 18:18	11866	E230H	2912	S	1800
OBB0530A0	06/01/2010 19:31	11866	E230H	2812	S	1097
OBB0530B0	06/01/2010 19:55	11866	E230H	2962	S	1747

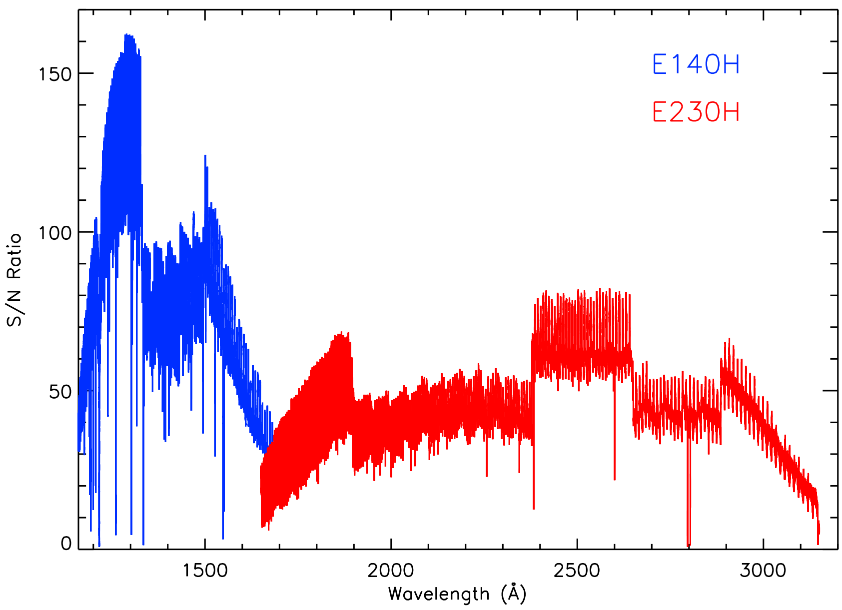

Figure 2.3: The dependence of signal to noise with wavelength. The wavelength ranges are the same as for Figure 2.2.

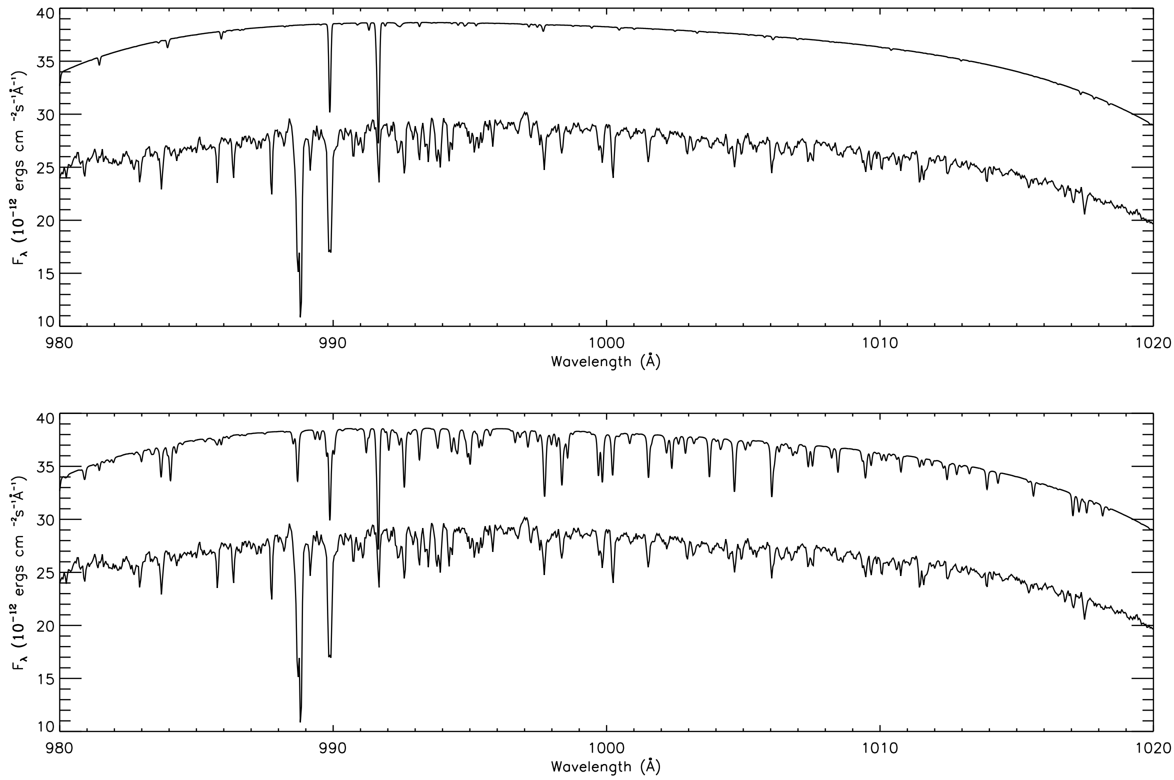

Figure 2.4: A comparison of the predicted synthetic (upper line) spectrum to the observed spectrum (bottom line). In the top plot, the spectrum has been synthesised using only the 1992 Kurucz data release and some lines from NIST (described in text), whereas in the bottom plot, the spectrum has been synthesised using lines from the 1992 Kurucz data, and the Kentucky database. The synthetic spectrum has been offset for clarity.

identification, and lines assigned an oscillator strength in this way were not used to measure any abundances. To improve the completeness of the linelist, the Kurucz (1992) and Kentucky lists are combined with data from the National Institute of Standards and Technology (NIST), and a list of resonant transitions from Verner et al. (1994).

2.3.2 Parameterisation of absorption features

Identification of the absorption features requires measurement of the centroid wavelength and the equivalent width. As discussed in Chapter 1, absorption features originating from the photosphere are pressure broadened resulting in a Lorentzian profile, whereas absorption features arising from the ISM are sharp and narrow, resulting in a Gaussian profile. In order to achieve the best fit to the observed profile, and hence measure the parameters to as higher accuracy as possible, both a Lorentzian and a Gaussian profile were fitted to the absorption feature using a chi square (χ^2) minimization procedure with the IDL routine MPFIT (Markwardt, 2009). The profile achieving the lowest χ^2 was used in the analysis.

2.3.3 Detections and identification

976 absorption features were measured and quantified to a confidence exceeding 3σ. The absorption features were identified using a velocity discrimination method. In the STIS spectra, the velocity of several well known absorption features, such as the C III sextuplet spanning 1174-1178Å, N V 1238 and 1242Å, N

Table 2.5: A list of absorption features that could not be identified, where $\lambda_{\rm Obs}$ is the observed wavelength with accompanying error $\delta\lambda_{\rm Obs}$, and W_λ is the equivalent width, with error δW_λ.

$\lambda_{\rm Obs}$(Å)	$\delta\lambda_{\rm Obs}$(mÅ)	W_λ(mÅ)	δW_λ(mÅ)
1171.277	1.9730	2.584	0.793
1174.424	1.3261	5.417	0.843
1186.174	2.8080	3.046	0.962
1186.355	0.9279	9.953	0.927
1196.733	1.7920	3.897	0.730
1198.240	0.9257	6.856	0.636
1199.443	1.0994	2.369	0.572
1201.548	2.2597	1.689	0.543
1204.561	2.0988	3.064	0.613
1206.756	1.4513	3.354	0.686
1206.812	2.4298	2.788	0.761
1228.604	2.9613	3.232	0.663
1232.311	3.4623	1.813	0.554
1253.405	2.0101	1.727	0.472
1255.177	3.0864	2.695	0.329
1270.950	4.4021	4.710	0.558
1274.017	1.8103	1.920	0.386
1285.088	2.8810	1.148	0.359
1291.912	2.3123	3.007	0.586
1292.590	2.7298	2.880	0.578
1295.987	2.6044	1.651	0.311
1302.927	2.8485	3.624	0.653
1318.082	1.0165	2.999	0.353
1321.307	1.4181	2.564	0.403
1322.416	1.3813	2.398	0.375
1333.462	2.3978	2.265	0.613
1442.574	2.4808	1.673	0.401
1499.254	3.6779	3.035	0.827
1513.608	3.2663	2.266	0.730

I 1193, and various others were calculated to obtain a rough estimate of the velocity of any components (photospheric or ISM) present in the spectrum. Using these velocities as a guide, the combined line list described above was searched to find a transition that would give a velocity as close to the estimate as possible. For absorption features that were identified using a transition from the Kentucky database, the statistical wavelength uncertainty obtained from fitting the feature and the listed uncertainty in the database were added in quadrature. This total wavelength uncertainty was then used to calculate the uncertainty on the line velocity. Out of the 976 detected aborption features, 947 could be identified using the aforementioned method. The identified absorption features are listed in the appendix, and the features that could not be identifed are listed in Table 2.5.

The analysis indicated the presence of three distinct velocity components along the line of sight. The average velocity $\bar{v}$ of each component was determined by calculating the mean of the measured velocities v_i, weighted by the inverse square of the calculated uncertainty δv_i of each line:

$$\bar{v} = \frac{\sum_{i=1}^{N} \frac{v_i}{\delta {v_i}^2}}{\sum_{i=1}^{N} \frac{1}{\delta {v_i}^2}}, \tag{2.1}$$

Table 2.6: A summary of the velocity components identified in the spectrum. Each velocity was calculated using the weighted mean of the various line velocities measured in the STIS data. The calculated photospheric velocity is compared to the value found by Vennes & Lanz (2001), and the ISM velocities with that of Redfield & Linsky (2008).

Origin	$v_{\rm Current}$ (km s^{-1})	$v_{\rm Previous}$ (km s^{-1})
Photosphere	23.8 ± 0.03	24.3 ± 1.7
LIC	19.4 ± 0.03	19.19 ± 0.09
Hyades	8.64 ± 0.03	8.61 ± 0.74

where N is the number of lines used to calculate the average. The corresponding uncertainty was calculated as:

$$\delta\bar{v} = \sqrt{\frac{1}{\sum_{i=1}^{N} \frac{1}{\delta v_i{}^2}}}. \tag{2.2}$$

When calculating the component velocities, lines measured in the FUSE spectrum were excluded as the wavelength calibration was poor, potentially skewing the result. Furthermore, only lines identified using the Kentucky database were used, as the inclusion of an error on the laboratory wavelength gives a better indication of the actual uncertainty of the measurement. The uncertainties quoted on the velocities are statistical only, and do not account for systematic uncertainties arising from the wavelength calibration of STIS. Admittedly, the uncertainties quoted on the laboratory wavelengths used in calculating the velocities are only estimates. For transitions in the Kentucky database that aren't assigned a formal error, the database estimates this based on the number of significant figures the wavelength is given to in the literature.

Of the three components, one was found to be photospheric, and two interstellar. The photospheric velocity was found to be 23.8 ± 0.03 km s^{-1}, while the two ISM velocities were 19.4 ± 0.03 km s^{-1} and 8.64 ± 0.03 km s^{-1}. In Table 2.6, the calculated photospheric velocity is compared to that found by Vennes & Lanz (2001), and the ISM velocities with those of Redfield & Linsky (2008) given in Chapter 1. Hereafter, the ISM velocities are referred to by the name of the cloud from which they originate as identified by Redfield & Linsky (2008), where the 19.4 ± 0.03 km s^{-1} velocity corresponds to the Local Interstellar Cloud (LIC), and the 8.64 ± 0.03 km s^{-1} velocity corresponds to the Hyades cloud. The velocities calculated in this study are in good agreement with those found in previous studies.

2.4 Model atmospheres and abundance determinations

Several photospheric metals were detected in the analysis, namely C, N, O, Al, Si, P, S, Fe, and Ni. Abundances for an arbitrary metal (X) quoted hereafter will be as a number fraction relative to H (X/H). The final metal abundances were calculated in a series of steps. First, the abundance of Al was calculated. This was done by first calculating a starting model assuming non-local thermodynamic equilibrium (NLTE) using TLUSTY (Hubeny, 1988), version 200 and synthesised using SYNSPEC (Hubeny & Lanz, 2011). The abundances of C, N, O, Si, Fe, and Ni were set to 1.99×10^{-7}, 1.60×10^{-7}, 3.51×10^{-7}, 8.68×10^{-7}, 3.30×10^{-6}, and 2.51×10^{-7} respectively (Barstow et al., 2003), and the abundances of P and S were set to 2.51×10^{-8} and 3.16×10^{-7} respectively (Vennes et al., 1996). $T_{\rm eff}$ and log g were set to 52500K and 7.53 respectively (as measured by Barstow et al. 2003).

Using this starting model, a further five models were calculated assuming NLTE with different Al abun-

Table 2.7: Model atoms used in calculating the initial model atmosphere.

Element	Ion	No of Levels
H	I	9
He	I	24
He	II	20
C	III	23
C	IV	41
N	III	32
N	IV	23
N	V	16
O	IV	39
O	V	40
O	VI	20
Si	III	30
Si	IV	23
P	IV	14
P	V	17
S	IV	15
S	V	12
S	VI	16
Fe	IV	43
Fe	V	42
Fe	VI	32
Ni	IV	38
Ni	V	48
Ni	VI	42

dances (summarised in Table 2.8). The Al abundance was then measured using the X-Ray spectral analysis package XSPEC (Arnaud, 1996), which utilises a χ^2 minimisation procedure to find the optimum value.

It was assumed that any changes to the C, N, O, Si, P, S, Fe, and Ni abundances would be small compared to the initial model used to calculate the Al abundance, implying that any flux redistribution that occurs due to variation in these values would likely be a second order effect. Therefore, another NLTE model atmosphere was calculated using the same C, N, O, Si, P, S, Fe, and Ni abundances, but now including the measured Al abundance. Then, SYNSPEC was used to vary the abundances of C, N, O, Si, P, S, Fe, and Ni individually in LTE. Like Al, five models were calculated with different abundances for each metal (summarised in Table 2.8), and XSPEC was then used to calculate the abundance.

XSPEC has difficulty in performing computations using spectra with many data points due to the large number of degrees of freedom. The coadded STIS spectra has in excess of 60,000 data points, meaning small sections of spectra containing the features of interest had to be selected to be analysed. The regions extracted, along with the wavelengths of any features analysed, are given in Table 2.9. This method is advantageous, in that systematic uncertainties due to poor continuum normalisation are minimised. The ionisation balance of metal species in the data were examined by fitting the absorption features of different ionisation stages for the same species of metal. Species containing multiple absorption features throughout the spectrum (Si IV for example) were fixed to have the same metal abundance. Features appearing to have multiple components not explained by photospheric absorption were modelled using the XSPEC model GABS. GABS is a preloaded model component in XSPEC that multiplies the model photospheric flux by a Gaussian absorption profile.

Table 2.8: The grid of abundances used in fitting the metal absorption features. $T_{\rm eff}$ and log g were fixed at 52500K and 7.53 respectively.

Metal	X/H				
C	2.00×10^{-8}	6.00×10^{-8}	2.00×10^{-7}	6.00×10^{-7}	2.00×10^{-6}
N	2.00×10^{-8}	6.00×10^{-8}	2.00×10^{-7}	6.00×10^{-7}	2.00×10^{-6}
O	2.00×10^{-8}	6.00×10^{-8}	2.00×10^{-7}	6.00×10^{-7}	2.00×10^{-6}
Al	2.00×10^{-8}	6.00×10^{-8}	2.00×10^{-7}	6.00×10^{-7}	2.00×10^{-6}
Si	2.00×10^{-8}	6.00×10^{-8}	2.00×10^{-7}	6.00×10^{-7}	2.00×10^{-6}
P	2.00×10^{-9}	6.00×10^{-9}	2.00×10^{-8}	6.00×10^{-8}	2.00×10^{-7}
S	2.00×10^{-8}	6.00×10^{-8}	2.00×10^{-7}	6.00×10^{-7}	2.00×10^{-6}
Fe	2.00×10^{-7}	6.00×10^{-7}	2.00×10^{-6}	6.00×10^{-6}	2.00×10^{-5}
Ni	2.00×10^{-8}	6.00×10^{-8}	2.00×10^{-7}	6.00×10^{-7}	2.00×10^{-6}

This profile is parameterised as

$$F_E = \exp\left(-\frac{S}{\sigma_l\sqrt{2\pi}}\exp\left[-\frac{(E-E_l)^2}{2\sigma_l^2}\right)\right), \tag{2.3}$$

where F_E is the flux, E_l is the centroid wavelength in keV, σ_l is the line width in keV, and S is the line strength. The profile is given in units of keV, as XSPEC is used predominantly for X-Ray astronomy. Dickinson et al. (2012) also modelled additional absorption features in this way in their analysis of the C IV doublet in WD0501+524. The parameter values determined from the GABS fit are given in Table 2.11. The velocity of the absorber is also given.

2.4.1 Carbon

The C IV 1548 and 1550Å resonance lines have been discussed multiple times in studies by Bruhweiler et al. (1999); Vennes & Lanz (2001); Bannister et al. (2003); and Dickinson et al. (2012) due to the presence of an absorption feature that is blueshifted with respect to the photospheric velocity, stating the feature to be circumstellar. A Gaussian was included when measuring the abundance, giving C IV/H as $2.13^{+0.29}_{-0.15} \times 10^{-7}$ (cf Figure 2.5 and 2.6). The velocities of these Gaussians were found to be $8.26^{+0.18}_{-0.14}$ and $8.30^{+0.13}_{-0.15}$ km s^{-1} assuming them to originate from transitions of C IV, in good agreement with the Hyades Cloud velocity determined by Redfield & Linsky (2008). Even after including a Gaussian profile in the fit, there is still a discrepancy between the flux observed in the coadded spectrum, and the flux predicted by the model for both the C IV 1548 and 1550Å lines. While this 'shelf' is not observed in Vennes & Lanz (2001)'s treatment of the C IV profiles, it is noted that this was done using lower resolution E140M observations of WD0501+524. This discrepancy most likely arises due to Ni IV transitions at 1548.220 and 1550.777Å with poor oscillator strength determinations.

Detections of the C III resonance line at 977.0201Å (hereafter C III 977Å) were made. The predicted photospheric profile, however, does not match the observed flux, as it does not descend deeply enough into the continuum. It is not possible to remedy this by increasing the abundance, as the profile is pressure broadened far beyond that observed. It is also not possible to fit the profile by including an additional Gaussian, as there are not enough data points in the line to give a unique fit. Lehner et al. (2003) noted that C III has been observed in the ISM along the line of sight to WD0501+524. The C III abundance was

Table 2.9: The list of lines examined to determine the abundances of the photospheric metals, and the spectral window extracted to perform the analysis.

Ion	Wavelength (Å)	f-value	Window (Å)	Ion	Wavelength (Å)	f-value	Window (Å)
C III	1174.9327	0.114	1174-1178	Fe IV	1592.050	0.3341	1590-1605
C III	1175.263	0.274	1174-1178	Fe IV	1601.652	0.3379	1590-1605
C III	1175.5903	0.069	1174-1178	Fe IV	1603.177	0.2679	1590-1605
C III	1175.7112	0.205	1174-1178	Fe V	1280.470	0.0236	1280-1290
C III	1175.9871	0.091	1174-1178	Fe V	1287.046	0.0363	1280-1290
C III	1176.3697	0.068	1174-1178	Fe V	1288.172	0.0541	1280-1290
C III	1247.383	0.163	1245-1255	Fe V	1293.382	0.0330	1290-1300
C IV	1548.202	0.190	1545-1555	Fe V	1297.549	0.0440	1290-1300
C IV	1550.777	0.095	1545-1555	Fe V	1311.828	0.1710	1305-1315
N IV	1718.551	0.173	1715-1725	Fe V	1320.409	0.1944	1320-1333
N V	1238.821	0.156	1235-1245	Fe V	1321.489	0.0905	1320-1333
N V	1242.804	0.078	1235-1245	Fe V	1323.271	0.1930	1320-1333
O IV	1338.615	0.118	1334-1344	Fe V	1330.405	0.2085	1320-1333
O IV	1342.99	0.011	1334-1344	Fe V	1331.189	0.0774	1320-1333
O IV	1343.514	0.104	1334-1344	Fe V	1331.639	0.1867	1320-1333
Al III	1854.716	0.556	1850-1860	Ni IV	1356.079	0.0963	1350-1360
Al III	1862.79	0.277	1860-1870	Ni IV	1398.193	0.3837	1395-1405
Si III	1206.4995	1.610	1200-1210	Ni IV	1399.947	0.2964	1395-1405
Si III	1206.5551	1.640	1200-1210	Ni IV	1400.682	0.2950	1395-1405
Si IV	1122.4849	0.819	1120-1130	Ni IV	1411.451	0.3507	1410-1422
Si IV	1128.3248	0.0817	1120-1130	Ni IV	1416.531	0.1949	1410-1422
Si IV	1128.3400	0.736	1120-1130	Ni IV	1419.577	0.1309	1410-1422
Si IV	1393.7546	0.508	1390-1400	Ni IV	1421.216	0.2863	1410-1422
Si IV	1402.7697	0.252	1400-1410	Ni IV	1430.190	0.1794	1425-1435
P IV	950.657	1.470	945-955	Ni IV	1432.449	0.1253	1425-1435
P V	1117.977	0.467	1115-1125	Ni IV	1452.220	0.3596	1450-1460
P V	1128.008	0.231	1125-1135	Ni IV	1498.893	0.1618	1495-1505
S IV	1062.662	0.052	1060-1070	Ni V	1230.435	0.2649	1230-1240
S IV	1072.974	0.045	1070-1080	Ni V	1232.807	0.1764	1230-1240
S VI	933.378	0.433	930-940	Ni V	1233.257	0.1605	1230-1240
S VI	944.523	0.213	940-950	Ni V	1234.393	0.1334	1230-1240
Fe IV	1542.155	0.1386	1540-1550	Ni V	1235.831	0.1982	1230-1240
Fe IV	1542.697	0.2818	1540-1550	Ni V	1236.277	0.1094	1230-1240
Fe IV	1544.486	0.2511	1540-1550	Ni V	1239.552	0.1116	1230-1240
Fe IV	1546.404	0.2070	1540-1550	Ni V	1241.627	0.2003	1240-1250
Fe IV	1562.751	0.2032	1560-1572	Ni V	1243.504	0.0815	1240-1250
Fe IV	1568.276	0.3012	1560-1572	Ni V	1243.662	0.1194	1240-1250
Fe IV	1569.222	0.1291	1560-1572	Ni V	1244.027	0.0503	1240-1250
Fe IV	1570.178	0.3147	1560-1572	Ni V	1245.176	0.2348	1240-1250
Fe IV	1570.416	0.2741	1560-1572				

Table 2.10: *Summary of the abundances determined in this work, along with 1σ errors.*

Ion	Abundance	-1σ	$+1\sigma$
C III	1.72×10^{-7}	0.02×10^{-7}	0.02×10^{-7}
C IV	2.13×10^{-7}	0.15×10^{-7}	0.29×10^{-7}
N IV	1.58×10^{-7}	0.14×10^{-7}	0.14×10^{-7}
N V	2.16×10^{-7}	0.04×10^{-7}	0.09×10^{-7}
O IV	4.12×10^{-7}	0.08×10^{-7}	0.08×10^{-7}
Al III	1.60×10^{-7}	0.08×10^{-7}	0.07×10^{-7}
Si III	3.16×10^{-7}	0.30×10^{-7}	0.31×10^{-7}
Si IV	3.68×10^{-7}	0.14×10^{-7}	0.13×10^{-7}
P IV	8.40×10^{-8}	1.18×10^{-8}	1.18×10^{-8}
P V	1.64×10^{-8}	0.02×10^{-8}	0.02×10^{-8}
S IV	1.71×10^{-7}	0.02×10^{-7}	0.02×10^{-7}
S VI	5.23×10^{-8}	0.13×10^{-8}	0.10×10^{-8}
Fe IV	1.83×10^{-6}	0.03×10^{-6}	0.03×10^{-6}
Fe V	5.00×10^{-6}	0.06×10^{-6}	0.06×10^{-6}
Ni IV	3.24×10^{-7}	0.05×10^{-7}	0.13×10^{-7}
Ni V	1.01×10^{-6}	0.03×10^{-6}	0.03×10^{-6}

Table 2.11: *The best fitting* XSPEC *Gaussian model parameters for a given transition, where $\lambda_{\rm lab}$ is the lab wavelength, $\lambda_{\rm obs}$ is the observed wavelength as calculated from E_l, and v is the corresponding velocity of the absorber. All parameters have been calculated to 1σ confidence.*

Ion	Parameter	Value	-1σ	$+1\sigma$
C IV	$\lambda_{\rm lab}$ (Å)	1548.203	-	-
	E_l (10^{-3}keV)	8.008122	0.0000047	0.0000038
	σ_l (10^{-7}keV)	1.34141	0.03611	0.03689
	S (10^{-7})	1.19420	0.0426	0.0489
	$\lambda_{\rm obs}$ (Å)	1548.246	0.000735	0.000909
	v (km s^{-1})	8.26	0.14	0.18
C IV	$\lambda_{\rm lab}$ (Å)	1550.777	-	-
	E_l (10^{-3}keV)	7.994829	0.0000036	0.0000040
	σ_l (10^{-7}keV)	1.26307	0.03597	0.02623
	S (10^{-7})	7.18607	0.20447	0.17263
	$\lambda_{\rm obs}$ (Å)	1550.820	0.000776	0.000698
	v (km s^{-1})	8.30	0.15	0.13
Si III	$\lambda_{\rm lab}$ (Å)	1206.4995	-	-
	E_l (10^{-3}keV)	10.276140	0.0000070	0.0000020
	σ_l (10^{-7}keV)	0.925806	0.026966	0.025814
	S (10^{-7})	4.79551	0.13501	0.14099
	$\lambda_{\rm obs}$ (Å)	1206.537	0.000235	0.000822
	v (km s^{-1})	9.24	0.06	0.20
Si IV	$\lambda_{\rm lab}$ (Å)	1393.7546	-	-
	E_l (10^{-3}keV)	8.895525	0.0000277	0.0000208
	σ_l (10^{-7}keV)	0.926033	0.183263	0.293867
	S (10^{-7})	0.434293	0.072113	0.098237
	$\lambda_{\rm obs}$ (Å)	1393.795	0.003259	0.004340
	v (km s^{-1})	8.73	0.70	0.93
Si IV	$\lambda_{\rm lab}$ (Å)	1402.7697	-	-
	E_l (10^{-3}keV)	8.838369	0.0000503	0.0000411
	σ_l (10^{-7}keV)	0.890117	0.341027	0.550783
	S (10^{-7})	0.206168	0.069738	0.087402
	$\lambda_{\rm obs}$ (Å)	1402.809	0.006523	0.007984
	v (km s^{-1})	8.31	1.39	1.71

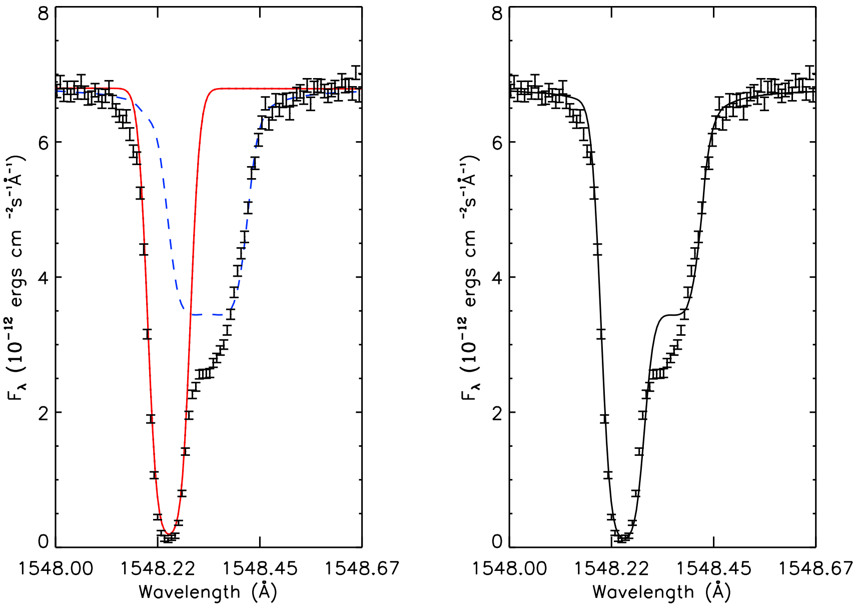

Figure 2.5: Addition of a Gaussian component (red solid line) to the photospheric (blue dashed line) component of C IV *1548Å. The left subplot shows the individual contributions to the absorption feature, while the right subplot shows the combined contribution from both lines. C* IV*/H=*2.13×10^{-7}*. The discrepancy is explained in text.*

calculated using the sextuplet transition spanning 1174-1178Å, giving C III/H=$1.72^{+0.02}_{-0.02} \times 10^{-7}$ (cf. Figure 2.7).

The calculated C III and IV abundances are in good agreement with the C III abundance obtained by Barstow et al. (2003) of $1.99^{+0.44}_{-0.88} \times 10^{-7}$, but not their C IV value of $4.00^{+0.44}_{-0.98} \times 10^{-7}$. It is noted, however, that the latter abundance was calculated without accounting for the circumstellar absorption.

2.4.2 Nitrogen

An N IV sextuplet near 920Å is available to fit, however, this region typically has low S/N. The best N IV line to use is the N IV 1718.551Å in the E230H spectrum due to it's high oscillator strength. N IV/H was found to be $1.58^{+0.14}_{-0.14} \times 10^{-7}$. The most prominent photospheric N V lines are the two doublet transitions at 1238.821 and 1242.804Å respectively. Fits to these lines yielded N V/H=$2.16^{+0.09}_{-0.04} \times 10^{-7}$.

2.4.3 Oxygen

It was not possible to include the well known O V 1371.296Å line, as it did not appear in the synthesised spectrum unless an O abundance of $\approx 10^{-6}$ was used. This problem may be related to that described by Vennes et al. (2000), where the ionization fraction for O IV/O V is poorly modelled. The authors ruled out $T_{\rm eff}$ and log g variations as being the cause, postulating the issue might be due to additional atmospheric consituents, stratification, or poor modelling of the O atoms. Vennes & Lanz (2001) bypassed this issue by using only the O IV lines to determine the abundance. This may also explain the large errors on the O abundance measurements made by Barstow et al. (2003) ($3.51^{+7.40}_{-2.00} \times 10^{-7}$). Therefore, the O IV lines listed in Table 2.9 were used. O IV/H was calculated as $4.12^{+0.08}_{-0.08} \times 10^{-7}$, in good agreement with Barstow et al.

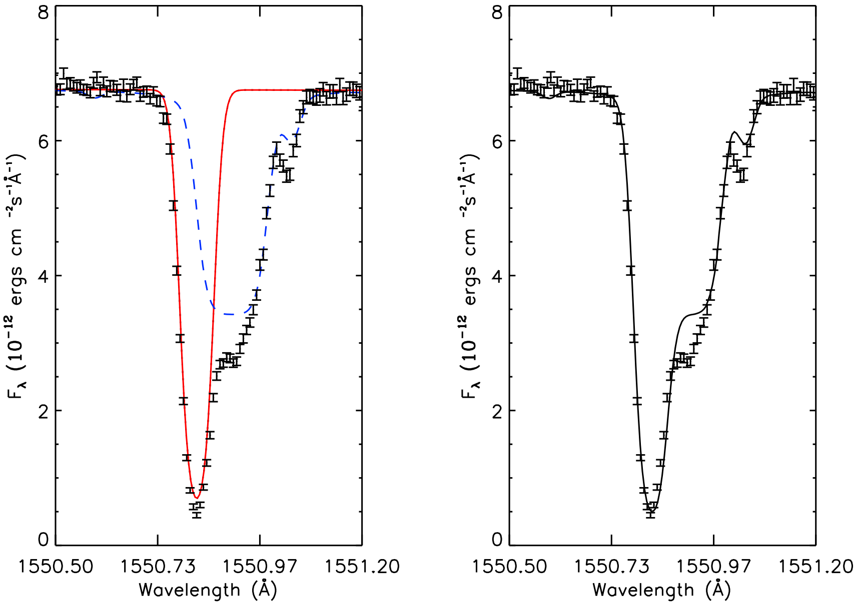

Figure 2.6: The same as Figure 2.5, but for the C IV *1550Å line.*

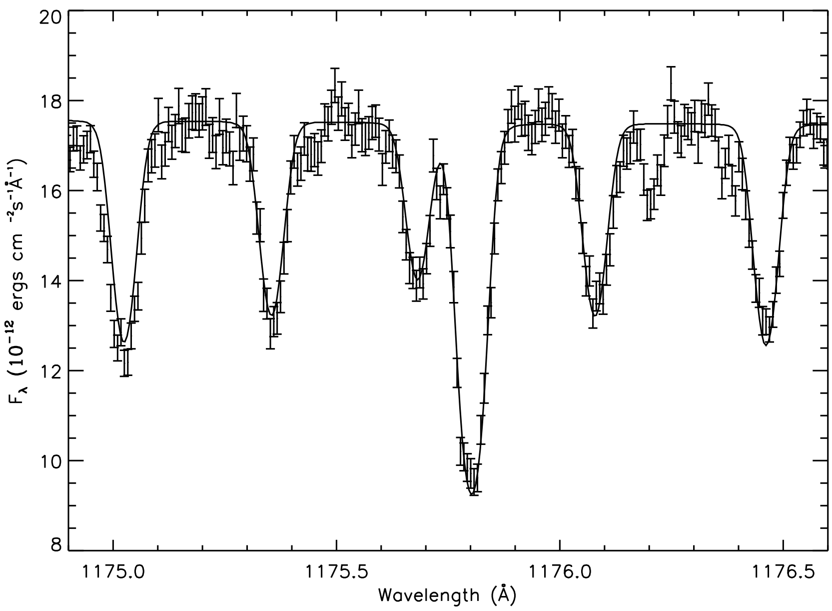

Figure 2.7: Comparison between the model and observed spectra for the C III *sextuplet spanning 1174-1177Å with C* III*/H*=1.72×10^{-7}.

(2003)'s value.

2.4.4 Aluminium

Resonant Al III lines were first observed in WD0501+524 by Holberg et al. (1998) using high dispersion IUE data, however, an estimate of the abundance was not provided. Assuming LTE, Holberg et al. (2003) estimated Al III/H=3.02×10^{-7}. Using NLTE models in this study, Al III/H=$1.60^{+0.07}_{-0.08} \times 10^{-7}$.

2.4.5 Silicon

The resonant Si III 1206.4995Å feature is blended with a circumstellar line. Including a Gaussian in the fit, Si III/H was measured to be $3.16^{+0.31}_{-0.30} \times 10^{-7}$ (see Figure 2.8). The velocity of this Gaussian, assuming it originates from Si III, was found to be $9.24^{+0.20}_{-0.06}$ km s^{-1}. There also appears to be a discrepancy between the predicted and observed flux in between the circumstellar and photospheric components. This could be due to an additional absorption feature, or a poor theoretical value for the broadening of the photopsheric component.

Possible contamination of the Si IV 1393.7546 and 1402.7697Å was noted by Holberg et al. (2003), stating that the two absorption profiles were asymmetrical, indicating the presence of a component blueshifted with respect to the photospheric velocity. This asymmetry was also observed in this analysis, and was accounted for by including a Gaussian into the fit. The abundance was further constrained by including the excited Si IV transitions at 1122.4849, 1128.3248, and 1128.3400Å. Si IV/H is found to be $3.68^{+0.13}_{-0.14} \times 10^{-7}$ The velocities of the Gaussians were measured as $8.73^{+0.93}_{-0.70}$ km s^{-1} and $8.31^{+1.71}_{-1.39}$ km s^{-1} for the Si IV 1393 and 1402Å lines respectively. The velocity of both Gaussians are in good agreement with the Hyades cloud velocity. Both of the measured Si abundances are not encompassed by the errors of Barstow et al. (2003)'s value of Si/H=$8.65^{+3.20}_{-3.50} \times 10^{-7}$.

2.4.6 Phosphorus

Resonant transitions of P have been observed in a selection of DA white dwarfs (see Barstow et al. 2014 for a complete list). Using spectra obtained from the *Orbiting and Retrievable Far and Extreme Ultraviolet Spectrograph* (ORFEUS), P was first discovered by Vennes et al. (1996), who found P/H=$2.51^{+1.47}_{-0.93} \times 10^{-7}$ assuming LTE. The P IV/H and P V/H abundances were found to be $8.40^{+1.18}_{-1.18} \times 10^{-8}$ and $1.64^{+0.02}_{-0.02} \times 10^{-8}$ respectively. The P V abundance is in agreement with that found by Vennes et al. (1996). The large uncertainty in the P IV abundance is most likely due to the proximity of the P IV line to the Ly-γ centroid, where the continuum varies rapidly with wavelength.

2.4.7 Sulphur

Vennes et al. (1996) also discovered S IV absorption features in *ORFEUS* telescope spectra of WD0501+524, calculating an LTE abundance of S IV/H=$3.16^{+3.15}_{-1.58} \times 10^{-7}$. Several more white dwarfs have been found to exhibit S IV and S VI absorption features (Barstow et al., 2014). Absorption features from S IV and S VI were available to fit. Values calculated were $1.71^{+0.02}_{-0.02} \times 10^{-7}$ and $5.23^{+0.10}_{-0.13} \times 10^{-8}$ for S IV and S VI respectively.

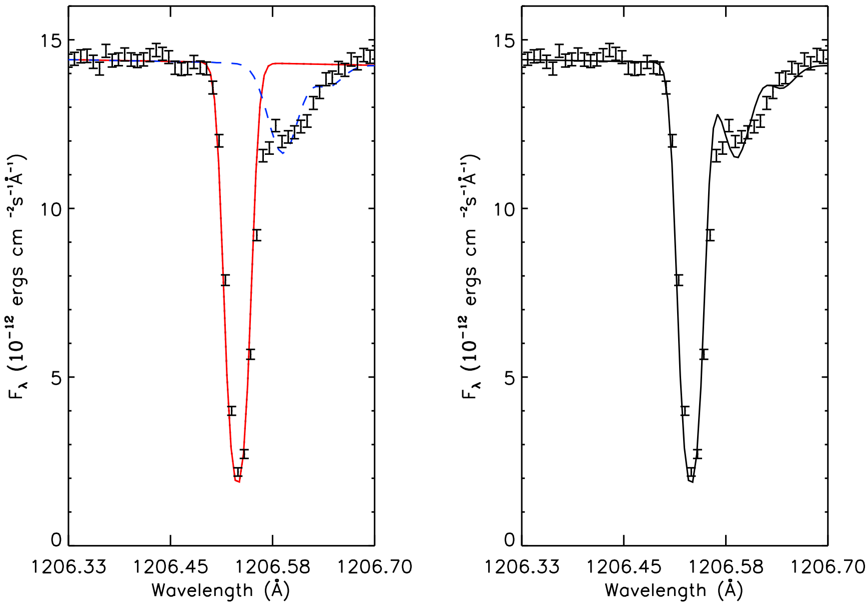

Figure 2.8: Addition of a Gaussian component (red solid line) to the photospheric (blue dashed line) Si III *1206Å. The left subplot shows the individual contributions to the absorption feature, while the right subplot shows the combined contribution from both lines. Si* III*/H*=3.16×10^{-7}.

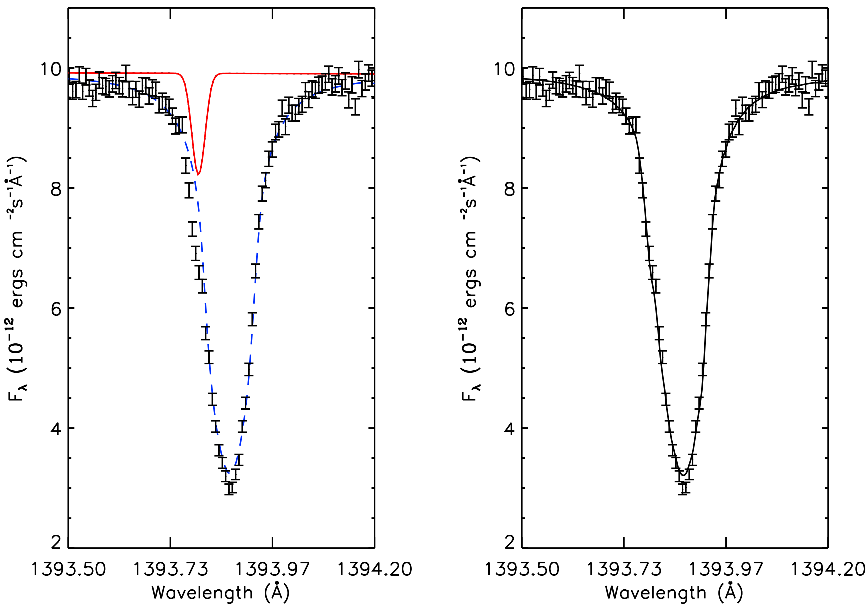

Figure 2.9: Same as Figure 2.8, but for the Si IV *1393Å line with Si* IV*/H*=3.68×10^{-7}.

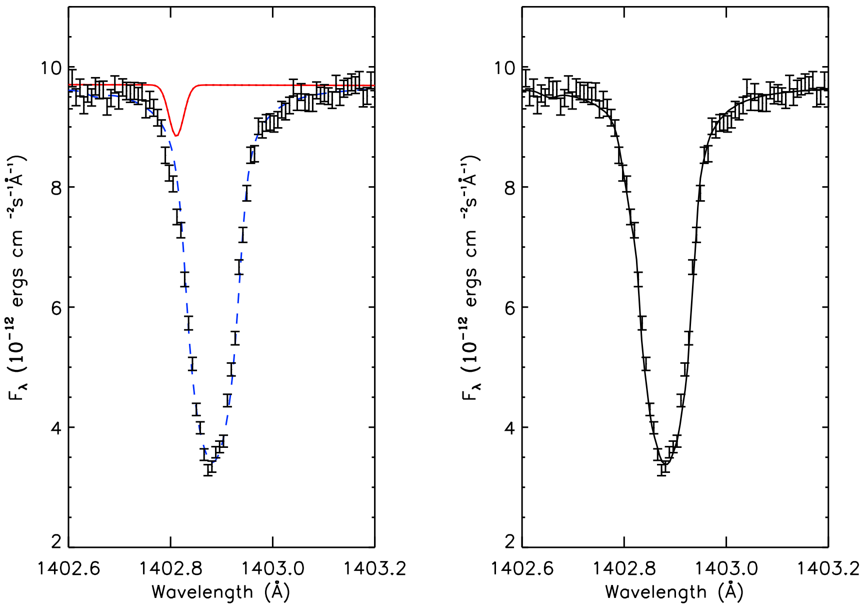

Figure 2.10: Same as Figure 2.9, but for the Si IV *1402Å line.*

The S IV value is in agreement with that found by Vennes et al. (1996), however, the S VI value differs by more than 80%.

2.4.8 Iron

Given the large number of Fe transitions available to fit, 12 of the strongest Fe IV and V lines from the Kentucky database were used. These transitions are listed in Table 2.9. The Fe IV and Fe V abundances were measured to be $1.83^{+0.03}_{-0.03} \times 10^{-6}$ and $5.00^{+0.06}_{-0.06} \times 10^{-6}$ respectively (cf. Figure 2.11). Our Fe V abundance is in agreement with the value obtained by Barstow et al. (2003) of Fe/H=$3.30^{+3.10}_{-1.20} \times 10^{-6}$.

2.4.9 Nickel

As with Fe, 12 of the strongest Ni IV/V transitions from the Kentucky database were used to measure the abundance. Ni IV/H and Ni IV/H were measured as $3.24^{+0.13}_{-0.05} \times 10^{-7}$ and $1.01^{+0.03}_{-0.03} \times 10^{-6}$ respectively (cf Figure 2.12). The Ni IV abundance is in good agreement with the value found by Barstow et al. (2003).

2.5 Discussion

By using exceptionally high S/N spectra from FUSE and STIS, 976 absorption features were detected, and of these, 947 could be successfully identified due to the combined line list of Kentucky and Kurucz (1992). ≈60% of the features measured could be attributed to Fe and Ni IV-VI transitions.

Discussion of the results is structured as follows. The circumstellar identifications made, and possible origins of these features are discussed first. Next, the observed abundances in WD0501+524 are compared to the solar values obtained by Asplund et al. (2009) and the predicted atmospheric abundances due to radiative levitation (see Chapter 1) from Chayer et al. (1994, 1995a,b) (cf Figure 2.13). Finally, the potential

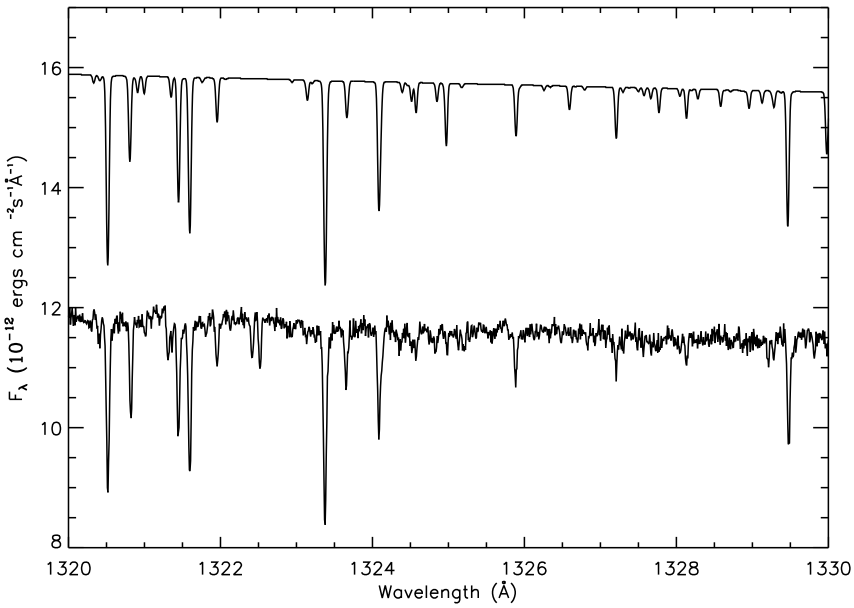

Figure 2.11: Comparison between the model (top line) and observed (bottom line) spectra for several Fe V *lines, with Fe* V*/H*=5.00×10^{-6}*. The synthetic spectrum is offset for clarity.*

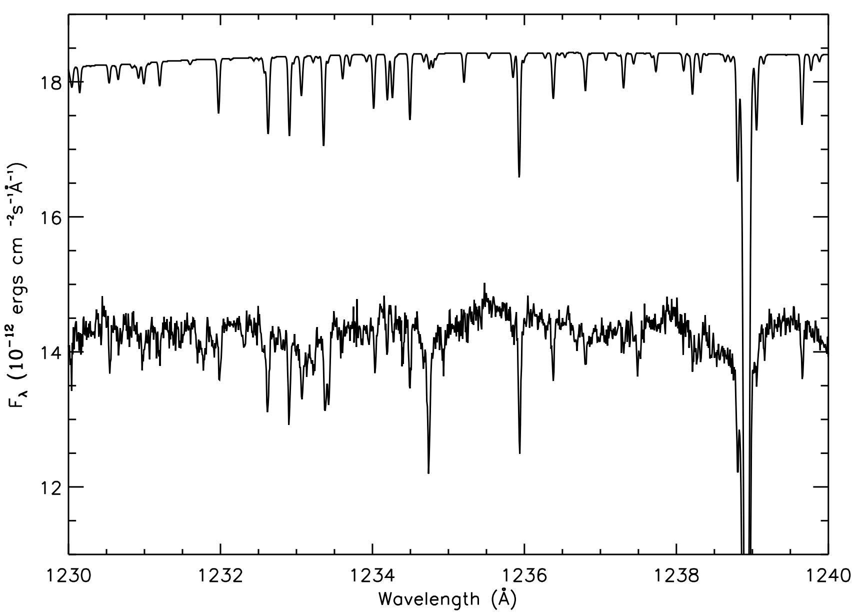

Figure 2.12: Comparison between the model (top line) and observed (bottom line) spectra for several Ni V *lines, with Ni* V*/H*=1.01×10^{-6}*. The synthetic spectrum is offset for clarity. The large absorption feature near 1239Å is from N* V*.*

consequences of including additional opacity by way of including more Fe and Ni transitions in NLTE radiative transfer models is considered to conclude this study.

2.5.1 Circumstellar absorption

Several circumstellar absorption features have been identified in this survey. As well as the thoroughly documented C IV 1548 and 1550Å lines, detections of circumstellar Si III and Si IV have also been made. The calculated C IV and Si IV circumstellar velocities are encompassed by the Hyades velocity measurement made both by Redfield & Linsky (2008), and by Preval et al. (2013). The formation of circumstellar features is discussed in Chapter 1. While the velocity of the Si III circumstellar line is not encompassed by the Hyades velocity measurement, the difference between the two values is small. Furthermore, the value is encompassed by Redfield & Linsky (2008). It is, therefore, reasonable to assume that the Si III feature is also of circumstellar origin. It is difficult to determine the origin of the C III 977Å. Because of the small number of data points composing the feature, it wasn't possible to fit an absorption feature accounting for both the photospheric and the additional component.

Assuming that these features do indeed arise from Strömgren sphere ionisation of a nearby interstellar cloud, it is possible that any atoms found as low ionisation species may also be found as high ionisation features. Detections of C, N, O, Mg, Si, Al, P, S, Ar, and Fe were made (see the Appendix), with velocities that are consistent with the Hyades cloud. Of these metals, only absorption features of C IV, Si III, and Si IV were detected. In the case of metals found in the photosphere with strong absorption (N, Al, P, S), it is possible that the signal from the circumstellar features has been masked by the photospheric component due to low column densities of these materials. Fe IV-VI does not have any resonant transitions in the NUV/FUV (900-3200Å), so it is not possible to say whether or not circumstellar Fe is present.

2.5.2 General abundance discussion

As the FUSE and STIS spectra have been composed of multiple observations, the uncertainty on the flux is extremely small. Misleadingly, abundance measurements made using these data will also has a very small uncertainty. The accuracy of any abundance measurement will depend upon the quality of the atomic data supplied in model atmosphere calculations, and correspondingly, the calculated ionisation balance of the metal being considered. The ionisation potential of a particular ion can be determined to good precision, however, the oscillator strength of a transition is rarely known to an accuracy exceeding 10%. Therefore, it is stressed that any uncertainties quoted in the abundances for this work be interpreted as a statistical quantity.

In Figure 2.13, the measured WD0501+524 abundances are plotted, along with the corresponding predicted radiative levitation abundances of Chayer et al. (1994, 1995a,b), and the observed solar abundances of Asplund et al. (2009). It can be seen that issues with the ionisation balance can introduce order of magnitude differences in the calculated abundance of different ionization stages. The largest discrepancy appears to be between P IV and P V, differing by ≈ 0.8 dex. Abundance determinations for C, N, and Si were in better agreement.

In comparison to the solar abundances of Asplund et al. (2009) and the radiative levitation abundances

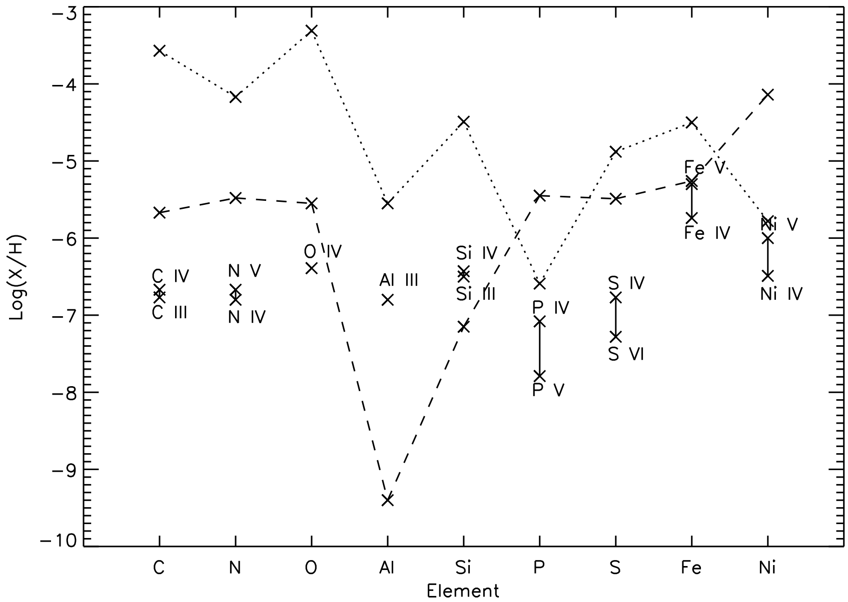

Figure 2.13: A comparison of abundances with respect to H for solar abundance (Asplund et al., 2009) (dotted line), atmospheric abundance as predicted from radiative levitation (dashed line) (Chayer et al. 1994, 1995a,b), and the atmospheric abundances determined in this study (solid line). The error bars are omitted for clarity.

from Chayer et al. (1994, 1995a,b), the only obvious agreement that can be seen is for Fe V and Ni V, where the former is in good agreement with the Chayer abundances, and the latter with the solar abundances.

2.5.3 Trans-Iron metals and other possible identifications

The vast majority of the absorption features present in WD0501+524's photosphere can be explained with Fe and Ni features. However, alternative identifications are possible. Of particular interest are the trans-iron metals, as these can only be synthesised in large stars.

Scandium

Two strong excited Sc IV transitions at 1424.662 and 1444.089Å have oscillator strengths of 1.71 and 1.34 respectively (Kentucky). No resonant transitions are available in this waveband. No features are detected around these wavelengths.

Titanium

Two Ti IV transitions at 1183.6283 and 1195.2036Å, oscillator strengths 0.145 and 0.150 respectively. No features are detected around these wavelengths.

Vanadium

There are many transitions of V IV and V V in the STIS waveband. The two strongest transitions originate from V V, and have wavelengths of 1490.1047 and 1499.5939Å, with oscillator strengths 1.25 and 1.29 respectively. No features are detected at, or around these wavelengths. Furthermore, LTE models from

SYNSPEC show that V V features begin to develop only at abundances of $\approx 10^{-6}$, which appears unlikely compared to Fe. An upper limit was placed on the V abundance in WD0501+524 of 1.00×10^{-8} by Holberg et al. (2003).

Chromium

There are many strong Cr VI features that fall into the FUSE and STIS waveband, however, the ionization potential of Cr V is higher than that for Fe V, meaning that any Cr VI lines will be much more difficult to detect than Fe VI features. The strongest Cr VI in the FUSE/STIS waveband is Cr VI 1107.220Å, with oscillator strength 1.35. No detections are made of this feature. The strongest Cr V line in the FUSE and STIS wavebands lies at 1127.631Å, with an oscillator strength of 0.815. No detections were made of this line. An upper limit was placed on the Cr abundance in WD0501+524 of 1.00×10^{-8} by Holberg et al. (2003).

Manganese

No resonant Mn IV-VI transitions are listed in the Kentucky database, however, there are several strong lines such as Mn VI 1333.874Å with an oscillator strength of 0.343. No detections were made of any of the listed strong Mn transitions. An upper limit was placed on the Mn abundance in WD0501+524 of 1.00×10^{-8} by Holberg et al. (2003).

Cobalt

Several transitions of Co IV-VI are listed in the Kentucky database, however, none of these are accompanied by oscillator strengths. None of the listed lines were detected in the analysis, and any possible lines were coincident with Fe or Ni transitions. An upper limit was placed on the Co abundance in WD0501+524 of 1.00×10^{-8} by Holberg et al. (2003).

Zinc

Zn is a recent proposed discovery by Rauch et al. (2013). Many of the Zn features claimed by the authors either have centroid wavelength uncertainties > 0.02 (e.g. Zn IV 1352.883Å), or do not appear in the spectrum used in the analysis presented in this thesis (e.g. Zn IV 1283.478Å). Furthermore, the vast majority of the features can be explained by Fe and Ni transitions. As all the proposed detections of Zn originate from excited transitions of Zn IV and Zn V, it is difficult to say whether or not this metal is present.

Arsenic

Two resonant transitions exist in the FUSE waveband, with wavelengths 987.70 and 1029.50Å. No oscillator strengths are recorded for these transitions. Two absorption features at 987.746 and 1029.536Å were detected, and identified as Fe V 987.673 and Fe IV 1029.446Å respectively, however, no oscillator strengths are given in the Kentucky database for either of these. It is therefore possible that these absorption features could be caused by either Fe or As.

Tin

The resonant Sn IV 1315Å detection was claimed by Vennes et al. (2005). It is coincident with an Fe V transition at 1314.527Å. Until more detections are made of this metal, it is unlikely this is a realistic identification.

Barium

A very speculative identification of the excited transitions Ba VI 953.39 and Ba VII 993.41Åwas made by Rauch et al. (2014b). The former is blended with an ISM N I line, however, meaning the signal from Ba VI is dominated by the N I ISM line. An absorption feature at 993.448Åwas detected, and identified as Ni IV 993.376Å. While it is possible that Ba VII could be blended with the Ni IV line, it seems highly unlikely due to it's high ionisation state. This is because the ionisation energy of Ba VII is 86eV, whereas for Fe VI, it is 99eV (Kramida et al., 2013). Only a handful of Fe VI features were detected in the aforementioned survey, and were of small equivalent width. As it takes a similar amount of energy to ionise Ba VII, it is logical to assume that any Ba VII absorption features would be very small. Furthermore, Rauch et al. (2014b) calculated a Ba mass fractional abundance 22,000 times solar, which appears to be unusually large.

Lead

A tentative detection of Pb IV 1313.072Å was made by Vennes et al. (2005) using three individual E140M STIS data of WD0501+524. The coadded spectrum used in this Chapter showed no absorption features in the region that Pb IV would appear.

2.5.4 Opacity considerations

Given that the spectrum of WD0501+524 is dominated by a large number of Fe and Ni lines, it raises the question of how well the opacity of these metals has been accounted for in model atmosphere calculations. The radiative levitation calculations of Chayer et al. (1995a) were performed using atomic datasets from different generations, and the resulting predicted atmospheric abundances were then compared with each other (cf. Chayer et al. 1995a, Figure 11). They concluded that both the number of lines included in such calculations, along with their respective oscillator strengths, had an effect on the predicted atmospheric abundances due to radiative levitation. This result further implies, that the atomic data sets used in these calculations must be as complete and as accurate as possible. It is seen in Figure 2.4 that significantly more Fe and Ni lines are included in the Kentucky database than the Kurucz (1992) data release. In fact, the latest data release from Kurucz (2011) contains more lines still. In Table 2.12, the number of available transitions for Fe and Ni IV-VII is given for the Kurucz (1992) and Kurucz (2011) data releases, the latter of which contains more than an order of magnitude transitions than the former.

This may, therefore, have an effect not only on the predicted radiative levitation abundances, but also on the spectral energy distribution in NLTE model atmosphere calculations. Such an effect was observed by Barstow et al. (1998) who compared $T_{\rm eff}$ and log g determinations using a pure H model atmosphere, and one with Fe and Ni. They found that, compared to the pure H models, the metal-polluted models yielded a

Table 2.12: The number of lines present in the Kurucz linelist in 1992 and 2011 for Fe and Ni IV-VII.

Ion	No of lines 1992	No of lines 2011
Fe IV	1,776,984	14,617,228
Fe V	1,008,385	7,785,320
Fe VI	475,750	9,072,714
Fe VII	90,250	2,916,992
Ni IV	1,918,070	15,152,636
Ni V	1,971,819	15,622,452
Ni VI	2,211,919	17,971,672
Ni VII	967,466	28,328,012
Total	10,420,643	111,467,026

lower $T_{\rm eff}$ by a few thousand K. Heavy metal line blanketing also causes significant flux attentuation in the EUV sector of the spectral energy distribution.

2.6 Conclusion

An in-depth spectroscopic survey of the hot DA white dwarf WD0501+524 has been performed using coadded FUSE and STIS spectra. The S/N of these spectra far exceeds any currently available for white dwarfs at present, and in the foreseeable future. Out of 976 detected absorption features, 947 were identified using a combined linelist from Kurucz (1992), and aided by the combined Kurucz/Kentucky line list. All lines detected in the FUSE spectrum now possess an identification, whereas only a handful in the STIS spectrum remain unknown. More than 60% of the absorption features identified can be attributed to highly ionized Fe and Ni features. This has raised questions on the efficacy of current model atmosphere calculations in accounting for the opacity bestowed by Fe and Ni. Circumstellar features attributed to Si IV 1393 and 1402Å have been detected. Their velocities are in agreement with the measured velocity of the Hyades cloud. A potentially new Si III circumstellar feature has also been detected.

2.7 Summary

- Three high S/N spectra were constructed of the hot DA white dwarf WD0501+524. One was constructed using 47 datasets obtained by FUSE, covering 910-1185Å, while the other two were obtained by STIS aboard the HST, consisting of 32 E140H and 66 E230H observations, covering the wavelength ranges of 1160-1650 and 1650-3200Å respectively.

- A spectral survey was conducted of these coadded spectra. 976 absorption features were detected, 947 of which can be assigned a detection. All FUSE absorption features are now identified, while only a few features in the STIS spectra remain. The vast majority of these identified features (600+) can be attributed to Fe and Ni IV-VI.

- An NLTE abundance for Al in WD0501+524 was derived, followed by updated abundance values for C, N, O, Si, P, S, Fe, and Ni.

- Atomic data used in previous model atmosphere calculations contain far fewer Fe and Ni transitions than are actually available today. This raises the question of how well model atmosphere calculations account for the opacity of Fe and Ni, and whether the completeness of atomic data has a significant effect on such calculations.

Chapter 3

Atomic data calculations for NLTE model atmospheres

3.1 Introduction

The presence of heavy metals in WD atmospheres can have dramatic effects on both the structure of the atmosphere, and the observed values of T_{eff} and log g. The additional opacity from these metals redistributes the flux from short wavelengths in the EUV, to longer ones in the UV and optical wavebands. In terms of the structure, the additional opacity decreases the amount of light passing from the deeper layers of the atmosphere, to the upper layers, increasing the temperature. This can be seen in Figure 3.1, where the variation of temperature with column mass (increasing depth) for a WD with T_{eff}=52500K and log g=7.53 is plotted both for a pure H atmosphere, and a fully line blanketed atmosphere (Preval et al. 2013 abundances).

The effect of heavy metal line blanketing on the measured T_{eff} of hot DA white dwarfs was effectively demonstrated by Barstow et al. (1998). The authors determined the T_{eff} and log g of several hot DA white dwarfs using a set of model atmosphere grids, which were either pure Hydrogen & Helium, or heavy metal-polluted. It was found that the T_{eff} determined using the pure H model grid was $\approx 4000 - 7000$K higher than if a heavy metal-polluted model grid were used. Conversely, there was little to no difference in the measured log g when using either model grid.

As well as the metal content of a white dwarf atmosphere, it can be inferred that the completeness of the atomic data supplied in model calculations can have a significant effect on the measured T_{eff} and log g. A study by Chayer et al. (1995a) considered the effects of radiative levitation on the observed atmospheric metal abundances at different T_{eff} and log g. In addition, these calculations were done using Fe data sets of varying line content. It was found that the number of transitions included in the calculation greatly affected the expected Fe abundance in the atmosphere (cf. Chayer et al. 1995a, Figure 11). This result implies that the macroscopic quantities determined in a white dwarf, such as metal abundance, are extremely sensitive to the input physics used to calculate the model grids. Therefore, this means that any atomic data that is supplied to the calculation must be as complete and accurate as possible in order to calculate the most representative model. While the Chayer et al. (1995a) study considered only the variations in observed Fe abundance, it is not unreasonable to assume that the set of atomic data supplied may also have an impact on the T_{eff} and log g measured.

Many studies using model atmospheres calculated by TLUSTY (e.g. Barstow et al. 1998; Vennes & Lanz 2001 etc.) utilised the Kurucz (1992) data release (hereafter Ku92) in conjunction with photoionization (PI) data from the Opacity Project (OP) for Fe, and approximate hydrogenic PI cross sections (σ_{HPI} in mega

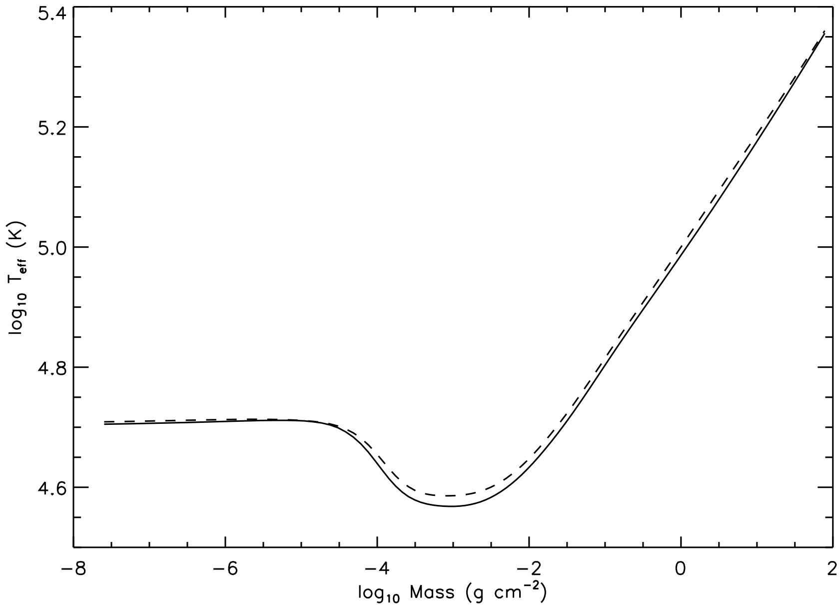

Figure 3.1: Variation of temperature with mass column (increasing depth) in a WD with $T_{\rm eff}$=52500K and log g=7.53. The solid curve is for a pure H model atmosphere, while the dashed curve is for a fully line blanketed model atmosphere with WD0501+524 abundances.

barns) for Ni, which can be calculated with the equation:

$$\sigma_{HPI} = \frac{2.815 \times 10^{47} Z^4}{\nu^3 n^5}, \tag{3.1}$$

where n is the principle quantum number of the state, ν is the incoming photon frequency, and $Z = N_z - N_e + 1$ is the effective charge, with N_z the number of protons and N_e the number of electrons. Model atmospheres using the Ku92 data include $\approx 10^7$ transitions of Fe and Ni in the calculation. The latest data release from Kurucz (2011) (hereafter Ku11) has $\approx 10^8$ transitions for Fe and Ni IV-VI alone.

In this Chapter, the dependency of model atmosphere calculations on the atomic data set supplied is considered in detail. The Ku11 data release is not accompanied by PI data, and needs to be calculated for Fe and Ni IV-VI. To this end, the atomic collision package AUTOSTRUCTURE is utilised. With the new PI data, model ions are constructed for use with TLUSTY. Using the metal abundances determined for WD0501+524 in Chapter 2, model atmospheres are calculated using both the Ku92 and Ku11 data sets, and compared directly. The differences between models using the Ku92 and Ku11 data with varying $T_{\rm eff}$ and log g are also considered.

3.2 Calculations

3.2.1 Atomic Data

The differences between the Ku92 and Ku11 data releases were touched upon in Chapter 2. In Table 2.12, it was shown that Ku11 has a factor ≈ 10 more transtions than Ku92. In Figures 3.2 and 3.3, a histogram is plotted showing the number of transitions per 15nm bin for the Ku92 and Ku11 data releases respectively. It

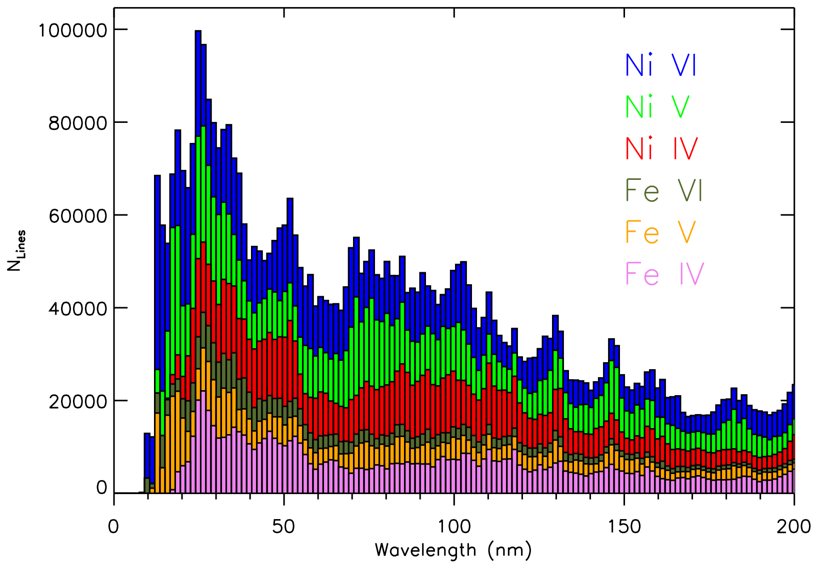

Figure 3.2: Number of available transitions from the Kurucz (1992) data release for Fe and Ni IV-VI.

is evident that the majority of the data improvements are in the EUV region (0-50nm). In both the Ku92 and Ku11 data sets, the atomic quantities are calculated using the Cowan Code (Cowan, 1981), which utilises the Hartree Fock method. This method assumes that the wavefunction of an N-electron atom/ion can be approximated as a slater determinant containing single particle spin-orbit wavefunctions χ, dependent upon position x. The slater determinant for such a system can be written generally as

$$\Psi(x_1, x_2, .., x_N) = \begin{vmatrix} \chi_1(x_1) & \chi_2(x_1) & \cdots & \chi_N(x_1) \\ \chi_1(x_2) & \chi_2(x_2) & \cdots & \chi_N(x_2) \\ \vdots & \vdots & \ddots & \vdots \\ \chi_1(x_N) & \chi_2(x_N) & \cdots & \chi_N(x_N) \end{vmatrix}. \tag{3.2}$$

Using the variational method, a set of N coupled equations can be derived for each χ, and then solved to determine the wavefunction and energy of the system.

3.2.2 AUTOSTRUCTURE

AUTOSTRUCTURE (Badnell, 1986, 1997, 2011) is an atomic structure package that can model several aspects of an arbitrary atom/ion a priori, including energy levels, transition oscillator strengths, excitation rates, PI cross sections, and many others. The software was written in Fortran 77, and has been adapted for use in Fortran 95. AUTOSTRUCTURE is supplied with a set of configurations describing the number of electrons and the quantum numbers occupied for a given atom or ion. The wavefunction P_{nl} for a particular configuration is obtained by solving the one particle Schrodinger equation

$$\left[\frac{d^2}{dr^2} - \frac{l(l+1)}{r^2} + 2V_{\mathrm{TFDA}}(r) + E_{nl}\right] P_{nl} = 0, \tag{3.3}$$

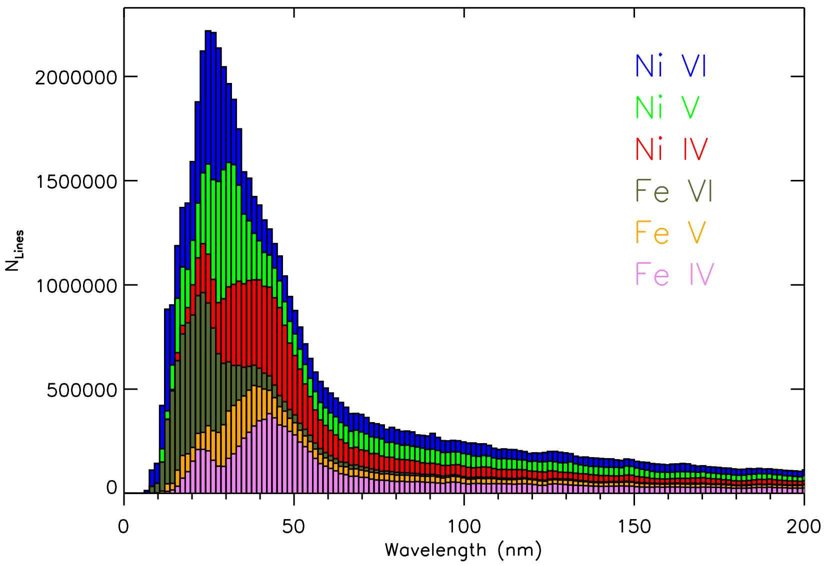

Figure 3.3: Number of available transitions from the Kurucz (2011) data release for Fe and Ni IV-VI.

where n and l are the principle and orbital angular momentum quantum numbers respectively, and V_{TFDA} is the Thomas-Fermi-Dirac-Amaldi (TFDA) potential, which accounts for the presence of other electrons, given by

$$V_{\mathrm{TFDA}} = \frac{Z_{\mathrm{eff}}(\lambda_{nl}, r)}{r} = -\frac{Z}{r}\phi(r), \tag{3.4}$$

where Z_{eff} is an effective charge 'seen' by the electron, a function of radial distance and scaling constants λ_{nl}, Z is the atomic number, and $\phi(r)$ is a continuous function given by

$$\phi(r) = \exp\left[-\frac{Zr}{2}\right] + \lambda_{nl}\left(1 - \exp\left[-\frac{Zr}{2}\right]\right). \tag{3.5}$$

λ_{nl}, like Z_{eff}, is related to the effective charge 'seen' by a particular valence electron, and typically has a value close to unity, and can be varied according to the task. For example, the parameters may be varied to minimise the energy functional of the solution, or they may be varied such that the difference between the calculated energy levels and a set of observed energy levels is minimised. Three coupling schemes are available in calculating the wavefunctions, dependent upon the resolution required, and the type of problem being considered. These are Spin-Orbit coupling (LS), Intermediate Coupling (IC), or Relativistic Intermediate Coupling (ICR). ICR is used in the case of heavy ions where the valence electrons are moving at relativistic speeds. In this case, $(Z\alpha)^2 \sim 1$.

For this work, IC is chosen with the aim of reproducing the energy levels from Ku11 as closely as possible. The energy level structure is first determined by running AUTOSTRUCTURE with the configurations used by Ku11 as input. These configurations are listed in Table 3.1, along with the number of configurations, the number of energy levels, and the number of E1 transitions (transitions that obey the electric dipole selection rules). With this information, 17 scaling parameters are then specified for orbitals 1s to 6s set initially to unity. The 1s parameter is fixed, as non relativistic corrections to this orbital tend to infinity for Fe and Ni. The result of parameter variation is given in Table 3.2.

Table 3.1: Configurations used in AUTOSTRUCTURE *calculations. Configurations in bold typeset represent the ground state configuration.*

Ion	Configurations	N_{config}	Levels	Lines
Fe IV	$\mathbf{3d^5}$, $3d^44d$, $3d^45d$, $3d^46d$, $3d^47d$, $3d^48d$	115	27,978	25,312,781
	$3d^49d$, $3d^410d$, $3d^34s4d$, $3d^34s5d$, $3d^34s6d$, $3d^34s7d$			
	$3d^34s8d$, $3d^34s9d$, $3d^34s10d$, $3d^24s^24d$, $3d^24s^25d$, $3d^24s^26d$			
	$3d^24s^27d$, $3d^24s^28d$, $3d^24s^29d$, $3d^24s^210d$, $3d^44s$, $3d^45s$			
	$3d^46s$, $3d^47s$, $3d^48s$, $3d^49s$, $3d^410s$, $3d^34s^2$			
	$3d^34s5s$, $3d^34s6s$, $3d^34s7s$, $3d^34s8s$, $3d^34s9s$, $3d^34s10s$			
	$3d^24s^25s$, $3d^24s^26s$, $3d^24s^27s$, $3d^24s^28s$, $3d^24s^29s$, $3d^24s^210s$			
	$3d^45g$, $3d^46g$, $3d^47g$, $3d^48g$, $3d^49g$, $3d^34s5g$			
	$3d^34s6g$, $3d^34s7g$, $3d^34s8g$, $3d^34s9g$, $3d^47i$, $3d^48i$			
	$3d^49i$, $3d^34s7i$, $3d^34s8i$, $3d^34s9i$, $3d^49l$, $3d^34s9l$, $3d^34p^2$			
	$3d^44p$, $3d^45p$, $3d^46p$, $3d^47p$, $3d^48p$, $3d^49p$			
	$3d^410p$, $3d^34s4p$, $3d^34s5p$, $3d^34s6p$, $3d^34s7p$, $3d^34s8p$			
	$3d^34s9p$, $3d^34s10p$, $3d^24s^24p$, $3d^24s^25p$, $3d^24s^26p$, $3d^24s^27p$			
	$3d^24s^28p$, $3d^24s^29p$, $3d^24s^210p$, $3d^44f$, $3d^45f$, $3d^46f$			
	$3d^47f$, $3d^48f$, $3d^49f$, $3d^410f$, $3d^34s4f$, $3d^34s5f$			
	$3d^34s6f$, $3d^34s7f$, $3d^34s8f$, $3d^34s9f$, $3d^34s10f$, $3d^24s^24f$			
	$3d^24s^25f$, $3d^24s^26f$, $3d^24s^27f$, $3d^24s^28f$, $3d^24s^29f$, $3d^24s^210f$			
	$3d^46h$, $3d^47h$, $3d^48h$, $3d^49h$, $3d^34s6h$, $3d^34s7h$			
	$3d^34s8h$, $3d^34s9h$, $3d^48k$, $3d^49k$, $3d^34s8k$, $3d^34s9k$			
Fe V	$\mathbf{3d^4}$, $3d^34d$, $3d^35d$, $3d^36d$, $3d^37d$, $3d^38d$	121	14,086	11,674,853
	$3d^39d$, $3d^310d$, $3d^24s4d$, $3d^24s5d$, $3d^24s6d$, $3d^24s7d$			
	$3d^24s8d$, $3d^24s9d$, $3d^24s10d$, $3d4s^24d$, $3d4s^25d$, $3d4s^26d$			
	$3d4s^27d$, $3d4s^28d$, $3d4s^29d$, $3d4s^210d$, $3d^34s$, $3d^35s$			
	$3d^36s$, $3d^37s$, $3d^38s$, $3d^39s$, $3d^310s$, $3d^24s^2$			
	$3d^24s5s$, $3d^24s6s$, $3d^24s7s$, $3d^24s8s$, $3d^24s9s$, $3d^24s10s$			
	$3d4s^25s$, $3d4s^26s$, $3d4s^27s$, $3d4s^28s$, $3d4s^29s$, $3d4s^210s$			
	$3d^35g$, $3d^36g$, $3d^37g$, $3d^38g$, $3d^39g$, $3d^310g$			
	$3d^24s5g$, $3d^24s6g$, $3d^24s7g$, $3d^24s8g$, $3d^24s9g$, $3d^24s10g$			
	$3d^37i$, $3d^38i$, $3d^39i$, $3d^24s7i$, $3d^24s8i$, $3d^24s9i$, $3d^24p^2$			
	$3d^34p$, $3d^35p$, $3d^36p$, $3d^37p$, $3d^38p$, $3d^39p$			
	$3d^310p$, $3d^311p$, $3d^24s4p$, $3d^24s5p$, $3d^24s6p$, $3d^24s7p$			
	$3d^24s8p$, $3d^24s9p$, $3d^24s10p$, $3d^24s11p$, $3d4s^24p$, $3d4s^25p$			
	$3d4s^26p$, $3d4s^27p$, $3d4s^28p$, $3d4s^29p$, $3d4s^210p$, $3d4s^211p$			
	$3d^34f$, $3d^35f$, $3d^36f$, $3d^37f$, $3d^38f$, $3d^39f$			
	$3d^310f$, $3d^311f$, $3d^24s4f$, $3d^24s5f$, $3d^24s6f$, $3d^24s7f$			
	$3d^24s8f$, $3d^24s9f$, $3d^24s10f$, $3d^24s11f$, $3d4s^24f$, $3d4s^25f$			
	$3d4s^26f$, $3d4s^27f$, $3d4s^28f$, $3d4s^29f$, $3d4s^210f$, $3d4s^211f$			
	$3d^36h$, $3d^37h$, $3d^38h$, $3d^39h$, $3d^24s6h$, $3d^24s7h$			
	$3d^24s8h$, $3d^24s9h$, $3d^38k$, $3d^39k$, $3d^24s8k$, $3d^24s9k$, p^53d^5			

Table 3.1: continued.

Ion	Configurations	N_{config}	Levels	Lines
Fe VI	$\mathbf{3d^3}$, $3d^24d$, $3d^25d$, $3d^26d$, $3d^27d$, $3d^28d$	146	22,257	13,731,648
	$3d^29d$, $3d^210d$, $3d^211d$, $3d4s4d$, $3d4s5d$, $3d4s6d$			
	$3d4s7d$, $3d4s8d$, $3d4s9d$, $3d4s10d$, $3d4s11d$, $4s^24d$			
	$4s^25d$, $4s^26d$, $4s^27d$, $4s^28d$, $4s^29d$, $4s^210d$			
	$3d^24s$, $3d^25s$, $3d^26s$, $3d^27s$, $3d^28s$, $3d^29s$			
	$3d^210s$, $3d4s2$, $3d4s5s$, $3d4s6s$, $3d4s7s$, $3d4s8s$			
	$3d4s9s$, $3d4s10s$, $4s^25s$, $4s^26s$, $4s^27s$, $4s^28s$			
	$4s^29s$, $4s^210s$, $3d^25g$, $3d^26g$, $3d^27g$, $3d^28g$			
	$3d^29g$, $3d4s5g$, $3d4s6g$, $3d4s7g$, $3d4s8g$, $3d4s9g$			
	$3d^27i$, $3d^28i$, $3d^29i$, $3d4s7i$, $3d4s8i$, $3d4s9i$			
	$3d4p^2$, $3p^5d^34p$, $3p^53d^35p$, $3p^53d^36p$, $3p^53d^37p$, $3p^53d^38p$			
	$3p^53d^39p$, $3p^5d^34f$, $3p^53d^35f$, $3p^53d^36f$, $3p^53d^37f$, $3p^53d^38f$			
	$3p^53d^39f$, $3d^24p$, $3d^25p$, $3d^26p$, $3d^27p$, $3d^28p$, $3d^29p$			
	$3d^210p$, $3d^211p$, $3d4s4p$, $3d4s5p$, $3d4s6p$, $3d4s7p$			
	$3d4s8p$, $3d4s9p$, $3d4s10p$, $3d4s11p$, $4s^24p$, $4s^25p$			
	$4s^26p$, $4s^27p$, $4s^28p$, $4s^29p$, $4s^210p$, $4s^211p$			
	$3d^24f$, $3d^25f$, $3d^26f$, $3d^27f$, $3d^28f$, $3d^29f$			
	$3d^210f$, $3d^211f$, $3d4s4f$, $3d4s5f$, $3d4s6f$, $3d4s7f$			
	$3d4s8f$, $3d4s9f$, $3d4s10f$, $3d4s11f$, $4s^24f$, $4s^25f$			
	$4s^26f$, $4s^27f$, $4s^28f$, $4s^29f$, $4s^210f$, $4s^211f$			
	$3d^26h$, $3d^27h$, $3d^28h$, $3d^29h$, $3d4s6h$, $3d4s7h$			
	$3d4s8h$, $3d4s9h$, $3d^28k$, $3d^29k$, $3d4s8k$, $3d4s9k$			
	$3p^53d^4$, $3p^53d^34s$, $3p^53d^35s$, $3p^53d^36s$, $3p^53d^37s$, $3p^53d^38s$			
	$3p^53d^39s$, $3p^53d^34d$, $3p^53d^35d$, $3p^53d^36d$, $3p^53d^37d$, $3p^53d^38d$			
	$3p^53d^39d$			
Ni IV	$\mathbf{3d^7}$, $3d^64s$, $3d^65s$, $3d^66s$, $3d^67s$, $3d^68s$	85	37,860	32,416,571
	$3d^69s$, $3d^54s^2$, $3d^54s5s$, $3d^54s6s$, $3d^54s7s$, $3d^54s8s$			
	$3d^54s9s$, $3d^44s^25s$, $3d^64d$, $3d^65d$, $3d^66d$, $3d^67d$			
	$3d^68d$, $3d^69d$, $3d^54s4d$, $3d^54s5d$, $3d^54s6d$, $3d^54s7d$			
	$3d^54s8d$, $3d^54s9d$, $3d^44s^24d$, $3d^54p^2$, $3d^65g$, $3d^66g$			
	$3d^67g$, $3d^68g$, $3d^69g$, $3d^54s5g$, $3d^54s6g$, $3d^54s7g$			
	$3d^54s8g$, $3d^54s9g$, $3d^67i$, $3d^68i$, $3d^69i$, $3d^54s7i$			
	$3d^54s8i$, $3d^54s9i$			
	$3d^64p$, $3d^65p$, $3d^66p$, $3d^67p$, $3d^68p$, $3d^69p$			
	$3d^54s4p$, $3d^54s5p$, $3d^54s6p$, $3d^54s7p$, $3d^54s8p$, $3d^54s9p$			
	$3d^44s^24p$, $3d^64f$, $3d^65f$, $3d^66f$, $3d^67f$, $3d^68f$			
	$3d^69f$, $3d^54s4f$, $3d^54s5f$, $3d^54s6f$, $3d^54s7f$, $3d^54s8f$			
	$3d^54s9f$, $3d^44s^24f$, $3d^66h$, $3d^67h$, $3d^68h$, $3d^69h$			
	$3d^54s6h$, $3d^54s7h$, $3d^54s8h$, $3d^54s9h$, $3d^68k$, $3d^69k$			
	$3d^54s8k$, $3d^54s9k$, $3p^53d^8$			

Table 3.1: continued.

Ion	Configurations	N_{config}	Levels	Lines
Ni V	$\mathbf{3d^6}$, $3d^54d$, $3d^55d$, $3d^56d$, $3d^57d$, $3d^58d$	87	37,446	34,066,259
	$3d^59d$, $3d^510d$, $3d^44s4d$, $3d^44s5d$, $3d^44s6d$, $3d^44s7d$			
	$3d^44s8d$, $3d^44s9d$, $3d^44s10d$, $3d^54s$, $3d^55s$, $3d^56s$			
	$3d^57s$, $3d^58s$, $3d^59s$, $3d^510s$, $3d^44s^2$, $3d^44s5s$			
	$3d^44s6s$, $3d^44s7s$, $3d^44s8s$, $3d^44s9s$, $3d^44s10s$, $3d^55g$			
	$3d^56g$, $3d^57g$, $3d^58g$, $3d^59g$, $3d^44s5g$, $3d^44s6g$			
	$3d^44s7g$, $3d^44s8g$, $3d^44s9g$, $3d^57i$, $3d^58i$, $3d^59i$			
	$3d^44s7i$, $3d^44s8i$, $3d^44s9i$, $3d^44p^2$			
	$3d^54p$, $3d^55p$, $3d^56p$, $3d^57p$, $3d^58p$, $3d^59p$			
	$3d^510p$, $3d^44s4p$, $3d^44s5p$, $3d^44s6p$, $3d^44s7p$, $3d^44s8p$			
	$3d^44s9p$, $3d^44s10p$, $3d^34s^24p$, $3d^54f$, $3d^55f$, $3d^56f$			
	$3d^57f$, $3d^58f$, $3d^59f$, $3d^510f$, $3d^44s4f$, $3d^44s5f$			
	$3d^44s6f$, $3d^44s7f$, $3d^44s8f$, $3d^44s9f$, $3d^56h$, $3d^57h$			
	$3d^58h$, $3d^59h$, $3d^44s6h$, $3d^44s7h$, $3d^44s8h$, $3d^44s9h$			
	$3d^58k$, $3d^59k$, $3d^44s8k$, $3d^44s9k$, $3p^53d^7$			
Ni VI	$\mathbf{3d^5}$, $3d^44d$, $3d^45d$, $3d^46d$, $3d^47d$, $3d^48d$	122	29,366	42,412,822
	$3d^49d$, $3d^410d$, $3d^34s4d$, $3d^34s5d$, $3d^34s6d$, $3d^34s7d$			
	$3d^34s8d$, $3d^34s9d$, $3d^34s10d$, $3d^24s^24d$, $3d^24s^25d$, $3d^24s^26d$			
	$3d^24s^27d$, $3d^24s^28d$, $3d^24s^29d$, $3d^24s^210d$, $3d^44s$, $3d^45s$			
	$3d^46s$, $3d^47s$, $3d^48s$, $3d^49s$, $3d^410s$, $3d^34s^2$			
	$3d^34s5s$, $3d^34s6s$, $3d^34s7s$, $3d^34s8s$, $3d^34s9s$, $3d^34s10s$			
	$3d^24s^25s$, $3d^24s^26s$, $3d^24s^27s$, $3d^24s^28s$, $3d^24s^29s$, $3d^24s^210s$			
	$3d^45g$, $3d^46g$, $3d^47g$, $3d^48g$, $3d^49g$, $3d^410g$			
	$3d^34s5g$, $3d^34s6g$, $3d^34s7g$, $3d^34s8g$, $3d^34s9g$, $3d^34s10g$			
	$3d^47i$, $3d^48i$, $3d^49i$, $3d^34s7i$, $3d^34s8i$, $3d^34s9i$, $3d^34p^2$			
	$3d^44p$, $3d^45p$, $3d^46p$, $3d^47p$, $3d^48p$, $3d^49p$			
	$3d^410p$, $3d^411p$, $3d^34s4p$, $3d^34s5p$, $3d^34s6p$, $3d^34s7p$			
	$3d^34s8p$, $3d^34s9p$, $3d^34s10p$, $3d^34s11p$, $3d^24s^24p$, $3d^24s^25p$			
	$3d^24s^26p$, $3d^24s^27p$, $3d^24s^28p$, $3d^24s^29p$, $3d^24s^210p$, $3d^24s^211p$			
	$3d^44f$, $3d^45f$, $3d^46f$, $3d^47f$, $3d^48f$, $3d^49f$			
	$3d^410f$, $3d^411f$, $3d^34s4f$, $3d^34s5f$, $3d^34s6f$, $3d^34s7f$			
	$3d^34s8f$, $3d^34s9f$, $3d^34s10f$, $3d^34s11f$, $3d^24s^24f$, $3d^24s^25f$			
	$3d^24s^26f$, $3d^24s^27f$, $3d^24s^28f$, $3d^24s^29f$, $3d^24s^210f$, $3d^24s^211f$			
	$3d^46h$, $3d^47h$, $3d^48h$, $3d^49h$, $3d^34s6h$, $3d^34s7h$			
	$3d^34s8h$, $3d^34s9h$, $3d^48k$, $3d^49k$, $3d^34s8k$, $3d^34s9k$, $3p^53d^6$			

Table 3.2: Calculated scaling parameters from AUTOSTRUCTURE *in IC.*

Orbital	Fe IV	Fe V	Fe VI	Ni IV	Ni V	Ni VI
$2s$	1.27136	1.26901	1.26352	1.31391	1.31355	1.31487
$2p$	1.10890	1.10716	1.10592	1.12294	1.12144	1.11996
$3s$	1.11519	1.12360	1.14834	1.09887	1.11219	1.12750
$3p$	1.07905	1.08949	1.10641	1.05876	1.07206	1.08779
$3d$	1.10512	1.08389	1.11233	1.06828	1.09148	1.10379
$4s$	1.17359	1.21672	1.24500	1.13492	1.15167	1.19770
$4p$	0.92665	1.00708	1.40784	0.91520	0.90669	0.92207
$4d$	1.48338	1.02701	1.24341	1.40156	1.48359	1.49036
$4f$	1.09963	1.41293	1.13062	1.08824	1.03771	1.10538
$5s$	0.93474	1.31696	1.08900	1.03946	1.03552	1.25294
$5p$	1.02441	1.00476	1.12634	0.99302	0.96743	1.00439
$5d$	1.12416	1.22077	1.11576	1.09409	1.08876	1.15671
$5f$	1.10263	1.03522	1.08938	1.06373	1.01089	1.01693
$5g$	1.14101	1.24661	1.26102	1.37199	1.17219	1.83712
$6s$	0.99837	1.13293	1.10759	1.02002	1.01140	1.05828

In Figure 3.4, the energy levels calculated by AUTOSTRUCTURE are compared to the energy levels calculated by Kurucz for ions Fe and Ni IV-VI. The agreeement between the two datasets is generally good, as demonstrated by the residuals between the AUTOSTRUCTURE energy levels and Ku11 in Figure 3.5.

Note that the number of transitions listed in Ku11 are less than the number of transitions calculated and predicted by AUTOSTRUCTURE . This is because the line list from Ku11 is truncated dependent upon a set of conditions. Observed or well known transitions with a log $gf < -9.99$, or predicted transitions with a log $gf < -7.5$ plus a Boltzmann factor are omitted. Purely autoionisation transitions (a transition between two autoionisation levels) are also omitted. In this study, the line list calculated by AUTOSTRUCTURE is truncated only by the autoionisation transitions. No log gf cutoff is applied. TLUSTY, however, DOES apply a frequency dependent cutoff, which is determined dynamically. Transitions are selected according to an upper and lower frequency boundary (ν_{max} and ν_{min} respectively)

$$\nu_{\rm max} = \mathbf{CNU1} \times 10^{11} \times T_{\rm eff} \quad , \quad \nu_{\rm min} = \frac{3.28805 \times 10^{15}}{\mathbf{CNU2}^2}, \tag{3.6}$$

where CNU1 and CNU2 are constants coded into TLUSTY that can be changed to vary the limits, and $T_{\rm eff}$ is the effective temperature. For the purposes of this analysis, CNU1=20, and CNU2=3, corresponding to lower and upper wavelength cutoffs of 28.6Å and 8205.9Å respectively.

After calculating a set of scaling parameters for a particular ion, the accompanying PI cross sections can be obtained. For simplicity, only direct, outer shell PI is considered, neglecting resonances from dielectronic recombination and radiative recombination. This approximation is justified due to the way TLUSTY accounts for heavy metal cross sections. TLUSTY samples a set of PI cross sections for particular photon energies, and may, therefore, miss any resonances in the PI cross section data.

As with calculating the energy levels of each configuration and set of quantum numbers, a set of configurations is also specified for the PI calculation. These configurations are obtained by removing the outermost electron in each of the configurations in Table 3.1. The resulting list of PI configurations is given in Table 3.3. The PI cross sections are evaluated for a table of 50 logarithmically spaced ejected electron energies

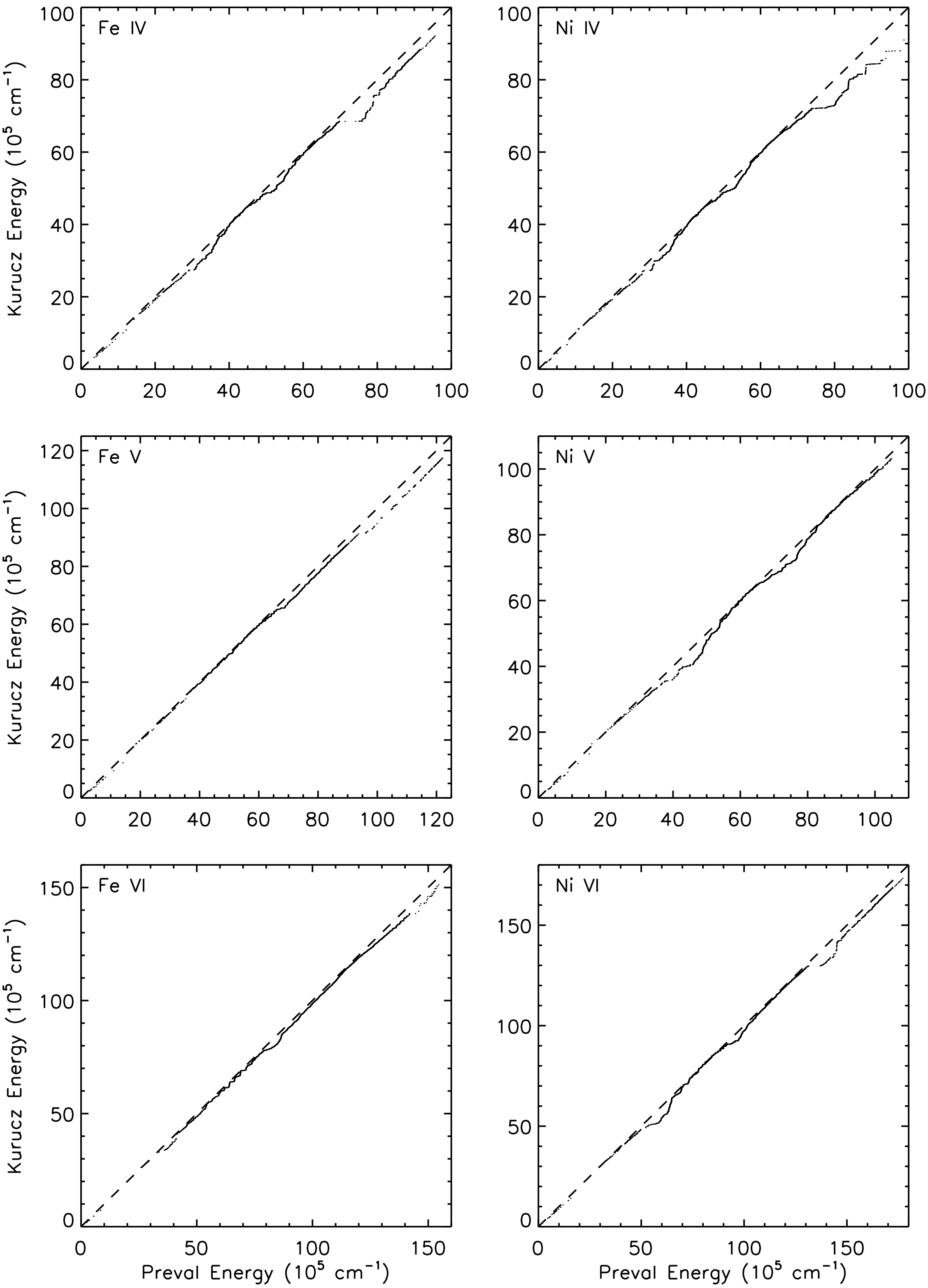

Figure 3.4: Comparison of energy levels determined in this work to that of Ku11. The dashed line is for equal Ku11 and AUTOSTRUCTURE *energies.*

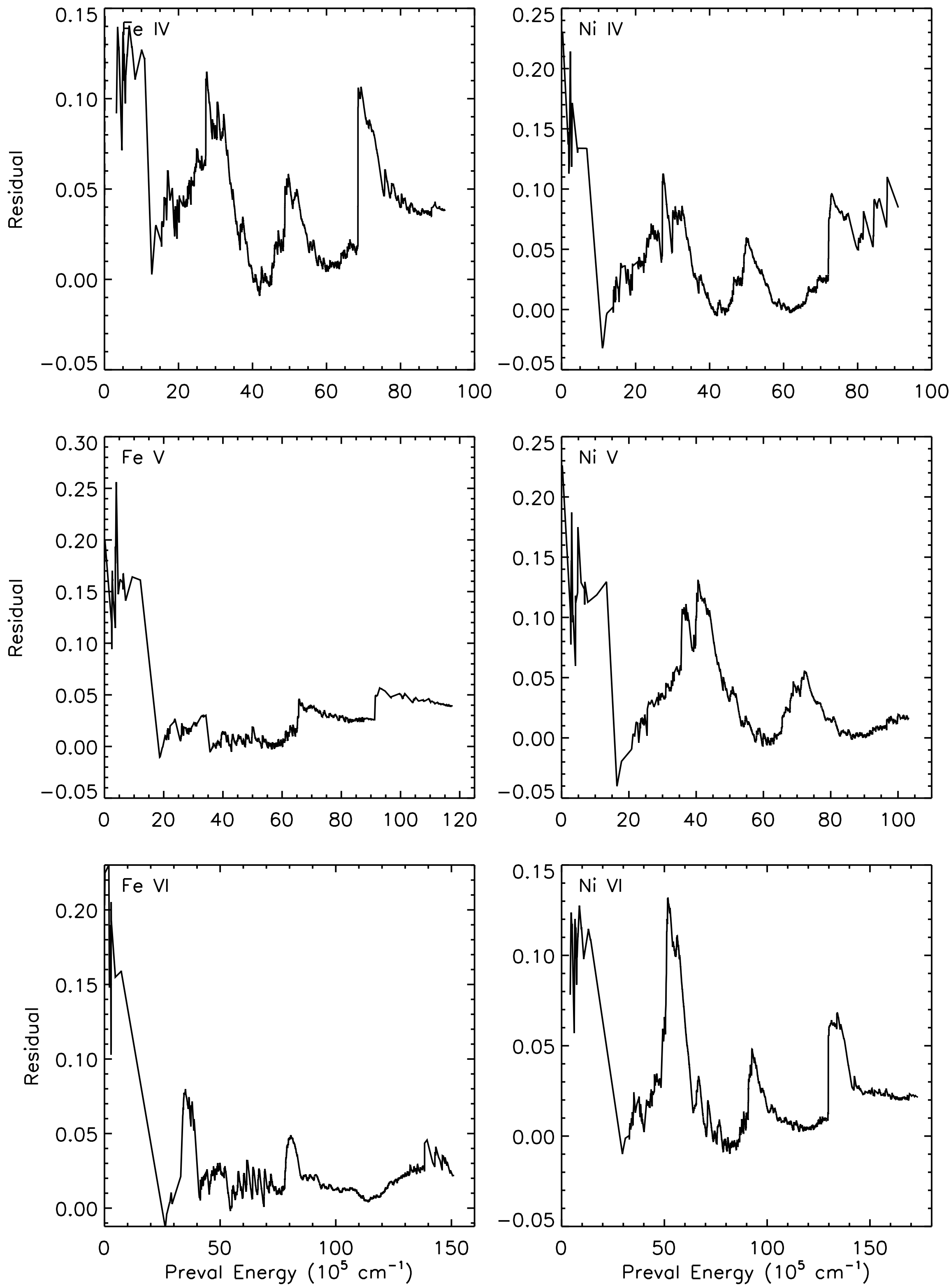

Figure 3.5: Residual between calculated energy levels (AUTOSTRUCTURE) and Ku11.

Table 3.3: *PI Configurations used in* AUTOSTRUCTURE *calculations.*

Ion	Configurations
Fe IV	$3d^4$, $3d^34s$, $3d^34p$, $3d^34s^2$
Fe V	$3p^53d^4$, $3d^3$, $3d^24s$, $3d^24p$, $3d4s^2$
Fe VI	$4s^2$, $3p^53d^3$, $3d^2$, $3d4s$, $3d4p$
Ni IV	$3p^53d^7$, $3d^6$, $3d^54s$, $3d^54p$, $3d^44s^2$
Ni V	$3p^53d^6$, $3d^5$, $3d^44s$, $3d^44p$, $3d^34s^2$
Ni VI	$3d^4$, $3p^53d^5$, $3d^34s$, $3d^34p$, $3d^24s^2$

spanning 0 to 100 Ryd. The cross sections in the ejected electron energy frame are then linearly interpolated to the incident photon energy frame using two point interpolation.

3.2.3 Model atoms

Representing all possible transitions that can occur for a particular atom/ion is computationally expensive. To treat the problem statistically, and hence make it tractable, a model ion is constructed, containing information on the bound/autoionisation energy levels, transitions, and bound-free cross sections. This model will use a truncated number of energy levels, so as to limit the number of transitions included in the radiative transfer solution. For ions with many energy levels, it is possible to group a number of levels together to form superlevels (Anderson, 1989), further decreasing the computational expense of calculating a model atmosphere.

The energy of a super level ($\bar{E}$) is calculated by taking the mean of a set of energy levels (E_i), weighted by the Boltzmann factor, and the statistical weight of the level (g_i):

$$\bar{E} = \frac{\sum_{i=1}^{N} E_i g_i \exp\left[-\frac{E_i}{kT}\right]}{\sum_{i=1}^{N} g_i \exp\left[-\frac{E_i}{kT}\right]}, \tag{3.7}$$

where k is the Boltzmann constant, and T is the temperature of the object being considered. For the work presented in this thesis, $T = 50000$K. The statistical weight of the superlevel, $\bar{g}$, is the sum of the statistical weights of all levels included in the superlevel:

$$\bar{g} = \sum_{i=1}^{N} g_i. \tag{3.8}$$

For each superlevel, an effective principal quantum is calculated:

$$n^* = \frac{Z}{\sqrt{\bar{E} - E_0}}, \tag{3.9}$$

where E_0 is the ionization energy of the ion. Note that $\bar{E}$ and E_0 are in Ryd.

For Fe and Ni, further input is required. Firstly, a list of the individual energy levels used to construct the superlevels is required, as well as the corresponding quantum numbers j, and three constants used to determine the line broadening, namely Sum A_i, C_4, and C_6. Sum A_i is the sum of all excitation rates from upper level i to all lower levels:

$$\mathrm{Sum}A_i = \sum_{j<i}^{N} A_{ij}. \tag{3.10}$$

C_4 is related to the Stark width of an energy level, which is the sensitivity of an energy level to the Stark effect, calculated as

$$C_4 = -\frac{c^2 e^4}{8\pi^2 hm} \sum_{k'} f_{kk'} \lambda^2, \tag{3.11}$$

where k and k' represent the initial and final states, $f_{kk'} = gf/g_k$ for $E_k < E_{k'}$ or $f_{kk'} = -gf/g_{k'}$ for $E_k > E_{k'}$. The sum covers all possible transitions from k to k'. C_6 is similar:

$$C_6 = \frac{3e^2 c}{8\pi^2 m} \alpha \sum_{k'} |f_{kk'} \lambda| , \tag{3.12}$$

where α is the atomic polarizability in atomic units. C_6 is akin to van der Waals' pressure broadening. Sum A_i, C_4, and C_6 are described in more detail in Kurucz (1981).

The second additional file is a list of electric dipole (E1) transitions. This contains the wavelength of the transitions in nm, the transition strength as log gf, and the indices of the levels involved in the transition (their position in the .gam file). Autoionisation transitions are not included in this list, as the corresponding levels involved are not populated for long enough to make a significant contribution to the overall opacity.

The final file contains a list of PI cross sections for each bound superlevel in the model ion. Again, the autoionisation levels are excluded. Typically, the cross sections are convolved with a Gaussian profile to form a Resonance Averaged Profile (Bautista et al., 1998). The purpose of this is to smooth out the autoionizing resonances, which are missed with the Opacity Sampling method. As direct PI has been employed in this work, there is no need to smooth the cross section. The PI cross section of a superlevel, $\bar{\sigma}_{PI}(E_\gamma)$, where E_γ is the incident photon energy, is calculated by taking the mean of the cross section for each level ($\sigma_i(E)$), weighted by g_i. This sum is performed for each incident photon energy :

$$\bar{\sigma}_{PI}(E_\gamma) = \frac{\sum_{i=1}^{N} \sigma_i(E) g_i}{\sum_{i=1}^{N} g_i} \tag{3.13}$$

Using the equations above, and the data calculated by AUTOSTRUCTURE, new model ions were constructed for Fe and Ni IV-VI. The Fe IV, V, and VI model ions have 93, 83, and 78 superlevels respectively, and the Ni IV, V, and VI model ions have 93, 93, and 87 superlevels respectively.

3.2.4 Model atmospheres

To assess the effects of the Ku11 opacity, the analysis was split into three parts. Firstly, two model atmospheres with the Ku92 and Ku11 data were calculated with $T_{\rm eff}$=52500K, log g=7.53, and abundances tabulated in Table 3.4. The model atoms listed in Table 2.7 are also used here. These abundances were taken from Table 2.10. They were chosen where the metal abundances had the lowest statistical error. The abundances were then remeasured using the method detailed in Chapter 2, and the absorption features listed in Table 2.9. Possible changes to the spectral energy distribution (SED) were considered next. Using the two model atmospheres described above, the residual between the Ku92 and Ku11 models was calculated in three different wavebands, namely the EUV (80-700Å), the UV (900-1700Å), and the optical (3200-5500Å).

Finally, the effects of the Ku92 and Ku11 atomic data on the calculated model with varying $T_{\rm eff}$ and log g was assessed. A model atmosphere grid was calculated for each set of atomic data, spanning $T_{\rm eff}$ of

Table 3.4: Metal abundances used in calculating the Ku11 line blanketed model atmosphere as a fraction of H. These abundances originate from Table 2.10, where the values with the lowest statistical uncertainty were used.

Metal	Abundance X/H
He	1.00×10^{-5}
C	1.72×10^{-7}
N	2.16×10^{-7}
O	4.12×10^{-7}
Al	1.60×10^{-7}
Si	3.68×10^{-7}
P	1.64×10^{-8}
S	1.71×10^{-7}
Fe	1.83×10^{-6}
Ni	1.01×10^{-6}

35000-100000K in steps of 2500K, and log g of 7.00, 8.00, and 9.00. To account for changes in the ionization balance with varying temperature, additional ions were included for C, N, O, and Si. The full list of model ions used for the Ku92 and Ku11 model atmosphere calculations are listed in Table 3.5. The same Fe and Ni model ions as listed in Table 2.7 are used with the Ku92 data, while the new ions described previously are used with the Ku11 data. The residuals of the two atmospheres at each point in the grid were calculated for the wavelength ranges 915-975Å in the UV, and 3700-4500Å in the optical. All model atmospheres were calculated with TLUSTY (Hubeny, 1988) version 201, and synthesised using SYNSPEC version 49 (Hubeny & Lanz, 2011). The EUV and UV spectra were synthesised using a list of transitions from Ku11.

3.3 Results & Discussion

3.3.1 Abundance variations

In Table 3.6, the WD0501+524 metal abundances determined in Chapter 2 are compared to the abundances determined using the Ku11 model. The values determined in the Ku11 model are quite similar to those determined in the Ku92 model. For example, for C III, the Ku92 model gave a value of $1.72^{+0.02}_{-0.02} \times 10^{-7}$, whereas the Ku11 model gave $1.74^{+0.02}_{-0.02} \times 10^{-7}$, a difference of $-0.02^{+0.02}_{-0.02} \times 10^{-7}$. However, in the case of N V, the Ku92 model gave $2.16^{+0.09}_{-0.04} \times 10^{-7}$, and the Ku11 model gave $1.21^{+0.01}_{-0.01} \times 10^{-7}$, which is a difference of $0.95^{+0.09}_{-0.04} \times 10^{-7}$. As well as N V, the abundances of O IV, P V, S IV, S VI, and Fe and Ni IV & V determined in the Ku11 model are consistent with a non-zero change from the Ku92 model (cf. Figure 3.6). It is noted, however, that ions with excellent atomic data, such as C, N, and Si, exhibit no differences between the Ku92 and Ku11 model values (bar N V), whereas ions with relatively poor/incomplete data such as P, S, Fe, and Ni exhibit large departures from the Ku92 model values. This would suggest that rather than the number of Fe and Ni transitions included in model atmosphere calculations, it is the quality of the atomic data supplied for each individual ion that causes a change in metal abundance. However, it is stressed that the differences between the Ku92 and Ku11 models have been quantified for only one star, meaning that this result is not conclusive. Therefore, until these model calculations are tested on multiple stars, and the atomic data is improved for the aforementioned ions, it would be difficult to determine observationally whether the Ku92

*Table 3.5: Model ions used to calculate the Ku92 and Ku11 model atmosphere grid spanning 35000-100000K, and log g spanning 7.00-9.00. The first three columns correspond to the ions used in the Ku92 calculations, and the last three columns to the ions in the Ku11 calculations. A '-' symbol in the 6th column means the same model ion was used as in the Ku92 calculation. Ions with a * next to the element name signify ions that were treated approximately by* TLUSTY *as a single level ion.*

Ku92 Element	Ion	No of Levels	Ku11 Element	Ion	No of Levels
H	I	9	H	I	-
H*	II	1	H*	II	-
He	I	24	He	I	-
He	II	20	He	II	-
He*	III	1	He*	I	-
C	I	26	C	I	-
C	II	22	C	II	-
C	III	23	C	III	-
C	IV	41	C	IV	-
C*	V	1	C*	V	-
N	I	21	N	I	-
N	II	26	N	II	-
N	III	32	N	III	-
N	IV	23	N	IV	-
N	V	16	N	V	-
N*	VI	1	N*	VI	-
O	I	22	O	I	-
O	II	29	O	II	-
O	III	29	O	III	-
O	IV	39	O	IV	-
O	V	40	O	V	-
O	VI	20	O	VI	-
O*	VII	1	O*	VII	-
Al	III	23	Al	III	-
Al*	IV	1	Al*	IV	-
Si	I	22	Si	I	-
Si	II	40	Si	II	-
Si	III	30	Si	III	-
Si	IV	23	Si	IV	-
Si*	V	1	Si*	V	-
P	IV	14	P	IV	-
P	V	17	P	V	-
P*	VI	1	P*	VI	-
S	III	20	S	III	-
S	IV	15	S	IV	-
S	V	12	S	V	-
S	VI	16	S	VI	-
S*	VII	1	S*	VII	-
Fe	IV	43	Fe	IV	93
Fe	V	42	Fe	V	83
Fe	VI	32	Fe	VI	78
Fe*	VII	1	Fe*	VII	-
Ni	IV	38	Ni	IV	93
Ni	V	48	Ni	V	93
Ni	VI	42	Ni	VI	87
Ni*	VII	1	Ni*	VII	-

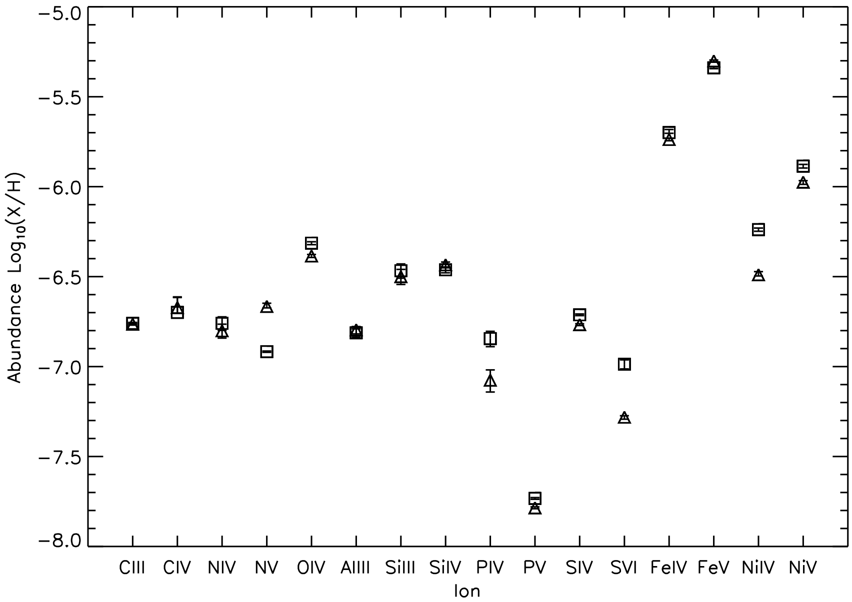

Figure 3.6: Plot of measure abundances for a model atmosphere calculated with the Ku92 data (triangles) and the Ku11 data (squares).

or Ku11 model was preferred.

3.3.2 SED variations

In Figure 3.7, the synthesised EUV spectra for the Ku92 and Ku11 models are plotted along with the residual between the two models, calculated as:

$$\text{Residual} = \frac{F_{Ku92} - F_{Ku11}}{F_{Ku92}}, \tag{3.14}$$

where F is the model flux. The EUV spectra in both the Ku92 and Ku11 model calculations are nearly identical for wavelengths > 200Å. Below this wavelength, the Ku11 model appears to emit more flux than the Ku92 model. As the Ku11 data is accompanied by calculations from AUTOSTRUCTURE, it is possible there are differences between the oscillator strengths from AUTOSTRUCTURE and Ku92. Therefore, this could result in a smaller opacity in the concerned wavelength regions, thus increasing the flux in the Ku11 model. There are little to no changes in the depths of the metal absorption features. This implies that the ionisation balance of various ions emitting in the EUV has not changed significantly between the Ku92 and Ku11 model. This is curious, as there were limited changes to the calculated metal abundances using lines in the UV.

As with Figure 3.7, the synthesised UV spectrum computed using the Ku92 and Ku11 data is plotted in Figure 3.8. There do not appear to be any significant changes to the H Lyman lines. However, multiple Fe and Ni absorption features have changed in strength.

In Figure 3.9, the optical spectrum of the Ku92 and Ku11 model atmospheres is plotted, along with the residual of the two. There is no detectable change in the continuum or the slope. Furthermore, there do not appear to be any significant differences in the calculated line profiles. In the Balmer line absorption cores,

Table 3.6: Summary of the abundances determined using a model atmosphere calculated with the Ku11 atomic data. The difference between these and the abundances determined in Chapter 2 are also given.

Ion	Preval et al. (2013)	This work	Difference
C III	$1.72^{+0.02}_{-0.02} \times 10^{-7}$	$1.74^{+0.02}_{-0.02} \times 10^{-7}$	$-0.02^{+0.02}_{-0.02} \times 10^{-7}$
C IV	$2.13^{+0.29}_{-0.15} \times 10^{-7}$	$2.00^{+0.44}_{-0.02} \times 10^{-7}$	$0.13^{+0.53}_{-0.15} \times 10^{-7}$
N IV	$1.58^{+0.14}_{-0.14} \times 10^{-7}$	$1.74^{+0.15}_{-0.15} \times 10^{-7}$	$-0.16^{+0.21}_{-0.21} \times 10^{-7}$
N V	$2.16^{+0.09}_{-0.04} \times 10^{-7}$	$1.21^{+0.01}_{-0.01} \times 10^{-7}$	$0.95^{+0.09}_{-0.04} \times 10^{-7}$
O IV	$4.12^{+0.08}_{-0.08} \times 10^{-7}$	$4.85^{+0.09}_{-0.09} \times 10^{-7}$	$-0.73^{+0.12}_{-0.12} \times 10^{-7}$
Al III	$1.60^{+0.07}_{-0.08} \times 10^{-7}$	$1.54^{+0.08}_{-0.08} \times 10^{-7}$	$0.06^{+0.11}_{-0.11} \times 10^{-7}$
Si III	$3.16^{+0.31}_{-0.30} \times 10^{-7}$	$3.41^{+0.31}_{-0.31} \times 10^{-7}$	$0.25^{+0.44}_{-0.43} \times 10^{-7}$
Si IV	$3.68^{+0.13}_{-0.14} \times 10^{-7}$	$3.45^{+0.13}_{-0.13} \times 10^{-7}$	$0.23^{+0.18}_{-0.19} \times 10^{-7}$
P IV	$8.40^{+1.18}_{-1.18} \times 10^{-8}$	$1.43^{+0.14}_{-0.14} \times 10^{-7}$	$0.59^{+1.83}_{-1.83} \times 10^{-8}$
P V	$1.64^{+0.02}_{-0.02} \times 10^{-8}$	$1.85^{+0.02}_{-0.02} \times 10^{-8}$	$0.21^{+0.03}_{-0.03} \times 10^{-8}$
S IV	$1.71^{+0.02}_{-0.02} \times 10^{-7}$	$1.94^{+0.02}_{-0.02} \times 10^{-7}$	$-0.23^{+0.03}_{-0.03} \times 10^{-7}$
S VI	$5.23^{+0.10}_{-0.13} \times 10^{-8}$	$1.03^{+0.06}_{-0.06} \times 10^{-7}$	$-0.51^{+0.06}_{-0.06} \times 10^{-8}$
Fe IV	$1.83^{+0.03}_{-0.03} \times 10^{-6}$	$2.00^{+0.08}_{-0.02} \times 10^{-6}$	$-0.17^{+0.09}_{-0.04} \times 10^{-6}$
Fe V	$5.00^{+0.06}_{-0.06} \times 10^{-6}$	$4.58^{+0.05}_{-0.05} \times 10^{-6}$	$0.42^{+0.08}_{-0.08} \times 10^{-6}$
Ni IV	$3.24^{+0.13}_{-0.05} \times 10^{-7}$	$5.77^{+0.12}_{-0.12} \times 10^{-7}$	$-2.53^{+0.18}_{-0.13} \times 10^{-7}$
Ni V	$1.01^{+0.03}_{-0.03} \times 10^{-6}$	$1.30^{+0.03}_{-0.03} \times 10^{-6}$	$0.29^{+0.04}_{-0.04} \times 10^{-6}$

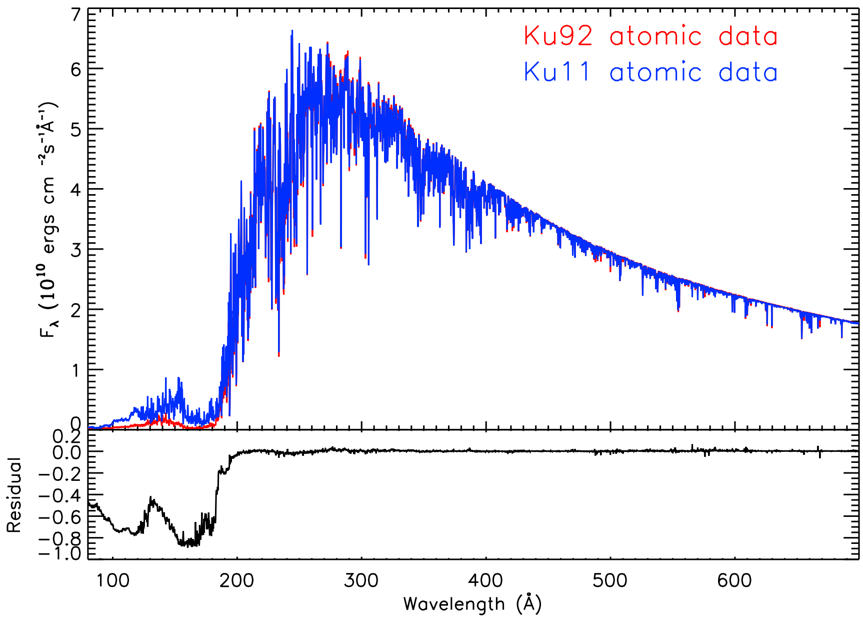

Figure 3.7: A comparison between synthesised EUV spectra calculated with the Ku92 data (red), and the Ku11 data (blue). The residual between the two models is plotted below.

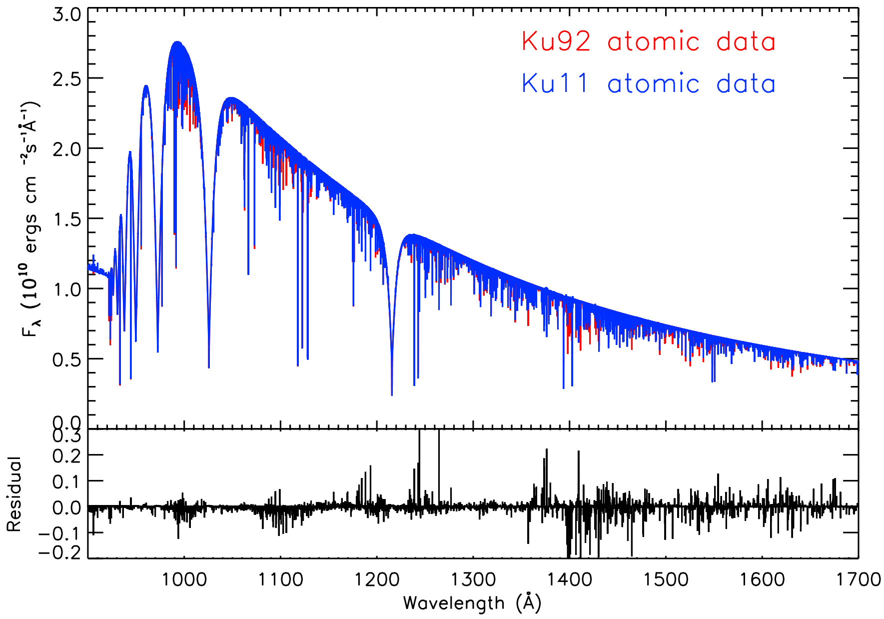

Figure 3.8: The same as Figure 3.7, but for the near and far ultraviolet region.

the residual does become non-zero in places, however, this is only $\sim 0.1 \times 10^{-3}$. Detecting such differences would be impossible.

In all cases (bar the EUV below 200Å), the residual between the Ku92 and Ku11 model atmospheres is zero for the continuum with slight increases/decreases for wavelength regions containing multiple absorption features. As these differences are so small, it is hard to envision an observational test that could be conducted to differentiate between these two models using the continuum only.

3.3.3 Structure variations

Despite the addition of many more transitions into the model atmosphere calculation, it appears that there has been no significant change in the overall atmospheric structure. In Figure 3.10, the variation of temperature with column mass is plotted for both the Ku92 and Ku11 model calculations. A very close examination of the distributions shows that the temperature is slightly higher in the deeper layers of the atmosphere for the Ku11 model. This is to be expected, as the increased opacity will scatter more radiation towards the inner layers of the atmosphere, thus increasing the temperature.

3.3.4 $T_{\rm eff}$ and log g dependency

Considering the residuals between the Ku92 and Ku11 model atmospheres, the differences between the two appear to be small. However, in the UV, there appears to be a $T_{\rm eff}$ and log g dependent variation. In Figure 3.11, a plot of the residual between the Ku92 and Ku11 models for the Lyman series is shown for temperatures 35000-100000K in steps of 2500K, and log g 7.0, 8.0, and 9.0. Starting from the lowest $T_{\rm eff}$, the residual between the two models decreases, reaching a minimum at some value of $T_{\rm eff}$ ($T_{\rm min}$), occuring at ≈52500, 65000, and 75000K. The residual then begins increasing for $T_{\rm eff} > T_{\rm min}$. With increasing log g, there will also be an increase in $T_{\rm eff}$ in the deeper layers of the atmosphere, causing a change in the ionisation

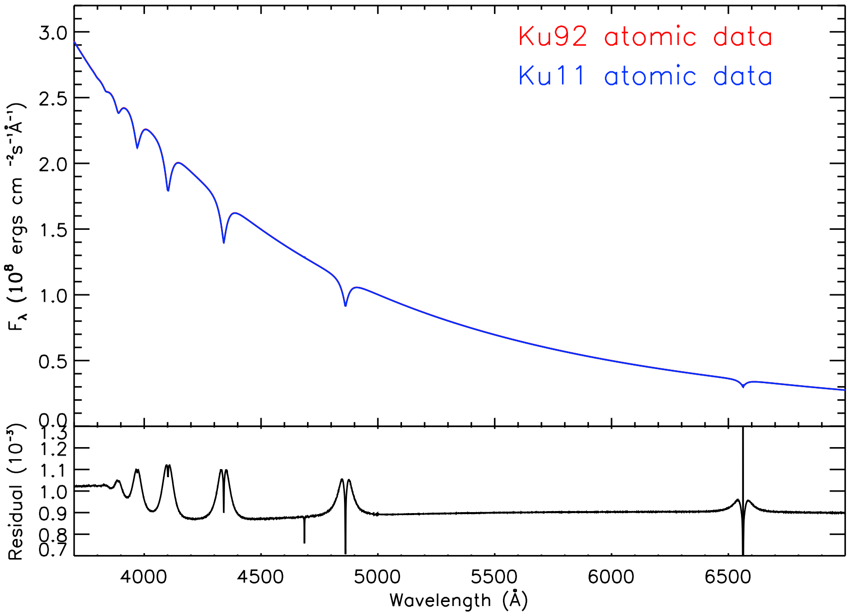

Figure 3.9: The same as Figure 3.7, but for the optical region.

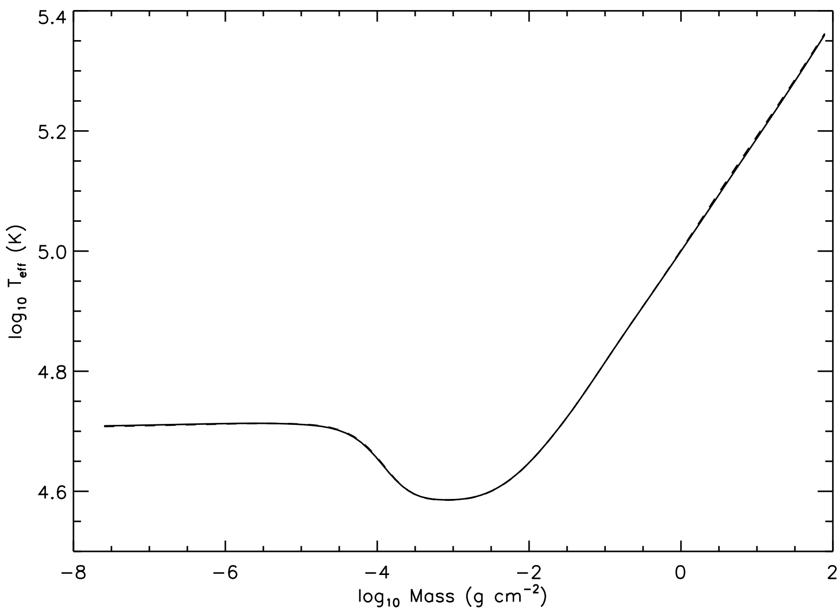

Figure 3.10: A comparison between the variation of temperature with column mass (deeper into the atmosphere). The solid curve is the Ku92 model, while the dashed curve is the Ku11 model.

balance. Therefore, this variation in $T_{\rm min}$ could be a consequence of not including certain model ions in the model atmosphere calculations.

In the case of the Balmer series, the residuals between the models are far less pronounced. In Figure 3.12, the models for the same temperatures and gravities are plotted in the Balmer region. Like the UV, the residuals vary with $T_{\rm eff}$ and log g, albeit by much smaller values.

3.3.5 Effective flux redistribution

The largest changes to the model flux occured in the EUV waveband below 200Å, where more flux was emitted by the Ku11 model. It is, perhaps, no coincidence that this region experienced the greatest change, as a larger number of transitions of Fe and Ni exists in this waveband. The redistributed flux from the EUV affected the Hydrogen Lyman and Balmer series, altering the broadening and depth of the lines. Admittedly, however, the effect of flux redistribution is more pronounced in the Lyman series. It appears then that changes to the EUV flux will affect wavebands that are closer to it, for example, the UV, whereas the optical region at longer wavelengths is relatively unchanged.

3.4 Conclusion

The effects of including additional opacity to model atmosphere calculations have been considered. Using the Ku11 energy levels as a reference, PI cross sections were calculated for ions Fe and Ni IV-VI, and model atoms constructed for use with TLUSTY. A model atmosphere was calculated with $T_{\rm eff} = 52500K$, log $g = 7.53$, and Preval et al. (2013) abundances using both the Ku92 data, and the Ku11 data.

Recalculation of the metal abundances for WD0501+524 using the Ku11 model showed little to no change for ions where good atomic data exist (C, N, Si), whereas for metals such as P, S, Fe and Ni, large deviations were observed. It is therefore likely that any abundance variations occuring between the Ku92 and Ku11 models are due to poor quality atomic data. In the EUV spectrum, there was a significant difference between the Ku92 and Ku11 models shortward of 200Å, where the latter appeared to emit more flux than the former. In the UV, the measured abundances for several species changed by statistically significant amounts as seen in Figure 3.6. Comparison of the two model atmospheres in the optical waveband showed little to no change in both the continuum flux, and the Balmer line absorption profiles.

The difference between the Ku92 and Ku11 models with varying $T_{\rm eff}$ and log g was considered in depth. This was done by calculating two model atmosphere grids for both the Ku92 and Ku11 atomic data spanning $T_{\rm eff}$ 35000-100000K in steps of 2500K, log g 7-9 in steps of 1.0 dex, and the Preval et al. (2013) abundances. Depending on the log g of the model, the residual of the Ku92 and Ku11 models in the UV waveband decreased from 35000K, reached a minimum for a particular $T_{\rm eff}$, and then began increasing for $T_{\rm eff}$ greater than this. The $T_{\rm eff}$ where the minimum occured increased with increasing gravity. It was noted that despite this variation, the residual was very small, and will unlikey be resolved in observation.

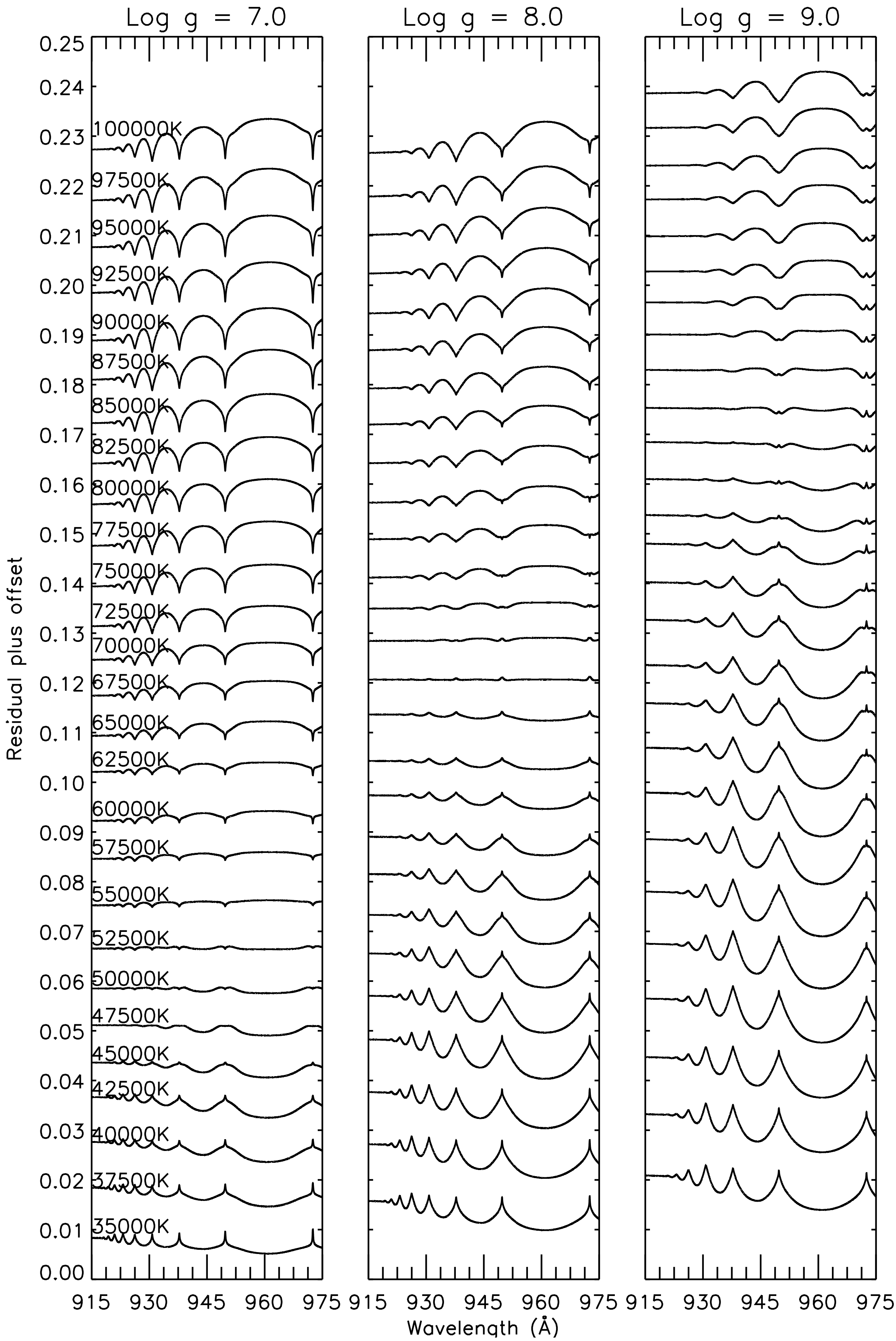

Figure 3.11: Plot of Lyman region residuals for the Ku92 and Ku11 models. From the bottom to the top, $T_{\rm eff}$ increases from 35000-100000K in steps of 2500K. From the left to the right, log g increases from 7.0 to 9.0 in steps of 1.0. Every spectrum above the lowest is offset by 0.01.

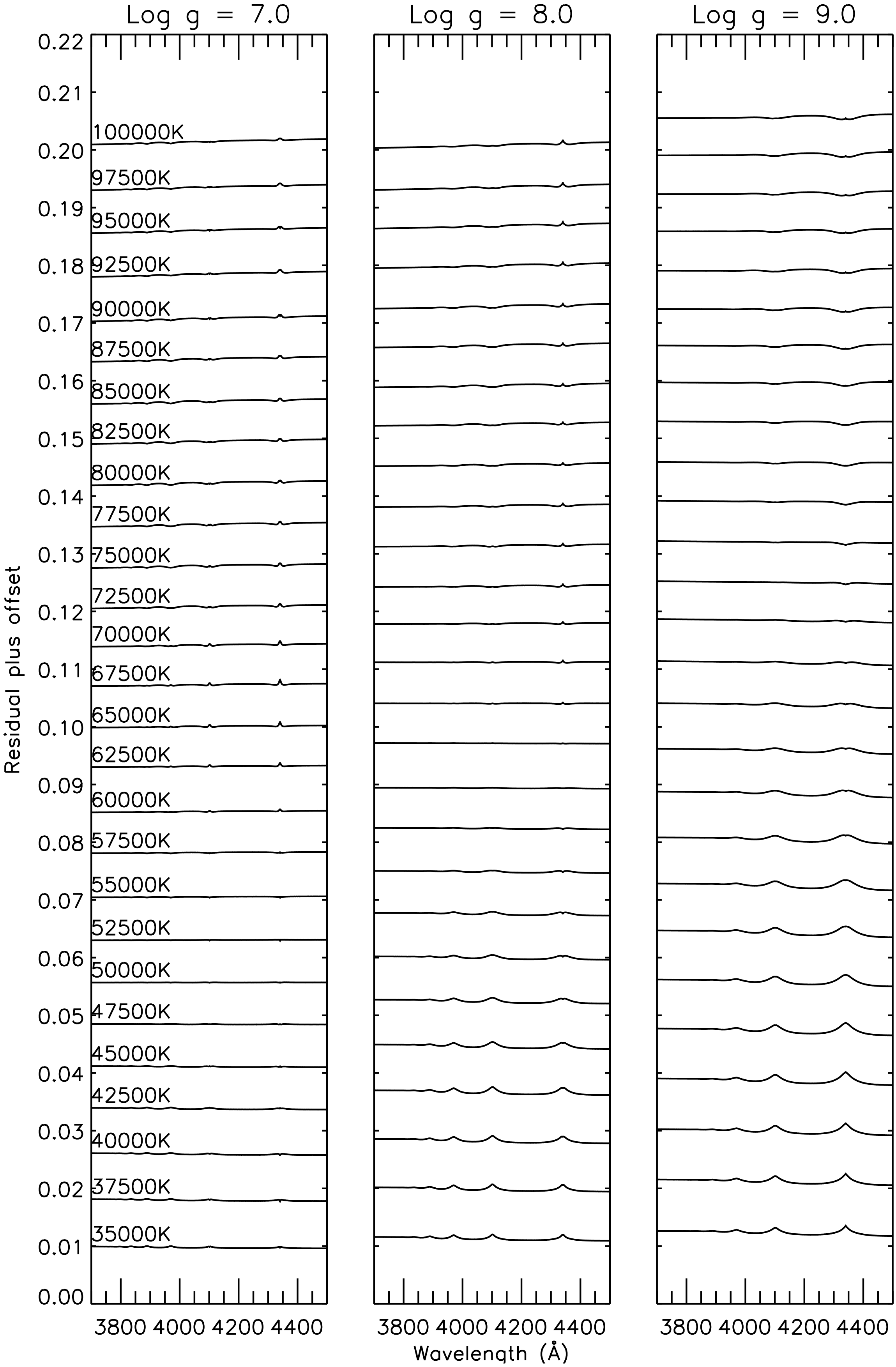

Figure 3.12: The same as Figure 3.11, but for the optical region. The spectrum closest to zero is offset by 0.008, while every spectrum above is offset by 0.008.

3.5 Summary

- Photoionisation cross sections based on the Ku11 data release were calculated for ions Fe and Ni IV-VI using AUTOSTRUCTURE . This included more than 100,000 energy levels, and more than 100,000,000 transitions. Model atoms based on these data were created.

- Model atmospheres based on the WD0501+524 models described in Chapter 2 were calculated using the Ku92 and Ku11 data.

- Comparison of the Ku92 and Ku11 models in the EUV waveband showed little to no difference in the continuum flux longward of 200Å.

- Shortward of 200Å, the Ku11 model appears to emit more flux than the Ku92 model. This could be caused by differences in the oscillator strengths between the AUTOSTRUCTURE and Ku92 transitions, hence resulting in a lower opacity at these wavelengths.

- Comparison of the Ku92 and Ku11 models in the UV and optical wavebands showed little to no differences in the continnum flux, making differentiation between the Ku92 and Ku11 models using continuum flux alone would likely be very difficult.

- Redetermination of the metal abundances in WD0501+524 using the Ku11 model showed statistically significant variations in N V, O IV, P V, S IV, S VI, and Fe and Ni IV & V. This may be due to poor atomic data for these ions.

- Two model grids were calculated to compare the differences between the Ku92 and Ku11 data when varying T_{eff} and log g. Starting from lower T_{eff}, the residual of the UV models tended towards zero for a particular value of T_{eff}, and then began to increase again. This particular T_{eff} increased with log g. No similar variation was seen for the optical waveband. This may be a consequence of omitting certain model ions from the model atmosphere calculation.

Chapter 4

The Lyman-Balmer line problem

4.1 Introduction

The measurement of $T_{\rm eff}$ and log g in white dwarf stars is an important venture. The former can give an indication of how far along the cooling curve an object is, and for the coolest stars, it can determine an upper limit on the age of the Milky Way. The latter can give information on the mass of the star, useful for determining mass distributions, which can in turn provide information on white dwarf formation mechanisms. Accurate determination of these parameters, therefore, is paramount. Typically, the $T_{\rm eff}$ and log g for a DA white dwarf are measured by comparing synthetic Lyman/Balmer line profiles with those in the observed data (Holberg et al., 1986). It may be reasonably expected that use of either the Lyman or Balmer line profiles to determine $T_{\rm eff}$ and log g does not matter, however, it has been shown on many occasions that this is not the case. In a study by Barstow et al. (2001), the $T_{\rm eff}$ and log g were determined for 11 DA white dwarfs using the Balmer series from ground-based optical data, and the Lyman series from space-based UV data taken with the *Orbiting Retrieveable Far and Extreme Ultraviolet Spectrometer* (ORFEUS), the *Hopkins Ultraviolet Telescope* (HUT), and the *Far Ultraviolet Spectroscopic Explorer* (FUSE). It was shown that there was a statistically significant difference between the $T_{\rm eff}$ and log g determined from the Lyman and Balmer line series. While it was not thought that the theoretical calculations were at fault in the analysis, the authors pointed out that any systematics present in the observational data would have to be addressed first.

Investigating this discrepancy further, Barstow et al. (2003) measured the $T_{\rm eff}$ and log g of 16 DA white dwarfs. An improvement of this study over Barstow et al. (2001) was the use of FUSE data as opposed to ORFEUS and HUT. A new data reduction pipeline for FUSE data was also developed by the authors. Applying this pipeline uniformly to all stars in the study removes any systematic effects associated with using UV data from several instruments. Comparison of the Lyman and Balmer line $T_{\rm eff}$ values showed good agreement up to ∼50000K, however, for white dwarfs in excess of this $T_{\rm eff}$, a systematic discrepancy is observed, increasing for higher values of $T_{\rm eff}$. Barstow et al. (2003) considered the possibility that the input opacity in model atmosphere calculations may be the cause of the temperature discrepancy. To this end, they calculated model grids with 0.1 and 10.0 times a measured WD0501+524 abundance (He/H=1×10^{-5}, C/H=4.00×10^{-7}, N/H=1.6×10^{-7}, O/H=9.70×10^{-7}, Si/H=3.00×10^{-7}, Fe/H=1.00×10^{-5}, and Ni/H=5.00×10^{-7}), and determined $T_{\rm eff}$ for the hot white dwarfs WD0501+524 (WD0501+527), and REJ2214-492 (WD2211-495). It was found that the discrepancy between the Lyman and Balmer line $T_{\rm eff}$ was smaller when using the higher abundance grid, however, it was still large enough to be statistically significant. This led the authors to conclude that the discrepancy may arise from shortcomings in the input physics supplied to the model atmosphere calculations. As this was thought to be a real effect independent of instrumentation, the presence of the discrepancy has come to be known as "The Lyman/Balmer Line" problem.

The most comprehensive study to date considering the Lyman/Balmer line problem is that of Lajoie & Bergeron (2007), utilising the data of 140 DA white dwarfs. This study, unlike Barstow et al. (2001) and Barstow et al. (2003), uses International Ultraviolet Explorer data, which covers 1200-1950Å in high dispersion mode, and 1150-3150Å in low dispersion mode, providing coverage of the Ly- α profile. The $T_{\rm eff}$ obtained from optical spectra was still done by fitting the Balmer lines. The authors used the IUE data to obtain two estimates of $T_{\rm eff}$. The first estimate was obtained using the UV slope method. This involves fitting a model spectrum to the slope of an IUE spectrum. As this method is quite insensitive to variations in log g (Bergeron et al., 1995), the latter was fixed to the value obtained from the Balmer line determination. $T_{\rm eff}$ was then varied using a minimization method to obtain the best fit. The second estimate was obtained using the V normalisation method (Finley et al., 1990). This is done by normalising the observed and synthetic spectra in the UV to the V magnitude of each white dwarf. The synthetic spectra were then fitted to the data. The authors found that within error, the optical and UV $T_{\rm eff}$ measurements up to 50000K, and no further than 75pc from the Earth were in agreement. It was hypothesised that the origin of the temperature discrepancy arose from interstellar reddening, affecting the continuum flux of the UV data. It should be noted, however, that several studies have shown that fitting only Ly α does not necessarily give a unique fit, making $T_{\rm eff}$ determination difficult.

In this Chapter, the Lyman/Balmer line problem is considered from the perspective of model atmosphere calculations, and the physics supplied to them. Three different variables are investigated to assess their impact on the measured $T_{\rm eff}$ and log g. These variables are the atmospheric composition, the opacity data, and the absorption profile broadening for the Lyman and Balmer lines. In total, 24 DA white dwarfs whose $T_{\rm eff} > 35000K$ are considered.

4.2 Observations

For this study, 24 DA white dwarf stars were chosen that had both UV and optical spectroscopic observations, and 35000$\leq$ $T_{\rm eff}$ $\leq$100000K, as this is the temperature range within which most objects suffering from the Lyman/Balmer line problem lie. Of these 24 stars, 12 have been observed to have metals in their atmosphere (WD0131-164, WD0229-481, WD0501+524, WD0556-375, WD0621-376, WD1029+537, WD1342+442, WD1738+669, WD1819+580, WD2111+498, WD2211-495, WD2309+105), and of these metal-polluted stars, five have Fe absorption features in their spectra (WD0501+524 (Preval et al., 2013), WD0556-375, WD0621-376, WD2111+498, and WD2211-495.(Barstow et al., 2003)). The sample was constructed by cross correlating the UV sample of Barstow et al. (2014) observed with FUSE, and the optical sample of Marsh et al. (1997) (both sets of observations described below), for which the Lyman and Balmer lines are available to fit. The former sample was obtained as a result of a multitude of programs with different aims, ranging from studies of the ISM, to classification of white dwarf photospheres. The latter sample was performed as part of a follow-up program to the ROSAT all-sky survey to measure $T_{\rm eff}$ and log g of several white dwarfs. Because of this, the sample used in this study is not biased towards a particular atmosphere composition, or a direction of observation.

4.2.1 Ultraviolet

All UV datasets were observed by FUSE, and were downloaded from the Mikulski Archive for Space Telescopes (MAST), calibrated by the latest (and final) reduction pipeline, CALFUSE 3.2 (see Dixon et al. 2007). A description of the hardware aboard FUSE is given in Chapter 2. In constructing the final spectra used in this work, each exposure from each segment of the observation was rebinned onto a common wavelength scale and coadded. The individual segments were then stitched together to give a single continuous spectrum spanning 910-1185Å. Where possible, only datasets taken with the LWRS aperture were used, as the other, smaller apertures were prone to source drift, which causes flux discontinuities, and could, hence, skew any measurements made. In the case where objects had no LWRS observations, but only MDRS observations, the fluxes from other segments (1aLiF etc) were multiplied by constant factors to match the flux of the 1aLiF segment. This segment was chosen, as flux attenuation in this segment was minimal compared to other segments in the observations used, providing a more reliable flux reference. For objects with multiple observations, the individual segments were coadded weighted by exposure time, and the flux errors were added in quadrature. The segments were then stitched together as per the method described above. A list of the datasets used, along with exposure times is given in Table 4.1.

4.2.2 Optical

White dwarfs in the northern hemisphere were observed using a 2.3m telescope at the Steward Observatory at Kitt Peak, while objects in the southern hemisphere were observed with the 1.9m Radcliffe Telescope based at the South African Astronomical Observatory (SAAO). Full details of the observation programme can be found in Marsh et al. (1997).

Four white dwarfs in the sample, WD0501+524, WD1057+719, WD1254+223, and WD1314+293 have been used as calibration standards for the HST due to their high intrinsic brightness, and have hence been observed extensively by STIS using the G430L grating. These spectra have been coadded and are publicly available[1]. Information on the datasets that comprise these spectra are given in Table 4.2.

4.3 Possible contributing factors

Several factors can affect measured values of $T_{\rm eff}$ and log g, and hence, the difference between those obtained from the Lyman and Balmer line series. What follows is a brief discussion of the possible contributions to changes in $T_{\rm eff}$ and log g.

4.3.1 Model atmosphere composition

The composition of a model atmosphere grid has been shown to drastically affect the measured $T_{\rm eff}$ of a white dwarf. Barstow et al. (1998) measured the $T_{\rm eff}$ and log g of several metal-polluted white dwarf stars using a pure H grid, and a line-blanketed model including ions of C, N, O, Si, Fe, and Ni. It was shown that the $T_{\rm eff}$ values determined using the pure H models were 3000-5000K higher than $T_{\rm eff}$ determined using metal-polluted grids, implying a composition dependency. Interestingly, no similar effect was observed for

[1] http://www.stsci.edu/hst/observatory/crds/calspec.html

Table 4.1: FUSE observations used in this analysis.

White Dwarf	Alt Name	Obs ID	Start Time/Date	Exposures	Exp Time (s)	Aperture
WD0004+330	GD2	P20411010	13:30:19 24/11/2000	7	10699.840	LWRS
WD0106-358		D02301010	06:29:36 21/11/2004	34	31193.000	LWRS
WD0131-164	PHL 1043	P20412010	07:45:04 10/12/2000	4	8619.000	LWRS
WD0229-481	REJ0230-47	M10504010	11:51:12 21/09/2002	2	5684.000	LWRS
		M10504030	03:23:45 31/12/2003	3	5020.000	LWRS
WD0232+035		P10405030	22:09:51 02/01/2004	29	16117.000	MDRS
WD0346-011	GD50	B12201040	10:25:34 22/12/2003	7	9427.000	LWRS
		B12201050	09:42:47 23/12/2003	6	8784.000	LWRS
		B12201020	04:43:34 20/12/2003	5	11276.000	LWRS
		B12201030	10:57:50 21/12/2003	7	13920.000	LWRS
WD0455-282		P10411030	09:39:51 07/02/2000	13	17675.000	MDRS
		P10411020	05:07:49 04/02/2000	8	10122.000	MDRS
		P10411010	02:14:28 03/02/2000	15	19667.000	MDRS
WD0501+524	G191-B2B	M10102020	06:10:18 17/02/2000	7	3450.000	LWRS
		M10306040	09:02:01 09/01/2001	1	503.000	LWRS
		M10306050	13:20:46 10/01/2001	1	503.000	LWRS
		M10306060	06:08:08 23/01/2001	5	2190.000	LWRS
		M10306070	04:46:29 25/01/2001	5	1926.000	LWRS
		M10306080	13:50:03 28/09/2001	5	2728.000	LWRS
		M10306090	09:54:26 21/11/2001	5	2703.000	LWRS
		M10306100	07:27:00 17/02/2002	16	8639.000	LWRS
		M10306110	02:05:28 23/02/2002	8	3645.000	LWRS
		M10306120	02:17:04 25/02/2002	14	7004.000	LWRS
		M10306130	21:00:11 00/01/1900	5	2358.000	LWRS
		M10306140	02:30:45 06/12/2002	3	702.000	LWRS
		M10306150	22:36:38 08/12/2002	4	1895.000	LWRS
		M10306160	19:14:29 05/02/2003	4	1980.000	LWRS
		M10306170	20:16:20 00/01/1900	8	4121.000	LWRS
		M10306180	18:23:04 25/01/2004	4	1735.000	LWRS
		M10313010	03:20:18 04/11/2004	5	1260.000	LWRS
		M10520010	21:46:19 07/12/2002	16	7061.000	LWRS
		P10412030	13:22:14 13/01/2000	21	15051.000	LWRS
		S30701010	09:40:58 14/01/2000	32	15456.000	LWRS

Table 4.1: Continued

White Dwarf	Alt Name	Obs ID	Start Time/Date	Exposures	Exp Time (s)	Aperture
WD0556-375		A03407010	12:19:05 10/12/1999	5	11328.000	MDRS
WD0621-376		P10415010	05:28:58 06/12/2000	19	8371.000	LWRS
WD0802+413		Z90311010	09:37:15 14/03/2004	4	9163.000	LWRS
WD1029+537		B00301010	04:40:49 25/03/2001	5	7408.000	LWRS
WD1057+719		Z90318010	16:12:29 08/04/2002	13	34203.000	LWRS
WD1234+481		M10524010	02:44:58 20/01/2003	6	6358.000	LWRS
		M10524020	20:29:19 18/03/2003	11	12735.000	LWRS
		P20409010	21:41:36 27/12/2000	6	12449.000	LWRS
WD1254+223	GD153	M10104030	12:33:26 06/03/2000	2	6319.000	LWRS
		M10104020	21:05:48 07/02/2001	5	8048.000	LWRS
		M10104010	21:32:55 29/04/2000	7	12084.000	LWRS
		P20418010	11:19:27 28/01/2001	5	9895.000	LWRS
WD1314+293	HZ43	M10105010	20:03:16 19/02/2000	8	6092.000	LWRS
		P10423010	21:19:36 22/04/2000	24	14418.000	LWRS
WD1342+443	PG1342+444	A03404020	23:01:52 11/01/2000	4	10679.000	LWRS
WD1615-154	EGGR 118	P20419010	12:40:19 29/08/2001	18	13908.000	MDRS
WD1631+781		I70101030	14:06:34 10/03/2003	2	2149.000	LWRS
		M10528020	04:09:52 12/01/2003	3	5382.000	LWRS
		M10528030	10:07:37 27/02/2003	2	5334.000	LWRS
		M10528040	20:02:02 13/02/2004	13	16306.000	LWRS
		M10528010	14:39:50 28/10/2002	5	10851.000	LWRS
		M10528050	16:57:21 20/03/2007	5	14496.000	LWRS
WD1636+351	WD1638+349	P20402010	14:22:15 28/03/2001	5	13782.000	LWRS
WD1725+586		Z90327010	23:49:29 13/05/2002	4	12449.000	LWRS
		U10381010	22:53:21 17/11/2006	4	5705.000	LWRS
WD1738+669	RE	M10529050	08:23:01 14/11/2006	3	5101.000	LWRS
		M10529010	16:51:13 02/09/2002	5	9009.000	LWRS
		M10529040	17:30:52 18/09/2006	3	4927.000	LWRS
		M10529020	17:29:13 29/10/2002	4	10843.000	LWRS
		M10529030	08:24:33 11/03/2003	3	6130.000	LWRS
		A03403010	15:40:59 05/05/2000	3	6647.000	LWRS

Table 4.1: Continued

White Dwarf	Alt Name	Obs ID	Start Time/Date	Exposures	Exp Time (s)	Aperture
WD1800+685		P20410010	08:14:46 23/12/2000	6	13176.000	LWRS
		M10530010	15:14:53 09/09/2000	4	16541.000	LWRS
		M10530030	19:44:18 17/09/2002	5	12448.000	LWRS
		M10530060	14:56:09 26/12/2002	5	8296.000	LWRS
		M10530040	10:29:46 18/09/2002	8	16290.000	LWRS
		M10530070	17:26:18 14/09/2006	6	18776.000	LWRS
		M10530020	23:58:35 02/09/2002	4	11967.000	LWRS
		M10530050	16:40:53 30/10/2002	5	16310.000	LWRS
WD1819+580		Z90328010	01:25:38 11/05/2002	8	5411.000	LWRS
WD1845+683		Z90329020	01:09:15 03/07/2002	6	7070.000	LWRS
		Z99003010	10:39:29 13/09/2002	3	11881.000	LWRS
		Z90329010	20:40:32 08/05/2002	10	36444.000	LWRS
WD1950-432		Z90332010	09:18:35 04/10/2002	7	14779.000	LWRS
WD2111+498	GD394	M10532020	05:18:54 04/09/2002	6	7957.000	LWRS
		M10532010	16:44:22 27/10/2002	5	4403.000	LWRS
		P10436010	18:04:49 20/06/2000	11	28310.000	LWRS
		M10107040	10:33:29 11/10/1999	8	5652.000	LWRS
		M10107060	11:00:21 13/10/1999	8	4688.000	LWRS
WD2146-433		Z90339010	15:14:10 06/10/2002	10	13690.000	LWRS
WD2152-548		M10515010	03:07:55 24/09/2002	3	4069.000	LWRS
		U10967010	10:58:44 08/08/2006	6	15752.000	LWRS

Table 4.1: Continued

White Dwarf	Alt Name	Obs ID	Start Time/Date	Exposures	Exp Time (s)	Aperture
WD2211-495	REJ2214-492	M10315010	18:26:46 07/05/2004	7	3699.000	LWRS
		M10303130	04:07:07 01/08/2002	8	3796.000	LWRS
		M10303150	17:20:00 25/09/2002	10	5460.000	LWRS
		M10303160	23:28:41 24/05/2003	13	6929.000	LWRS
		M10303140	14:23:40 10/06/2002	7	3774.000	LWRS
		M10315040	17:27:33 06/07/2004	7	3889.000	LWRS
		M10303180	04:14:39 17/09/2003	12	5875.000	LWRS
		M10303030	19:43:40 25/10/1999	9	4160.000	LWRS
		M10303040	21:45:44 01/11/1999	7	2976.000	LWRS
		M10303080	06:09:32 24/10/2000	9	3954.000	LWRS
		M10303090	09:29:25 24/10/2000	11	5025.000	LWRS
		M10303120	10:28:36 25/10/2000	11	5430.000	LWRS
		M10303050	06:55:16 03/06/2000	11	5157.000	LWRS
		M10303020	17:18:58 21/10/1999	5	2720.000	LWRS
		M10303060	05:15:34 29/06/2000	8	4193.000	LWRS
		M10303070	20:43:02 17/08/2000	12	5260.000	LWRS
		M10303100	12:49:19 24/10/2000	9	5795.000	LWRS
		M20303110	05:28:46 25/10/2000	13	5877.000	LWRS
WD2309+105	GD246	M10106010	04:50:06 12/11/2000	4	1566.000	LWRS
		M10106040	00:50:35 10/12/1999	8	3371.000	LWRS
		P10441010	10:12:27 19/07/2000	29	14810.000	LWRS
WD2331-475	LB1526	M10517010	08:46:55 23/09/2002	4	8291.000	LWRS
		P10442010	14:16:05 23/06/2000	21	19356.000	LWRS
		P10442020	14:16:59 07/11/1999	30	20180.000	LWRS

Table 4.2: STIS observations used in this analysis. All datasets were obtained using the G430L grating.

White Dwarf	Alt Name	Obs ID	Start Date/Time	Exp Time (s)
WD0501+524	G191-B2B	O4D101020	18/10/1997 18:35:59	150.0
		O4D102020	22/11/1997 19:19:23	150.0
		O53002030	23/02/1999 06:21:08	60.0
		O69U05020	20/01/2001 06:17:46	240.0
		O69U06020	22/02/2001 11:28:32	240.0
		O8V203020	29/10/2003 02:59:11	70.0
		OBBC07020	15/03/2010 13:08:59	200.0
		OBNF05020	31/01/2011 04:39:20	200.0
		O8V203030	29/10/2003 03:49:11	70.0
		OBBC07010	15/03/2010 13:03:29	200.0
		OBNF05010	31/01/2011 04:33:50	200.0
		OBVP07010	06/11/2011 12:47:55	200.0
		OBVP07020	06/11/2011 12:53:25	200.0
		OC3I14020	14/10/2012 18:11:54	220.0
		OC3I14030	14/10/2012 19:01:02	220.0
		OCGA06020	02/02/2014 06:24:49	220.0
		OCGA06030	02/02/2014 06:30:39	220.0
WD1057+719		O5K005020	27/02/2000 17:50:11	612.0
		O5K006020	17/04/2000 08:59:00	612.0
		O69U03020	02/05/2001 15:45:09	610.0
WD1254+223	GD153	O3TT42020	21/05/1997 10:35:06	252.0
		O3TT43020	28/05/1997 07:09:44	252.0
		O3TT44020	04/06/1997 11:45:01	252.0
		O3TT45020	10/06/1997 22:38:24	252.0
		O3TT46020	18/06/1997 04:40:32	252.0
		O3TT47020	25/06/1997 04:27:55	252.0
		O3TT48020	01/07/1997 12:19:59	252.0
		O4D103020	12/11/1997 01:41:54	180.0
		O4A502030	17/05/1998 21:04:01	240.0
		O8V2020D0	05/01/2004 09:50:01	220.0
		OBC402050	14/01/2011 01:09:33	260.0
		O8V2020E0	05/01/2004 09:44:11	220.0
		OBC402040	14/01/2011 01:03:03	260.0
		OBTO10040	01/01/2013 17:18:00	260.0
		OBTO10050	01/01/2013 17:24:30	260.0
		OC5506040	02/01/2013 01:16:53	260.0
		OC5506050	02/01/2013 01:23:23	260.0
		OCGA05040	20/01/2014 15:54:51	260.0
		OCGA05050	20/01/2014 16:01:21	260.0

Table 4.2: Continued

White Dwarf	Alt Name	Obs ID	Start Date/Time	Exp Time (s)
WD1314+293	HZ43	O57T01010	17/12/1998 21:30:49	120.0
		O57T02010	19/12/1998 18:38:44	120.0
		O69U07020	06/11/2000 18:21:47	200.0
		O69U08020	10/12/2000 22:16:42	200.0

log g. Ideally, tests of this dependency would be done with a model atmosphere grid that accounted for all possible changes in metal abundances. Such a grid, however, would require a very large number of models to be calculated to account for the various permutations. As each model can take up to a day to converge, the computational time required to calculate an entire grid can quickly become untenable.

4.3.2 Stark broadening tables

The Stark broadening effect arises from perturbations to the energy level structure of an atom/ion by an electric field. For a white dwarf star, the electric field arises from the free electrons in the atmosphere. The density, and temperature of this electron gas is closely related to $T_{\rm eff}$ and log g. An increase in log g will compress the atmosphere, pushing the free electrons closer together, increasing the electron density, and hence increasing the Stark broadening. An increase in $T_{\rm eff}$ will cause the atmosphere to expand, increasing the spacing between the free electrons, resulting in a decreased electron density, and hence a lower Stark broadening. Therefore, as these effects are so closely related, it is likely that poor quantification of these changes will impact upon the measured values of $T_{\rm eff}$ and log g. Currently, two Stark broadening tables are available, namely the Lemke (1997) tables (Lemke tables hereafter) and the Tremblay & Bergeron (2009) tables (Tremblay tables hereafter). Both are calculated using the unified theory of Vidal et al. (1973) (VCS hereafter). However, the Tremblay tables account for non-ideal effects induced by proton perturbations. The result of this is a shift in the central wavelength of the Lyman and Balmer line profiles. This is also accompanied by a change in the line shape, making the profile asymmetric. Furthermore, the Tremblay tables include an additional opacity source neglected by the Lemke tables, namely H bound-bound Stark broadening.

4.3.3 Atomic data completeness

Analysis of *Extreme Ultraviolet Explorer* (EUVE) data gave an indication that the completeness of the atomic data used to calculate the model atmosphere can have a significant effect on measured parameters. Lanz et al. (1996) calculated a grid of model atmospheres to fit EUVE data for WD0501+524 including >9,000,000 Fe and Ni IV-VII transitions. Prior to this, model atmosphere calculations only included Fe and Ni lines that had been observed in laboratory experiments (∼300,000 transitions), however, models using this limited dataset failed to reproduce the continuum, and other features of the spectrum. With the extended dataset, and additional He opacity, Lanz et al. (1996) was able to reproduce the shape of the EUV continuum.

This implies that the number of transitions included does indeed play a significant role in calculating atmospheric quantities, and, consequently, the $T_{\rm eff}$ and log g measured. For this work, two atomic datasets are available, one from Kurucz (1992), and the other from Kurucz (2011) (Ku92 and Ku11 hereafter respectively). The differences between these two datasets are discussed in Chapter 2, however, Ku92 contains ∼9,000,000 transitions for Fe and Ni IV-VII, wherea Ku11 contains ∼160,000,000 transitions for Fe and Ni IV-VII.

Table 4.3: Abundances used in calculating the models.

Ion	Preval et al. (2013)	Barstow et al. (2003)
C	1.72×10^{-7}	1.99×10^{-7}
N	2.16×10^{-7}	1.60×10^{-7}
O	4.12×10^{-7}	3.51×10^{-7}
Al	1.60×10^{-7}	N/A
Si	3.68×10^{-7}	8.65×10^{-7}
P	1.64×10^{-8}	N/A
S	1.71×10^{-7}	N/A
Fe	1.83×10^{-6}	3.30×10^{-6}
Ni	1.01×10^{-6}	2.40×10^{-7}

4.4 Model Atmospheres

All model atmospheres in this Chapter were calculated using TLUSTY (Hubeny, 1988) version 201 in NLTE, and the model spectra synthesised using SYNSPEC version 49 (Hubeny & Lanz, 2011). In order to try and disentangle the various contributions of different aspects of the model atmosphere, it is necessary to compute several permutations of the factors described above. Three atmospheric compositions were utilised. The first was a pure H model grid, and was calculated for $T_{\rm eff}$=17500K to 120000K in steps of 2500K, and log g=6.5 to 9.5 in steps of 0.25 dex. The other two were metal-polluted atmospheric compositions. Two were specified to assess the effect of including different species into the calculation on the measured $T_{\rm eff}$ and log g. The first composition was based on the values determined by Barstow et al. (2003) from their analysis of WD0501+524, including He, C, N, O, Si, Fe, and Ni (see Table 4.3). The second of these compositions was based on the updated metal abundances calculated by Preval et al. (2013) for WD0501+524, including He, C, N, O, Al, Si, P, S, Fe, and Ni (see Table 4.3 for abundances used). In both of the metal-polluted grids, the He abundance was fixed at 1.00×10^{-5} as a number fraction of H. Abundances from WD0501+524 were used, as they are well constrained due to the number of observations and studies performed on the star. The model ions included in the atmosphere calculation are the same as given in Table 3.5, however, for models using the Barstow et al. (2003) abundances, Al, P, and S were omitted. The metal-polluted models were calculated for $T_{\rm eff}$ =35000K to 100000K in steps of 2500K, and log g=6.5 to 9.5 in steps of 0.25 dex.

The two atomic datasets, Ku92 and Ku11, were used in calculating the metal-polluted model atmospheres. Ku92 was supplemented by photoionisation (PI) cross section data from the OP for Fe, and the PI data for Ni was calculated using an hydrogenic approximation. Ku11, however, did not have any accompanying PI cross section data. This was calculated using the atomic structure package AUTOSTRUCTURE (Badnell, 1986, 1997, 2011). Full details of the AUTOSTRUCTURE calculations can be found in Chapter 3.

Hereafter, the model atmosphere grids using the Preval et al. (2013) abundances, and the Ku92 and Ku11 atomic datasets will be referred to as Prevold and Prevnew respectively. Likewise, the model atmosphere grids utilising the Barstow et al. (2003) abundances, and the Ku 92 and Ku11 atomic datasets will be referred to as Barsold and Barsnew respectively. Each of the pure H and metal-polluted model grids is synthesised using either the Lemke Stark broadening tables, or the Tremblay Stark broadening tables, resulting in 10 model atmospheres in total.

4.5 Method

All data were fitted using the X-Ray analysis package XSPEC (Arnaud, 1996). The model spectra are convolved with the relevant instrumental Gaussian, which in XSPEC is provided as a channel resolution. The observational data were fitted by interpolating between a set of previously calculated model atmospheres, and the optimum T_{eff} and log g is determined using a chi square minimisation procedure.

For the FUSE data, photospheric and interstellar features were removed during the fitting procedure to leave behind the Lyman lines. The Lyman β, γ, δ, and ϵ lines were isolated, and fit simultaneously, each forced to have the same T_{eff} and log g. The redshift and normalisation, however, were allowed to vary freely to account for the poor wavelength calibration of FUSE (caused by source drift in the field of view), and any possible flux discontinuities in the detector segments respectively. The data were fit with all parameters allowed to vary. However, as the redshift was used solely for aligning the model spectra with the data, it was frozen during error calculations.

The optical data obtained from Kitt Peak and the SAAO are corrected for atmospheric distortion, however, this can sometimes fail to fully correct the slope of the spectrum. To account for this, a multiplicative model is defined in XSPEC, taking the form $AE + B$, where E is the energy in keV, and A and B are two variable parameters. Balmer β, γ, δ, and ϵ were, like the FUSE data, isolated, and fit simultaneously, having the same T_{eff} and log g, and their own redshift and normalisation parameters. In addition, each line had independent A and B parameters, which were allowed to vary freely. The data were first fit with all parameters free. After this initial fit, the A and B parameters were then frozen, and the data fit again. Finally, the redshift was frozen for error calculations.

Spectra taken with the Steward Observatory and the SAAO telescope were not supplied with errors. For each of these objects, a fractional error relative to the flux is estimated based upon the scatter of the data. The spectra were then fitted using a pure H model grid, synthesised with the Lemke Stark broadening tables. Once the optimum fit was found, the fractional errors on the flux were scaled by a constant factor to give a reduced chi square (χ^2_{red}) of unity, or as close as possible. The scaled flux errors were used for all subsequent fits. This process was also applied to objects observed with FUSE and STIS for consistency. Errors on the T_{eff} and log g were determined assuming two degrees of freedom to 1σ confidence, corresponding to $\Delta\chi_{\text{red}} = 2.2957$.

All T_{eff} and log g results calculated using the Lemke and Tremblay broadening tables are given in Tables 4.4 and 4.5 respectively.

4.6 Results - Pure H

Figure 4.1 shows the measured Lyman and Balmer T_{eff} values using a Pure H model, synthesised with the Lemke and Tremblay broadening tables. Below 52000K, there appears to be good agreement between the Lyman and Balmer T_{eff} for both the Lemke and Tremblay results. Above this temperature, a discrepancy between the Lyman and Balmer T_{eff} becomes apparent for several stars. The scatter about the Lyman=Balmer line appears to get worse with increasing T_{eff} . The largest discrepancy occurs for WD1738+669, where the difference is in excess of 10000K. Comparing the Lemke results with the Trem-

Table 4.4: List of measured $T_{\rm eff}$ and log g values for the pure H, Prevold, Prevnew, Barsold, and Barsnew grids using the Lemke broadening tables. The Lyman values are given by columns with "Ly", while the Balmer values are given by "Bal". $\Delta T_{\rm eff}$ is the difference between the Lyman and Balmer $T_{\rm eff}$, and Δlog g is the difference between the measured Lyman and Balmer log g values.

Star	Grid	$T_{\rm eff}$ Ly	log g Ly	$T_{\rm eff}$ Bal	log g Bal	$\Delta T_{\rm eff}$	Δ log g
WD0004+330	PureH	47711^{+284}_{-290}	$7.714^{+0.032}_{-0.034}$	46178^{+556}_{-536}	$7.740^{+0.071}_{-0.064}$	1533^{+624}_{-610}	$-0.026^{+0.078}_{-0.073}$
	Prevold	45739^{+232}_{-243}	$7.742^{+0.035}_{-0.034}$	44994^{+533}_{-498}	$7.757^{+0.065}_{-0.066}$	746^{+581}_{-554}	$-0.016^{+0.074}_{-0.074}$
	Prevnew	45912^{+239}_{-250}	$7.742^{+0.036}_{-0.034}$	45109^{+528}_{-500}	$7.755^{+0.065}_{-0.066}$	804^{+580}_{-559}	$-0.014^{+0.074}_{-0.075}$
	Barsold	45559^{+224}_{-235}	$7.743^{+0.035}_{-0.034}$	44889^{+521}_{-493}	$7.760^{+0.064}_{-0.066}$	670^{+567}_{-546}	$-0.016^{+0.073}_{-0.074}$
	Barsnew	45845^{+236}_{-247}	$7.742^{+0.035}_{-0.034}$	45075^{+525}_{-494}	$7.756^{+0.065}_{-0.066}$	771^{+575}_{-552}	$-0.014^{+0.074}_{-0.075}$
WD0131-163	PureH	44758^{+251}_{-246}	$7.796^{+0.037}_{-0.038}$	45081^{+599}_{-558}	$7.912^{+0.052}_{-0.052}$	-323^{+649}_{-610}	$-0.116^{+0.064}_{-0.065}$
	Prevold	43216^{+197}_{-192}	$7.822^{+0.035}_{-0.036}$	43734^{+521}_{-504}	$7.921^{+0.051}_{-0.051}$	-518^{+557}_{-539}	$-0.098^{+0.062}_{-0.063}$
	Prevnew	43375^{+204}_{-198}	$7.822^{+0.036}_{-0.036}$	43894^{+520}_{-504}	$7.919^{+0.051}_{-0.052}$	-518^{+558}_{-541}	$-0.097^{+0.062}_{-0.063}$
	Barsold	43083^{+192}_{-186}	$7.824^{+0.035}_{-0.036}$	43607^{+515}_{-499}	$7.922^{+0.051}_{-0.051}$	-524^{+550}_{-532}	$-0.098^{+0.062}_{-0.063}$
	Barsnew	43339^{+202}_{-196}	$7.823^{+0.036}_{-0.036}$	43864^{+516}_{-501}	$7.920^{+0.051}_{-0.051}$	-525^{+555}_{-538}	$-0.096^{+0.062}_{-0.063}$
WD0229-481	PureH	59406^{+565}_{-542}	$7.583^{+0.039}_{-0.040}$	61581^{+2268}_{-2087}	$7.346^{+0.125}_{-0.121}$	-2175^{+2337}_{-2156}	$0.237^{+0.131}_{-0.127}$
	Prevold	55839^{+453}_{-435}	$7.616^{+0.039}_{-0.039}$	59836^{+2254}_{-2024}	$7.383^{+0.122}_{-0.125}$	-3996^{+2299}_{-2070}	$0.233^{+0.128}_{-0.131}$
	Prevnew	55919^{+453}_{-436}	$7.617^{+0.039}_{-0.039}$	59782^{+2266}_{-2043}	$7.386^{+0.121}_{-0.124}$	-3863^{+2311}_{-2089}	$0.232^{+0.127}_{-0.131}$
	Barsold	55617^{+444}_{-428}	$7.613^{+0.039}_{-0.039}$	59600^{+2244}_{-2001}	$7.380^{+0.123}_{-0.126}$	-3983^{+2288}_{-2046}	$0.233^{+0.129}_{-0.132}$
	Barsnew	55815^{+451}_{-434}	$7.618^{+0.039}_{-0.039}$	59727^{+2248}_{-2048}	$7.380^{+0.123}_{-0.125}$	-3912^{+2293}_{-2093}	$0.238^{+0.129}_{-0.131}$
WD0346-011	PureH	40558^{+152}_{-151}	$9.157^{+0.031}_{-0.032}$	39990^{+442}_{-402}	$9.120^{+0.050}_{-0.050}$	568^{+468}_{-429}	$0.037^{+0.059}_{-0.059}$
	Prevold	39936^{+137}_{-150}	$9.161^{+0.030}_{-0.030}$	39376^{+368}_{-359}	$9.120^{+0.049}_{-0.050}$	561^{+393}_{-389}	$0.041^{+0.057}_{-0.058}$
	Prevnew	40104^{+132}_{-134}	$9.162^{+0.031}_{-0.031}$	39540^{+376}_{-365}	$9.120^{+0.049}_{-0.050}$	564^{+399}_{-389}	$0.042^{+0.058}_{-0.059}$
	Barsold	39801^{+145}_{-146}	$9.159^{+0.030}_{-0.030}$	39259^{+364}_{-354}	$9.120^{+0.049}_{-0.050}$	542^{+392}_{-383}	$0.039^{+0.057}_{-0.058}$
	Barsnew	40099^{+132}_{-134}	$9.162^{+0.031}_{-0.031}$	39541^{+375}_{-365}	$9.120^{+0.049}_{-0.050}$	558^{+398}_{-389}	$0.042^{+0.058}_{-0.059}$
WD0501+524	PureH	62863^{+185}_{-186}	$7.537^{+0.013}_{-0.014}$	57421^{+293}_{-286}	$7.612^{+0.019}_{-0.019}$	5442^{+347}_{-341}	$-0.075^{+0.023}_{-0.024}$
	Prevold	58756^{+161}_{-160}	$7.573^{+0.013}_{-0.013}$	55587^{+278}_{-276}	$7.632^{+0.019}_{-0.019}$	3169^{+322}_{-319}	$-0.059^{+0.023}_{-0.024}$
	Prevnew	58771^{+158}_{-157}	$7.574^{+0.013}_{-0.013}$	55595^{+275}_{-272}	$7.631^{+0.019}_{-0.019}$	3176^{+317}_{-314}	$-0.058^{+0.023}_{-0.023}$
	Barsold	58539^{+161}_{-158}	$7.573^{+0.013}_{-0.013}$	55364^{+278}_{-274}	$7.632^{+0.019}_{-0.019}$	3176^{+321}_{-316}	$-0.059^{+0.023}_{-0.024}$
	Barsnew	58677^{+159}_{-157}	$7.577^{+0.013}_{-0.013}$	55523^{+275}_{-272}	$7.631^{+0.019}_{-0.019}$	3154^{+318}_{-314}	$-0.054^{+0.023}_{-0.023}$

Table 4.4: Continued.

Star	Grid	$T_{\rm eff}$ Ly	log g Ly	$T_{\rm eff}$ Bal	log g Bal	$\Delta T_{\rm eff}$	Δ log g
WD0556-375	PureH	63403^{+2447}_{-2283}	$7.445^{+0.138}_{-0.140}$	63910^{+2598}_{-2374}	$7.567^{+0.138}_{-0.145}$	-507^{+3569}_{-3293}	$-0.122^{+0.195}_{-0.202}$
	Prevold	59302^{+1896}_{-1859}	$7.475^{+0.139}_{-0.140}$	61803^{+2603}_{-2311}	$7.596^{+0.136}_{-0.141}$	-2501^{+3221}_{-2965}	$-0.120^{+0.194}_{-0.199}$
	Prevnew	59309^{+1888}_{-1840}	$7.478^{+0.140}_{-0.140}$	61792^{+2595}_{-2315}	$7.595^{+0.135}_{-0.141}$	-2483^{+3209}_{-2957}	$-0.117^{+0.194}_{-0.198}$
	Barsold	59097^{+1891}_{-1845}	$7.474^{+0.139}_{-0.140}$	61540^{+2633}_{-2305}	$7.595^{+0.136}_{-0.142}$	-2443^{+3242}_{-2952}	$-0.121^{+0.195}_{-0.199}$
	Barsnew	59218^{+1881}_{-1849}	$7.480^{+0.140}_{-0.140}$	61735^{+2596}_{-2311}	$7.595^{+0.136}_{-0.142}$	-2516^{+3206}_{-2960}	$-0.115^{+0.195}_{-0.199}$
WD0621-376	PureH	69799^{+584}_{-575}	$7.381^{+0.029}_{-0.029}$	59020^{+1798}_{-1665}	$7.124^{+0.101}_{-0.103}$	10780^{+1891}_{-1761}	$0.256^{+0.105}_{-0.107}$
	Prevold	64706^{+478}_{-478}	$7.422^{+0.029}_{-0.029}$	57813^{+1806}_{-1647}	$7.158^{+0.102}_{-0.102}$	6893^{+1868}_{-1715}	$0.265^{+0.106}_{-0.106}$
	Prevnew	64572^{+474}_{-462}	$7.422^{+0.029}_{-0.029}$	57839^{+1848}_{-1671}	$7.156^{+0.101}_{-0.102}$	6733^{+1907}_{-1733}	$0.266^{+0.105}_{-0.106}$
	Barsold	64488^{+485}_{-471}	$7.422^{+0.029}_{-0.029}$	57582^{+1773}_{-1619}	$7.156^{+0.102}_{-0.102}$	6906^{+1839}_{-1686}	$0.266^{+0.106}_{-0.106}$
	Barsnew	64494^{+476}_{-463}	$7.424^{+0.029}_{-0.029}$	57683^{+1834}_{-1649}	$7.154^{+0.101}_{-0.102}$	6811^{+1895}_{-1712}	$0.270^{+0.106}_{-0.107}$
WD1029+537	PureH	45138^{+332}_{-344}	$7.797^{+0.053}_{-0.054}$	44752^{+791}_{-724}	$7.731^{+0.077}_{-0.077}$	385^{+857}_{-802}	$0.066^{+0.094}_{-0.094}$
	Prevold	43530^{+293}_{-282}	$7.823^{+0.052}_{-0.054}$	43589^{+711}_{-673}	$7.738^{+0.077}_{-0.076}$	-59^{+769}_{-729}	$0.085^{+0.093}_{-0.093}$
	Prevnew	43694^{+302}_{-289}	$7.825^{+0.053}_{-0.054}$	43708^{+708}_{-668}	$7.737^{+0.077}_{-0.076}$	-14^{+770}_{-728}	$0.087^{+0.093}_{-0.093}$
	Barsold	43390^{+284}_{-273}	$7.825^{+0.052}_{-0.054}$	43488^{+707}_{-672}	$7.740^{+0.077}_{-0.077}$	-97^{+761}_{-725}	$0.085^{+0.093}_{-0.093}$
	Barsnew	43655^{+299}_{-286}	$7.826^{+0.053}_{-0.054}$	43683^{+704}_{-663}	$7.738^{+0.077}_{-0.076}$	-28^{+764}_{-722}	$0.088^{+0.093}_{-0.093}$
WD1057+719	PureH	40927^{+148}_{-145}	$7.893^{+0.032}_{-0.032}$	40752^{+293}_{-289}	$7.914^{+0.036}_{-0.037}$	175^{+329}_{-323}	$-0.020^{+0.049}_{-0.049}$
	Prevold	40042^{+121}_{-136}	$7.920^{+0.031}_{-0.031}$	39969^{+271}_{-251}	$7.916^{+0.036}_{-0.036}$	73^{+297}_{-285}	$0.004^{+0.048}_{-0.048}$
	Prevnew	40148^{+126}_{-121}	$7.918^{+0.031}_{-0.031}$	40067^{+276}_{-257}	$7.915^{+0.036}_{-0.037}$	82^{+304}_{-284}	$0.003^{+0.048}_{-0.048}$
	Barsold	39972^{+123}_{-142}	$7.921^{+0.031}_{-0.032}$	39917^{+265}_{-248}	$7.916^{+0.036}_{-0.036}$	55^{+292}_{-286}	$0.005^{+0.048}_{-0.049}$
	Barsnew	40137^{+125}_{-120}	$7.919^{+0.031}_{-0.031}$	40066^{+275}_{-256}	$7.915^{+0.036}_{-0.037}$	72^{+302}_{-283}	$0.004^{+0.048}_{-0.048}$
WD1234+481	PureH	53950^{+288}_{-306}	$7.746^{+0.030}_{-0.028}$	54032^{+1019}_{-979}	$7.547^{+0.071}_{-0.072}$	-82^{+1059}_{-1025}	$0.199^{+0.077}_{-0.077}$
	Prevold	51005^{+227}_{-222}	$7.779^{+0.029}_{-0.029}$	52476^{+985}_{-914}	$7.560^{+0.071}_{-0.072}$	-1471^{+1011}_{-940}	$0.219^{+0.077}_{-0.078}$
	Prevnew	51195^{+236}_{-226}	$7.780^{+0.029}_{-0.029}$	52521^{+968}_{-908}	$7.559^{+0.071}_{-0.072}$	-1325^{+997}_{-935}	$0.221^{+0.077}_{-0.077}$
	Barsold	50735^{+225}_{-218}	$7.779^{+0.029}_{-0.029}$	52295^{+971}_{-906}	$7.560^{+0.071}_{-0.072}$	-1560^{+997}_{-932}	$0.218^{+0.077}_{-0.078}$
	Barsnew	51090^{+232}_{-225}	$7.780^{+0.030}_{-0.029}$	52446^{+967}_{-908}	$7.559^{+0.071}_{-0.072}$	-1356^{+995}_{-935}	$0.222^{+0.077}_{-0.078}$

Table 4.4: Continued.

Star	Grid	$T_{\rm eff}$ Ly	log g Ly	$T_{\rm eff}$ Bal	log g Bal	$\Delta T_{\rm eff}$	Δ log g
WD1254+223	PureH	38982^{+86}_{-83}	$7.772^{+0.023}_{-0.022}$	39005^{+144}_{-143}	$7.818^{+0.020}_{-0.021}$	-23^{+168}_{-165}	$-0.046^{+0.031}_{-0.030}$
	Prevold	38304^{+71}_{-69}	$7.797^{+0.021}_{-0.021}$	38427^{+134}_{-132}	$7.819^{+0.020}_{-0.021}$	-123^{+151}_{-149}	$-0.022^{+0.030}_{-0.030}$
	Prevnew	38382^{+74}_{-71}	$7.796^{+0.022}_{-0.021}$	38499^{+134}_{-133}	$7.819^{+0.020}_{-0.021}$	-117^{+153}_{-151}	$-0.023^{+0.030}_{-0.030}$
	Barsold	38266^{+70}_{-68}	$7.799^{+0.021}_{-0.021}$	38395^{+133}_{-131}	$7.820^{+0.020}_{-0.021}$	-129^{+150}_{-148}	$-0.020^{+0.030}_{-0.029}$
	Barsnew	38378^{+73}_{-71}	$7.797^{+0.022}_{-0.021}$	38502^{+134}_{-132}	$7.819^{+0.020}_{-0.021}$	-124^{+152}_{-150}	$-0.022^{+0.030}_{-0.030}$
WD1314+293	PureH	50476^{+160}_{-157}	$7.877^{+0.017}_{-0.017}$	49731^{+423}_{-410}	$7.928^{+0.035}_{-0.035}$	745^{+452}_{-439}	$-0.051^{+0.039}_{-0.039}$
	Prevold	48035^{+134}_{-132}	$7.905^{+0.017}_{-0.017}$	48118^{+399}_{-393}	$7.940^{+0.035}_{-0.035}$	-83^{+421}_{-414}	$-0.035^{+0.039}_{-0.039}$
	Prevnew	48248^{+137}_{-135}	$7.905^{+0.017}_{-0.017}$	48253^{+395}_{-388}	$7.939^{+0.035}_{-0.035}$	-6^{+418}_{-411}	$-0.034^{+0.039}_{-0.039}$
	Barsold	47798^{+130}_{-128}	$7.906^{+0.017}_{-0.017}$	47950^{+397}_{-390}	$7.941^{+0.035}_{-0.035}$	-152^{+417}_{-410}	$-0.035^{+0.039}_{-0.039}$
	Barsnew	48167^{+135}_{-133}	$7.906^{+0.017}_{-0.017}$	48195^{+392}_{-386}	$7.939^{+0.035}_{-0.035}$	-28^{+415}_{-408}	$-0.033^{+0.039}_{-0.039}$
WD1342+443	PureH	63725^{+1696}_{-1585}	$8.069^{+0.122}_{-0.121}$	59112^{+2502}_{-2300}	$8.214^{+0.118}_{-0.170}$	4612^{+3022}_{-2793}	$-0.145^{+0.170}_{-0.208}$
	Prevold	59255^{+1391}_{-1310}	$8.114^{+0.121}_{-0.124}$	56495^{+2281}_{-2140}	$8.236^{+0.108}_{-0.166}$	2761^{+2671}_{-2509}	$-0.122^{+0.162}_{-0.207}$
	Prevnew	59350^{+1389}_{-1310}	$8.111^{+0.121}_{-0.124}$	56509^{+2264}_{-2046}	$8.239^{+0.106}_{-0.167}$	2841^{+2656}_{-2429}	$-0.128^{+0.161}_{-0.209}$
	Barsold	58824^{+1378}_{-1265}	$8.110^{+0.121}_{-0.124}$	56176^{+2285}_{-2112}	$8.235^{+0.109}_{-0.167}$	2648^{+2668}_{-2462}	$-0.125^{+0.163}_{-0.208}$
	Barsnew	59099^{+1388}_{-1293}	$8.109^{+0.122}_{-0.124}$	56354^{+2390}_{-1966}	$8.234^{+0.112}_{-0.165}$	2746^{+2764}_{-2353}	$-0.125^{+0.165}_{-0.207}$
WD1636+351	PureH	39451^{+263}_{-250}	$7.849^{+0.056}_{-0.057}$	36318^{+296}_{-287}	$7.767^{+0.051}_{-0.052}$	3133^{+396}_{-381}	$0.082^{+0.076}_{-0.077}$
	Prevold	38691^{+216}_{-207}	$7.870^{+0.053}_{-0.055}$	35994^{+276}_{-267}	$7.767^{+0.051}_{-0.052}$	2696^{+350}_{-338}	$0.103^{+0.074}_{-0.075}$
	Prevnew	38783^{+224}_{-212}	$7.869^{+0.054}_{-0.055}$	36038^{+277}_{-268}	$7.767^{+0.051}_{-0.052}$	2745^{+356}_{-342}	$0.103^{+0.074}_{-0.076}$
	Barsold	38644^{+212}_{-202}	$7.872^{+0.053}_{-0.054}$	35989^{+274}_{-265}	$7.767^{+0.051}_{-0.052}$	2655^{+346}_{-334}	$0.105^{+0.074}_{-0.075}$
	Barsnew	38779^{+223}_{-212}	$7.870^{+0.054}_{-0.055}$	36047^{+276}_{-269}	$7.767^{+0.051}_{-0.052}$	2733^{+355}_{-342}	$0.104^{+0.074}_{-0.075}$
WD1725+586	PureH	52673^{+944}_{-937}	$8.134^{+0.092}_{-0.095}$	52543^{+2057}_{-1923}	$8.243^{+0.151}_{-0.148}$	129^{+2263}_{-2139}	$-0.109^{+0.177}_{-0.176}$
	Prevold	49848^{+798}_{-788}	$8.157^{+0.092}_{-0.094}$	50510^{+1882}_{-1774}	$8.254^{+0.150}_{-0.146}$	-662^{+2044}_{-1941}	$-0.096^{+0.176}_{-0.174}$
	Prevnew	50176^{+804}_{-807}	$8.165^{+0.092}_{-0.094}$	50699^{+1860}_{-1754}	$8.252^{+0.150}_{-0.146}$	-523^{+2026}_{-1931}	$-0.087^{+0.176}_{-0.173}$
	Barsold	49465^{+789}_{-750}	$8.147^{+0.093}_{-0.095}$	50258^{+1875}_{-1757}	$8.254^{+0.151}_{-0.146}$	-793^{+2034}_{-1911}	$-0.108^{+0.177}_{-0.175}$
	Barsnew	49980^{+793}_{-806}	$8.150^{+0.091}_{-0.096}$	50628^{+1863}_{-1745}	$8.252^{+0.150}_{-0.146}$	-648^{+2025}_{-1922}	$-0.102^{+0.176}_{-0.175}$

Table 4.4: Continued.

Star	Grid	$T_{\rm eff}$ Ly	log g Ly	$T_{\rm eff}$ Bal	log g Bal	$\Delta T_{\rm eff}$	Δ log g
WD1738+669	PureH	88040^{+1010}_{-986}	$7.902^{+0.032}_{-0.032}$	76409^{+1741}_{-1723}	$7.693^{+0.098}_{-0.081}$	11631^{+2012}_{-1986}	$0.209^{+0.103}_{-0.088}$
	Prevold	79363^{+854}_{-819}	$7.956^{+0.034}_{-0.031}$	74084^{+1752}_{-1856}	$7.728^{+0.105}_{-0.084}$	5280^{+1949}_{-2028}	$0.228^{+0.110}_{-0.090}$
	Prevnew	79016^{+815}_{-825}	$7.956^{+0.033}_{-0.032}$	73973^{+1784}_{-1840}	$7.732^{+0.105}_{-0.085}$	5043^{+1961}_{-2017}	$0.224^{+0.110}_{-0.091}$
	Barsold	79014^{+864}_{-831}	$7.960^{+0.034}_{-0.031}$	73729^{+1825}_{-1767}	$7.725^{+0.106}_{-0.086}$	5285^{+2020}_{-1952}	$0.235^{+0.111}_{-0.091}$
	Barsnew	79058^{+855}_{-832}	$7.960^{+0.033}_{-0.032}$	74024^{+1780}_{-1817}	$7.725^{+0.110}_{-0.081}$	5034^{+1975}_{-1998}	$0.235^{+0.115}_{-0.087}$
WD1800+685	PureH	43879^{+263}_{-252}	$7.700^{+0.036}_{-0.036}$	43679^{+813}_{-786}	$7.698^{+0.086}_{-0.087}$	200^{+855}_{-825}	$0.002^{+0.093}_{-0.094}$
	Prevold	42558^{+201}_{-224}	$7.732^{+0.035}_{-0.036}$	42688^{+766}_{-706}	$7.703^{+0.085}_{-0.086}$	-130^{+792}_{-741}	$0.029^{+0.092}_{-0.093}$
	Prevnew	42696^{+207}_{-207}	$7.732^{+0.036}_{-0.034}$	42797^{+763}_{-716}	$7.702^{+0.085}_{-0.086}$	-101^{+791}_{-745}	$0.030^{+0.092}_{-0.092}$
	Barsold	42440^{+202}_{-226}	$7.734^{+0.036}_{-0.036}$	42607^{+761}_{-694}	$7.704^{+0.085}_{-0.086}$	-167^{+787}_{-730}	$0.030^{+0.092}_{-0.093}$
	Barsnew	42668^{+204}_{-210}	$7.733^{+0.036}_{-0.034}$	42781^{+759}_{-710}	$7.702^{+0.085}_{-0.086}$	-113^{+785}_{-741}	$0.031^{+0.092}_{-0.092}$
WD1819+580	PureH	45285^{+313}_{-303}	$8.613^{+0.064}_{-0.066}$	44840^{+524}_{-492}	$7.774^{+0.053}_{-0.053}$	445^{+611}_{-578}	$0.840^{+0.083}_{-0.085}$
	Prevold	43784^{+284}_{-272}	$8.624^{+0.063}_{-0.065}$	43769^{+483}_{-464}	$7.776^{+0.052}_{-0.053}$	15^{+560}_{-538}	$0.847^{+0.082}_{-0.084}$
	Prevnew	44046^{+298}_{-285}	$8.626^{+0.063}_{-0.065}$	43885^{+480}_{-462}	$7.775^{+0.052}_{-0.053}$	160^{+564}_{-543}	$0.850^{+0.082}_{-0.084}$
	Barsold	43591^{+272}_{-260}	$8.624^{+0.063}_{-0.065}$	43674^{+480}_{-462}	$7.778^{+0.052}_{-0.053}$	-82^{+552}_{-530}	$0.847^{+0.081}_{-0.083}$
	Barsnew	44012^{+295}_{-282}	$8.626^{+0.063}_{-0.065}$	43860^{+477}_{-458}	$7.776^{+0.052}_{-0.053}$	152^{+560}_{-538}	$0.851^{+0.082}_{-0.084}$
WD1845+683	PureH	36749^{+122}_{-119}	$8.196^{+0.043}_{-0.045}$	43823^{+783}_{-752}	$7.666^{+0.086}_{-0.087}$	-7074^{+792}_{-762}	$0.530^{+0.096}_{-0.098}$
	Prevold	36306^{+105}_{-104}	$8.211^{+0.041}_{-0.044}$	42844^{+743}_{-688}	$7.671^{+0.085}_{-0.087}$	-6538^{+751}_{-696}	$0.540^{+0.094}_{-0.097}$
	Prevnew	36382^{+109}_{-107}	$8.210^{+0.041}_{-0.044}$	42948^{+740}_{-695}	$7.670^{+0.085}_{-0.087}$	-6566^{+748}_{-703}	$0.540^{+0.095}_{-0.097}$
	Barsold	36276^{+103}_{-102}	$8.212^{+0.042}_{-0.044}$	42764^{+738}_{-676}	$7.672^{+0.084}_{-0.087}$	-6488^{+745}_{-684}	$0.540^{+0.094}_{-0.097}$
	Barsnew	36383^{+109}_{-106}	$8.211^{+0.041}_{-0.044}$	42931^{+735}_{-689}	$7.670^{+0.085}_{-0.087}$	-6548^{+743}_{-698}	$0.541^{+0.094}_{-0.097}$
WD2111+498	PureH	36824^{+54}_{-53}	$8.404^{+0.017}_{-0.017}$	38919^{+311}_{-304}	$7.863^{+0.045}_{-0.045}$	-2095^{+316}_{-309}	$0.542^{+0.048}_{-0.048}$
	Prevold	36371^{+47}_{-46}	$8.410^{+0.017}_{-0.017}$	38354^{+288}_{-281}	$7.862^{+0.045}_{-0.045}$	-1983^{+292}_{-285}	$0.548^{+0.048}_{-0.048}$
	Prevnew	36460^{+48}_{-47}	$8.410^{+0.017}_{-0.017}$	38427^{+290}_{-282}	$7.862^{+0.045}_{-0.045}$	-1967^{+294}_{-286}	$0.549^{+0.048}_{-0.048}$
	Barsold	36332^{+46}_{-46}	$8.410^{+0.017}_{-0.017}$	38322^{+286}_{-279}	$7.862^{+0.045}_{-0.045}$	-1990^{+289}_{-283}	$0.548^{+0.048}_{-0.048}$
	Barsnew	36461^{+47}_{-47}	$8.410^{+0.017}_{-0.017}$	38431^{+289}_{-282}	$7.862^{+0.045}_{-0.045}$	-1970^{+293}_{-286}	$0.549^{+0.048}_{-0.048}$

Table 4.4: Continued.

Star	Grid	$T_{\rm eff}$ Ly	log g Ly	$T_{\rm eff}$ Bal	log g Bal	$\Delta T_{\rm eff}$	Δ log g
WD2152-548	PureH	44876^{+274}_{-282}	$7.848^{+0.044}_{-0.044}$	44799^{+957}_{-876}	$7.806^{+0.092}_{-0.092}$	77^{+996}_{-920}	$0.042^{+0.102}_{-0.102}$
	Prevold	43314^{+231}_{-223}	$7.873^{+0.042}_{-0.043}$	43677^{+873}_{-827}	$7.814^{+0.091}_{-0.091}$	-363^{+903}_{-856}	$0.059^{+0.101}_{-0.100}$
	Prevnew	43480^{+239}_{-230}	$7.873^{+0.042}_{-0.043}$	43798^{+867}_{-822}	$7.813^{+0.091}_{-0.091}$	-318^{+899}_{-853}	$0.060^{+0.101}_{-0.100}$
	Barsold	43174^{+223}_{-215}	$7.875^{+0.042}_{-0.042}$	43582^{+867}_{-821}	$7.816^{+0.092}_{-0.091}$	-408^{+896}_{-848}	$0.059^{+0.101}_{-0.100}$
	Barsnew	43445^{+237}_{-228}	$7.875^{+0.042}_{-0.043}$	43779^{+861}_{-816}	$7.813^{+0.091}_{-0.091}$	-334^{+893}_{-847}	$0.061^{+0.101}_{-0.100}$
WD2211-495	PureH	73767^{+323}_{-319}	$7.447^{+0.019}_{-0.020}$	63827^{+2400}_{-2154}	$7.294^{+0.120}_{-0.167}$	9940^{+2422}_{-2177}	$0.153^{+0.121}_{-0.168}$
	Prevold	68068^{+273}_{-273}	$7.495^{+0.019}_{-0.019}$	62253^{+2416}_{-2148}	$7.336^{+0.118}_{-0.137}$	5815^{+2431}_{-2165}	$0.159^{+0.120}_{-0.138}$
	Prevnew	67906^{+266}_{-267}	$7.497^{+0.019}_{-0.019}$	62351^{+2450}_{-2184}	$7.337^{+0.118}_{-0.136}$	5555^{+2464}_{-2200}	$0.160^{+0.120}_{-0.137}$
	Barsold	67871^{+274}_{-277}	$7.496^{+0.019}_{-0.019}$	61964^{+2393}_{-2138}	$7.336^{+0.118}_{-0.139}$	5907^{+2409}_{-2156}	$0.160^{+0.120}_{-0.140}$
	Barsnew	67867^{+267}_{-271}	$7.499^{+0.018}_{-0.019}$	62172^{+2408}_{-2140}	$7.335^{+0.119}_{-0.139}$	5694^{+2423}_{-2157}	$0.164^{+0.120}_{-0.141}$
WD2309+105	PureH	56548^{+238}_{-222}	$7.767^{+0.021}_{-0.020}$	54336^{+819}_{-792}	$8.126^{+0.058}_{-0.059}$	2213^{+853}_{-822}	$-0.359^{+0.062}_{-0.062}$
	Prevold	53195^{+192}_{-186}	$7.796^{+0.020}_{-0.020}$	52275^{+773}_{-732}	$8.131^{+0.058}_{-0.059}$	920^{+796}_{-755}	$-0.335^{+0.062}_{-0.062}$
	Prevnew	53386^{+193}_{-187}	$7.800^{+0.020}_{-0.020}$	52434^{+762}_{-724}	$8.128^{+0.058}_{-0.059}$	953^{+786}_{-747}	$-0.329^{+0.061}_{-0.062}$
	Barsold	52907^{+187}_{-181}	$7.794^{+0.020}_{-0.020}$	52009^{+762}_{-729}	$8.133^{+0.058}_{-0.059}$	899^{+784}_{-751}	$-0.339^{+0.061}_{-0.062}$
	Barsnew	53253^{+191}_{-184}	$7.799^{+0.020}_{-0.020}$	52360^{+760}_{-724}	$8.130^{+0.058}_{-0.059}$	893^{+784}_{-747}	$-0.331^{+0.061}_{-0.062}$
WD2331-475	PureH	59753^{+288}_{-284}	$7.606^{+0.019}_{-0.019}$	55127^{+1341}_{-1252}	$7.643^{+0.091}_{-0.092}$	4626^{+1371}_{-1284}	$-0.037^{+0.093}_{-0.094}$
	Prevold	56081^{+233}_{-228}	$7.638^{+0.019}_{-0.019}$	53436^{+1269}_{-1199}	$7.661^{+0.090}_{-0.091}$	2645^{+1290}_{-1221}	$-0.023^{+0.092}_{-0.093}$
	Prevnew	56158^{+232}_{-228}	$7.639^{+0.019}_{-0.019}$	53481^{+1244}_{-1180}	$7.660^{+0.090}_{-0.091}$	2677^{+1266}_{-1202}	$-0.021^{+0.092}_{-0.093}$
	Barsold	55844^{+229}_{-225}	$7.637^{+0.019}_{-0.019}$	53233^{+1259}_{-1184}	$7.661^{+0.090}_{-0.091}$	2611^{+1280}_{-1205}	$-0.024^{+0.092}_{-0.093}$
	Barsnew	56049^{+231}_{-227}	$7.640^{+0.019}_{-0.019}$	53411^{+1244}_{-1179}	$7.659^{+0.090}_{-0.091}$	2638^{+1265}_{-1200}	$-0.019^{+0.092}_{-0.093}$

Table 4.5: Same as Table 4.4, but for the Tremblay broadening tables.

Star	Grid	$T_{\rm eff}$ Ly	log g Ly	$T_{\rm eff}$ Bal	log g Bal	$\Delta T_{\rm eff}$	Δ log g
WD0004+330	PureH	49237^{+296}_{-287}	$7.893^{+0.033}_{-0.034}$	47286^{+588}_{-554}	$7.790^{+0.063}_{-0.074}$	1950^{+658}_{-624}	$0.103^{+0.071}_{-0.081}$
	Prevold	46995^{+251}_{-244}	$7.920^{+0.033}_{-0.033}$	46031^{+542}_{-530}	$7.800^{+0.065}_{-0.063}$	964^{+597}_{-583}	$0.120^{+0.073}_{-0.071}$
	Prevnew	47225^{+259}_{-255}	$7.921^{+0.033}_{-0.034}$	46147^{+539}_{-526}	$7.797^{+0.066}_{-0.064}$	1078^{+598}_{-585}	$0.124^{+0.073}_{-0.072}$
	Barsold	46763^{+242}_{-234}	$7.920^{+0.033}_{-0.033}$	45903^{+535}_{-523}	$7.803^{+0.065}_{-0.062}$	860^{+587}_{-573}	$0.117^{+0.073}_{-0.071}$
	Barsnew	47148^{+256}_{-251}	$7.922^{+0.033}_{-0.033}$	46103^{+534}_{-521}	$7.798^{+0.065}_{-0.064}$	1045^{+592}_{-578}	$0.124^{+0.073}_{-0.072}$
WD0131-163	PureH	46237^{+234}_{-258}	$7.994^{+0.031}_{-0.034}$	47347^{+632}_{-604}	$7.959^{+0.054}_{-0.052}$	-1110^{+674}_{-657}	$0.035^{+0.063}_{-0.062}$
	Prevold	44465^{+205}_{-207}	$8.014^{+0.035}_{-0.032}$	45722^{+557}_{-552}	$7.970^{+0.052}_{-0.050}$	-1257^{+594}_{-590}	$0.044^{+0.063}_{-0.060}$
	Prevnew	44680^{+214}_{-215}	$8.016^{+0.036}_{-0.033}$	45899^{+557}_{-550}	$7.968^{+0.053}_{-0.050}$	-1219^{+596}_{-591}	$0.048^{+0.064}_{-0.060}$
	Barsold	44285^{+198}_{-199}	$8.015^{+0.035}_{-0.032}$	45558^{+548}_{-545}	$7.971^{+0.052}_{-0.050}$	-1273^{+583}_{-580}	$0.043^{+0.063}_{-0.060}$
	Barsnew	44630^{+212}_{-212}	$8.016^{+0.036}_{-0.033}$	45853^{+551}_{-545}	$7.968^{+0.052}_{-0.050}$	-1223^{+590}_{-585}	$0.048^{+0.064}_{-0.060}$
WD0229-481	PureH	61683^{+623}_{-551}	$7.722^{+0.039}_{-0.036}$	63275^{+2319}_{-2131}	$7.415^{+0.122}_{-0.128}$	-1592^{+2401}_{-2201}	$0.307^{+0.128}_{-0.133}$
	Prevold	57688^{+420}_{-429}	$7.752^{+0.039}_{-0.031}$	61405^{+2301}_{-2093}	$7.452^{+0.118}_{-0.123}$	-3717^{+2339}_{-2137}	$0.300^{+0.124}_{-0.127}$
	Prevnew	57765^{+420}_{-420}	$7.753^{+0.039}_{-0.031}$	61382^{+2295}_{-2103}	$7.454^{+0.118}_{-0.122}$	-3618^{+2333}_{-2144}	$0.299^{+0.124}_{-0.126}$
	Barsold	57430^{+414}_{-442}	$7.750^{+0.039}_{-0.031}$	61142^{+2320}_{-2075}	$7.450^{+0.119}_{-0.123}$	-3712^{+2356}_{-2121}	$0.301^{+0.125}_{-0.127}$
	Barsnew	57652^{+420}_{-429}	$7.754^{+0.039}_{-0.032}$	61308^{+2292}_{-2095}	$7.450^{+0.119}_{-0.123}$	-3657^{+2330}_{-2139}	$0.305^{+0.125}_{-0.127}$
WD0346-011	PureH	40515^{+176}_{-174}	$9.371^{+0.033}_{-0.033}$	41168^{+423}_{-459}	$9.244^{+0.052}_{-0.048}$	-653^{+458}_{-491}	$0.127^{+0.062}_{-0.058}$
	Prevold	39968^{+152}_{-163}	$9.372^{+0.030}_{-0.032}$	40462^{+379}_{-404}	$9.241^{+0.052}_{-0.048}$	-494^{+408}_{-436}	$0.131^{+0.060}_{-0.058}$
	Prevnew	40125^{+154}_{-156}	$9.373^{+0.033}_{-0.033}$	40655^{+389}_{-415}	$9.241^{+0.052}_{-0.048}$	-530^{+418}_{-443}	$0.131^{+0.062}_{-0.058}$
	Barsold	39836^{+162}_{-159}	$9.369^{+0.030}_{-0.030}$	40317^{+373}_{-392}	$9.241^{+0.052}_{-0.048}$	-481^{+406}_{-423}	$0.128^{+0.060}_{-0.057}$
	Barsnew	40121^{+154}_{-156}	$9.373^{+0.033}_{-0.033}$	40654^{+388}_{-414}	$9.242^{+0.052}_{-0.048}$	-533^{+417}_{-443}	$0.131^{+0.062}_{-0.058}$
WD0501+524	PureH	63966^{+199}_{-197}	$7.616^{+0.013}_{-0.013}$	59241^{+295}_{-295}	$7.686^{+0.020}_{-0.020}$	4725^{+356}_{-355}	$-0.070^{+0.023}_{-0.024}$
	Prevold	59720^{+173}_{-169}	$7.654^{+0.013}_{-0.013}$	57204^{+274}_{-279}	$7.708^{+0.020}_{-0.020}$	2516^{+324}_{-327}	$-0.054^{+0.023}_{-0.023}$
	Prevnew	59689^{+169}_{-166}	$7.654^{+0.013}_{-0.013}$	57213^{+268}_{-278}	$7.707^{+0.020}_{-0.019}$	2476^{+317}_{-323}	$-0.053^{+0.023}_{-0.023}$
	Barsold	59471^{+171}_{-169}	$7.654^{+0.013}_{-0.013}$	56964^{+274}_{-277}	$7.709^{+0.020}_{-0.020}$	2507^{+323}_{-324}	$-0.055^{+0.023}_{-0.023}$
	Barsnew	59589^{+169}_{-166}	$7.657^{+0.013}_{-0.013}$	57140^{+270}_{-277}	$7.707^{+0.020}_{-0.020}$	2449^{+319}_{-323}	$-0.050^{+0.023}_{-0.023}$

Table 4.5: Continued.

Star	Grid	$T_{\rm eff}$ Ly	log g Ly	$T_{\rm eff}$ Bal	log g Bal	$\Delta T_{\rm eff}$	Δ log g
WD0556-375	PureH	65571^{+2388}_{-2249}	$7.560^{+0.139}_{-0.137}$	65920^{+2668}_{-2437}	$7.631^{+0.144}_{-0.143}$	-349^{+3580}_{-3316}	$-0.070^{+0.200}_{-0.198}$
	Prevold	60780^{+1963}_{-1792}	$7.584^{+0.141}_{-0.140}$	63654^{+2665}_{-2389}	$7.666^{+0.148}_{-0.140}$	-2874^{+3310}_{-2986}	$-0.081^{+0.204}_{-0.198}$
	Prevnew	60924^{+1953}_{-1791}	$7.595^{+0.140}_{-0.140}$	63656^{+2664}_{-2388}	$7.668^{+0.147}_{-0.139}$	-2732^{+3303}_{-2985}	$-0.073^{+0.203}_{-0.198}$
	Barsold	60685^{+1947}_{-1778}	$7.590^{+0.141}_{-0.140}$	63403^{+2683}_{-2414}	$7.664^{+0.149}_{-0.141}$	-2718^{+3315}_{-2998}	$-0.075^{+0.205}_{-0.199}$
	Barsnew	60845^{+1954}_{-1792}	$7.596^{+0.140}_{-0.140}$	63608^{+2683}_{-2390}	$7.664^{+0.148}_{-0.140}$	-2763^{+3319}_{-2987}	$-0.068^{+0.204}_{-0.199}$
WD0621-376	PureH	73588^{+568}_{-566}	$7.528^{+0.028}_{-0.031}$	60746^{+1849}_{-1731}	$7.150^{+0.104}_{-0.104}$	12842^{+1934}_{-1821}	$0.378^{+0.108}_{-0.109}$
	Prevold	67677^{+477}_{-477}	$7.579^{+0.029}_{-0.029}$	59453^{+1892}_{-1705}	$7.190^{+0.113}_{-0.105}$	8224^{+1951}_{-1771}	$0.389^{+0.116}_{-0.109}$
	Prevnew	67502^{+464}_{-479}	$7.577^{+0.029}_{-0.029}$	59530^{+1899}_{-1733}	$7.189^{+0.112}_{-0.105}$	7971^{+1955}_{-1798}	$0.388^{+0.115}_{-0.109}$
	Barsold	67437^{+479}_{-483}	$7.579^{+0.029}_{-0.029}$	59187^{+1881}_{-1683}	$7.188^{+0.114}_{-0.106}$	8250^{+1941}_{-1751}	$0.392^{+0.117}_{-0.110}$
	Barsnew	67447^{+470}_{-483}	$7.580^{+0.029}_{-0.029}$	59362^{+1883}_{-1724}	$7.186^{+0.113}_{-0.105}$	8085^{+1941}_{-1790}	$0.394^{+0.117}_{-0.109}$
WD1029+537	PureH	46281^{+375}_{-356}	$7.969^{+0.052}_{-0.050}$	46223^{+827}_{-798}	$7.822^{+0.075}_{-0.075}$	58^{+908}_{-873}	$0.147^{+0.091}_{-0.090}$
	Prevold	44551^{+317}_{-312}	$7.996^{+0.052}_{-0.048}$	44858^{+767}_{-705}	$7.830^{+0.074}_{-0.074}$	-307^{+830}_{-771}	$0.166^{+0.090}_{-0.089}$
	Prevnew	44763^{+313}_{-327}	$7.996^{+0.051}_{-0.049}$	44991^{+770}_{-703}	$7.828^{+0.074}_{-0.074}$	-229^{+831}_{-775}	$0.168^{+0.090}_{-0.089}$
	Barsold	44371^{+304}_{-304}	$7.996^{+0.051}_{-0.049}$	44736^{+753}_{-698}	$7.831^{+0.074}_{-0.074}$	-365^{+812}_{-762}	$0.165^{+0.090}_{-0.089}$
	Barsnew	44709^{+320}_{-318}	$7.996^{+0.052}_{-0.049}$	44958^{+762}_{-698}	$7.829^{+0.074}_{-0.074}$	-249^{+826}_{-767}	$0.168^{+0.090}_{-0.089}$
WD1057+719	PureH	41592^{+149}_{-149}	$8.023^{+0.033}_{-0.033}$	41784^{+304}_{-304}	$8.011^{+0.039}_{-0.042}$	-192^{+339}_{-338}	$0.012^{+0.051}_{-0.054}$
	Prevold	40570^{+121}_{-120}	$8.044^{+0.032}_{-0.034}$	40903^{+283}_{-277}	$8.013^{+0.038}_{-0.041}$	-334^{+307}_{-302}	$0.032^{+0.050}_{-0.054}$
	Prevnew	40702^{+128}_{-125}	$8.044^{+0.032}_{-0.035}$	41029^{+282}_{-283}	$8.011^{+0.039}_{-0.041}$	-327^{+309}_{-309}	$0.033^{+0.050}_{-0.053}$
	Barsold	40487^{+117}_{-117}	$8.046^{+0.032}_{-0.034}$	40834^{+278}_{-276}	$8.013^{+0.038}_{-0.041}$	-347^{+302}_{-300}	$0.033^{+0.049}_{-0.054}$
	Barsnew	40687^{+124}_{-124}	$8.045^{+0.032}_{-0.034}$	41021^{+282}_{-280}	$8.012^{+0.038}_{-0.041}$	-334^{+308}_{-306}	$0.033^{+0.050}_{-0.054}$
WD1234+481	PureH	55972^{+293}_{-285}	$7.931^{+0.027}_{-0.027}$	55716^{+1063}_{-1019}	$7.628^{+0.073}_{-0.074}$	257^{+1103}_{-1058}	$0.303^{+0.078}_{-0.079}$
	Prevold	52688^{+242}_{-237}	$7.962^{+0.027}_{-0.027}$	53985^{+999}_{-961}	$7.644^{+0.073}_{-0.074}$	-1298^{+1027}_{-990}	$0.318^{+0.078}_{-0.078}$
	Prevnew	52920^{+241}_{-234}	$7.963^{+0.027}_{-0.027}$	54024^{+981}_{-944}	$7.642^{+0.073}_{-0.074}$	-1105^{+1010}_{-973}	$0.321^{+0.078}_{-0.078}$
	Barsold	52367^{+244}_{-249}	$7.962^{+0.027}_{-0.027}$	53764^{+990}_{-953}	$7.645^{+0.073}_{-0.074}$	-1396^{+1019}_{-985}	$0.317^{+0.078}_{-0.079}$
	Barsnew	52804^{+239}_{-231}	$7.964^{+0.027}_{-0.027}$	53945^{+980}_{-943}	$7.643^{+0.073}_{-0.074}$	-1141^{+1008}_{-971}	$0.321^{+0.078}_{-0.078}$

Table 4.5: Continued.

Star	Grid	$T_{\rm eff}$ Ly	log g Ly	$T_{\rm eff}$ Bal	log g Bal	$\Delta T_{\rm eff}$	Δ log g
WD1254+223	PureH	39896^{+100}_{-98}	$7.982^{+0.021}_{-0.019}$	39868^{+147}_{-145}	$7.909^{+0.021}_{-0.021}$	28^{+177}_{-175}	$0.073^{+0.029}_{-0.028}$
	Prevold	39059^{+83}_{-79}	$7.994^{+0.020}_{-0.018}$	39212^{+135}_{-134}	$7.910^{+0.021}_{-0.021}$	-153^{+159}_{-155}	$0.084^{+0.029}_{-0.027}$
	Prevnew	39169^{+85}_{-81}	$7.994^{+0.020}_{-0.018}$	39297^{+136}_{-134}	$7.909^{+0.021}_{-0.021}$	-128^{+160}_{-157}	$0.085^{+0.029}_{-0.027}$
	Barsold	39000^{+80}_{-78}	$7.996^{+0.020}_{-0.018}$	39169^{+134}_{-132}	$7.911^{+0.021}_{-0.021}$	-170^{+156}_{-153}	$0.085^{+0.029}_{-0.027}$
	Barsnew	39162^{+84}_{-81}	$7.995^{+0.020}_{-0.018}$	39298^{+136}_{-134}	$7.910^{+0.021}_{-0.021}$	-136^{+159}_{-157}	$0.085^{+0.029}_{-0.027}$
WD1314+293	PureH	52361^{+173}_{-172}	$8.071^{+0.017}_{-0.018}$	51290^{+447}_{-444}	$8.025^{+0.038}_{-0.037}$	1071^{+479}_{-476}	$0.046^{+0.041}_{-0.041}$
	Prevold	49567^{+145}_{-144}	$8.099^{+0.017}_{-0.017}$	49483^{+414}_{-408}	$8.037^{+0.037}_{-0.037}$	84^{+439}_{-432}	$0.062^{+0.041}_{-0.040}$
	Prevnew	49845^{+148}_{-148}	$8.101^{+0.017}_{-0.017}$	49632^{+410}_{-403}	$8.035^{+0.037}_{-0.036}$	212^{+436}_{-430}	$0.066^{+0.041}_{-0.040}$
	Barsold	49260^{+139}_{-139}	$8.099^{+0.017}_{-0.017}$	49278^{+412}_{-405}	$8.038^{+0.037}_{-0.037}$	-18^{+434}_{-428}	$0.061^{+0.041}_{-0.040}$
	Barsnew	49741^{+146}_{-145}	$8.101^{+0.017}_{-0.017}$	49565^{+406}_{-401}	$8.036^{+0.037}_{-0.036}$	176^{+432}_{-426}	$0.065^{+0.041}_{-0.040}$
WD1342+443	PureH	66102^{+1808}_{-1677}	$8.210^{+0.119}_{-0.119}$	61251^{+2559}_{-2380}	$8.250^{+0.148}_{-0.123}$	4851^{+3133}_{-2911}	$-0.040^{+0.190}_{-0.171}$
	Prevold	61153^{+1377}_{-1346}	$8.248^{+0.119}_{-0.116}$	58436^{+2350}_{-2254}	$8.252^{+0.168}_{-0.108}$	2717^{+2723}_{-2625}	$-0.004^{+0.206}_{-0.158}$
	Prevnew	61166^{+1386}_{-1346}	$8.242^{+0.119}_{-0.116}$	58459^{+2301}_{-2194}	$8.254^{+0.168}_{-0.108}$	2708^{+2686}_{-2574}	$-0.011^{+0.206}_{-0.158}$
	Barsold	60598^{+1337}_{-1345}	$8.244^{+0.120}_{-0.117}$	58115^{+2306}_{-2258}	$8.251^{+0.168}_{-0.108}$	2483^{+2665}_{-2629}	$-0.007^{+0.206}_{-0.159}$
	Barsnew	61035^{+1368}_{-1341}	$8.245^{+0.119}_{-0.116}$	58413^{+2328}_{-2214}	$8.252^{+0.168}_{-0.108}$	2622^{+2700}_{-2588}	$-0.008^{+0.206}_{-0.159}$
WD1636+351	PureH	40418^{+240}_{-233}	$8.042^{+0.055}_{-0.056}$	37023^{+300}_{-293}	$7.858^{+0.053}_{-0.053}$	3395^{+384}_{-374}	$0.184^{+0.076}_{-0.077}$
	Prevold	39540^{+237}_{-227}	$8.061^{+0.055}_{-0.058}$	36636^{+279}_{-272}	$7.857^{+0.053}_{-0.053}$	2904^{+366}_{-354}	$0.204^{+0.076}_{-0.078}$
	Prevnew	39668^{+247}_{-234}	$8.062^{+0.055}_{-0.058}$	36690^{+281}_{-274}	$7.857^{+0.053}_{-0.053}$	2978^{+374}_{-360}	$0.205^{+0.076}_{-0.078}$
	Barsold	39462^{+231}_{-222}	$8.059^{+0.055}_{-0.058}$	36622^{+276}_{-270}	$7.857^{+0.053}_{-0.053}$	2840^{+360}_{-349}	$0.202^{+0.076}_{-0.078}$
	Barsnew	39658^{+245}_{-234}	$8.063^{+0.055}_{-0.058}$	36697^{+281}_{-274}	$7.857^{+0.053}_{-0.053}$	2961^{+373}_{-360}	$0.205^{+0.076}_{-0.078}$
WD1725+586	PureH	54276^{+959}_{-901}	$8.287^{+0.099}_{-0.098}$	54337^{+2213}_{-2013}	$8.351^{+0.157}_{-0.155}$	-61^{+2412}_{-2205}	$-0.064^{+0.185}_{-0.183}$
	Prevold	51169^{+792}_{-726}	$8.311^{+0.095}_{-0.096}$	52073^{+2033}_{-1822}	$8.360^{+0.155}_{-0.154}$	-903^{+2181}_{-1961}	$-0.049^{+0.182}_{-0.182}$
	Prevnew	51483^{+823}_{-749}	$8.310^{+0.095}_{-0.097}$	52288^{+1990}_{-1802}	$8.358^{+0.155}_{-0.154}$	-806^{+2153}_{-1951}	$-0.048^{+0.182}_{-0.182}$
	Barsold	50823^{+758}_{-697}	$8.311^{+0.094}_{-0.096}$	51770^{+2016}_{-1810}	$8.362^{+0.155}_{-0.155}$	-947^{+2154}_{-1939}	$-0.050^{+0.182}_{-0.182}$
	Barsnew	51427^{+812}_{-745}	$8.320^{+0.094}_{-0.096}$	52211^{+1989}_{-1803}	$8.358^{+0.155}_{-0.154}$	-784^{+2149}_{-1950}	$-0.039^{+0.181}_{-0.181}$

Table 4.5: Continued.

Star	Grid	T_{eff} Ly	log g Ly	T_{eff} Bal	log g Bal	ΔT_{eff}	Δ log g
WD1738+669	PureH	92679^{+998}_{-1055}	$8.047^{+0.033}_{-0.034}$	79041^{+1815}_{-1753}	$7.796^{+0.084}_{-0.117}$	13638^{+2071}_{-2046}	$0.252^{+0.090}_{-0.122}$
	Prevold	82989^{+895}_{-873}	$8.106^{+0.033}_{-0.033}$	76358^{+1852}_{-1761}	$7.822^{+0.084}_{-0.089}$	6630^{+2057}_{-1966}	$0.285^{+0.090}_{-0.095}$
	Prevnew	82544^{+844}_{-851}	$8.105^{+0.033}_{-0.033}$	76304^{+1818}_{-1764}	$7.826^{+0.083}_{-0.088}$	6240^{+2004}_{-1958}	$0.278^{+0.089}_{-0.094}$
	Barsold	82562^{+875}_{-887}	$8.113^{+0.033}_{-0.033}$	76134^{+1878}_{-1796}	$7.821^{+0.084}_{-0.090}$	6428^{+2072}_{-2003}	$0.292^{+0.091}_{-0.096}$
	Barsnew	82678^{+881}_{-878}	$8.110^{+0.033}_{-0.033}$	76373^{+1844}_{-1769}	$7.826^{+0.083}_{-0.089}$	6305^{+2044}_{-1975}	$0.284^{+0.089}_{-0.094}$
WD1800+685	PureH	45694^{+252}_{-239}	$7.936^{+0.035}_{-0.034}$	44836^{+884}_{-806}	$7.783^{+0.087}_{-0.088}$	857^{+919}_{-841}	$0.153^{+0.094}_{-0.094}$
	Prevold	44034^{+228}_{-207}	$7.961^{+0.036}_{-0.033}$	43741^{+804}_{-758}	$7.788^{+0.087}_{-0.087}$	293^{+835}_{-786}	$0.173^{+0.094}_{-0.093}$
	Prevnew	44239^{+237}_{-216}	$7.962^{+0.036}_{-0.033}$	43860^{+799}_{-754}	$7.786^{+0.087}_{-0.087}$	379^{+833}_{-784}	$0.176^{+0.094}_{-0.093}$
	Barsold	43871^{+219}_{-200}	$7.962^{+0.036}_{-0.033}$	43645^{+799}_{-753}	$7.789^{+0.087}_{-0.087}$	226^{+828}_{-779}	$0.173^{+0.094}_{-0.093}$
	Barsnew	44190^{+237}_{-212}	$7.963^{+0.036}_{-0.033}$	43837^{+794}_{-750}	$7.787^{+0.087}_{-0.087}$	353^{+828}_{-779}	$0.176^{+0.094}_{-0.093}$
WD1819+580	PureH	46045^{+335}_{-322}	$8.796^{+0.064}_{-0.065}$	46108^{+539}_{-525}	$7.860^{+0.054}_{-0.054}$	-63^{+634}_{-616}	$0.936^{+0.084}_{-0.085}$
	Prevold	44560^{+297}_{-290}	$8.807^{+0.065}_{-0.065}$	44883^{+505}_{-471}	$7.862^{+0.054}_{-0.054}$	-323^{+586}_{-553}	$0.946^{+0.084}_{-0.085}$
	Prevnew	44873^{+292}_{-302}	$8.811^{+0.065}_{-0.066}$	45010^{+508}_{-470}	$7.860^{+0.054}_{-0.054}$	-137^{+585}_{-558}	$0.951^{+0.084}_{-0.085}$
	Barsold	44325^{+289}_{-274}	$8.808^{+0.064}_{-0.066}$	44770^{+492}_{-467}	$7.863^{+0.054}_{-0.054}$	-445^{+571}_{-541}	$0.945^{+0.083}_{-0.085}$
	Barsnew	44833^{+291}_{-300}	$8.812^{+0.065}_{-0.066}$	44976^{+502}_{-466}	$7.860^{+0.054}_{-0.054}$	-142^{+580}_{-554}	$0.951^{+0.084}_{-0.085}$
WD1845+683	PureH	37059^{+126}_{-122}	$8.330^{+0.047}_{-0.049}$	44996^{+832}_{-773}	$7.751^{+0.082}_{-0.083}$	-7936^{+841}_{-782}	$0.579^{+0.095}_{-0.096}$
	Prevold	36573^{+109}_{-106}	$8.341^{+0.046}_{-0.047}$	43920^{+743}_{-737}	$7.751^{+0.086}_{-0.077}$	-7347^{+750}_{-745}	$0.590^{+0.097}_{-0.091}$
	Prevnew	36663^{+111}_{-109}	$8.342^{+0.046}_{-0.048}$	44021^{+751}_{-724}	$7.754^{+0.081}_{-0.082}$	-7358^{+759}_{-732}	$0.587^{+0.094}_{-0.095}$
	Barsold	36534^{+107}_{-104}	$8.343^{+0.046}_{-0.047}$	43820^{+743}_{-727}	$7.751^{+0.087}_{-0.076}$	-7286^{+751}_{-734}	$0.591^{+0.098}_{-0.090}$
	Barsnew	36664^{+112}_{-108}	$8.342^{+0.046}_{-0.047}$	43997^{+746}_{-720}	$7.755^{+0.082}_{-0.082}$	-7332^{+755}_{-728}	$0.588^{+0.094}_{-0.094}$
WD2111+498	PureH	36989^{+61}_{-60}	$8.574^{+0.018}_{-0.018}$	39837^{+330}_{-311}	$7.957^{+0.045}_{-0.047}$	-2848^{+336}_{-316}	$0.617^{+0.048}_{-0.050}$
	Prevold	36530^{+52}_{-52}	$8.575^{+0.018}_{-0.018}$	39183^{+293}_{-284}	$7.956^{+0.045}_{-0.046}$	-2654^{+297}_{-289}	$0.619^{+0.048}_{-0.050}$
	Prevnew	36629^{+54}_{-53}	$8.576^{+0.018}_{-0.018}$	39271^{+295}_{-286}	$7.955^{+0.045}_{-0.046}$	-2643^{+300}_{-291}	$0.621^{+0.048}_{-0.050}$
	Barsold	36480^{+52}_{-51}	$8.575^{+0.018}_{-0.018}$	39141^{+290}_{-283}	$7.956^{+0.045}_{-0.046}$	-2661^{+294}_{-287}	$0.619^{+0.048}_{-0.050}$
	Barsnew	36629^{+54}_{-53}	$8.576^{+0.018}_{-0.018}$	39273^{+294}_{-286}	$7.955^{+0.045}_{-0.046}$	-2644^{+299}_{-291}	$0.621^{+0.048}_{-0.050}$

Table 4.5: Continued.

Star	Grid	$T_{\rm eff}$ Ly	log g Ly	$T_{\rm eff}$ Bal	log g Bal	$\Delta T_{\rm eff}$	Δ log g
WD2152-548	PureH	45873^{+269}_{-279}	$7.987^{+0.038}_{-0.041}$	46018^{+977}_{-934}	$7.886^{+0.094}_{-0.095}$	-145^{+1013}_{-975}	$0.101^{+0.101}_{-0.104}$
	Prevold	44189^{+227}_{-222}	$8.009^{+0.043}_{-0.035}$	44765^{+912}_{-835}	$7.894^{+0.093}_{-0.095}$	-577^{+940}_{-864}	$0.115^{+0.103}_{-0.101}$
	Prevnew	44394^{+235}_{-230}	$8.010^{+0.044}_{-0.036}$	44895^{+911}_{-831}	$7.892^{+0.093}_{-0.094}$	-502^{+940}_{-863}	$0.118^{+0.103}_{-0.101}$
	Barsold	44019^{+219}_{-214}	$8.010^{+0.044}_{-0.035}$	44653^{+896}_{-829}	$7.896^{+0.093}_{-0.095}$	-634^{+923}_{-856}	$0.114^{+0.103}_{-0.101}$
	Barsnew	44349^{+234}_{-228}	$8.011^{+0.044}_{-0.036}$	44869^{+902}_{-826}	$7.893^{+0.093}_{-0.094}$	-520^{+931}_{-856}	$0.118^{+0.103}_{-0.101}$
WD2211-495	PureH	74457^{+336}_{-325}	$7.486^{+0.019}_{-0.019}$	65655^{+2390}_{-2213}	$7.330^{+0.121}_{-0.157}$	8802^{+2413}_{-2237}	$0.156^{+0.122}_{-0.158}$
	Prevold	68507^{+299}_{-288}	$7.540^{+0.020}_{-0.023}$	64035^{+2494}_{-2222}	$7.377^{+0.120}_{-0.122}$	4472^{+2512}_{-2240}	$0.163^{+0.121}_{-0.124}$
	Prevnew	68334^{+290}_{-280}	$7.542^{+0.021}_{-0.023}$	64172^{+2478}_{-2246}	$7.378^{+0.119}_{-0.122}$	4162^{+2495}_{-2263}	$0.164^{+0.121}_{-0.124}$
	Barsold	68290^{+305}_{-292}	$7.541^{+0.020}_{-0.023}$	63706^{+2426}_{-2206}	$7.377^{+0.120}_{-0.123}$	4585^{+2445}_{-2225}	$0.164^{+0.122}_{-0.125}$
	Barsnew	68281^{+292}_{-283}	$7.545^{+0.021}_{-0.023}$	63964^{+2501}_{-2217}	$7.376^{+0.120}_{-0.122}$	4316^{+2518}_{-2235}	$0.169^{+0.122}_{-0.124}$
WD2309+105	PureH	58020^{+237}_{-232}	$7.876^{+0.020}_{-0.020}$	56298^{+842}_{-809}	$8.200^{+0.061}_{-0.063}$	1722^{+875}_{-842}	$-0.324^{+0.064}_{-0.066}$
	Prevold	54402^{+208}_{-205}	$7.903^{+0.020}_{-0.020}$	54003^{+780}_{-753}	$8.206^{+0.061}_{-0.061}$	399^{+807}_{-780}	$-0.304^{+0.064}_{-0.064}$
	Prevnew	54599^{+209}_{-207}	$7.905^{+0.019}_{-0.020}$	54162^{+762}_{-735}	$8.203^{+0.060}_{-0.061}$	437^{+790}_{-764}	$-0.298^{+0.064}_{-0.064}$
	Barsold	54078^{+203}_{-199}	$7.900^{+0.020}_{-0.020}$	53689^{+776}_{-749}	$8.209^{+0.061}_{-0.061}$	389^{+802}_{-775}	$-0.309^{+0.064}_{-0.064}$
	Barsnew	54466^{+207}_{-204}	$7.905^{+0.020}_{-0.020}$	54085^{+760}_{-736}	$8.204^{+0.061}_{-0.061}$	381^{+788}_{-763}	$-0.299^{+0.064}_{-0.064}$
WD2331-475	PureH	62395^{+286}_{-302}	$7.747^{+0.019}_{-0.018}$	56891^{+1394}_{-1291}	$7.712^{+0.101}_{-0.098}$	5503^{+1423}_{-1326}	$0.035^{+0.103}_{-0.100}$
	Prevold	58167^{+226}_{-226}	$7.782^{+0.019}_{-0.020}$	55015^{+1331}_{-1216}	$7.732^{+0.100}_{-0.097}$	3152^{+1350}_{-1237}	$0.049^{+0.102}_{-0.099}$
	Prevnew	58249^{+223}_{-224}	$7.783^{+0.019}_{-0.020}$	55054^{+1313}_{-1194}	$7.730^{+0.100}_{-0.097}$	3196^{+1332}_{-1214}	$0.053^{+0.102}_{-0.099}$
	Barsold	57916^{+220}_{-223}	$7.780^{+0.019}_{-0.020}$	54779^{+1325}_{-1214}	$7.733^{+0.101}_{-0.098}$	3136^{+1343}_{-1235}	$0.047^{+0.103}_{-0.100}$
	Barsnew	58135^{+223}_{-224}	$7.784^{+0.019}_{-0.020}$	54977^{+1316}_{-1191}	$7.730^{+0.100}_{-0.098}$	3158^{+1334}_{-1212}	$0.054^{+0.102}_{-0.100}$

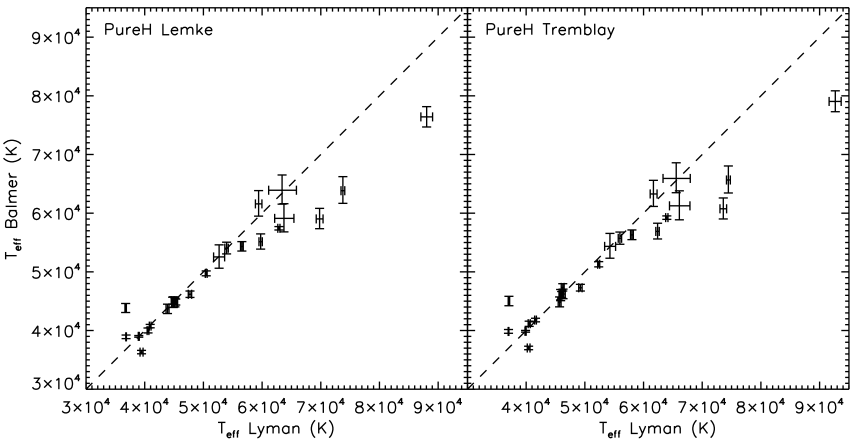

Figure 4.1: Plot of calculated $T_{\rm eff}$ using a pure H model grid. The left plot shows the results obtained for spectra synthesised with the Lemke tables, and the right plot is for results obtained with spectra synthesised with the Tremblay tables. The dashed line is for equal Lyman and Balmer line $T_{\rm eff}$. The far outlier on the top right of the plots is WD1738+669.

blay, the discrepancy between the Lyman and Balmer $T_{\rm eff}$ values decreases for eight white dwarfs, namely WD0229-481, WD0501+524, WD0556-375, WD1029+537, WD1725+586, WD1819+580, WD2211-495, and WD2309+105. Excluding WD0501+524, the $T_{\rm eff}$ discrepancy is within the uncertainties of the individual Lyman and Balmer $T_{\rm eff}$ measurements. While the decrease in $T_{\rm eff}$ discrepancy for WD0501+524 is statistically significant ($\Delta T_{Lemke} - \Delta T_{Tremblay} = 717^{+497}_{-492}$K), this is only one star out of a sample of 24.

The corresponding measured log g values are plotted in Figure 4.2. A large scatter is present for all values of log g, although it is noted there are several stars where the Lyman and Balmer line values are in good agreement. Nine white dwarf stars have a smaller log g discrepancy using the Tremblay models when compared to measurements made with the Lemke tables. These objects are WD0131-163,WD0501+524, WD0556-375, WD1057+719, WD1314+293, WD1342+443, WD1725+586, WD2309+105, and WD2331-475. However, unlike the $T_{\rm eff}$ measurements, the differences between the Lemke and Tremblay log g discrepancies are within the uncertainties of the individual Lyman and Balmer measurements.

As there are metal-polluted white dwarfs in the sample, it is not surprising that there is a large amount of scatter. This is evident in Tables 4.4 and 4.5, where the difference between the Lyman and Balmer $T_{\rm eff}$ for the metal-rich white dwarfs WD2211-492 and WD1738+699 is in excess of 8000K.

4.7 Results - Preval et al. (2013) model grids

The measured Lyman and Balmer $T_{\rm eff}$ using the Prevold model grid are plotted in Figure 4.3 for both the Lemke and Tremblay broadening tables. Good agreement is seen between the Lyman and Balmer $T_{\rm eff}$ values up to 52000K, and a few stars are in good agreement at $T_{\rm eff}$ ∼60000K. There are, however, a handful of stars where there are large deviations from the Lyman=Balmer line.

For the Prevold grid, seven white dwarf stars have smaller $T_{\rm eff}$ discrepancies when using the Tremblay models compared to the Lemke models, namely WD0229-481, WD0346-011, WD0501+524, WD1234+481, WD1342+443, WD2211+495, and WD2309+105. For the Prevnew grid, the same white dwarfs plus WD1819+580 have smaller $T_{\rm eff}$ discrepancies using the Tremblay models. In both the Prevold and Prevnew grids, the

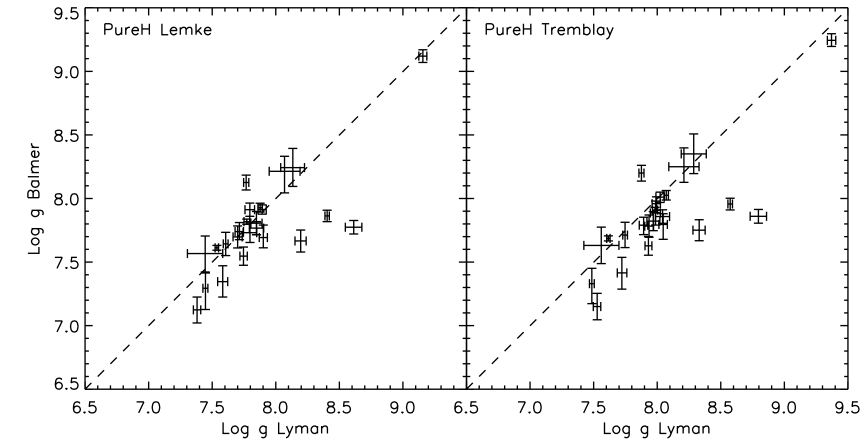

Figure 4.2: Plot of calculated log g using a pure H model grid. The left plot shows the results obtained for spectra synthesised with the Lemke tables, and the right plot is for results obtained with spectra synthesised with the Tremblay tables. The dashed line is for equal Lyman and Balmer line $T_{\rm eff}$. The outlier near log $g > 9$ is the heavy white dwarf WD0346-011.

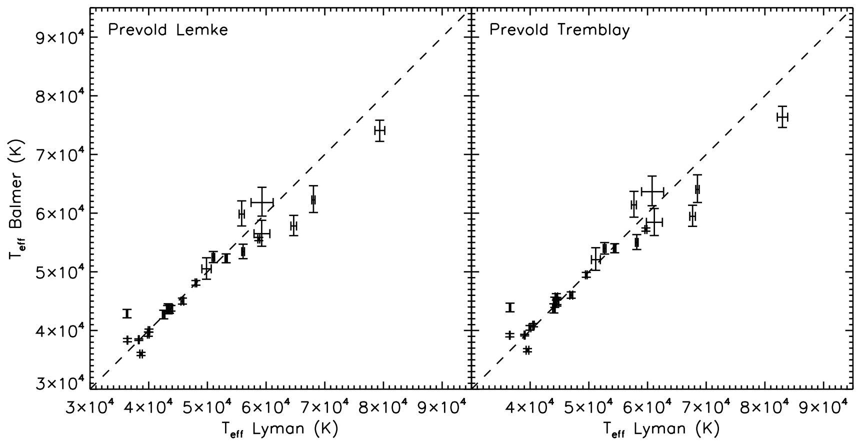

Figure 4.3: Plot of calculated $T_{\rm eff}$ using a Prevold model grid. The left plot shows the results obtained for spectra synthesised with the Lemke tables, and the right plot is for results obtained with spectra synthesised with the Tremblay tables. The dashed line is for equal Lyman and Balmer line $T_{\rm eff}$. The far outlier on the top right of the plots is WD1738+669.

difference between the discrepancies measured using the Lemke and Tremblay models are within the uncertainties of the individual Lyman and Balmer $T_{\rm eff}$ measurements for all of these objects with the exception of WD0501+524 ($\Delta T_{Lemke} - \Delta T_{Tremblay} = 653^{+456}_{-456}$ and 700^{+451}_{-449}K for the Prevold and Prevnew grids respectively).

Figure 4.4 shows the corresponding log g values. Large scatter about the Lyman=Balmer line is observed for some stars. Comparing the log g discrepancies measured in the Prevold and Prevnew grids, six white dwarfs have smaller discrepancies when using the Tremblay models compared to the Lemke models. These white dwarfs are WD0131-163, WD0501+524, WD0556-375, WD1342+443, WD1725+586, and WD2309+105. In all cases, however, the difference between the discrepancies measured in the Lemke and Tremblay models were within the uncertainties of the individual Lyman and Balmer measurements.

In Figures 4.5 and 4.6, the differences between the Prevold and Prevnew $T_{\rm eff}$ are plotted for each star for the Lyman and Balmer values respectively. It is evident in both plots that there is very little difference between the measured Prevold and Prevnew $T_{\rm eff}$. Only a few differences in Figure 4.5 are inconsistent with

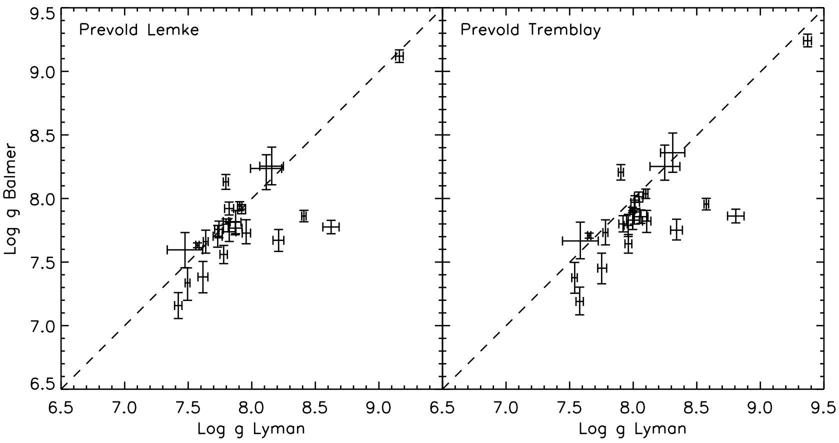

Figure 4.4: Plot of calculated log g using a Prevold model grid. The left plot shows the results obtained for spectra synthesised with the Lemke tables, and the right plot is for results obtained with spectra synthesised with the Tremblay tables. The dashed line is for equal Lyman and Balmer line $T_{\rm eff}$*. The outlier near log* $g > 9$ *is the heavy white dwarf WD0346-011.*

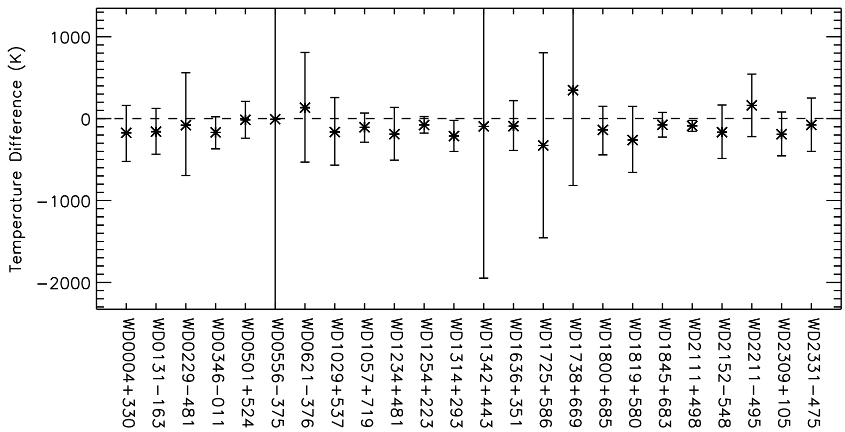

Figure 4.5: Differences between calculated Lyman Prevold $T_{\rm eff}$ *and Lyman Prevnew* $T_{\rm eff}$*, plotted against their respective stars.*

zero, while all differences in Figure 4.6 are consistent with zero. Because there is little difference between the Prevold and Prevnew results, the plots for the latter are omitted.

The Prevold $T_{\rm eff}$ results appear to be quite similar to those found using the pure H model grid. It is noted, however, that the scatter in the Prevold $T_{\rm eff}$ is much less than that observed for the pure H values. The largest improvement in the Lyman and Balmer $T_{\rm eff}$ discrepancy occurs for WD1738+669, where the difference is now ∼3000K, compared to >10000K when using the pure H model grid to measure $T_{\rm eff}$. No such improvements are evident for the measured log g values.

4.8 Results - Barstow et al. (2003) model grids

As with the Prevold model grid, the Barsold model grid significantly improves the agreement between the measured Lyman and Balmer line $T_{\rm eff}$. In Figure 4.7, the calculated Lyman $T_{\rm eff}$ are plotted against the Balmer $T_{\rm eff}$ using both the Lemke and Tremblay broadening tables.

In the Barsold grid, eight white dwarfs, namely WD0229-481, WD0346-011, WD0501+524, WD1234+481,

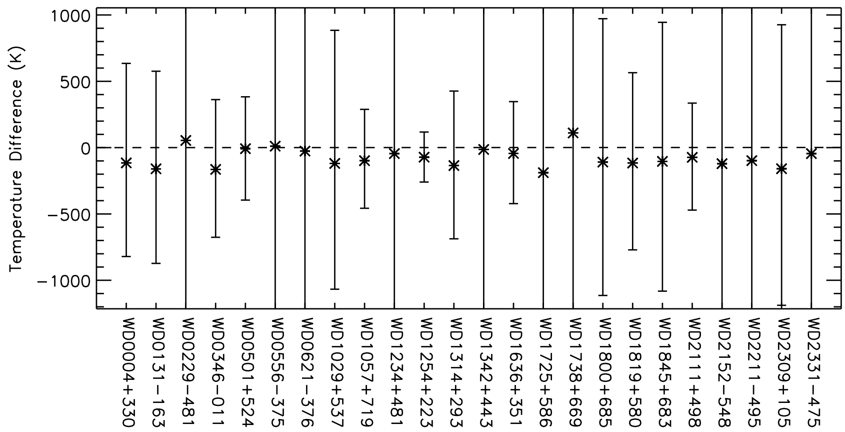

Figure 4.6: Differences between calculated Balmer Prevold $T_{\rm eff}$ and Balmer Prevnew $T_{\rm eff}$, plotted against their respective stars.

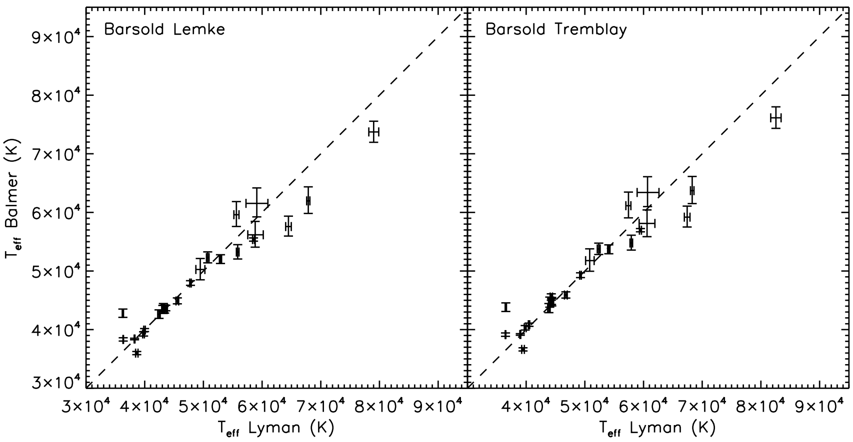

Figure 4.7: Plot of calculated $T_{\rm eff}$ using a Barsold model grid. The left plot shows the results obtained for spectra synthesised with the Lemke tables, and the right plot is for results obtained with spectra synthesised with the Tremblay tables. The dashed line is for equal Lyman and Balmer line $T_{\rm eff}$. The far outlier on the top right of the plots is WD1738+669.

WD1314+293, WD1342+443, WD2211-495, and WD2309+105 have smaller Lyman and Balmer $T_{\rm eff}$ discrepancies when using the Tremblay models compared to the Lemke models. For the Barsnew grid, WD0229-481, WD0346-011, WD0501+524, WD1234+481, WD1342+443, WD1819+580, WD2211-495, and WD2309+105 also exhibit a smaller discrepancy when using the Tremblay tables. In both the Barsold and Barsnew grids, the difference between the Lemke and Tremblay $T_{\rm eff}$ discrepancies were smaller than the individual Lyman and Balmer $T_{\rm eff}$ measurements for all stars with the exception of WD0501+524 ($\Delta T_{Lemke} - \Delta T_{Tremblay} = 669^{+456}_{-453}$ and 705^{+450}_{-450}K for the Barsold and Barsnew grids respectively).

The Lyman and Balmer log g values calculated using the Barsold model grid are plotted in Figure 4.8, using both the Lemke and Tremblay broadening tables. As in the Prevold case, the log g values are highly scattered about the Lyman=Balmer line.

For both the Barsold and Barsnew grids, the differences in log g discrepancy between the Lyman and Balmer measurements was smaller when using the Tremblay models compared to the Lemke models for six white dwarfs. These objects are WD0131-163, WD0501+524, WD0556-375, WD1342+443, WD1725+586, and WD2309+105. For all of these objects, however, the difference between log g discrepancies measured with

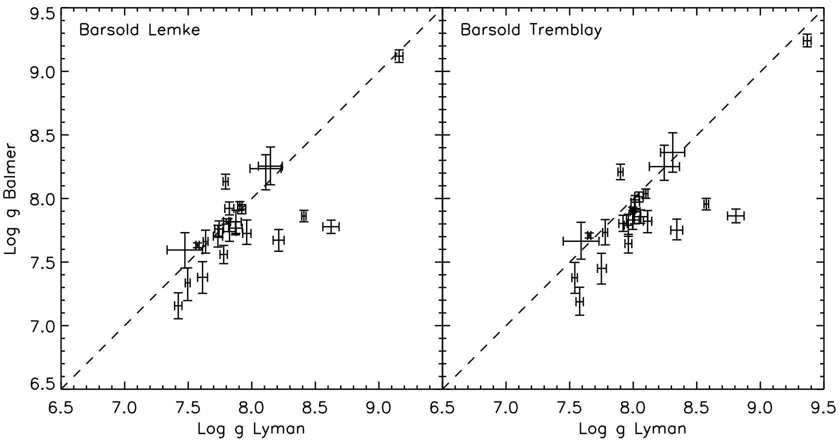

Figure 4.8: Plot of calculated log g using a Barsold model grid. The left plot shows the results obtained for spectra synthesised with the Lemke tables, and the right plot is for results obtained with spectra synthesised with the Tremblay tables. The dashed line is for equal Lyman and Balmer line $T_{\rm eff}$. The outlier near log $g > 9$ is the massive white dwarf WD0346-011.

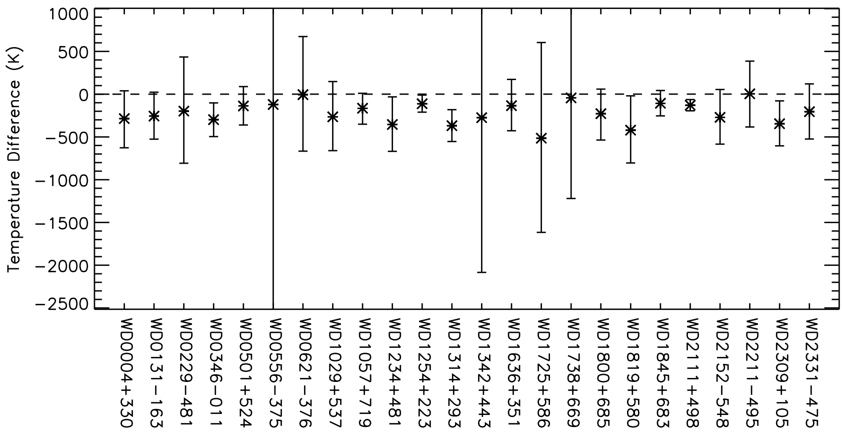

Figure 4.9: Differences between calculated Lyman Barsold $T_{\rm eff}$ and Lyman Barsnew $T_{\rm eff}$, plotted against their respective stars.

the Lemke and Tremblay models were smaller than the individual Lyman and Balmer log g measurements.

Like the Prevold and Prevnew cases, there do not appear to be any significant differences between the Barsold and Barsnew $T_{\rm eff}$ values. In Figure 4.9, the differences between the Barsold and Barsnew Lyman $T_{\rm eff}$ are plotted against their respective stars, while in Figure 4.10, the differences for the Balmer values are plotted. All of the differences (bar a few values in Figure 4.9) are consistent with zero difference.

4.9 Discussion

It has been shown that while there is generally good agreement between the Lyman and Balmer $T_{\rm eff}$ for stars with $T_{\rm eff}$ <60000K, stars in excess of this temperature quickly begin to show large discrepancies. The largest discrepancies arise from measurements made using the pure hydrogen grid, and improve significantly when using metal-polluted model grids. The measured log g values in all cases do not appear to be heavily dependent upon the model grid used. There is a large amount of scatter about the Lyman=Balmer line, and is focused between log g=7-8.5.

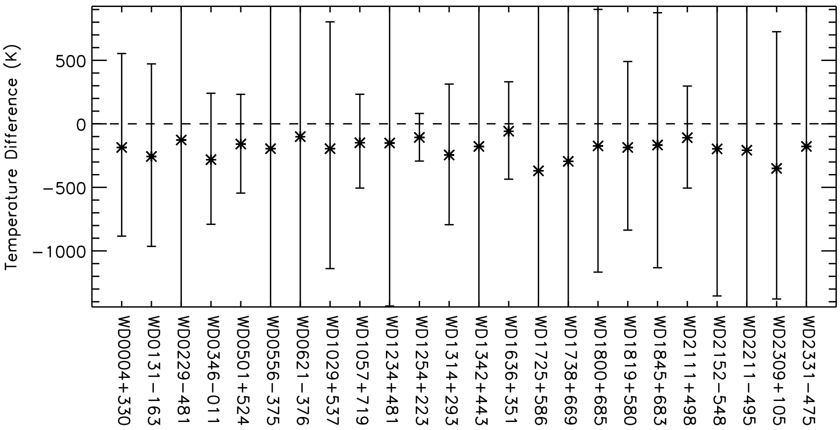

Figure 4.10: Differences between calculated Balmer Barsold $T_{\rm eff}$ and Balmer Barsnew $T_{\rm eff}$, plotted against their respective stars.

Interestingly, WD0501+524 stood out with regards to $T_{\rm eff}$ measurements made using the Lemke and Tremblay models. Subtracting the Tremblay $\Delta T_{\rm eff}$ from the Lemke value results in a difference between the two models that is statistically significant. This occurs for the pure H, Prevold, Prevnew, Barsold, and Barsnew grids, with the differences between the Lemke and Tremblay discrepancies being 717^{+497}_{-492}, 653^{+456}_{-456}, 700^{+451}_{-449}, 669^{+456}_{-453}, and 705^{+450}_{-450}K respectively. As the pure H model grid exhibits roughly the same difference between the Lemke and Tremblay values, the improvement does not appear to be due to the metal composition of the grid used. Instead, the UV and optical data used for WD0501+524 was constructed using many more observations than other stars in the sample, resulting in a lower uncertainty on the flux. This translates into a smaller uncertainty on the measured $T_{\rm eff}$ and log g.

For all of the metal-polluted model grids, there appears to be an interesting dichotomy. At ∼60000K, there are three objects, one of which lies on the Lyman=Balmer line (WD0556-375), and the other two lying below it (WD1342+443 and WD0621-376). For increasing temperatures, there are three more objects, again below the Lyman=Balmer line. Below 60000K, the majority of the objects in the study are either on the Lyman=Balmer line, or are scattered very closely to it (with the exception of WD2111+498). The dichotomy, then, is a branch of objects that follows the Lyman=Balmer line at higher temperatures, and another branch that departs from the line. While it is tempting to say that one branch corresponds to pure H white dwarfs and the other to metal-polluted stars, Vennes et al. (2006) has shown WD0556-375 to have large quantities of Fe present in STIS observations of the object. Furthermore, all stars with $T_{\rm eff}$ >60000K in this sample have been shown to be metal-polluted.

Use of the Ku92 or the Ku11 atomic data does not appear to make any difference to the agreement between the Lyman and Balmer line $T_{\rm eff}$ in both the Preval et al. (2013) and the Barstow et al. (2003) abundance model grids. It confirms that Ku92 data, coupled with PI cross section data from the OP, is adequate to account for line blanketing in model atmospheres. Furthermore, it also validates the technique utilised in Chapter 3 to calculate PI cross sections. This means that this technique may also be used with other atoms and ions.

In order to deduce the factors that provide the largest contributions to the Lyman/Balmer line problem, it is necessary to consider the various differences between the model atmosphere grids. Firstly, the differences

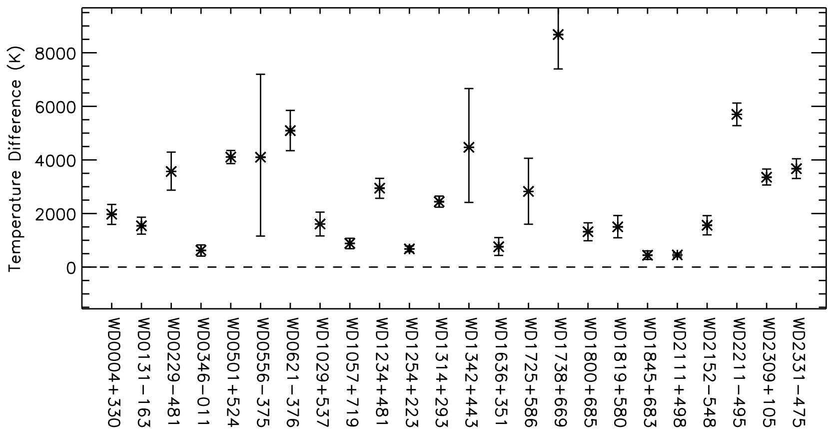

Figure 4.11: Differences between calculated Lyman Pure H $T_{\rm eff}$ and Lyman Prevold $T_{\rm eff}$, plotted against their respective stars.

between the pure H and Prevold grids are discussed, followed by a comparison of the Lemke and Tremblay results. The differences between the Prevold and Barsold results are considered, concluding with the possible origin of the Lyman/Balmer line problem.

4.9.1 Grid comparisons - Pure H/Prevold

As was highlighted in Barstow et al. (1998), measurements of $T_{\rm eff}$ performed with a pure H grid were significantly higher than measurements obtained with a metal-polluted grid. In Figure 4.11, the Lyman $T_{\rm eff}$ determined with a metal-polluted model grid (Prevold) was subtracted from the corresponding $T_{\rm eff}$ calculated with a pure H model, and plotted against the corresponding white dwarf. In general, the values are very scattered, and deviate quite strongly from zero difference, the largest being >8000K for WD1738+669.

The same plot is given in Figure 4.12, but for the Balmer series. In this case, many of the differences are consistent with zero to 1σ confidence, the largest of which is >3000K. This implies the Lyman line series is more sensitive to line blanketing effects than the Balmer series. This appears to suggest that $T_{\rm eff}$ values obtained using the Balmer series are more representative of the actual $T_{\rm eff}$ for the object in question. Furthermore, this also implies that higher order absorption series for H, such as the Paschen series, are less sensitive to the composition of the model atmosphere being used to determine $T_{\rm eff}$. If true, this could allow highly accurate $T_{\rm eff}$ determinations to be performed by using spectra from the upcoming James Webb Space Telescope (due to launch in 2018), which is able to observe the Paschen H series.

4.9.2 Grid Comparisons - Lemke/Tremblay

The Lemke and Tremblay Stark broadening tables were both calculated using the unified VCS theory but with different opacity sources included in the calculations. In Figure 4.13, the Lyman $T_{\rm eff}$ values using a pure H model grid, synthesised with the Lemke broadening tables, are plotted against the corresponding $T_{\rm eff}$ calculated with the same grid synthesised with the Tremblay tables. Translation from the measured Lemke $T_{\rm eff}$ to the new Tremblay $T_{\rm eff}$ may be done with an equation of the form:

$$T_{\rm Trem} = AT_{\rm Lem} + B, \tag{4.1}$$

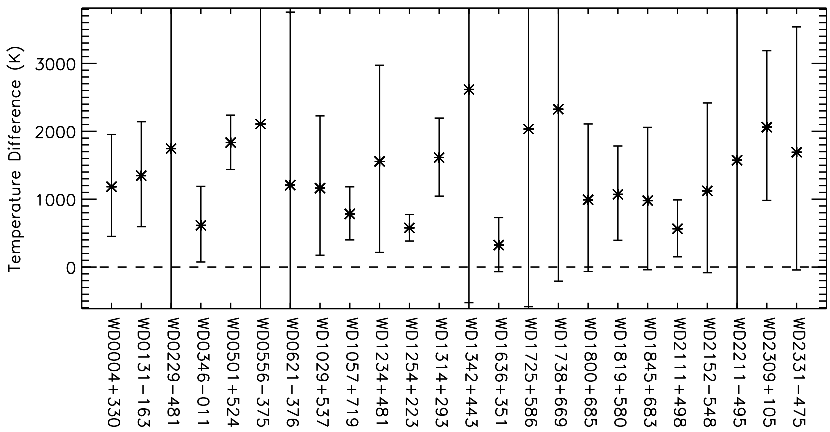

Figure 4.12: Differences between calculated Balmer Pure H $T_{\rm eff}$ and Balmer Prevold $T_{\rm eff}$, plotted against their respective stars.

Table 4.6: Straight line coefficients to translate Lemke $T_{\rm eff}$ to Tremblay $T_{\rm eff}$.

Model	Line Series	A	B
Pure H	Lyman	1.0601 ± 0.0034	-1789.68 ± 191.93
Pure H	Balmer	1.0325 ± 0.0139	238.69 ± 662.87
Prevold	Lyman	1.0568 ± 0.0033	-1641.02 ± 177.54
Prevold	Balmer	1.0418 ± 0.0134	-704.33 ± 621.83

where A and B are variable parameters determined by fitting the above equation to the measured Lemke and Tremblay $T_{\rm eff}$, and are tabulated in Table 4.6 for the Lyman and Balmer values. It is possible to do the same with the log g values. Plotted in Figure 4.14 are the measured log g values using a pure H model grid, with the Lemke values along the x axis, and the Tremblay values along the y axis. The measured Lemke log g can be translated to the new Tremblay value with a similar equation:

$$\log g_{\rm Trem} = C \log g_{\rm Lem} + D, \tag{4.2}$$

where C and D are again constants determined from fitting the equation to the measured Lemke and Tremblay log g values. The values of these constants are tabulated in Table 4.7 for the Lyman and Balmer log g measurements. Interestingly, repeating this exercise with the metal-polluted grid Prevold yields similar results (see Tables 4.6 and 4.7). This appears to imply that Stark broadening of the Lyman and Balmer H series is very insensitive to the composition of the atmosphere. It should be noted, however, that the Lemke and Tremblay tables are calculated using approximation techniques, and also under the assumption that the atmosphere is devoid of any metals. It would be constructive, therefore, to repeat the broadening calculations under the assumption of a metal-polluted atmosphere to assess the effects on the synthesised line profile.

Table 4.7: Straight line coefficients to translate Lemke log g to Tremblay log g.

Model	Line Series	C	D
Pure H	Lyman	1.0457 ± 0.0165	-0.2772 ± 0.1278
Pure H	Balmer	1.0495 ± 0.0421	-0.3048 ± 0.3246
Prevold	Lyman	1.0401 ± 0.0166	-0.2330 ± 0.1292
Prevold	Balmer	1.0442 ± 0.0424	-0.2639 ± 0.3271

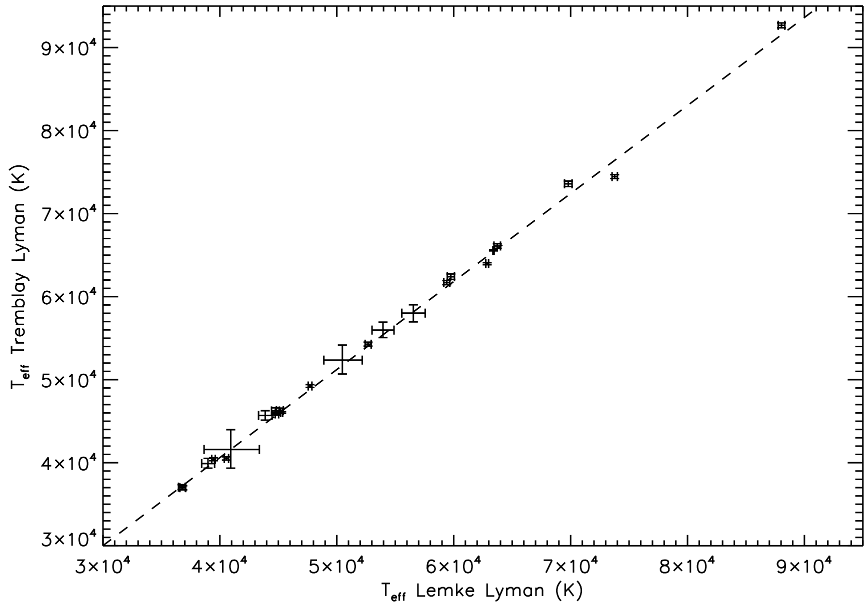

Figure 4.13: Plot of determined $T_{\rm eff}$ using the Lyman lines synthesised with the Lemke tables (x axis) and the Tremblay tables (y axis) with a pure H model atmosphere grid. The dashed line is the straight line best fit to the data (see text).

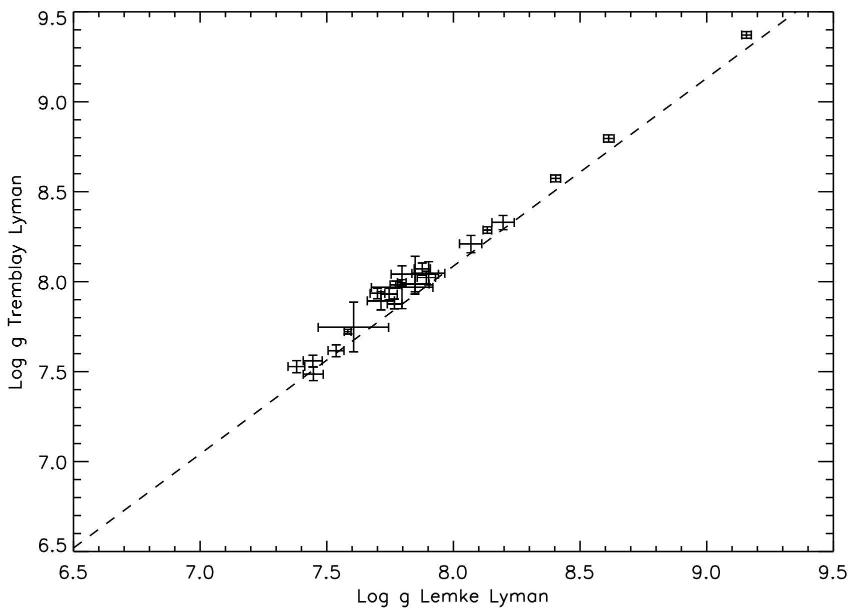

Figure 4.14: Same as Figure 4.13, but for log g.

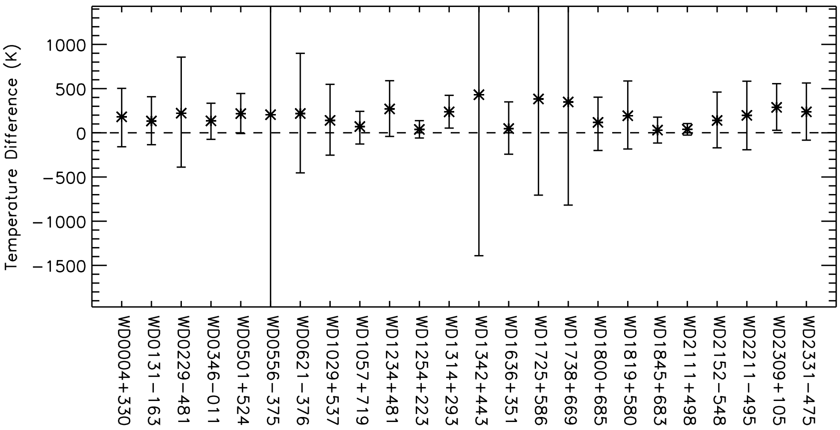

Figure 4.15: Plot of the temperature difference between values determined using the Prevold and Barsold grid for the Lyman series.

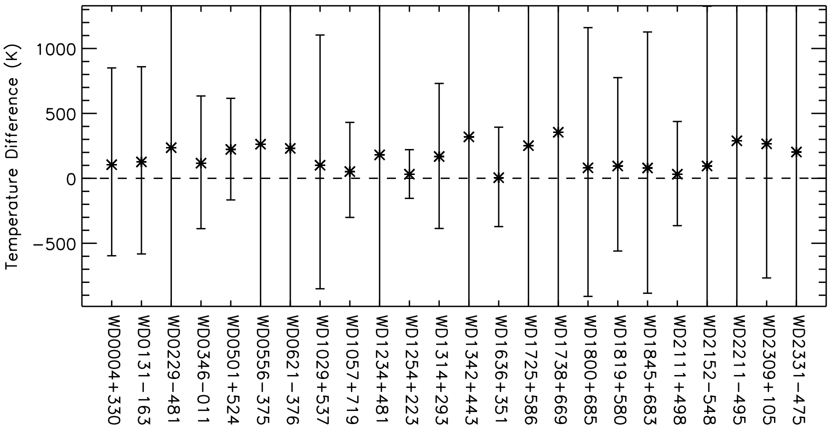

Figure 4.16: Same as Figure 4.15, but for the Balmer series.

4.9.3 Grid Comparisons - Prevold/Barsold

The effect of using either the Preval et al. (2013) or Barstow et al. (2003) abundances on the calculated $T_{\rm eff}$was assessed by plotting the difference between the two values for both the Lyman and Balmer line series using the Lemke broadening tables (see Figures 4.15 and 4.16). It can be seen that in both cases, the differences are very small, and are consistent with zero (bar WD1314+293 for the Lyman series). While both the Prevold and Barsold models include Fe and Ni at different abundances, the Prevold grid includes three additional metals, namely Al, P, and S. As the differences between the temperatures calculated using either the Prevold or Barsold grid are consistent with zero, this implies two things. Firstly, the additional opacity contributed by Al, P, and S is negligible in comparison to the combined opacity contributed by the other species in the model atmosphere, namely C, N, O, Si, Fe, and Ni. Secondly, as the abundances between the two model grids are not exactly the same, it is implied that the exact composition of the model atmosphere used to calculate $T_{\rm eff}$ is not particularly important, rather, the average contribution of all of the species in the atmosphere dictates the value of the measured $T_{\rm eff}$.

4.9.4 Origin of the Lyman/Balmer line problem

Many potential contributing factors to the Lyman/Balmer line problem have been discussed above. Model atmospheres have been calculated using differing numbers of transitions from two data releases, Ku92, and Ku11, where the former contains ∼9,000,000 Fe and Ni IV-VII lines, and the latter contains ∼160,000,000 Fe and Ni IV-VII lines. It has been shown that the use of a more extensive atomic dataset does not alter the measured $T_{\rm eff}$ and log g by a significant amount.

The use of two different Stark broadening tables results in different values for $T_{\rm eff}$ and log g, but did not significantly decrease the difference between values determined from the Lyman and Balmer line series. Furthermore, as these broadening tables were calculated under the assumption of a pure H atmosphere, it is not possible to rule out heavy metal contributions to Stark broadening.

The differences between measured $T_{\rm eff}$ and log g values using the Prevold and Barsold model grids were considered, and it was shown that both grids gave similar results. This was curious, as it could be expected that the Prevold grid has more opacity than the Barsold grid. This appears to suggest that the Prevold and Barsold grids have similar opacities, despite the fact that the former grid includes Al, P, and S.

Therefore, it is apparent that the largest contributing factor to the Lyman/Balmer line problem is the composition of the atmosphere, and the average contribution of all species in the model to the opacity. This is further reinforced by the observation that all stars above 60000K happen to contain metals in their atmosphere. Considering the case of WD0501+524, metal species heavier than Ni have been discovered, such as Ge (see Vennes et al. 2005), but have not been included in calculations in this thesis. Future exploration of the Lyman/Balmer line problem, therefore, could investigate the effects of including the heavier species into model atmosphere calculations. In addition, contributions to the broadening of Lyman and Balmer line absorption features from heavy metals could be quantified through new Stark broadening calculations.

While not a focal point of this work, the large scatter of log g values shown in the Results needs to be addressed. This is also related to Stark broadening, and can, therefore, be investigated in tandem with additional calculations of Stark broadening tables.

4.10 Conclusions

The Lyman/Balmer line problem has been discussed, and possible contributing factors considered. Model atmosphere grids were calculated using TLUSTY, and were synthesised with SYNSPEC. Two sets of atomic data for Fe and Ni were used, one from Ku92, and one from Ku11, the former supplemented by PI cross section data from the OP, and the latter supplemented by data calculated with AUTOSTRUCTURE. Three atmospheric compositions were specified, one pure H, and two metal-polluted atmospheres. The metal-polluted atmospheres were calculated using metal abundances based on two spectroscopic analyses of WD0501+524, one by Barstow et al. (2003), and one by Preval et al. (2013). Finally, the model atmospheres were synthesised using two Stark broadening tables from Lemke (1997) and Tremblay & Bergeron (2009). It was found that $T_{\rm eff}$ derived using either Ku92 or Ku11 models did not differ by a significant amount, regardless of the line series being analysed. Therefore, given that the computational time for Ku11 models is significantly larger than for Ku92 models, the benefit of using the extended dataset is not significant.

As observed by Barstow et al. (1999), there are significant differences between $T_{\rm eff}$ calculated using a pure H model, and $T_{\rm eff}$ calculated using a metal-polluted model. However, it was shown that this $T_{\rm eff}$ difference was much larger for the Lyman lines than the Balmer lines, where the former displayed differences of 5000-10000K, and the latter only 1000-2000K. Therefore, this suggests that, when only Balmer line data is available for a white dwarf, fitting the $T_{\rm eff}$ with a pure H grid will give a reasonable approximation of the correct value.

While the Lemke and Tremblay Stark broadening tables do produce changes in the measured $T_{\rm eff}$ and $\log g$, these changes are small, and do not improve the discrepancy between the Lyman or Balmer line $T_{\rm eff}$ and $\log g$. When plotting the pure H Lyman Lemke $T_{\rm eff}$ against the Lyman Tremblay $T_{\rm eff}$ for all the objects in the sample, it was found that the two quantities were related by a simple linear polynomial. Furthermore, repeating the exercise using the Prevold quantities, a strikingly similar relation also worked. Comparison of the coefficients used in these straight lines found them to be consistent with each other to 1σ confidence, implying that the Stark broadening of the profiles was very insensitive to the presence of metals in the atmosphere.

A more severe discrepancy is seen in this work, between the $\log g$ values measured for the Lyman and Balmer lines. This may be due to deficiencies in the Stark broadening calculations, and needs to be investigated further. The Lyman/Balmer line problem, then, no longer applies to $T_{\rm eff}$ only, but also includes the measurement of $\log g$. The issue can then be restated as follows:

"Is it possible to extract values of $T_{\rm eff}$ and $\log g$ that are in agreement with values measured from the Lyman and Balmer line series?"

The Lyman/Balmer line problem appears to arise from the overall opacity included in the model atmosphere calculation. The influence of metals on Stark broadening cannot be ruled out due to the calculation methods used to produce the Lemke/Tremblay tables. As Fe and Ni have already been included in the models, it may be the case that additional opacity sources need to be included in NLTE model atmosphere calculations (such as Ge in WD0501+524) in order to resolve the discrepancy between the measured Lyman and Balmer $T_{\rm eff}$ and $\log g$ values.

4.11 Summary

- Introducing metals into model atmospheres causes a drop in the measured $T_{\rm eff}$ by ∼3000-7000K, confirming the observations made by Barstow et al. (1998).
- $T_{\rm eff}$ values determined using pure H and metal-polluted grids show large differences for Lyman profiles, but small differences for Balmer profiles, several of which are consistent with zero.
- Using either the Ku92 or Ku11 atomic datasets in calculating the model atmospheres produces little to no changes in the measured $T_{\rm eff}$ and $\log g$.
- $T_{\rm eff}$ and $\log g$ values determined with the Lemke tables can be converted to their Tremblay counterparts using a simple linear relation.

- The Balmer line profiles are less sensitive to changes in atmospheric composition than the Lyman lines. The Balmer lines, therefore, can be used to obtain a close approximation of the real $T_{\rm eff}$ when Lyman and metal absorption data is unavailable.

- The determined $T_{\rm eff}$ is dependent upon the average contribution of all species in the model atmosphere, and appears to be insensitive to the exact value of each metal abundance.

- The Lyman/Balmer line problem may arise as a result of missing heavy metal opacity sources. In the case of WD0501+524, one source could be Ge.

Chapter 5

Extreme ultraviolet physics with white dwarfs

5.1 Introduction

The Extreme Ultraviolet (EUV, 80-800Å) is, perhaps, one of the least explored wavebands in observing white dwarf stars. To date, only a handful of observatories have been launched to either perform all-sky surveys, or spectroscopic observations. Historically, the EUV was regarded as a waveband that would not produce useful data for objects outside the solar system. It was concluded by Aller (1959) that the large cross section of H and He would result in significant attenuation of EUV flux, making the ISM essentially opaque to such radiation. This idea, however, was rejected by Cruddace et al. (1974), who calculated the effective cross section of the ISM due to a multitude of different metal species. In Figure 5.1 , the absorption cross section of several species is plotted against wavelength, showing that while H I, He I, and He II provided a large contribution, it might actually be possible to observe the EUV waveband.

Launched on the 7th June 1992, the EUVE performed an all sky survey of the extreme ultraviolet waveband, whilst also taking spectra of objects of interest. The EUVE spectrometer was equipped with three observing modes, namely LW, MW, and SW, covering wavelengths 280-760Å, 140-380Å, and 70-190Å respectively. The final compilation of observations comprised 1106 EUVE sources, 131 of which were white dwarf stars. The observatory was decommissioned on the 31st January 2001, and re-entered the Earth's atmosphere on the 30th January 2002.

Attempts to fit the EUVE spectrum of WD0501+524 have historically been difficult, particularly at short wavelength regions where line blanketing effects are strongest. Attempts to predict soft X-ray data of a sample of white dwarfs from the *Einstein* observatory (Kahn et al., 1984) showed that the predicted flux in this region was far in excess of that observed. Therefore, reconciling measured parameters in the EUV with those measured in the UV and optical wavebands could not be successful. This feat was eventually achieved by Lanz et al. (1996), who were able to calculate a self consistent solution that satisfied the EUV, UV, and optical wavebands. This study improved on earlier work by using the most accurate line blanketing calculations to date using an atomic dataset containing more than 9,000,000 Fe and Ni transitions. Fitting the EUV came with a caveat, however, as significant quantities of interstellar He needed to be included, far more than was observed in the ISM. A more exotic solution was proposed by Barstow et al. (1998), who were able to reproduce the EUV spectrum of WD0501+524 by stratifying Fe in the photosphere, with increasing abundance deeper in the atmosphere. This, however, was the only metal that was stratified, raising the question as to why other metals in the atmosphere were not arranged in a similar configuration.

In this final Chapter, a study is presented on fitting EUVE spectroscopic data of metal-polluted DA white dwarfs, and how the quality of such fits are affected by the model atmosphere composition, and the

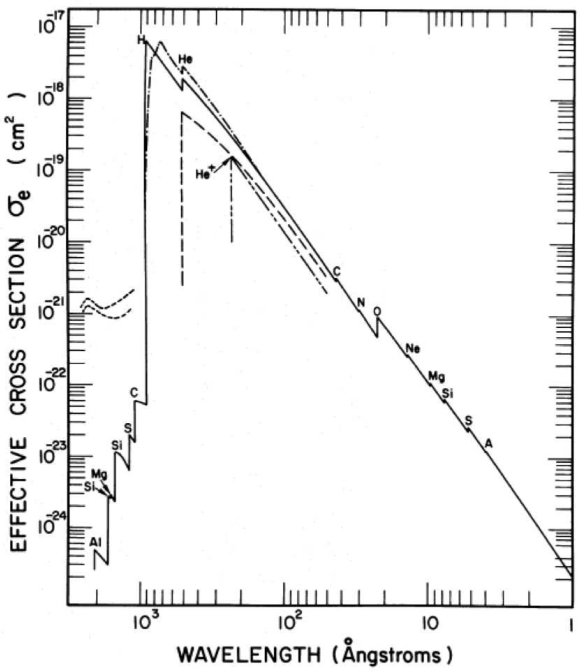

Figure 5.1: Plot of effective cross section of the ISM versus the wavelength of light being absorbed by the cloud. Credit: Cruddace et al. (1974).

Table 5.1: EUVE data sets from the EUVE spectral atlas Craig et al. (1997)

WD Name	Alt Name	EUVE name (2EUVE J)	Exp time (kS)	Obs Date & time
WD0232+035	Feige 24	0235+03.7	28	31/10/1995 18:19:05
WD0455-282	MCT 0455-2812	0457-28.1	52	14/11/1993 21:32:06
WD0501+527	G191-B2B	0505+52.8	43	05/03/1994 21:42:03
WD0621-376	REJ0623-374	0623-37.6	34	23/11/1993 15:51:03
WD2211-495	REJ2214-492	2214-49.3	121	12/08/1994 16:54:05
WD2331-475	MCT 2331-431	2334-47.2	54	08/08/1993 10:29:03
WD2350-706	HD223816B	2353-70.3	59	05/08/1993 23:59:03

heavy metal atomic data used to account for line blanketing effects. Seven white dwarfs identified as being metal rich by Craig et al. (1997) were analysed using newly calculated model grids containing 160 million Fe and Ni IV-VII transitions, and an assessment of the quality of these fits was made.

5.2 Observations

A spectral atlas has been compiled by Craig et al. (1997), and contains fully reduced and calibrated EUVE spectra for several white dwarf stars with various compositions. In this sample, seven hot DA white dwarfs were identified as being metal rich, namely WD0232+035, WD0455-282, WD0501+524, WD0621-376, WD2211-492, WD2331-475, and WD2350-706. Listed in Table 5.1 are details of the observations.

Spectra from the Craig et al. (1997) sample do not come with flux errors. The error on the flux was estimated by converting the flux from counts cm^{-2} s^{-1} Å^{-1} to counts, and taking the square root of this number. The fractional error was then multiplied by counts cm^{-2} s^{-1} Å^{-1} to obtain the estimated error. This approach is valid for bright sources, where the background flux is negligible compared to the source flux.

Table 5.2: Abundances used in calculating the models.

Ion	Preval et al. (2013)	Barstow et al. (2003)
C	1.72×10^{-7}	1.99×10^{-7}
N	2.16×10^{-7}	1.60×10^{-7}
O	4.12×10^{-7}	3.51×10^{-7}
Al	1.60×10^{-7}	N/A
Si	3.68×10^{-7}	8.65×10^{-7}
P	1.64×10^{-8}	N/A
S	1.71×10^{-7}	N/A
Fe	1.83×10^{-6}	3.30×10^{-6}
Ni	1.01×10^{-6}	2.40×10^{-7}

5.3 Model atmospheres

All model atmospheres used in this work were calculated using TLUSTY (Hubeny, 1988) version 201, and were synthesised using SYNSPEC version 49 (Hubeny & Lanz, 2011). The linelist supplied to SYNSPEC came from the Ku11 dataset. The models were calculated for T_{eff} =35000K to 100000K in steps of 2500K, and log g=6.5 to 9.5 in steps of 0.25 dex.

Two different atmospheric compositions were specified, both of which were based on the measured abundances of WD0501+524 by Preval et al. (2013) and Barstow et al. (2003). WD0501+524 was chosen as the abundance reference, because of the extensive studies and high quality spectra available for it. The abundances used are tabulated in Table 5.2. In addition, grids were calculated with multiples of 0.001, 0.01, 0.1, 1.0, and 10.0 times these abundances.

For both the Preval et al. (2013) and Barstow et al. (2003) abundances, model grids were calculated using the Ku92 and Ku11 atomic data sets. The Ku92 dataset was supplemented by photoionisation (PI) cross sections from the Opacity Project (OP) for the Fe ions, and approximate hydrogenic PI cross sections for Ni. Model grids calculated with the Preval et al. (2013) abundances, and the Ku92 or Ku11 datasets will be referred to as Prevold and Prevnew respectively, while models calculated with the Barstow et al. (2003) abundances will be referred to as Barsold and Barsnew respectively.

5.4 Method

The observational data were analysed using the X-Ray analysis program XSPEC (Arnaud, 1996). The model atmosphere grids were convolved with an instrumental Gaussian with resolution of 300 for all spectra. Only the LW and MW spectra were utilised in this work, as the fluxes in the SW spectra are severely attenuated by line blanketing effects. The photospheric models were multiplied by three preloaded model components in XSPEC named ZBABS, HEILIN, and LYMAN to account for the opacity of the ISM.

ZBABS models the ISM attentuation of the photospheric spectrum dependent upon the the column densities of H I, He I, and He II (n_{H}, n_{HeI}, and n_{HeII} respectively). HEILIN models the voigt absorption profiles of He I given n_{HeI}, and the doppler width of the He I absorbers (b_{HeI}). Finally, LYMAN models the voigt absorption profiles of He II given n_{HeII}, and the doppler width of the He II absorbers (b_{HeI}). In fitting the spectra, the column densities, doppler widths, T_{eff} and log g were fixed to be the same values for both the

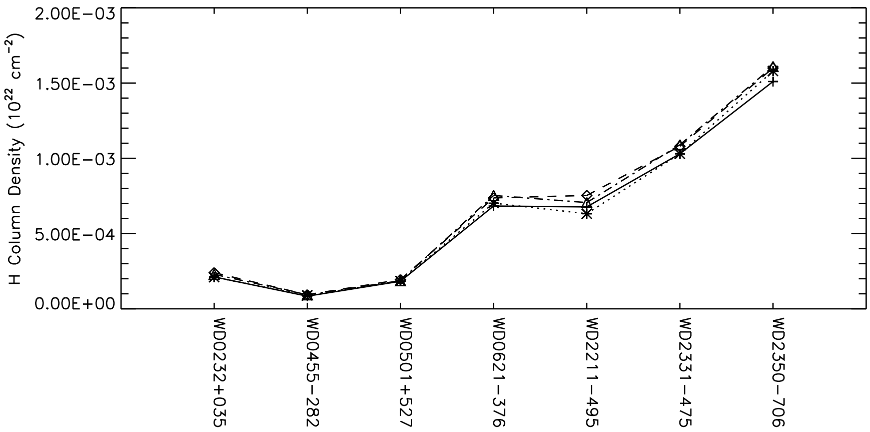

*Figure 5.2: Plot of the measured H column density values using either the Barsold grid (solid line, + pointers), the Barsnew grid (dotted line, * markers), the Prevold grid (dashed line, diamond markers), and the Prevnew grid (dot-dash line, triangle markers).*

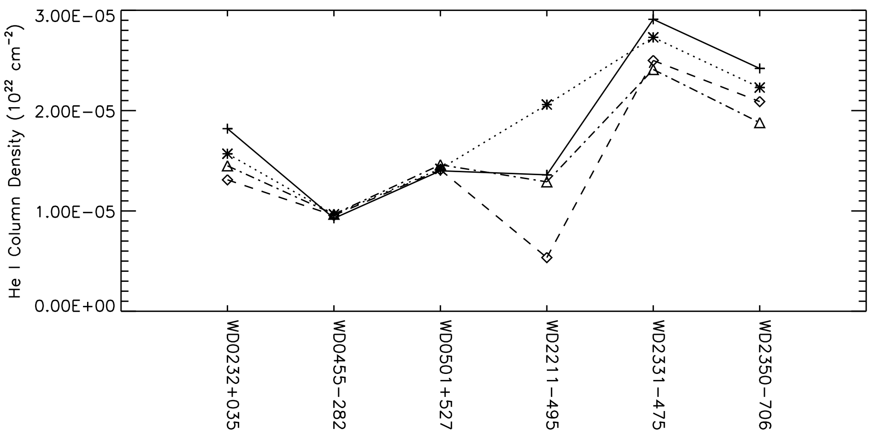

Figure 5.3: Same as Figure 5.2, but for the He I *column density values.*

LW and MW spectra. Each spectra, however, was allowed to have a unique redshift and normalisation to account for poor wavelength and flux calibration respectively. All parameters were initially allowed to vary freely to provide a first estimate of the best fit. The parameter space for the redshift was then scanned to give the lowest chi square value. The redshifts were then frozen, as they are only important for alignment of the models with the observed spectra.

5.5 Results

The measured parameters for each star are given in Table 5.3. Plotted in Figures 5.2, 5.3, 5.4, 5.5, 5.6, 5.7, 5.8, and 5.9 are the measured values for $n_{\rm H}$, $n_{\rm HeI}$, $n_{\rm HeII}$, $b_{\rm HeI}$, $b_{\rm HeII}$, Z, $T_{\rm eff}$ and log g using each model grid respectively. The He I edge was not detected in WD0621-376, WD2211-495, WD2331-475, and WD2350-706. For these cases, the He I absorption profiles were neglected. However, the flux attenuation due to He I was still included, as it affects other sections of the spectrum. An exception to this is the case of WD0621-376. Attempts to fit a value for the He I column density resulted in the parameter taking values of $\sim 10^{-22}$. Therefore, the He I column density was set to zero, and frozen during fitting.

*Table 5.3: List of measured parameters from fitting the EUVE spectra of seven white dwarfs using the Barsold, Barsnew, Prevold, and Prevnew model grids. The column densities are in units of 10^{22} cm^{-2}, and the Doppler widths are in units of km s^{-1}. Quantities marked with a * mean the hard limit of the grid was reached.*

Star name	Grid	$\chi^2_{\rm red}$	$n_{\rm H}$ (10^{22} cm^{-2})	$n_{\rm HeI}$ (10^{22} cm^{-2})	$n_{\rm HeII}$ (10^{22} cm^{-2})
WD0232+035	Barsold	4.032	$2.117^{+0.161}_{-0.177} \times 10^{-4}$	$1.819^{+0.336}_{-0.299} \times 10^{-5}$	$7.014^{+0.254}_{-0.247} \times 10^{-5}$
WD0232+035	Barsnew	4.091	$2.098^{+0.136}_{-0.149} \times 10^{-4}$	$1.570^{+0.281}_{-0.252} \times 10^{-5}$	$7.232^{+0.244}_{-0.243} \times 10^{-5}$
WD0232+035	Prevold	4.686	$2.396^{+0.119}_{-0.129} \times 10^{-4}$	$1.313^{+0.240}_{-0.217} \times 10^{-5}$	$6.436^{+0.254}_{-0.259} \times 10^{-5}$
WD0232+035	Prevnew	4.727	$2.293^{+0.128}_{-0.140} \times 10^{-4}$	$1.448^{+0.266}_{-0.240} \times 10^{-5}$	$6.252^{+0.259}_{-0.259} \times 10^{-5}$
WD0455-282	Barsold	3.791	$8.378^{+0.014}_{-0.014} \times 10^{-5}$	$9.261^{+0.255}_{-0.253} \times 10^{-6}$	$5.394^{+0.169}_{-0.172} \times 10^{-5}$
WD0455-282	Barsnew	5.145	$8.865^{+0.009}_{-0.009} \times 10^{-5}$	$9.656^{+0.204}_{-0.201} \times 10^{-6}$	$4.330^{+0.107}_{-0.108} \times 10^{-5}$
WD0455-282	Prevold	4.112	$9.330^{+0.015}_{-0.014} \times 10^{-5}$	$9.546^{+0.249}_{-0.248} \times 10^{-6}$	$4.688^{+0.172}_{-0.181} \times 10^{-5}$
WD0455-282	Prevnew	4.340	$9.300^{+0.009}_{-0.010} \times 10^{-5}$	$9.670^{+0.209}_{-0.216} \times 10^{-6}$	$4.130^{+0.137}_{-0.110} \times 10^{-5}$
WD0501+527	Barsold	13.532	$1.830^{+0.010}_{-0.010} \times 10^{-4}$	$1.397^{+0.019}_{-0.020} \times 10^{-5}$	$6.339^{+0.103}_{-0.080} \times 10^{-5}$
WD0501+527	Barsnew	14.794	$1.853^{+0.009}_{-0.010} \times 10^{-4}$	$1.420^{+0.018}_{-0.019} \times 10^{-5}$	$6.317^{+0.079}_{-0.080} \times 10^{-5}$
WD0501+527	Prevold	17.499	$1.943^{+0.010}_{-0.010} \times 10^{-4}$	$1.405^{+0.019}_{-0.020} \times 10^{-5}$	$5.086^{+0.104}_{-0.082} \times 10^{-5}$
WD0501+527	Prevnew	18.428	$1.874^{+0.009}_{-0.010} \times 10^{-4}$	$1.461^{+0.018}_{-0.018} \times 10^{-5}$	$5.679^{+0.076}_{-0.076} \times 10^{-5}$
WD0621-376	Barsold	4.004	$6.827^{+0.099}_{-0.119} \times 10^{-4}$		$4.623^{+0.301}_{-0.280} \times 10^{-5}$
WD0621-376	Barsnew	3.697	$7.016^{+0.098}_{-0.091} \times 10^{-4}$		$4.493^{+0.299}_{-0.278} \times 10^{-5}$
WD0621-376	Prevold	4.905	$7.369^{+0.130}_{-0.255} \times 10^{-4}$		$3.629^{+0.302}_{-0.297} \times 10^{-5}$
WD0621-376	Prevnew	4.350	$7.528^{+0.106}_{-0.129} \times 10^{-4}$		$2.850^{+0.295}_{-0.271} \times 10^{-5}$
WD2211-495	Barsold	18.158	$6.774^{+0.026}_{-0.184} \times 10^{-4}$	$1.356^{+0.080}_{-0.036} \times 10^{-5}$	$6.234^{+0.098}_{-0.104} \times 10^{-5}$
WD2211-495	Barsnew	17.773	$6.323^{+0.220}_{-0.219} \times 10^{-4}$	$2.056^{+0.358}_{-0.359} \times 10^{-5}$	$6.883^{+0.128}_{-0.126} \times 10^{-5}$
WD2211-495	Prevold	19.053	$7.530^{+0.173}_{-0.196} \times 10^{-4}$	$5.353^{+3.068}_{-2.662} \times 10^{-6}$	$5.141^{+0.141}_{-0.130} \times 10^{-5}$
WD2211-495	Prevnew	17.964	$7.058^{+0.124}_{-0.194} \times 10^{-4}$	$1.291^{+0.342}_{-0.342} \times 10^{-5}$	$4.864^{+0.101}_{-0.129} \times 10^{-5}$
WD2331-475	Barsold	2.081	$1.033^{+0.101}_{-0.102} \times 10^{-3}$	$2.913^{+1.266}_{-1.166} \times 10^{-5}$	$8.262^{+0.571}_{-0.572} \times 10^{-5}$
WD2331-475	Barsnew	2.080	$1.032^{+0.084}_{-0.081} \times 10^{-3}$	$2.733^{+1.115}_{-0.951} \times 10^{-5}$	$8.252^{+0.478}_{-0.505} \times 10^{-5}$
WD2331-475	Prevold	1.938	$1.083^{+0.103}_{-0.111} \times 10^{-3}$	$2.501^{+1.442}_{-1.196} \times 10^{-5}$	$6.659^{+0.638}_{-0.609} \times 10^{-5}$
WD2331-475	Prevnew	1.961	$1.087^{+0.095}_{-0.083} \times 10^{-3}$	$2.410^{+1.379}_{-0.963} \times 10^{-5}$	$6.655^{+0.566}_{-0.553} \times 10^{-5}$
WD2350-706	Barsold	2.354	$1.509^{+0.113}_{-0.111} \times 10^{-3}$	$2.422^{+1.203}_{-1.170} \times 10^{-5}$	$5.611^{+0.491}_{-0.502} \times 10^{-5}$
WD2350-706	Barsnew	2.288	$1.580^{+0.111}_{-0.110} \times 10^{-3}$	$2.226^{+1.114}_{-0.959} \times 10^{-5}$	$5.890^{+0.525}_{-0.513} \times 10^{-5}$
WD2350-706	Prevold	2.222	$1.604^{+0.124}_{-0.131} \times 10^{-3}$	$2.090^{+1.502}_{-1.235} \times 10^{-5}$	$4.617^{+0.606}_{-0.524} \times 10^{-5}$
WD2350-706	Prevnew	2.228	$1.612^{+0.145}_{-0.113} \times 10^{-3}$	$1.877^{+1.332}_{-1.069} \times 10^{-5}$	$4.865^{+0.472}_{-0.528} \times 10^{-5}$

Table 5.3: Continued

Star name	Grid	$\chi^2_{\rm red}$	$b_{\rm HeI}$	$b_{\rm HeII}$	Z	$T_{\rm eff}$ (K)	log g
WD0232+035	Barsold	4.032	$0.33^{+0.02}_{-0.01}$	$54.20^{+1.91}_{-1.98}$	$8.8322^{+0.1521}_{-0.1736}$	68065^{+623}_{-617}	$7.929^{+0.097}_{-0.115}$
WD0232+035	Barsnew	4.091	$0.34^{+0.02}_{-0.01}$	$53.83^{+2.06}_{-2.15}$	$9.5252^{+0.1564}_{-0.1657}$	71707^{+884}_{-868}	$8.344^{+0.093}_{-0.094}$
WD0232+035	Prevold	4.686	$0.36^{+0.04}_{-0.02}$	$57.86^{+1.71}_{-1.68}$	$9.8157^{+0.1280}_{-0.1368}$	68464^{+612}_{-582}	$8.302^{+0.103}_{-0.102}$
WD0232+035	Prevnew	4.727	$0.35^{+0.03}_{-0.02}$	$57.18^{+1.76}_{-1.76}$	$10.0000^{+0.0000*}_{-0.0562}$	69014^{+620}_{-549}	$8.399^{+0.081}_{-0.081}$
WD0455-282	Barsold	3.791	$29.59^{+3.44}_{-2.51}$	$4.80^{+0.48}_{-0.34}$	$0.9510^{+0.0067}_{-0.0069}$	62981^{+432}_{-400}	$6.933^{+0.190}_{-0.119}$
WD0455-282	Barsnew	5.145	$30.16^{+3.52}_{-2.45}$	$4.53^{+0.34}_{-0.29}$	$1.0001^{+0.0191}_{-0.0008}$	60448^{+146}_{-138}	$6.500^{+0.007}_{-0.000*}$
WD0455-282	Prevold	4.112	$30.26^{+3.71}_{-2.58}$	$27.28^{+1.30}_{-1.41}$	$0.9530^{+0.0066}_{-0.0064}$	57347^{+546}_{-743}	$7.236^{+0.089}_{-0.108}$
WD0455-282	Prevnew	4.340	$30.47^{+3.70}_{-2.50}$	$27.22^{+1.41}_{-1.71}$	$1.0000^{+0.0264}_{-0.0012}$	58055^{+410}_{-278}	$6.977^{+0.034}_{-0.057}$
WD0501+527	Barsold	13.532	$1.18^{+0.33}_{-0.17}$	$42.17^{+0.98}_{-0.94}$	$1.0001^{+0.0209}_{-0.0011}$	55833^{+193}_{-213}	$6.957^{+0.035}_{-0.040}$
WD0501+527	Barsnew	14.794	$0.95^{+0.27}_{-0.13}$	$42.36^{+1.01}_{-0.99}$	$1.0000^{+0.0154}_{-0.0004}$	54707^{+217}_{-203}	$6.806^{+0.025}_{-0.028}$
WD0501+527	Prevold	17.499	$5.66^{+1.01}_{-1.40}$	$41.15^{+0.94}_{-0.99}$	$1.0003^{+0.0116}_{-0.0021}$	51499^{+172}_{-201}	$6.748^{+0.021}_{-0.027}$
WD0501+527	Prevnew	18.428	$0.69^{+0.12}_{-0.06}$	$18.14^{+0.62}_{-0.59}$	$1.0000^{+0.0071}_{-0.0004}$	54111^{+201}_{-199}	$7.186^{+0.023}_{-0.023}$
WD0621-376	Barsold	4.004		$22.80^{+4.04}_{-3.05}$	$9.2300^{+0.3685}_{-0.2167}$	59220^{+1332}_{-541}	$6.500^{+0.218}_{-0.000*}$
WD0621-376	Barsnew	3.697		$23.86^{+3.76}_{-8.29}$	$9.1444^{+0.2462}_{-0.1986}$	60633^{+865}_{-612}	$6.500^{+0.127}_{-0.000*}$
WD0621-376	Prevold	4.905		$28.49^{+5.79}_{-4.80}$	$9.5461^{+0.4539}_{-0.2895}$	56636^{+2056}_{-930}	$6.658^{+0.384}_{-0.158}$
WD0621-376	Prevnew	4.350		$31.13^{+1.85}_{-1.69}$	$9.4842^{+0.2607}_{-0.1717}$	58036^{+881}_{-607}	$6.500^{+0.169}_{-0.000}$
WD2211-495	Barsold	18.158		$9.34^{+0.72}_{-0.40}$	$9.5502^{+0.0246}_{-0.0266}$	64998^{+56}_{-230}	$7.159^{+0.037}_{-0.045}$
WD2211-495	Barsnew	17.773		$22.91^{+1.03}_{-1.02}$	$10.0000^{+0.0000*}_{-0.0052}$	68562^{+297}_{-270}	$7.396^{+0.048}_{-0.047}$
WD2211-495	Prevold	19.053		$29.23^{+0.66}_{-0.61}$	$9.8900^{+0.0267}_{-0.0293}$	63337^{+275}_{-275}	$7.219^{+0.062}_{-0.053}$
WD2211-495	Prevnew	17.964		$15.78^{+0.99}_{-0.80}$	$10.0000^{+0.0000*}_{-0.0018}$	64821^{+203}_{-360}	$7.235^{+0.030}_{-0.049}$
WD2331-475	Barsold	2.081		$10.92^{+2.99}_{-1.89}$	$0.9236^{+0.0290}_{-0.0298}$	57422^{+3155}_{-3698}	$7.353^{+0.395}_{-0.537}$
WD2331-475	Barsnew	2.080		$15.49^{+3.14}_{-1.85}$	$1.0008^{+0.8828}_{-0.0189}$	58073^{+2331}_{-2689}	$7.504^{+0.202}_{-0.372}$
WD2331-475	Prevold	1.938		$16.20^{+4.24}_{-2.00}$	$0.9384^{+0.0235}_{-0.0261}$	54029^{+2229}_{-2531}	$6.691^{+0.404}_{-0.191}$
WD2331-475	Prevnew	1.961		$16.00^{+3.72}_{-1.90}$	$1.0009^{+1.0642}_{-0.0160}$	54889^{+1469}_{-2624}	$6.886^{+0.261}_{-0.327}$
WD2350-706	Barsold	2.354		$11.38^{+5.20}_{-2.37}$	$5.9837^{+0.8277}_{-0.9624}$	72928^{+2329}_{-5113}	$7.750^{+0.301}_{-0.232}$
WD2350-706	Barsnew	2.288		$20.01^{+4.25}_{-5.54}$	$1.0019^{+1.4095}_{-0.0205}$	60440^{+1380}_{-1880}	$6.646^{+0.529}_{-0.146}$
WD2350-706	Prevold	2.222		$14.37^{+6.62}_{-3.64}$	$0.9242^{+0.0173}_{-0.0200}$	54618^{+2160}_{-3095}	$6.548^{+0.349}_{-0.048}$
WD2350-706	Prevnew	2.228		$37.25^{+6.61}_{-6.00}$	$1.0002^{+2.1287}_{-0.0151}$	57067^{+1284}_{-2398}	$6.750^{+0.297}_{-0.250}$

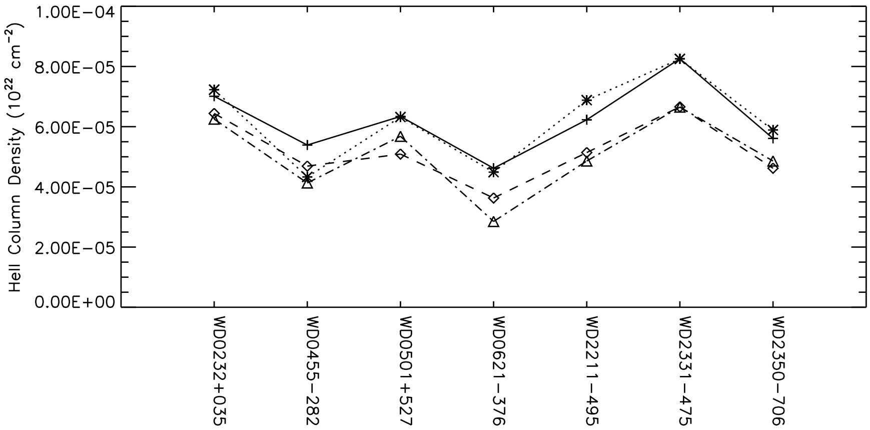

Figure 5.4: Same as Figure 5.2, but for the He II *column density values.*

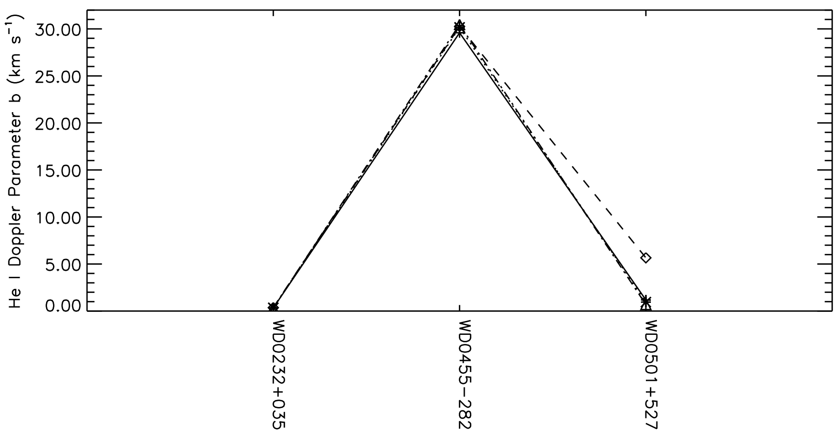

Figure 5.5: Same as Figure 5.2, but for the He I *Doppler parameter (b) values.*

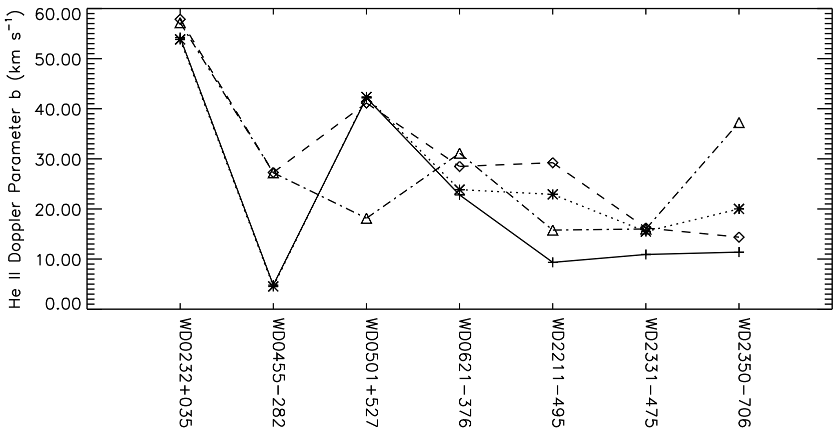

Figure 5.6: Same as Figure 5.2, but for the He II *doppler parameter (b) values.*

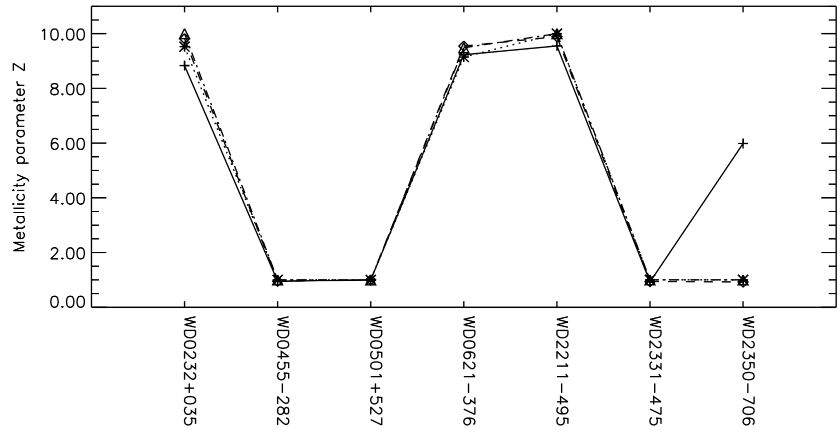

Figure 5.7: Same as Figure 5.2, but for the Z values.

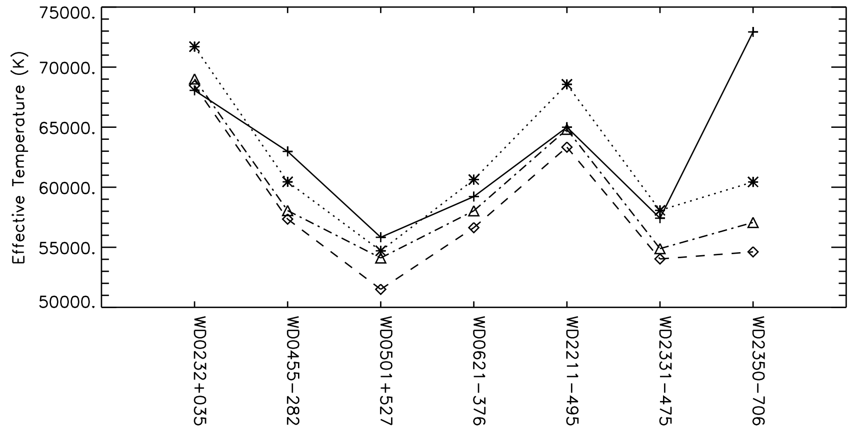

Figure 5.8: Same as Figure 5.2, but for the $T_{\rm eff}$ values.

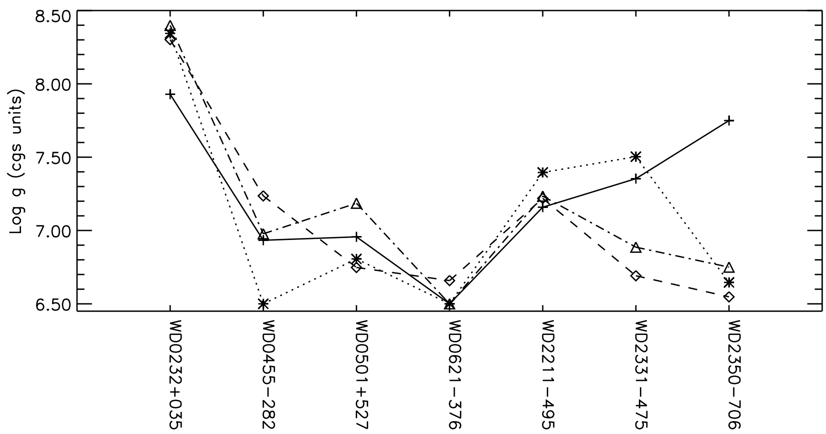

Figure 5.9: Same as Figure 5.2, but for the log g values.

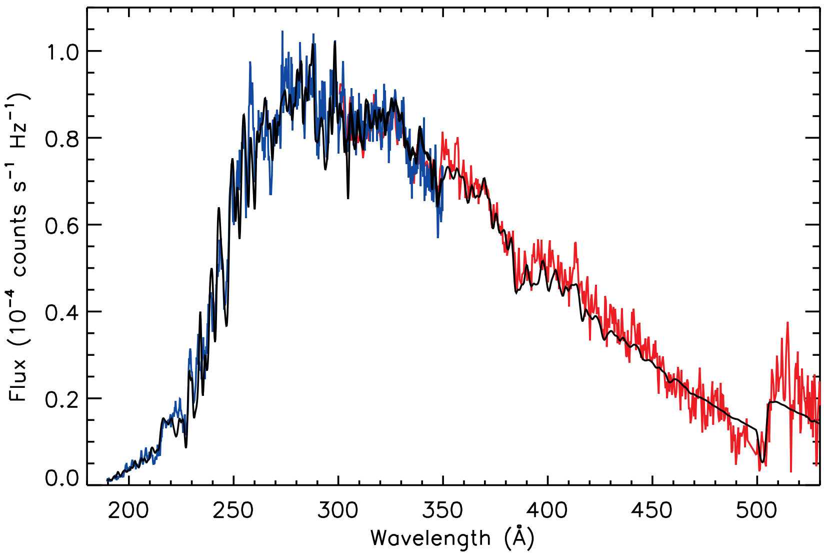

Figure 5.10: Plot of the EUVE spectrum of WD0232+035. The red curve is for the LW spectrum, the blue curve is for the MW spectrum, and the black curve is the best fitting model using the Barsold grid.

5.5.1 WD0232+035

A metal rich white dwarf in a binary system with an M dwarf. The He I edge is fairly well reproduced. The continuum, and several short wavelength metal absorption features are very well reproduced. The best fitting model was Barsold (see Figure 5.10).

5.5.2 WD0455-282

The continuum is well reproduced, and the short wavelength absorption features are well matched to the observed data. The best fitting model was Barsold (see Figure 5.11).

5.5.3 WD0501+524

A very well studied white dwarf with large amounts of Fe and Ni. The continuum is well reproduced, however, many absorption features are not very well reproduced at short wavelengths. The best fitting model grid was Barsold (see Figure 5.12).

5.5.4 WD0621-376

The He I column density is extremely uncertain. When fitting, the He I column density defaulted to very small values, and the quality of the fit was insensitive to variations in the parameter. For this reason, the He I column density was set to 0, and frozen. The continuum is matched reasonably well, as are the metal absorption features. The best fitting model grid was Barsnew (see Figure 5.13).

5.5.5 WD2211-495

Like WD0501+524, the fit had a very large $\chi^2_{\rm red}$, however, it can also be seen that the continuum is reproduced well, as are the absorption features at shorter wavelengths, more so than WD0501+524. The

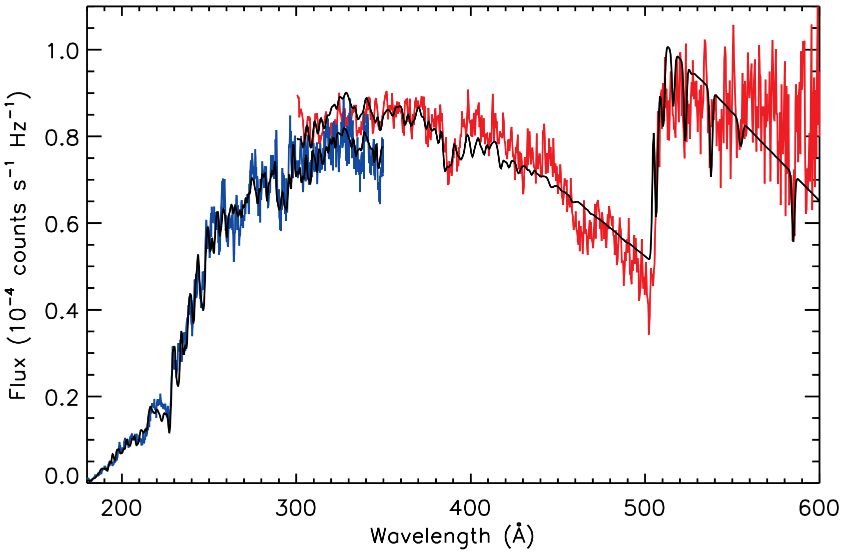

Figure 5.11: Plot of the EUVE spectrum of WD0455-282. The red curve is for the LW spectrum, the blue curve is for the MW spectrum, and the black curve is the best fitting model using the Barsold grid.

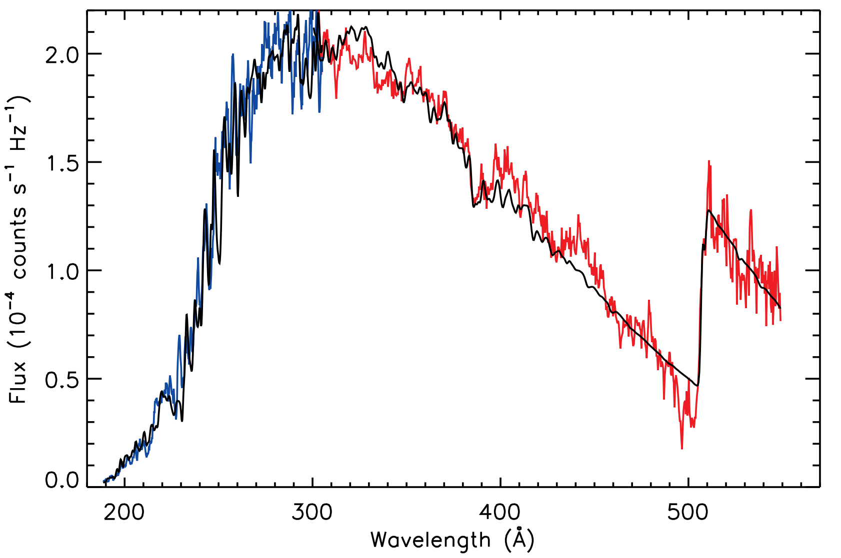

Figure 5.12: Plot of the EUVE spectrum of WD0501+524. The red curve is for the LW spectrum, the blue curve is for the MW spectrum, and the black curve is the best fitting model using the Barsold grid.

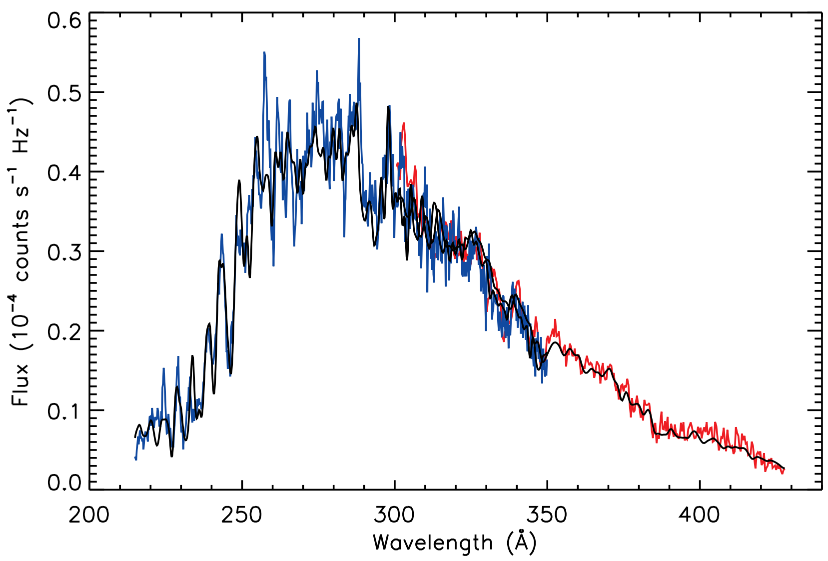

Figure 5.13: Plot of the EUVE spectrum of WD0621-376. The red curve is for the LW spectrum, the blue curve is for the MW spectrum, and the black curve is the best fitting model using the Barsnew grid.

largest contribution to the $\chi^2_{\rm red}$ is an erroneous emission spike near 260Å. The best fitting model grid is Barsnew (see Figure 5.14).

5.5.6 WD2331-475

The best fits were obtained for this star, with $\chi^2_{\rm red}$ ranging between 1.94 and 2.08. The LW spectrum was excluded from the fit, as the S/N was extremely poor. The poor S/N was most likely caused by a large H column density. Excellent agreement is seen both in terms of the continuum, and the absorption features. The best fitting model grid was Prevold (see Figure 5.15).

5.5.7 WD2350-706

Like WD2331-475, the continuum is very well reproduced, and the heavy metal absorption features are well modelled. The LW spectrum was omitted from the analysis due to poor S/N. As a consequence, HEILIN was removed from the XSPEC fit. $\chi^2_{\rm red}$ is restricted between 2.22 and 2.35. The best fitting model grid was Prevold (see Figure 5.16).

5.6 Discussion

5.6.1 The role of P and S in white dwarfs

The main difference between the Preval et al. (2013) and Barstow et al. (2003) models is the presence of P and S in the photosphere. These two metals have been observed extensively in white dwarf spectra, for example, in WD0501+524 by Vennes et al. (1996), who observed resonant transitions of these metals in an ORFEUS spectrum. In addition, later observations of GD71, REJ1918+595 and REJ0605-482 showed the presence of P in FUSE spectra of these white dwarfs. While intriguing, it is important to note that

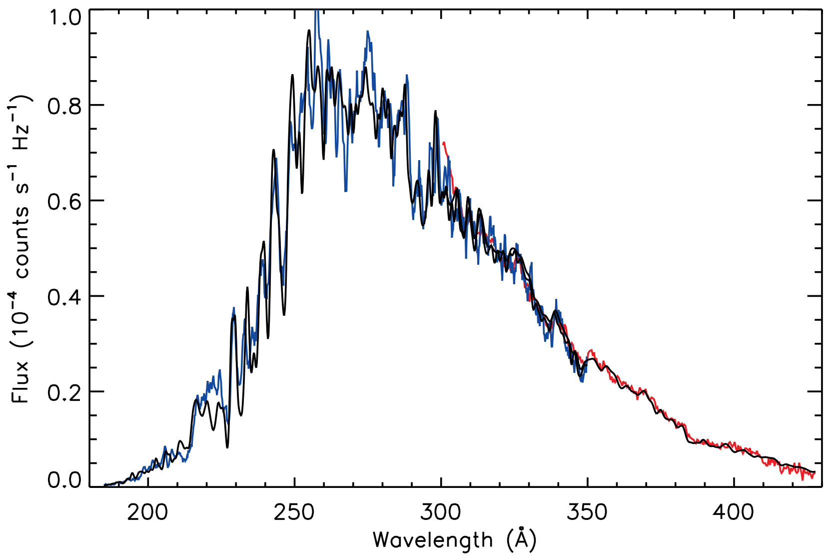

Figure 5.14: Plot of the EUVE spectrum of WD2211-495. The red curve is for the LW spectrum, the blue curve is for the MW spectrum, and the black curve is the best fitting model using the Barsnew grid.

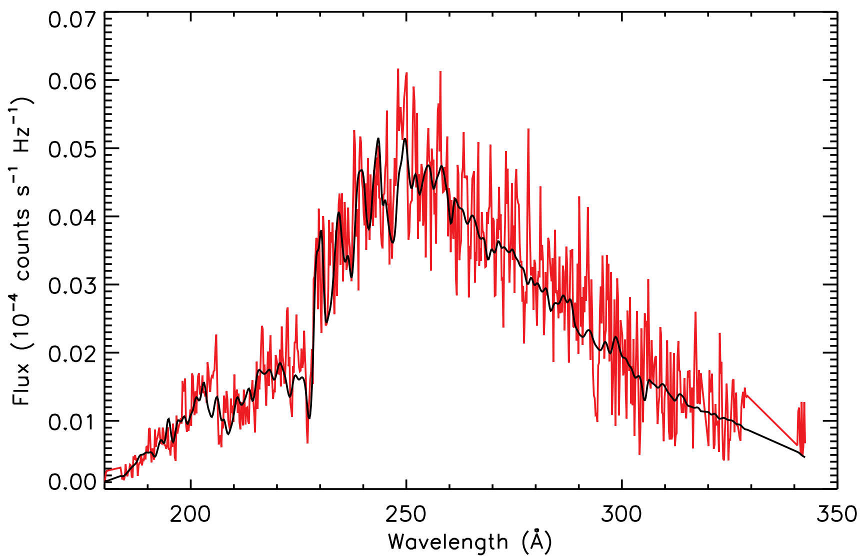

Figure 5.15: Plot of the EUVE spectrum of WD2331-475. The red curve is for the MW spectrum, and the black curve is the best fitting model using the Prevold grid.

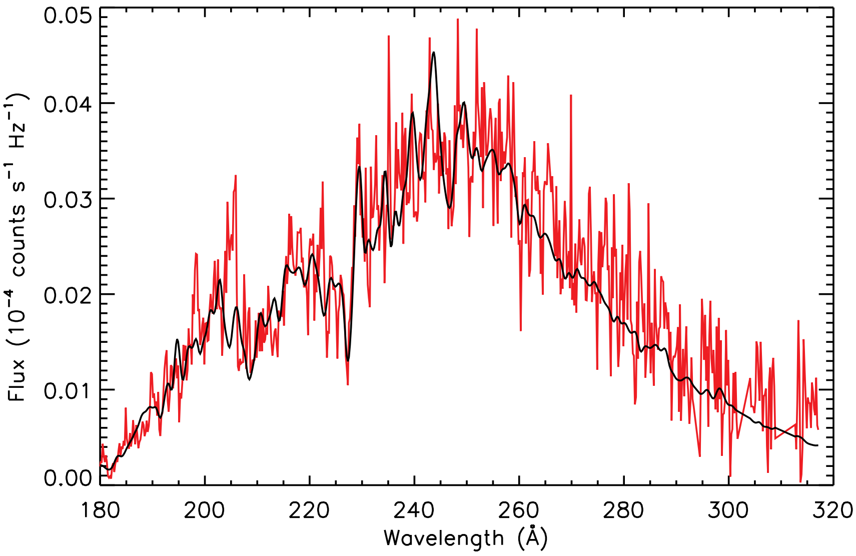

Figure 5.16: Plot of the EUVE spectrum of WD2350-706. The red curve is for the MW spectrum, and the black curve is the best fitting model using the Prevold grid.

the velocity resolution of both ORFEUS and FUSE data is insufficient to determine the origin of P and S. Furthermore, all observations of P and S features in DA white dwarfs has been for resonant transitions only (P v 1118 and 1128Å, S iv 1062 and 1072Å, and S vi 933 and 944Å). A concrete association of these metals with the photosphere of the star requires the observation of excited transitions.

In Figures 5.17 and 5.18, the EUVE spectrum of WD0501+524, and the best fitting model using the Barsold and Prevold model grids is plotted respectively over the wavelength range 320-370Å. It can be seen that, in the Prevold model, there is additional absorption near 346 and 349Å. This absorption corresponds to a strong P v doublet transition (wavelengths 347.23020 and 348.19184Å), a strong P v transition (wavelength 348.19184Å), an S iv quadruplet (wavelengths 349.0453, 349.0729, 349.1025, and 349.1302Å), and a P v triplet (wavelengths 349.2369, and 349.2455Å twice, as both of these transitions conclude with a transition with quantum number j values of 3/2 and 5/2 respectively). All of these features arise from excited transitions. The presence of Fe or Ni as being the cause of the feature may be ruled out, as the measured Z for both Barsold and Prevold are very similar. Furthermore, there are very similar amounts of Fe and Ni in both models. It is evident that the Barsold fit is superior to the Prevold fit, as the latter model fit is in better agreement with the observational data.

A similar case occurs for WD0232+035. In Figures 5.19 and 5.20, the EUVE spectrum of WD0232+035 is plotted with the best fitting models from the Barsold and Prevold grids respectively. It can be seen that agreement between the model and the observational data is best for the Prevold near 347Å, although additional absorption at 349Å (populated by the S iv quadruplet) is in disagreement with observation. For the Barsold fit, no discrepancy is seen at 349Å.

Therefore, this suggests that P and S may not be of photospheric origin in WD0501+524. This conclusion can be further supported by observations made by Preval et al. (2013), who showed that there was a discrepancy between the abundance measurements of P iv and P v, and S iv and S vi. If the features do not arise from the photosphere, then it is possible that they are circumstellar in nature, given their high

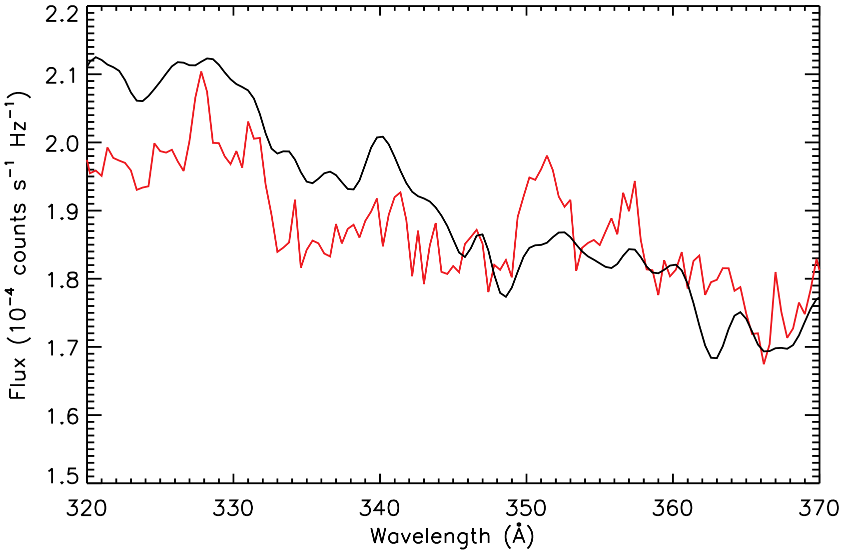

Figure 5.17: Plot of the EUVE spectrum of WD0501+524 (red curve) in the region 320-370Å. The black curve is the best fitting model using the Barsold model grid.

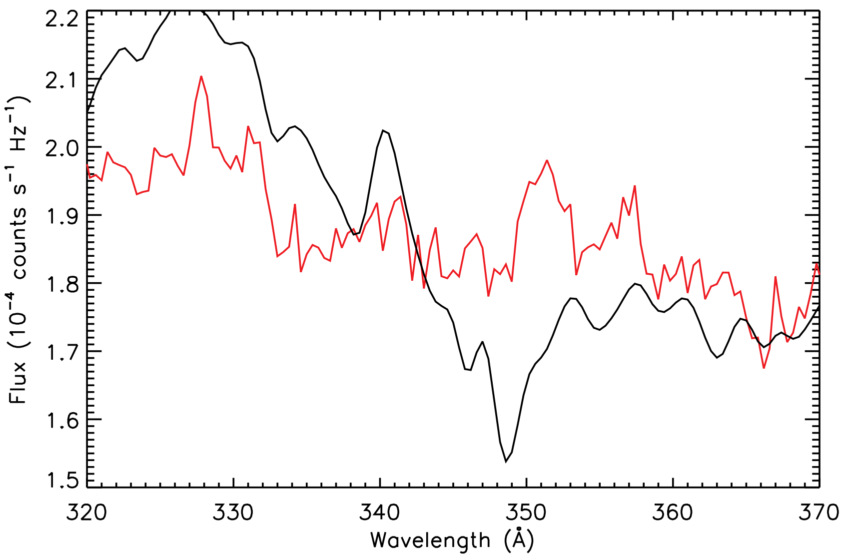

Figure 5.18: The same as Figure 5.17, but the black curve is now the best fitting model using the Prevold model grid.

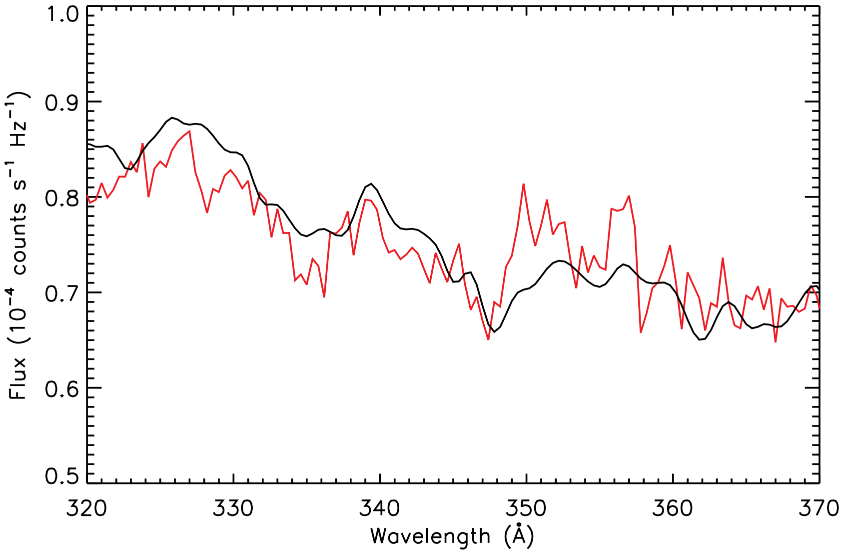

Figure 5.19: Plot of the EUVE spectrum of WD0232+035 (red curve) in the region 320-370Å. The black curve is the best fitting model using the Barsold model grid.

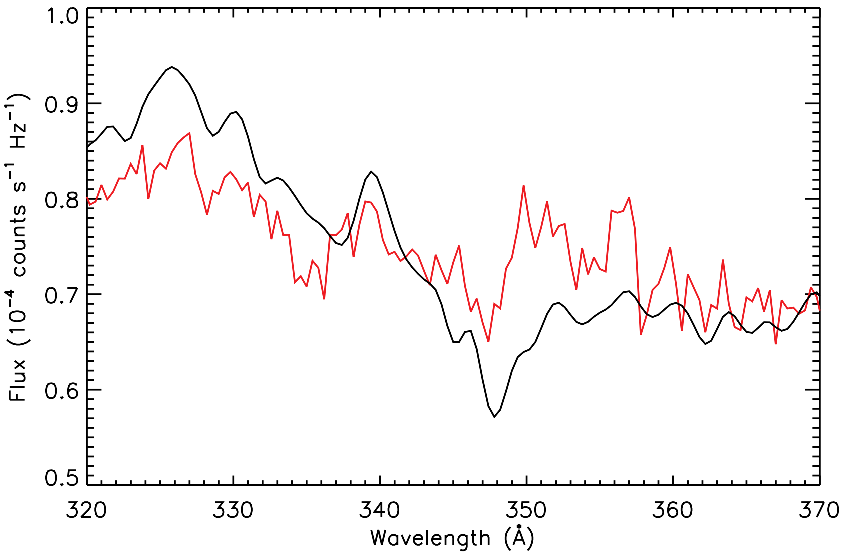

Figure 5.20: The same as Figure 5.19, but the black curve is now the best fitting model using the Prevold model grid.

ionisation states.

5.6.2 Atomic data

The fits obtained in this study are improved from previous studies, as absorption features in the short wavelength range are well matched in a number of cases. Previous studies of the EUV spectrum of WD0501+524 such as Barstow et al. (1996) used limited atomic datasets consisting of observed Fe and Ni transitions only (∼300,000 lines). Use of an extended dataset containing ∼9,000,000 predicted and observed Fe and Ni transitions significantly improved the quality of the fit, in that the continuum could be reproduced (Lanz et al., 1996). However, including even more transitions in the model atmosphere calculation presented in this Chapter has not improved the quality of fits significantly. Comparing the models with Ku92 and Ku11 atomic data, all of the fits are of a similar quality as shown by the $\chi^2_{\rm red}$ values in Table 5.3. This implies that the opacity of heavy metals is accounted for equally well in the Ku92 models and the Ku11 models. Aside from the composition of the atmosphere, which has been demonstrated to be an important factor in the quality of the fit, another aspect to consider is the synthesised model atmospheres used to make the measurements in this study. While the radiative transfer solution calculated by TLUSTY used the Ku92 and Ku11 datasets, the synthesised spectra made use of the Ku11 dataset. As the flux redistribution has not been affected by the use of either Ku92 or Ku11, it appears likely that the success of fitting several of the white dwarfs in this study has been due to using the Ku11 line list when synthesising the model spectra.

5.7 Conclusion

A study has been conducted comparing EUVE spectra with the prediction of model atmosphere calculations. Four model atmosphere grids were used comprising two different atmospheric compositions, and two different atomic data sets from Ku92 and Ku11. The model atmosphere grid calculated with Ku92 and Ku11 data with Preval et al. (2013) abundances were referred to as Prevold and Prevnew, while the grids calculated with Barstow et al. (2003) abundances and Ku92 and Ku11 data were referred to as Barsold and Barsnew respectively. The quality of fits for all model grids were rather similar for each star. The use of either the Ku92 or Ku11 data in the model atmosphere calculations does not appear to make a significant difference to the quality of the fit, however, in the case of WD0501+524, fits using model grids calculated with Barstow et al. (2003) abundances had a significantly lower $\chi^2_{\rm red}$ compared to those fit with Preval et al. (2013) grids.

Comparison of the Barsold and Prevold model grids in the region 320-370Å showed that a cluster of excited P and S features could be resolved in the latter grid. Concurrently, it was seen in several stars such as WD0501+524 that the predicted absorption from P and S was not observed in the EUVE data, implying that previous observations of P and S in far UV spectra may not pertain to the photosphere as originally thought.

5.8 Summary

- Seven metal rich white dwarf stars observed by the EUVE were analysed, with the aim of fitting model atmospheres to their spectra.
- Model atmosphere grids were calculated using the Ku92 and Ku11 atomic datasets, as well as the Preval et al. (2013) and Barstow et al. (2003) metal abundances.
- There was no preference over the atomic dataset used in the model atmosphere calculations, however, the model fits appeared to favour the Barstow et al. (2003) abundances in WD0501+524. This was evident by Figures 5.19 and 5.20, with the latter showing disagreement between predicted and observed flux due to addition P and S absorption.
- The improvement in EUV fits in this analysis over previous work, therefore, is not thought to be the opacity sources used in calculating the model atmospheres, but is most likely due to the quality and completeness used to synthesise the model spectra.

Chapter 6

Concluding remarks

6.1 Introduction

The central theme of this thesis has been atomic data, and the impact it can have on model atmosphere calculations. The work presented in this thesis most certainly would not have been possible 20, or even 10 years ago. A single model atmosphere typically required 24-36 hours to converge, with higher abundances/metallicities requiring 48-72 hours. For a single metallicity (multiple of WD0501+524 abundance), there were 351 grid points corresponding to the different effective temperatures ($T_{\rm eff}$) and surface gravity (log g) values. Therefore, performing an entire grid calculation one point at a time would take 8424-25272 hours (351-1053 days). By using the supercomputing cluster ALICE based at the University of Leicester, >350 calculations could be performed in parallel, dramatically reducing the computational time to 24-72 hours for an entire grid. With this computing power, it may soon become possible to compute model atmosphere grids that account for not only $T_{\rm eff}$, log g, and metallicity, but also more complicated grids that allow for individual abundance variations. This would allow for assessments of NLTE effects in model atmospheres, in particular, how the populations of different metal species affect the structure of the atmosphere, and other species present.

In this concluding Chapter, an executive summary is given of the work presented in this thesis, with each section followed by suggestions for future work. The Chapter concludes with final remarks.

6.2 Summaries and future work

A spectroscopic survey of WD0501+524 was performed, examining coadded FUSE and STIS spectra of the object. 976 absorption features were detected, and by using an extensive line list combining the Kurucz (1992) and Kentucky databases, 947 of these features could be successfully identified. $\approx$ 60% of these absorption features were found to originate from transitions of Fe and Ni IV-VI. As previous model atmosphere calculations utilised data from Kurucz (1992) and the Opacity Project, a question arose regarding the efficacy of such calculations in accurately accounting for line blanketing effects. It was this result that provided inspiration for the rest of the thesis.

Other surveys of WD0501+524, have claimed detections of trans-Fe metals, such as Zn (Rauch et al., 2013) and Ba (Rauch et al., 2014b). Model atoms incorporating Zn and Ba into the NLTE code Tubingen Model Atmosphere Program (TMAP, Werner & Dreizler 1999) were designed (see Rauch et al. 2014a,b), however, the number of super-transitions included in the solution for these metals was far less than that of Fe and Ni. For comparison, the model atmosphere calculations presented in this thesis using the Kurucz (2011) (Ku11 hereafter) included 528 Fe and Ni super levels and 23507 super-transitions, the Zn model atom used by Rauch et al. (2014a) included 240 NLTE super levels, 13 LTE super levels, and 2302 super-transitions, and the Ba model atom included 293 NLTE super levels, 6 LTE levels, and 1592 super-transitions. Currently, TLUSTY does not have the capability to model Zn, Ba, or other metals more massive than Ni. Therefore, as a comparison to the TMAP results, a modification of TLUSTY is required, and more extensive model atoms need to be designed. It may also be the case, however, that a further extension of the Fe and Ni line list is warranted. In the survey of WD0501+524 presented in this thesis, a more extensive line list of Fe and Ni transitions was adequate to identify $> 95\%$ of the detections in the spectrum. Therefore, it may simply be the case that additional Fe and Ni transitions can explain the unidentified absorption features. Every survey of WD0501+524 yields something new in it's spectrum. It will be interesting to see what future studies claim.

The Kurucz (1992) database (Ku92 hereafter), containing $\approx 9,000,000$ Fe and Ni IV-VII transitions, has been superceded by the Kurucz (2011) database (Ku11 hereafter), containing $\approx 160,000,000$ Fe and Ni IV-VII transitions. The Ku92 database was supplemented by photoionisation (PI) cross section data from the Opacity Project. However, no analogue existed for the Ku11 database. To fill this gap, the atomic structure program AUTOSTRUCTURE was used to calculate the cross sections required to allow TLUSTY to utilise the Ku11 database. The calculated AUTOSTRUCTURE energies were generally in good agreement with those presented in Ku11, with differences not exceeding 35%.

Comparison of a model atmosphere calculated with Ku11 data to a model calculated with Ku92 data showed no significant differences between the spectral energy distributions in the UV and optical wavebands. However, there were rather significant small flux changes in the EUV waveband as demonstrated by Figure 3.7, where the residual between the Ku92 and Ku11 models was as high as 0.9. Furthermore, there were changes to the ionisation balances of several metals, the largest of which were Fe and Ni. This was confirmed by re-measuring the metal abundances of WD0501+524. The residual between the Ku92 and Ku11 Lyman and Balmer lines was calculated, and while no significant differences were shown between the atmospheres, there appeared to be a trend showing the residuals become smaller up to a particular $T_{\rm eff}$, which then began increasing as $T_{\rm eff}$ increased. This could suggest that the Ku11 data becomes more significant for higher $T_{\rm eff}$. In terms of the atomic data calculations, it is obvious that the AUTOSTRUCTURE energies do not completely match the Ku11 data. How much of an effect this has on the PI cross sections is unknown, and should be investigated. This can be done by using term corrections to improve the agreement between the AUTOSTRUCTURE and Ku11 energies.

This thesis has explored the Lyman/Balmer line problem from many different angles, such as the atomic data used in model atmosphere calculations (Ku92 and Ku11), the atmospheric composition (Barstow et al. 2003 and Preval et al. 2013) specified when calculating model atmospheres, and the Stark broadening tables used to synthesise the Lyman and Balmer line profiles (Lemke 1997 and Tremblay & Bergeron 2009). As was shown previously by Barstow et al. (1998), the $T_{\rm eff}$ and log g measurements of a white dwarf differ significantly when using a pure H model grid, or a metal-polluted grid. For some stars, the use of a metal-polluted grid resolved the difference between the Lyman and Balmer $T_{\rm eff}$ measurements, while in other cases it only reduced the discrepancy. The use of either the Ku92 or the Ku11 data sets in the model atmosphere calculation was found to be inconsequential, as the measured values were consistent with each other. Furthermore, the use of either the Barstow et al. (2003) or the Preval et al. (2013) atmosphere compositions also did not appear to matter greatly, implying that the average opacity contributions from all metals in the atmosphere was more important than the individual contributions. Overall, the dependency of the Lyman/Balmer $T_{\rm eff}$ discrepancy appears to be on the metal composition, and the average opacity. It could very well be the case that additional opacity in the form of trans-iron metals needs to be included into the model atmosphere calculations in order to resolve the discrepancy between the Lyman and Balmer $T_{\rm eff}$. There are two possibilities as to where this may come from. The first is from metals already present in the model atmosphere. If the atomic data for a particular ion is not complete, it may have a knock on effect on the rest of the spectrum. Given the differences reported are relatively small, this improvement will probably be a second order effect. The second possibility is from metals that have not yet been accounted for in the models. For example, Vennes et al. (2005) reported the discovery of Ge IV in the photospheric spectrum of WD0501+524, which was confirmed in the study reported earlier in this thesis. This metal, however, was not added to the model atmosphere, as TLUSTY is not currently equipped to utilise such a high mass ion. It would be worth repeating the analysis of the Lyman/Balmer line problem with the newly discovered heavy metals included in the model atmosphere calculations. Furthermore, an investigation into the completeness of atomic data for other species such as P and S is warranted.

Historically, fitting EUV spectra of metal-polluted white dwarfs has been difficult. In particular, the short wavelength (< 230Å) spectrum has been particularly troublesome. While the ISM He II opacity can be used to adjust the continuum, the discrepancy arises from reproducing the blends of lines due to Fe and Ni absorption features. To investigate this issue, seven white dwarfs observed by the Extreme Ultraviolet Explorer (EUVE) and identified as being metal rich by Craig et al. (1997) was analysed, and attempts to fit their observed spectra were made. The model atmospheres used in the analysis were calculated with two sets of atomic data (Ku92 and Ku11), and two atmospheric compositions (Barstow et al. 2003 and Preval et al. 2013). The grids also included a variable metallicity Z, where $Z = 1$ represented one times the abundance of WD0501+524. The short wavelength spectrum of six white dwarf stars could be convincingly reproduced. The exception to this case was WD0501+524.

Examination of the 320-370Å region in the LW spectrum revealed something unexpected. The Prevold model predicted that there should be two strong absorption features located between 340 and 350Åin WD0501+524, which arose as a blend of excited P and S absorption features. In the observed data of WD0501+524, neither of these absorption features was present. The Barsold model did not predict the presence of these absorption features, and was able to match the continuum. As resonant features of P and S have been observed in the FUSE spectrum for WD0501+524 (Preval et al., 2013), and no excited transitions are observed, this implies the P and S absorption features could originate from the ISM or possibly be circumstellar. While not explored in this thesis, it may be possible to put constraints on the P and S abundance by using the 320-370Åregion in EUVE spectra. Furthermore, in conjunction with spectra from FUSE, it may also be possible to measure the column density of any P and S features.

The model grids utilised only considered multiples of metal abundances relative to WD0501+524. As Fe and Ni contribute the largest opacity, it may be worth splitting this multiplicative abundance into light metals (C-S) and heavy metals (Fe-Ni). In addition, it is interesting that the star with the poorest fit was WD0501+524, while this also happens to be a star with claimed detections of Ge, Zn, and Ba. It may be possible that to fully reconcile the predicted models with the observed data, a model grid has to be calculated that accounts for these additional metals. With this in mind, it is interesting that stars with more Fe and Ni in their atmospheres (WD0232-035 and WD2211-495) achieve better fits than WD0501+524.

The work done by Barstow et al. (1998) also presents an opportunity to further the analysis presented in this thesis. The authors were able to explain the EUVE spectrum of WD0501+524 by stratifying Fe in the model, with large abundances deeper into the atmosphere, gradually depleting towards the top of the atmosphere. If the atmosphere of WD0501+524 is indeed configured in this way, this could be indicative of on-going mass loss for the white dwarf. Therefore, a repeat of the analysis by Barstow et al. (1998) using the Ku11 atomic data may yield a new insight into any possible stratification of Fe in WD0501+524.

6.3 Final remarks

The last dedicated EUV observatory to be launched into orbit was, and still remains, the EUVE. As the satellite was decommisioned on 31st Jaunary 2001, astronomers have been EUV blind for more than 13 years at the time of this thesis going to print. The only access astronomers have had since this time is through the *Joint Plasma Dynamic Experiment* (JPEX), which is a retrievable high resolution (R$\sim$3000-4000) EUV spectrometer that is launched via a sounding rocket. JPEX has observed two stars, one of which is WD0501+524 (Cruddace et al., 2002; Barstow et al., 2005). The EUVE performed an all sky survey, and also performed spectroscopic observations of more than 350 targets. Several of these targets were extragalactic. Again, no probe has performed an EUV all sky survey since the EUVE. In comparision, all sky surveys of the Cosmic Microwave Background have been performed by three observatories, namely the *Cosmic Background Explorer* (COBE), the *Wilkinson Microwave Anisotropy Probe* (WMAP), and more recently, the *PLANCK* surveyor. Our understanding of the EUV spectrum of white dwarf stars is improving, as demonstrated by the work presented in this thesis. The EUV is a spectroscopic goldmine, and even at the resolution offered by the EUVE, it is possible to put constraints on the metal abundances relative to WD0501+524. Furthermore, other quantities such as $T_{\rm eff}$, log g, and the column densities of H and He clouds can be extracted. At higher resolution, it may even become possible for individual metal abundances to be determined. Therefore, the EUV is not only a photospheric probe, but also an ISM probe, making the case for a dedicated EUV probe compelling.

Throughout this thesis, atomic data have been the main focal point. Several tests have been performed to assess their role in stellar atmosphere modelling. Considering the results obtained in turn, the vast majority of unidentified lines in the spectrum of WD0501+524 could be explained by using an expanded line list from the Kentucky database. In addressing the Lyman/Balmer line problem, models using the Ku11 atomic dataset had no advantage over the Ku92 dataset. Instead, the average opacity of metal species in the atmosphere determined the size of the discrepancy. In the EUV, again there was no advantage to using a model grid calculated with the Ku11 dataset over one calculated with the Ku92 dataset. The major improvement to the fits was the number of transitions used to synthesise the EUV spectra. Therefore, the main conclusion of this thesis is that the Fe and Ni atomic data provided by the Ku92 dataset are adequate for reproducing the observed spectra, and that there is no benefit to be gained by using as extensive a dataset as Ku11. However, this does not mean that no more atomic data needs to be included. As was seen for WD0501+524, there are still significant discrepancies between observed and model spectra. Whether this is due to additional metal species, or an incomplete list of Fe and Ni transitions remains to be seen, and should be the subject of future investigations.

This has been a very exciting project to undertake, due to the multiple areas of physics required. My journey has allowed me to meet many different people with different interests and stories. The enthusiasm of the white dwarf community is one I have yet to see matched, and with good reason. The physics and observations of white dwarf stars continue to divulge information on more familiar topics, such as the evolution of stars and structure of the ISM, as well as more exotic areas such as the variation of the fine structure constant (see Berengut et al. (2013); Bagdonaite et al. (2014)). These curious objects often do not get the attention they deserve, both in the scientific community, as well as the media. Hopefully, the work described in this thesis has shown that white dwarf stars are not only interesting in their own right, but are also extremely useful tools for the astronomical community.

Appendix A

WD0501+524 line list

Table A.1: List of detected absorption features from FUSE. Wavelengths (λ's) are given in Å, wavelength uncertainties ($\delta\lambda$) in mÅ, equivalent widths and uncertainties (W_λ and δW_λ respectively) in mÅ, and velocities and uncertainties (v and δv respectively) in km s^{-1}. The Origin column indicates the determined origin of the line, where PHOT=Photosphere, ISM1=LIC, and ISM2=Hyades. The List column indicates the atomic database referencing the transition, where 1=Kentucky database, 2=Kurucz (1992),3=NIST, and 4=Verner et al. (1994).

$\lambda_{\rm obs}$	$\delta\lambda_{\rm obs}$	W_λ	δW_λ	Ion	$\lambda_{\rm lab}$	$\delta\lambda_{\rm lab}$	v	δv	$\delta v_{\rm tot}$	List	Origin
916.503	0.533	168.903	2.369	H I	916.429	0.004	24.18	0.17	0.17	1	ISM1
917.254	0.600	170.652	2.643	H I	917.181	0.005	24.02	0.20	0.20	1	ISM1
918.196	0.574	196.800	2.500	H I	918.129	0.007	21.78	0.19	0.19	1	ISM1
918.964	7.564	10.266	2.198	N IV	918.893	7.500	23.16	2.47	3.48	1	PHOT
919.428	0.360	178.807	1.626	H I	919.351	0.009	25.00	0.12	0.12	1	ISM1
921.032	0.347	189.055	1.609	H I	920.963	0.012	22.45	0.11	0.11	1	ISM1
922.090	2.485	10.595	1.404	N IV	921.994	7.600	31.22	0.81	2.60	1	PHOT
922.607	2.409	10.460	1.358	N IV	922.519	7.600	28.60	0.78	2.59	1	PHOT
923.220	0.352	209.245	1.687	H I	923.150	0.016	22.64	0.11	0.11	1	ISM1
923.757	3.069	9.727	1.454	N IV	923.676	7.600	26.29	1.00	2.66	1	PHOT
924.371	2.257	31.913	1.255	S V	924.220	7.600	48.98	0.73	2.57	1	PHOT
				N IV	924.284	7.600	28.22	0.73	2.57	1	PHOT
925.048	5.040	8.874	1.068	O I	925.017	0.076	9.96	1.63	1.63	1	ISM2
926.303	0.364	213.638	1.712	H I	926.226	0.023	25.04	0.12	0.12	1	ISM1
929.576	2.364	29.657	1.253	O I	929.517	0.077	19.09	0.76	0.76	1	ISM1
930.806	0.391	219.237	1.896	H I	930.748	0.035	18.62	0.13	0.13	1	ISM1
932.761	7.649	14.606	2.183	Fe V	932.665	7.000	30.86	2.46	3.33	1	PHOT
933.494	0.659	34.182	1.190	S VI	933.378	7.800	37.26	0.21	2.51	1	PHOT
933.762	4.268	4.243	0.976	Ni V	933.662	7.800	32.11	1.37	2.85	1	PHOT
934.538	8.337	4.203	1.394	Fe V	934.430	7.000	34.65	2.67	3.49	1	PHOT
936.701	1.339	16.857	1.427	O I	936.629	0.078	22.89	0.43	0.43	1	ISM1
937.869	0.431	237.415	2.052	H I	937.803	0.056	20.97	0.14	0.14	1	ISM1
942.773	8.899	12.156	1.992	Fe V	942.649	7.200	39.44	2.83	3.64	1	PHOT
944.628	0.624	34.575	1.077	S VI	944.523	7.900	33.33	0.20	2.51	1	PHOT
948.743	1.083	18.406	1.564	O I	948.686	0.080	18.16	0.34	0.34	1	ISM1
949.800	0.459	240.337	2.246	H I	949.743	0.100	18.00	0.15	0.15	1	ISM1
950.745	3.482	9.800	1.622	P IV	950.657	5.700	27.75	1.10	2.11	1	PHOT
950.963	6.694	6.397	1.734	O I	950.885	0.081	24.72	2.11	2.11	1	ISM1
952.480	7.528	15.564	2.106	N I	952.415	0.570	20.52	2.37	2.38	1	ISM1
952.904	7.551	4.761	1.388	C IV	952.800	9.800	32.72	2.38	3.89	1	PHOT
953.491	3.391	6.012	1.141	N I	953.415	0.580	23.83	1.07	1.08	1	ISM1
953.741	2.102	10.362	1.145	N I	953.671	0.580	22.10	0.66	0.69	1	ISM1
954.042	1.515	13.842	1.068	N I	953.970	0.081	22.66	0.48	0.48	1	ISM1
955.426	0.979	23.714	0.965	N IV	955.334	8.100	28.87	0.31	2.56	1	PHOT
955.933	11.454	12.783	2.140	Fe V	955.825	7.400	33.87	3.59	4.28	1	PHOT

Table A.1: Continued.

$\lambda_{\rm obs}$	$\delta\lambda_{\rm obs}$	W_λ	δW_λ	Ion	$\lambda_{\rm lab}$	$\delta\lambda_{\rm lab}$	v	δv	$\delta v_{\rm tot}$	List	Origin
957.807	9.016	3.560	0.718	Fe V	957.716	7.400	28.49	2.82	3.65	1	PHOT
959.670	4.104	3.459	0.889	Ni IV	959.581	8.200	27.81	1.28	2.86	1	PHOT
963.844	2.470	6.690	0.887	C IV	963.742	10.000	31.73	0.77	3.20	1	PHOT
964.058	4.927	3.995	1.041	C IV	963.965	10.000	28.92	1.53	3.47	1	PHOT
964.716	4.720	7.257	1.205	C IV	964.627	14.000	27.66	1.47	4.59	1	PHOT
965.093	4.756	8.363	0.865	C III	964.970	59.000	38.21	1.48	18.39	1	PHOT
971.795	0.678	44.210	1.404	O I	971.737	0.084	17.85	0.21	0.21	1	ISM1
				O I	971.738	0.084	17.72	0.21	0.21	1	ISM1
				O I	971.738	0.084	17.52	0.21	0.21	1	ISM1
972.595	0.490	243.342	2.312	H I	972.537	0.200	17.96	0.15	0.16	1	ISM1
976.513	1.369	13.199	1.031	O I	976.448	0.085	19.92	0.42	0.42	1	ISM1
977.076	0.277	104.392	1.086	C III	977.020	0.850	17.15	0.08	0.27	1	PHOT
978.931	5.539	4.688	0.972	Fe V	978.822	7.700	33.38	1.70	2.90	1	PHOT
				Fe V	978.837	7.700	28.79	1.70	2.90	1	PHOT
980.911	4.037	4.967	1.183	Fe V	980.813	7.800	29.95	1.23	2.68	1	PHOT
982.936	2.070	6.411	1.248	Fe V	982.832	7.800	31.72	0.63	2.46	1	PHOT
983.722	2.136	20.703	0.776	Fe V	983.618	7.800	31.70	0.65	2.46	1	PHOT
				Fe V	983.628	7.800	28.65	0.65	2.46	1	PHOT
985.775	1.291	14.647	1.636	Fe V	985.673	7.800	31.02	0.39	2.40	1	PHOT
				Fe V	985.690	7.800	25.85	0.39	2.40	1	PHOT
986.352	1.715	11.503	1.050	Fe V	986.260	7.800	27.97	0.52	2.43	1	PHOT
987.746	0.969	18.890	1.053	Fe V	987.673	7.900	22.16	0.29	2.42	1	PHOT
988.706	1.582	67.299	2.108	O I	988.655	0.087	15.49	0.48	0.48	1	ISM2
988.825	0.671	53.873	1.699	O I	988.773	0.087	15.64	0.20	0.21	1	ISM2
989.170	1.804	9.699	0.988	Fe IV	989.042	0.870	38.68	0.55	0.61	1	PHOT
989.880	0.698	76.028	1.413	N III	989.799	8.700	24.53	0.21	2.64	1	PHOT
				Fe V	989.686	7.900	58.77	0.21	2.40	1	PHOT
				Ni V	989.686	8.700	58.77	0.21	2.64	1	PHOT
				Fe V	989.832	7.900	14.54	0.21	2.40	1	PHOT
				Fe V	989.872	7.900	2.42	0.21	2.40	1	PHOT
991.669	1.186	15.773	1.023	Fe V	991.570	7.900	29.93	0.36	2.42	1	PHOT
992.396	4.348	11.821	1.521	Fe IV	922.292	0.880	22.78	1.41	1.34	1	PHOT
992.603	1.627	14.353	1.125	Fe V	992.522	7.900	24.47	0.49	2.44	1	PHOT
993.150	2.142	12.917	1.160	Fe V	993.074	8.000	22.94	0.65	2.50	1	PHOT
993.448	3.073	20.272	1.529	Ni IV	993.376	8.800	21.73	0.93	2.81	1	PHOT
993.791	2.859	13.937	1.451	Ni V	993.680	8.800	33.49	0.86	2.79	1	PHOT
				Fe V	993.704	8.000	26.25	0.86	2.56	1	PHOT
993.916	2.297	12.770	1.241	Fe V	993.838	0.880	23.53	0.69	0.74	1	PHOT
994.235	2.160	11.821	1.200	Fe V	994.142	8.000	28.04	0.65	2.50	1	PHOT
994.349	2.595	8.259	1.164	Fe V	994.234	8.000	34.68	0.78	2.54	1	PHOT
995.173	2.990	5.745	1.053	O V	995.087	8.800	25.91	0.90	2.80	1	PHOT
995.327	3.798	4.940	1.042	N IV	995.244	8.800	25.00	1.14	2.89	1	PHOT
				Al V	995.250	88.000	23.19	1.14	26.53	1	PHOT
				Fe V	995.256	8.000	21.39	1.14	2.67	1	PHOT
995.836	2.545	7.602	1.001	Ni V	995.744	8.800	27.70	0.77	2.76	1	PHOT

Table A.1: Continued.

$\lambda_{\rm obs}$	$\delta\lambda_{\rm obs}$	W_λ	δW_λ	Ion	$\lambda_{\rm lab}$	$\delta\lambda_{\rm lab}$	v	δv	$\delta v_{\rm tot}$	List	Origin
997.717	1.860	22.820	0.669	Fe V	997.652	0.000	19.53	0.56	0.56	2	PHOT
998.358	2.249	10.771	0.936	Fe V	998.285	8.000	21.92	0.68	2.50	1	PHOT
999.723	3.466	6.712	0.994	Fe V	999.657	8.100	19.79	1.04	2.64	1	PHOT
999.847	2.116	10.361	0.920	Fe V	999.763	8.100	25.19	0.63	2.51	1	PHOT
				S IV	999.777	8.900	20.99	0.63	2.74	1	PHOT
1000.232	1.117	18.673	0.851	Fe V	1000.140	8.100	27.58	0.33	2.45	1	PHOT
1000.909	7.803	6.219	1.131	Fe V	1000.766	8.100	42.84	2.34	3.37	1	PHOT
1001.529	1.929	20.385	0.666	Fe V	1001.451	8.100	23.35	0.58	2.49	1	PHOT
1002.189	7.066	6.889	1.155	N III	1002.107	8.900	24.53	2.11	3.40	1	PHOT
				Fe V	1002.112	8.100	23.04	2.11	3.22	1	PHOT
1002.945	2.510	7.040	0.759	N III	1002.853	9.000	27.50	0.75	2.79	1	PHOT
1003.194	5.076	10.122	0.726	Fe IV	1003.088	0.900	31.80	1.52	1.54	1	PHOT
				Fe V	1003.115	8.100	23.61	1.52	2.86	1	PHOT
1003.828	8.008	5.783	1.180	Fe V	1003.680	8.100	44.21	2.39	3.40	1	PHOT
1004.685	2.997	8.247	0.518	Fe V	1004.424	8.100	77.90	0.89	2.58	1	PHOT
				Fe V	1004.622	8.100	18.80	0.89	2.58	1	PHOT
1004.935	3.302	5.345	0.845	Fe V	1004.910	8.100	7.46	0.98	2.61	1	PHOT
1005.427	10.174	11.169	1.644	Si III	1005.349	0.900	23.26	3.03	3.05	1	PHOT
1006.054	1.961	13.318	0.903	Fe V	1005.982	8.200	21.46	0.58	2.51	1	PHOT
1006.421	6.017	7.187	1.089	N IV	1006.339	9.000	24.43	1.79	3.22	1	PHOT
1006.786	5.326	12.701	0.760	Fe IV	1006.707	0.900	23.53	1.59	1.61	1	PHOT
1007.379	2.624	8.273	0.865	Fe V	1007.292	8.200	25.89	0.78	2.56	1	PHOT
1007.531	2.651	7.665	0.826	Fe V	1007.450	8.200	24.10	0.79	2.56	1	PHOT
1008.570	9.773	7.520	1.273	O IV	1008.490	64.000	23.78	2.91	19.24	1	PHOT
1009.080	7.755	4.583	0.937	Fe V	1008.995	8.200	25.26	2.30	3.35	1	PHOT
1009.449	3.005	11.700	0.927	Fe V	1009.375	8.200	21.98	0.89	2.59	1	PHOT
1009.664	1.507	6.457	1.290	Fe V	1009.585	8.200	23.46	0.45	2.48	1	PHOT
				Fe V	1009.596	8.200	20.19	0.45	2.48	1	PHOT
1010.064	2.267	8.672	0.592	Fe IV	1009.988	6.500	22.56	0.67	2.04	1	PHOT
1010.605	4.529	2.194	0.555	O IV	1010.529	9.100	22.55	1.34	3.02	1	PHOT
1010.759	5.240	3.469	0.252	Fe IV	1010.670	0.910	26.40	1.55	1.58	1	PHOT
				Fe IV	1010.670	0.000	26.40	1.55	1.55	2	PHOT
				Fe V	1010.682	8.200	22.84	1.55	2.89	1	PHOT
				Fe V	1010.683	8.200	22.54	1.55	2.89	1	PHOT
1011.452	1.419	6.585	0.683	Fe V	1011.367	8.200	25.20	0.42	2.47	1	PHOT
1011.598	2.709	3.734	0.548	Fe V	1011.512	8.200	25.49	0.80	2.56	1	PHOT
1012.248	9.196	2.502	0.790	C VI	1012.174	22.000	21.92	2.72	7.06	1	PHOT
1012.489	2.868	8.391	0.801	Ni V	1012.411	9.100	23.10	0.85	2.83	1	PHOT
1012.892	6.897	4.316	0.900	Ni V	1012.805	0.000	25.75	2.04	2.04	2	PHOT
				Ni VI	1012.810	9.100	24.27	2.04	3.38	1	PHOT
				Ni VI	1012.812	9.100	23.68	2.04	3.38	1	PHOT
				Fe V	1012.814	8.300	23.09	2.04	3.19	1	PHOT
1013.903	1.687	4.275	0.781	P IV	1013.815	6.500	26.02	0.50	1.99	1	PHOT
				Fe IV	1013.818	0.920	25.14	0.50	0.57	1	PHOT
				Fe V	1013.831	8.300	21.29	0.50	2.50	1	PHOT

Table A.1: Continued.

$\lambda_{\rm obs}$	$\delta\lambda_{\rm obs}$	W_λ	δW_λ	Ion	$\lambda_{\rm lab}$	$\delta\lambda_{\rm lab}$	v	δv	$\delta v_{\rm tot}$	List	Origin
1014.579	15.051	4.361	1.176	N IV	1014.491	9.200	26.00	4.45	5.21	1	PHOT
1015.440	3.872	4.409	0.713	Fe V	1015.359	8.300	23.92	1.14	2.70	1	PHOT
1015.869	8.870	4.872	1.018	S III	1015.779	6.500	26.56	2.62	3.25	1	PHOT
1016.472	9.726	3.646	0.893	C III	1016.399	0.920	21.53	2.87	2.88	1	PHOT
1016.768	3.218	3.000	0.580	Ge VI	1016.680	9.200	25.95	0.95	2.87	1	PHOT
				Fe V	1016.681	8.300	25.65	0.95	2.62	1	PHOT
				Ni IV	1016.689	9.200	23.29	0.95	2.87	1	PHOT
				O V	1016.690	65.000	23.00	0.95	19.19	1	PHOT
1017.069	2.525	7.068	0.731	Fe V	1016.998	8.300	20.93	0.74	2.56	1	PHOT
1017.484	1.729	12.676	0.778	Fe V	1017.387	0.001	28.58	0.51	0.51	1	PHOT
1020.392	8.884	3.753	0.914	Fe IV	1020.304	0.930	25.86	2.61	2.62	1	PHOT
1020.743	3.528	7.018	0.823	Fe V	1020.684	9.300	17.33	1.04	2.92	1	PHOT
1021.253	10.514	3.909	1.002	Fe V	1021.168	8.400	24.95	3.09	3.95	1	PHOT
				Fe V	1021.176	8.400	22.61	3.09	3.95	1	PHOT
1025.463	1.312	8.543	1.328	S I	1025.400	66.000	18.42	0.38	19.30	1	ISM1
1028.148	5.229	3.532	0.832	Fe V	1028.066	8.500	23.91	1.52	2.91	1	PHOT
				Si V	1028.070	94.000	22.75	1.52	27.45	1	PHOT
1029.536	1.721	10.569	0.638	Fe IV	1029.446	0.940	26.21	0.50	0.57	1	PHOT
1030.595	0.895	17.559	0.683	P IV	1030.515	0.950	23.42	0.26	0.38	1	PHOT
				P IV	1030.515	0.950	23.30	0.26	0.38	1	PHOT
1031.973	3.742	4.185	0.682	O VI	1031.930	67.000	12.49	1.09	19.49	1	ISM2
1033.190	1.943	4.521	0.555	P IV	1033.112	0.950	22.75	0.56	0.63	1	PHOT
				O III	1033.123	6.800	19.44	0.56	2.05	1	PHOT
1035.598	1.318	7.702	0.532	P IV	1035.516	0.960	23.77	0.38	0.47	1	PHOT
1036.372	0.146	90.346	0.538	C II	1036.337	0.960	10.21	0.04	0.28	1	ISM2
1037.046	0.827	14.690	0.575	C II	1037.018	0.960	8.04	0.24	0.37	1	ISM2
1038.728	2.563	3.690	0.527	Si VI	1038.640	96.000	25.40	0.74	27.72	1	PHOT
1039.270	0.343	52.100	0.401	O I	1039.230	0.096	11.54	0.10	0.10	1	ISM2
				Ni IV	1039.188	9.600	23.66	0.10	2.77	1	PHOT
				S VI	1039.196	9.600	21.35	0.10	2.77	1	PHOT
1040.002	1.976	5.209	0.531	S V	1039.916	9.600	24.79	0.57	2.83	1	PHOT
1043.197	8.231	6.748	0.947	Ni V	1043.109	9.700	25.29	2.37	3.66	1	PHOT
1045.788	0.954	11.012	0.544	Fe V	1045.697	8.800	26.09	0.27	2.54	1	PHOT
				P IV	1045.708	0.970	22.94	0.27	0.39	1	PHOT
				Ge V	1045.713	9.700	21.50	0.27	2.79	1	PHOT
1046.186	5.304	6.241	0.834	Fe V	1046.102	8.800	24.07	1.52	2.94	1	PHOT
				Fe V	1046.112	6.200	21.21	1.52	2.34	1	PHOT
1046.392	4.767	1.798	0.504	O IV	1046.313	9.800	22.64	1.37	3.12	1	PHOT
				Ni IV	1046.317	0.000	21.49	1.37	1.37	2	PHOT
1047.959	9.692	1.620	0.210	O V	1047.880	98.000	22.60	2.77	28.17	1	PHOT
				Fe IV	1047.884	0.980	21.46	2.77	2.79	1	PHOT
1048.246	5.503	6.270	0.812	Ar I	1048.220	0.070	7.44	1.57	1.57	1	ISM2
1049.745	1.229	7.095	0.971	P IV	1049.651	0.980	26.99	0.35	0.45	1	PHOT
1050.141	1.724	15.402	0.500	Fe V	1050.057	8.900	23.98	0.49	2.59	1	PHOT
				Ge V	1050.057	9.800	23.98	0.49	2.84	1	PHOT

Table A.1: Continued.

$\lambda_{\rm obs}$	$\delta\lambda_{\rm obs}$	W_λ	δW_λ	Ion	$\lambda_{\rm lab}$	$\delta\lambda_{\rm lab}$	v	δv	$\delta v_{\rm tot}$	List	Origin
				Fe V	1050.062	8.900	22.55	0.49	2.59	1	PHOT
1051.015	6.329	2.063	0.591	Fe V	1050.930	8.900	24.25	1.81	3.12	1	PHOT
				Fe V	1050.940	6.200	21.39	1.81	2.53	1	PHOT
1054.050	2.361	3.755	0.526	Fe V	1053.956	6.300	26.74	0.67	1.91	1	PHOT
				Fe V	1053.957	9.000	26.45	0.67	2.65	1	PHOT
				O IV	1053.970	70.000	22.76	0.67	19.92	1	PHOT
				Ni V	1053.972	9.900	22.19	0.67	2.89	1	PHOT
				Fe IV	1053.977	0.990	20.76	0.67	0.73	1	PHOT
1054.353	3.058	3.151	0.521	Si VI	1054.260	99.000	26.45	0.87	28.16	1	PHOT
				Fe V	1054.267	6.300	24.46	0.87	1.99	1	PHOT
1054.669	1.800	5.888	0.557	S IV	1054.589	9.900	22.74	0.51	2.86	1	PHOT
				Ge V	1054.590	9.900	22.46	0.51	2.86	1	PHOT
1055.152	9.736	9.914	1.193	Fe V	1055.096	0.990	16.05	2.77	2.78	1	PHOT
1056.475	11.273	3.278	0.843	Fe V	1056.391	6.300	23.84	3.20	3.66	1	PHOT
				Fe IV	1056.391	0.000	23.84	3.20	3.20	2	PHOT
1057.059	7.827	4.414	0.523	Ni VI	1056.976	0.000	23.54	2.22	2.22	2	PHOT
1060.646	4.261	11.193	0.899	Fe V	1060.586	9.100	16.96	1.20	2.84	1	PHOT
1062.743	0.573	21.872	0.530	S IV	1062.662	7.100	22.85	0.16	2.01	1	PHOT
1063.186	4.913	10.985	0.997	Ni V	1063.092	10.000	26.51	1.39	3.14	1	PHOT
				Ni VI	1063.097	10.000	25.10	1.39	3.14	1	PHOT
1064.033	5.791	3.034	0.677	Fe II	1063.972	0.100	17.19	1.63	1.63	1	ISM1
1064.362	6.626	4.469	0.511	S IV	1064.284	10.000	21.97	1.87	3.38	1	PHOT
				Fe V	1064.287	9.100	21.13	1.87	3.17	1	PHOT
1066.705	0.300	95.881	0.474	Si IV	1066.614	1.000	25.55	0.08	0.29	1	PHOT
				Si IV	1066.636	1.000	19.31	0.08	0.29	1	PHOT
				P IV	1066.645	1.000	16.89	0.08	0.29	1	PHOT
1072.740	1.395	10.853	0.734	Ge V	1072.661	10.000	22.08	0.39	2.82	1	PHOT
1073.073	0.655	21.142	0.688	S IV	1072.974	7.300	27.66	0.18	2.05	1	PHOT
1084.044	0.537	77.106	1.497	N II	1083.994	1.000	13.83	0.15	0.31	1	ISM2
1084.660	10.764	10.732	2.434	Fe V	1084.632	9.500	7.74	2.98	3.97	1	PHOT
1085.840	7.006	18.068	2.373	S IV	1085.723	11.000	32.31	1.93	3.60	1	PHOT
				Fe V	1085.729	9.500	30.65	1.93	3.26	1	PHOT
1086.778	8.445	14.764	2.363	N IV	1086.688	11.000	24.83	2.33	3.83	1	PHOT
1088.045	7.082	9.008	2.200	Fe V	1087.982	6.700	17.36	1.95	2.69	1	PHOT
1089.555	2.108	10.055	0.471	Ni V	1089.493	11.000	17.06	0.58	3.08	1	PHOT
1092.829	4.341	3.769	0.787	Fe V	1092.742	6.800	23.87	1.19	2.21	1	PHOT
1094.163	7.173	8.705	1.238	Ge V	1094.082	11.000	22.20	1.97	3.60	1	PHOT
				Ge VI	1094.084	11.000	21.65	1.97	3.60	1	PHOT
1094.781	2.994	5.611	0.778	Fe V	1094.688	9.700	25.47	0.82	2.78	1	PHOT
				Ni V	1094.700	11.000	22.18	0.82	3.12	1	PHOT
				Ni VI	1094.702	11.000	21.63	0.82	3.12	1	PHOT
1096.891	2.239	9.717	0.591	Fe V	1096.773	6.800	32.25	0.61	1.96	1	PHOT
1103.803	6.682	9.154	1.322	N IV	1103.714	11.000	24.17	1.82	3.50	1	PHOT
1105.582	3.438	13.028	1.132	Ni V	1105.564	11.000	4.88	0.93	3.13	1	PHOT
1110.017	2.713	5.495	0.824	P IV	1109.923	1.100	25.39	0.73	0.79	1	PHOT

Table A.1: Continued.

$\lambda_{\rm obs}$	$\delta\lambda_{\rm obs}$	W_λ	δW_λ	Ion	$\lambda_{\rm lab}$	$\delta\lambda_{\rm lab}$	v	δv	$\delta v_{\rm tot}$	List	Origin
				Si III	1109.940	1.100	20.80	0.73	0.79	1	PHOT
1112.727	2.372	9.392	0.568	P IV	1112.628	1.100	26.68	0.64	0.70	1	PHOT
				Fe V	1112.647	7.000	21.56	0.64	1.99	1	PHOT
				Fe V	1112.648	7.000	21.29	0.64	1.99	1	PHOT
1113.306	3.224	11.787	1.078	Ni V	1113.198	11.000	29.09	0.87	3.09	1	PHOT
				Si III	1113.204	1.100	27.47	0.87	0.92	1	PHOT
				S IV	1113.210	11.000	25.85	0.87	3.09	1	PHOT
				S IV	1113.210	11.000	25.85	0.87	3.09	1	PHOT
				Si V	1113.213	11.000	25.05	0.87	3.09	1	PHOT
1114.006	3.478	3.021	0.645	Ni IV	1113.983	11.000	6.19	0.94	3.10	1	PHOT
1116.886	3.492	3.999	0.780	Fe V	1116.807	7.100	21.21	0.94	2.12	1	PHOT
1117.013	2.103	6.775	0.857	Ni V	1116.914	11.000	26.57	0.56	3.01	1	PHOT
1118.030	0.349	69.220	0.876	P V	1117.977	7.900	14.21	0.09	2.12	1	PHOT
1122.093	2.407	17.799	1.137	N IV	1122.055	11.000	10.15	0.64	3.01	1	PHOT
1122.554	0.380	58.735	0.854	Si IV	1122.485	1.100	18.43	0.10	0.31	1	PHOT
1128.064	0.371	73.149	0.843	P V	1128.008	8.100	14.88	0.10	2.15	1	PHOT
1128.398	0.385	93.200	0.942	Si IV	1128.340	1.100	15.41	0.10	0.31	1	PHOT
1128.756	2.695	12.968	0.643	Ni VI	1128.711	11.000	11.95	0.72	3.01	1	PHOT
1133.119	3.793	7.773	0.542	Ni V	1133.051	11.000	17.99	1.00	3.08	1	PHOT
1134.206	1.602	9.588	0.814	N I	1134.165	0.110	10.76	0.42	0.42	1	ISM2
1135.010	1.651	19.530	1.558	N I	1134.980	0.110	7.92	0.44	0.44	1	ISM2
1138.314	3.947	5.945	0.588	Ni V	1138.234	0.000	21.07	1.04	1.04	2	PHOT
				Ni V	1138.243	1.200	18.73	1.04	1.09	1	PHOT
1140.546	5.524	5.577	1.012	Fe V	1140.450	10.000	25.24	1.45	3.00	1	PHOT
				Ni VI	1140.458	12.000	23.13	1.45	3.47	1	PHOT
1144.421	6.820	19.945	1.140	S IV	1144.368	12.000	13.88	1.79	3.62	1	PHOT
1144.978	0.944	11.483	1.782	Fe II	1144.938	0.120	10.47	0.25	0.25	1	ISM2
				Si III	1144.888	1.200	23.57	0.25	0.40	1	PHOT
				Ni VI	1144.890	12.000	23.04	0.25	3.15	1	PHOT
1146.881	5.527	3.919	0.933	S V	1146.800	83.000	21.17	1.44	21.74	1	PHOT
1147.130	8.065	3.447	1.044	Ni VI	1147.045	12.000	22.22	2.11	3.78	1	PHOT
1151.104	7.620	6.405	1.251	Ni V	1151.059	12.000	11.72	1.98	3.70	1	PHOT
				Ni V	1151.086	12.000	4.69	1.98	3.70	1	PHOT
1152.068	2.193	24.425	1.293	Si V	1151.965	12.000	26.81	0.57	3.17	1	PHOT
				Ni V	1151.973	12.000	24.72	0.57	3.17	1	PHOT
				Ni V	1151.985	12.000	21.60	0.57	3.17	1	PHOT
1164.964	1.094	3.436	0.586	Ni V	1164.889	12.000	19.30	0.28	3.10	1	PHOT
1165.396	1.386	2.030	0.614	N III	1165.300	86.000	24.70	0.36	22.13	1	PHOT
				Ni VI	1165.304	12.000	23.67	0.36	3.11	1	PHOT
1166.773	2.164	2.206	0.647	Ni V	1166.673	12.000	25.70	0.56	3.13	1	PHOT
1166.891	1.781	2.697	0.648	Fe V	1166.818	11.000	18.76	0.46	2.86	1	PHOT
1171.208	1.219	2.723	0.505	N III	1171.107	12.000	25.86	0.31	3.09	1	PHOT
				Ni V	1171.121	12.000	22.27	0.31	3.09	1	PHOT
1171.535	1.015	1.368	0.245	Ni V	1171.443	0.000	23.54	0.26	0.26	2	PHOT
				Fe V	1171.446	15.000	22.78	0.26	3.85	1	PHOT

Table A.1: Continued.

$\lambda_{\rm obs}$	$\delta\lambda_{\rm obs}$	W_λ	δW_λ	Ion	$\lambda_{\rm lab}$	$\delta\lambda_{\rm lab}$	v	δv	$\delta v_{\rm tot}$	List	Origin
1172.426	1.037	5.648	0.717	P IV	1172.327	1.200	25.32	0.27	0.41	1	PHOT
				N IV	1172.343	12.000	21.22	0.27	3.08	1	PHOT
1173.311	1.426	3.823	0.605	Ni V	1173.199	12.000	28.62	0.36	3.09	1	PHOT
1173.864	2.466	1.823	0.603	Al V	1173.772	12.000	23.50	0.63	3.13	1	PHOT
				Ni VI	1173.781	0.000	21.20	0.63	0.63	2	PHOT
1175.020	0.619	22.935	0.835	Fe IV	1174.920	8.700	25.52	0.16	2.23	1	PHOT
				Fe IV	1174.932	8.700	22.45	0.16	2.23	1	PHOT
				C III	1174.933	1.200	22.20	0.16	0.34	1	PHOT
1175.356	0.737	15.232	0.823	C III	1175.263	1.200	23.72	0.19	0.36	1	PHOT
				Fe IV	1175.274	1.200	20.92	0.19	0.36	1	PHOT
1175.678	1.043	7.874	0.756	Fe V	1175.574	11.000	26.52	0.27	2.82	1	PHOT
				C III	1175.590	1.200	22.44	0.27	0.41	1	PHOT
1175.804	0.395	33.198	0.820	Ni IV	1175.704	12.000	25.50	0.10	3.06	1	PHOT
				C III	1175.711	1.200	23.71	0.10	0.32	1	PHOT
1176.081	0.772	21.508	0.901	C III	1175.987	1.200	23.96	0.20	0.36	1	PHOT
1176.198	1.224	4.127	0.620	C III	1176.100	87.000	24.98	0.31	22.18	1	PHOT
1176.459	0.608	19.015	0.747	C III	1176.370	1.200	22.68	0.15	0.34	1	PHOT
				S IV	1176.374	12.000	21.66	0.15	3.06	1	PHOT
1176.610	3.111	1.885	0.606	Ni IV	1176.526	12.000	21.40	0.79	3.16	1	PHOT
1176.953	1.066	2.981	0.468	Ni V	1176.864	12.000	22.67	0.27	3.07	1	PHOT
1177.060	1.005	7.691	0.638	N III	1176.962	12.000	24.96	0.26	3.07	1	PHOT
				Ni VI	1176.966	12.000	23.94	0.26	3.07	1	PHOT
				Al V	1176.970	88.000	22.92	0.26	22.41	1	PHOT
				Fe IV	1176.973	1.200	22.16	0.26	0.40	1	PHOT
1177.144	1.097	1.534	0.381	N IV	1177.047	12.000	24.71	0.28	3.07	1	PHOT
				Ni VI	1177.055	12.000	22.67	0.28	3.07	1	PHOT
1179.021	1.229	12.057	0.563	Ni V	1178.919	12.000	25.94	0.31	3.07	1	PHOT
				Ni V	1178.935	12.000	21.87	0.31	3.07	1	PHOT
1179.367	2.775	6.506	1.027	P III	1179.266	1.200	25.68	0.71	0.77	1	PHOT
				O IV	1179.270	120.000	24.66	0.71	30.51	1	PHOT
1179.493	3.816	6.120	1.091	N III	1179.398	12.000	24.15	0.97	3.20	1	PHOT
1180.092	1.155	2.177	0.425	Al III	1180.000	8800.000	23.37	0.29	2235.57	1	PHOT
				Fe IV	1180.005	1.200	22.10	0.29	0.42	1	PHOT
				Ni V	1180.005	12.000	22.10	0.29	3.06	1	PHOT
				Ge IV	1180.010	88.000	20.83	0.29	22.36	1	PHOT
				O IV	1180.010	88.000	20.83	0.29	22.36	1	PHOT
1180.766	2.487	3.997	0.662	O IV	1180.660	88.000	26.92	0.63	22.35	1	PHOT
1182.089	0.681	7.389	0.585	Ni V	1182.001	12.000	22.32	0.17	3.05	1	PHOT
1182.658	2.550	2.541	0.641	O IV	1182.567	12.000	23.07	0.65	3.11	1	PHOT
				O III	1182.575	8.900	21.04	0.65	2.35	1	PHOT
1182.956	2.019	1.132	0.290	Fe IV	1182.852	1.200	26.36	0.51	0.60	1	PHOT
				P III	1182.867	1.200	22.56	0.51	0.60	1	PHOT
1183.450	1.530	3.012	0.502	S IV	1183.352	12.000	24.83	0.39	3.06	1	PHOT
				Ni IV	1183.365	12.000	21.53	0.39	3.06	1	PHOT
1186.043	1.132	2.782	0.484	Ni V	1185.950	13.000	23.51	0.29	3.30	1	PHOT

Table A.1: Continued.

$\lambda_{\rm obs}$	$\delta\lambda_{\rm obs}$	W_λ	δW_λ	Ion	$\lambda_{\rm lab}$	$\delta\lambda_{\rm lab}$	v	δv	$\delta v_{\rm tot}$	List	Origin
1186.680	1.094	3.882	0.472	Fe VI	1186.575	13.000	26.53	0.28	3.30	1	PHOT
1187.792	1.180	2.685	0.419	Ge IV	1187.681	13.000	28.02	0.30	3.29	1	PHOT
1188.137	1.507	1.869	0.402	N IV	1188.040	89.000	24.48	0.38	22.46	1	PHOT
1189.115	0.192	22.980	0.478	Ge IV	1189.028	13.000	21.94	0.05	3.28	1	PHOT
1189.647	0.800	5.326	0.517	Fe VI	1189.546	13.000	25.45	0.20	3.28	1	PHOT
				S IV	1189.550	13.000	24.45	0.20	3.28	1	PHOT
				Ni V	1189.561	13.000	21.67	0.20	3.28	1	PHOT
1190.231	0.729	2.683	0.352	S III	1190.191	0.000	10.08	0.18	0.18	4	ISM2
1190.451	0.128	38.444	0.455	Si II	1190.416	0.890	8.81	0.03	0.23	1	ISM2
1190.495	0.150	18.389	0.367	Si II	1190.416	0.890	19.90	0.04	0.23	1	ISM1
				N III	1190.390	130.000	26.44	0.04	32.74	1	PHOT
				Ni VI	1190.391	0.000	26.19	0.04	0.04	2	PHOT
				Ni VI	1190.397	13.000	24.68	0.04	3.27	1	PHOT
1192.092	0.570	11.621	0.585	S IV	1191.993	13.000	24.90	0.14	3.27	1	PHOT
				O III	1191.995	1.300	24.40	0.14	0.36	1	PHOT
				Al III	1192.000	9000.000	23.14	0.14	2263.36	1	PHOT
1192.999	2.434	3.794	0.654	O IV	1192.900	90.000	24.88	0.61	22.62	1	PHOT
				Fe V	1192.909	11.000	22.62	0.61	2.83	1	PHOT
1193.165	3.278	1.990	0.547	Ni V	1193.074	13.000	22.87	0.82	3.37	1	PHOT
1193.325	0.135	46.295	0.479	Si II	1193.290	0.900	8.79	0.03	0.23	1	ISM2
1193.368	0.141	25.670	0.407	Si II	1193.290	0.900	19.60	0.04	0.23	1	ISM1
1194.252	0.581	6.483	0.414	P V	1194.157	9.000	23.85	0.15	2.26	1	PHOT
1194.638	2.687	2.348	0.500	Fe V	1194.542	12.000	24.09	0.67	3.09	1	PHOT
1195.285	1.299	1.920	0.284	Ni V	1195.186	13.000	24.83	0.33	3.28	1	PHOT
				Fe V	1195.187	12.000	24.58	0.33	3.03	1	PHOT
1196.327	1.447	2.258	0.453	Fe V	1196.248	12.000	19.80	0.36	3.03	1	PHOT
1197.380	1.347	2.446	0.399	Ni V	1197.276	0.000	26.04	0.34	0.34	2	PHOT
1197.536	1.262	0.953	0.290	Fe V	1197.443	12.000	23.28	0.32	3.02	1	PHOT
1199.581	0.299	16.508	0.551	N I	1199.550	0.130	7.75	0.07	0.08	1	ISM2
1199.626	0.133	35.063	0.478	N I	1199.550	0.130	18.99	0.03	0.05	1	ISM1
1200.257	0.342	14.825	0.516	N I	1200.223	0.130	8.49	0.09	0.09	1	ISM2
1200.301	0.129	30.336	0.403	N I	1200.223	0.130	19.48	0.03	0.05	1	ISM1
1200.602	1.698	3.798	0.704	Al V	1200.515	13.000	21.73	0.42	3.27	1	PHOT
1200.605	1.501	3.526	0.633	Al V	1200.515	13.000	22.47	0.37	3.27	1	PHOT
				Ni VI	1200.521	13.000	20.98	0.37	3.27	1	PHOT
1200.656	2.416	1.726	0.515	Al V	1200.565	13.000	22.72	0.60	3.30	1	PHOT
1200.746	0.786	8.548	0.603	N I	1200.710	0.130	8.99	0.20	0.20	1	ISM2
1200.787	0.180	20.561	0.433	N I	1200.710	0.130	19.23	0.04	0.06	1	ISM1
1201.383	0.808	1.305	0.183	Ni IV	1201.298	13.000	21.21	0.20	3.25	1	PHOT
1201.899	1.617	3.592	0.516	Ni IV	1201.808	13.000	22.70	0.40	3.27	1	PHOT
1202.036	0.780	6.454	0.493	Ni VI	1201.956	13.000	19.95	0.19	3.25	1	PHOT
1202.136	1.411	2.387	0.453	Ni V	1202.029	13.000	26.69	0.35	3.26	1	PHOT
1202.518	0.973	2.651	0.401	Ni V	1202.413	13.000	26.18	0.24	3.25	1	PHOT
				Ni V	1202.432	13.000	21.44	0.24	3.25	1	PHOT
				P IV	1202.433	1.300	21.19	0.24	0.40	1	PHOT

Table A.1: Continued.

$\lambda_{\rm obs}$	$\delta\lambda_{\rm obs}$	W_λ	δW_λ	Ion	$\lambda_{\rm lab}$	$\delta\lambda_{\rm lab}$	v	δv	$\delta v_{\rm tot}$	List	Origin
				P IV	1202.433	1.300	21.19	0.24	0.40	1	PHOT
1202.992	2.940	3.697	0.644	O IV	1202.900	92.000	22.93	0.73	22.94	1	PHOT
				Fe V	1202.902	12.000	22.43	0.73	3.08	1	PHOT
1203.581	1.528	1.000	0.303	Ni VI	1203.472	13.000	27.15	0.38	3.26	1	PHOT
1203.872	1.557	3.635	0.299	Ni V	1203.765	13.000	26.65	0.39	3.26	1	PHOT
				Ni VI	1203.771	13.000	25.15	0.39	3.26	1	PHOT
				Ni V	1203.776	0.000	23.91	0.39	0.39	2	PHOT
1204.815	1.140	1.023	0.271	Fe IV	1204.714	1.300	25.13	0.28	0.43	1	PHOT
				Al IV	1204.726	13.000	22.15	0.28	3.25	1	PHOT
				S IV	1204.726	13.000	22.15	0.28	3.25	1	PHOT
1205.231	2.002	3.532	0.583	Ni VI	1205.145	13.000	21.39	0.50	3.27	1	PHOT
1205.389	2.166	2.511	0.566	Ni V	1205.303	13.000	21.39	0.54	3.28	1	PHOT
1205.536	1.743	3.135	0.569	Ni VI	1205.432	13.000	25.86	0.43	3.26	1	PHOT
				Ni V	1205.447	13.000	22.13	0.43	3.26	1	PHOT
1206.534	0.126	32.199	0.501	Si III	1206.500	1.300	8.45	0.03	0.32	1	ISM2
1206.592	1.448	10.805	0.847	Si III	1206.500	1.300	22.86	0.36	0.48	1	PHOT
1215.411	0.285	75.060	1.197	D I	1215.338	0.000	18.11	0.07	0.07	3	ISM1
1222.196	1.935	2.033	0.381	Fe V	1222.107	8.400	21.83	0.47	2.11	1	PHOT
1223.269	1.533	3.485	0.309	O III	1223.165	1.300	25.49	0.38	0.49	1	PHOT
1225.852	1.183	2.794	0.220	O III	1225.764	1.300	21.52	0.29	0.43	1	PHOT
				P VI	1225.767	13.000	20.79	0.29	3.19	1	PHOT
1227.534	2.539	3.056	0.590	Al V	1227.430	95.000	25.40	0.62	23.21	1	PHOT
1227.635	0.290	8.521	0.333	Fe V	1227.530	12.000	25.64	0.07	2.93	1	PHOT
				S IV	1227.542	13.000	22.71	0.07	3.18	1	PHOT
				Fe IV	1227.547	9.500	21.49	0.07	2.32	1	PHOT
1228.701	1.737	1.342	0.306	Fe V	1228.599	12.000	24.89	0.42	2.96	1	PHOT
				N IV	1228.604	13.000	23.67	0.42	3.20	1	PHOT
				Fe VI	1228.605	13.000	23.43	0.42	3.20	1	PHOT
				O IV	1228.610	130.000	22.20	0.42	31.72	1	PHOT
				N III	1228.613	13.000	21.47	0.42	3.20	1	PHOT
1229.507	1.417	2.758	0.357	S IV	1229.409	13.000	23.90	0.35	3.19	1	PHOT
1229.938	0.152	17.270	0.312	Ge IV	1229.840	13.000	23.89	0.04	3.17	1	PHOT
1230.541	1.624	3.219	0.487	Ni V	1230.435	13.000	25.83	0.40	3.19	1	PHOT
				N IV	1230.445	13.000	23.39	0.40	3.19	1	PHOT
				Fe IV	1230.454	1.300	21.20	0.40	0.51	1	PHOT
1232.622	1.101	2.773	0.347	Ni V	1232.524	14.000	23.84	0.27	3.42	1	PHOT
1232.905	0.687	3.833	0.300	Ni V	1232.807	14.000	23.83	0.17	3.41	1	PHOT
				Ni IV	1232.818	14.000	21.16	0.17	3.41	1	PHOT
1233.073	1.305	2.547	0.327	Ni V	1232.964	14.000	26.50	0.32	3.42	1	PHOT
				Fe V	1232.970	8.600	25.04	0.32	2.11	1	PHOT
1233.236	1.874	1.701	0.338	O III	1233.126	1.400	26.74	0.46	0.57	1	PHOT
				Fe V	1233.144	12.000	22.37	0.46	2.95	1	PHOT
1233.378	1.320	3.391	0.404	S I	1233.345	0.960	8.02	0.32	0.40	1	ISM2
1233.426	1.499	2.633	0.379	S I	1233.345	0.960	19.69	0.36	0.43	1	ISM1
				N III	1233.330	96.000	23.34	0.36	23.34	1	PHOT

Table A.1: Continued.

λ_{obs}	$\delta\lambda_{obs}$	W_λ	δW_λ	Ion	λ_{lab}	$\delta\lambda_{lab}$	v	δv	δv_{tot}	List	Origin
1234.040	2.414	2.502	0.306	Fe V	1233.933	12.000	26.00	0.59	2.97	1	PHOT
				O III	1233.944	1.400	23.32	0.59	0.68	1	PHOT
1234.194	1.425	1.455	0.325	Ni V	1234.103	14.000	22.06	0.35	3.42	1	PHOT
1234.493	1.777	2.071	0.253	Ni V	1234.393	14.000	24.29	0.43	3.43	1	PHOT
				Al V	1234.400	140.000	22.59	0.43	34.00	1	PHOT
				Si III	1234.406	1.400	21.13	0.43	0.55	1	PHOT
1234.741	0.691	4.033	0.347	P IV	1234.640	9.700	24.52	0.17	2.36	1	PHOT
				Fe V	1234.647	8.600	22.82	0.17	2.09	1	PHOT
1235.936	0.527	5.357	0.302	Ni V	1235.831	14.000	25.47	0.13	3.40	1	PHOT
1236.376	1.034	2.473	0.297	Ni VI	1236.270	14.000	25.70	0.25	3.40	1	PHOT
				Ni V	1236.276	14.000	24.25	0.25	3.40	1	PHOT
				Ni V	1236.277	14.000	24.01	0.25	3.40	1	PHOT
				Ni V	1236.290	14.000	20.85	0.25	3.40	1	PHOT
1236.806	2.080	1.227	0.300	Ni V	1236.702	14.000	25.21	0.50	3.43	1	PHOT
				Ni V	1236.710	0.000	23.27	0.50	0.50	2	PHOT
				O III	1236.715	1.400	22.06	0.50	0.61	1	PHOT
				O III	1236.718	1.400	21.33	0.50	0.61	1	PHOT
				S IV	1236.718	14.000	21.33	0.50	3.43	1	PHOT
1237.303	2.036	2.451	0.429	Ni V	1237.201	14.000	24.72	0.49	3.43	1	PHOT
				Ni V	1237.204	14.000	23.99	0.49	3.43	1	PHOT
				N IV	1237.212	14.000	22.05	0.49	3.43	1	PHOT
1238.809	1.837	1.057	0.207	Ni V	1238.703	14.000	25.65	0.44	3.42	1	PHOT
				Ni V	1238.706	14.000	24.93	0.44	3.42	1	PHOT
				S IV	1238.717	14.000	22.27	0.44	3.42	1	PHOT
1238.919	0.204	42.135	0.464	Ni IV	1238.812	14.000	25.89	0.05	3.39	1	PHOT
				N V	1238.821	14.000	23.72	0.05	3.39	1	PHOT
1239.653	1.546	1.292	0.273	Ni V	1239.552	14.000	24.43	0.37	3.41	1	PHOT
1240.514	1.331	1.408	0.262	Fe V	1240.410	8.700	25.14	0.32	2.13	1	PHOT
				N III	1240.419	14.000	22.96	0.32	3.40	1	PHOT
				Fe IV	1240.423	9.700	21.99	0.32	2.37	1	PHOT
1240.709	1.944	1.444	0.300	Al V	1240.600	140.000	26.34	0.47	33.83	1	PHOT
				N IV	1240.612	14.000	23.44	0.47	3.42	1	PHOT
1240.973	1.788	2.985	0.460	Al IV	1240.861	14.000	27.06	0.43	3.41	1	PHOT
1241.147	1.734	2.880	0.426	Ni V	1241.047	14.000	24.16	0.42	3.41	1	PHOT
				Ni V	1241.052	14.000	22.95	0.42	3.41	1	PHOT
1241.430	1.522	1.724	0.351	Ni V	1241.319	14.000	26.81	0.37	3.40	1	PHOT
1241.531	1.227	3.746	0.409	Ni V	1241.422	14.000	26.32	0.30	3.39	1	PHOT
				O IV	1241.430	98.000	24.39	0.30	23.67	1	PHOT
				Fe V	1241.442	8.700	21.49	0.30	2.12	1	PHOT
1241.736	0.728	3.704	0.328	Ni V	1241.627	14.000	26.32	0.18	3.38	1	PHOT
				N IV	1241.644	14.000	22.21	0.18	3.38	1	PHOT
1242.083	1.573	1.418	0.201	Ni V	1241.972	14.000	26.79	0.38	3.40	1	PHOT
				Ni VI	1241.974	14.000	26.31	0.38	3.40	1	PHOT
1242.180	0.589	3.080	0.288	Ni V	1242.071	14.000	26.31	0.14	3.38	1	PHOT
				N III	1242.076	14.000	25.10	0.14	3.38	1	PHOT

Table A.1: Continued.

λ_{obs}	$\delta\lambda_{\mathrm{obs}}$	W_λ	δW_λ	Ion	λ_{lab}	$\delta\lambda_{\mathrm{lab}}$	v	δv	δv_{tot}	List	Origin
				Fe IV	1242.089	1.400	21.96	0.14	0.37	1	PHOT
				N III	1242.093	14.000	21.00	0.14	3.38	1	PHOT
1242.449	2.476	3.766	0.538	Fe V	1242.343	12.000	25.58	0.60	2.96	1	PHOT
				Fe V	1242.352	12.000	23.41	0.60	2.96	1	PHOT
1242.905	0.117	54.372	0.344	N V	1242.804	14.000	24.36	0.03	3.38	1	PHOT
1243.329	1.576	1.294	0.265	O IV	1243.220	140.000	26.28	0.38	33.76	1	PHOT
				Fe V	1243.228	8.700	24.36	0.38	2.13	1	PHOT
				N IV	1243.232	14.000	23.39	0.38	3.40	1	PHOT
1243.606	1.290	3.886	0.232	Ni V	1243.504	14.000	24.59	0.31	3.39	1	PHOT
1243.766	1.008	2.070	0.171	Ni V	1243.662	0.000	25.07	0.24	0.24	2	PHOT
				Ni VI	1243.665	14.000	24.35	0.24	3.38	1	PHOT
1244.286	0.162	17.715	0.272	Fe V	1244.182	12.000	25.06	0.04	2.89	1	PHOT
1245.059	1.030	2.074	0.307	Ni V	1244.958	14.000	24.32	0.25	3.38	1	PHOT
				Ni V	1244.969	14.000	21.67	0.25	3.38	1	PHOT
1245.169	1.268	2.689	0.366	O IV	1245.060	98.000	26.25	0.31	23.60	1	PHOT
				Ni V	1245.065	14.000	25.04	0.31	3.38	1	PHOT
				Ni V	1245.074	14.000	22.87	0.31	3.38	1	PHOT
1245.283	0.713	5.431	0.367	Ni V	1245.176	14.000	25.76	0.17	3.37	1	PHOT
				Ni IV	1245.178	14.000	25.28	0.17	3.37	1	PHOT
				O IV	1245.195	14.000	21.19	0.17	3.37	1	PHOT
1245.553	1.080	2.341	0.319	O III	1245.449	9.800	25.03	0.26	2.37	1	PHOT
				O IV	1245.454	14.000	23.83	0.26	3.38	1	PHOT
1245.637	1.604	1.198	0.292	Ni IV	1245.543	14.000	22.63	0.39	3.39	1	PHOT
				Fe IV	1245.545	1.400	22.14	0.39	0.51	1	PHOT
1245.729	0.984	1.568	0.173	Ni IV	1245.620	14.000	26.23	0.24	3.38	1	PHOT
1246.645	1.358	0.755	0.210	Ni V	1246.547	14.000	23.57	0.33	3.38	1	PHOT
1246.919	2.866	1.975	0.381	Ni V	1246.808	14.000	26.69	0.69	3.44	1	PHOT
				Ni V	1246.821	14.000	23.56	0.69	3.44	1	PHOT
1247.206	1.065	1.098	0.143	S I	1247.134	0.980	17.31	0.26	0.35	1	ISM1
				S I	1247.160	0.980	11.06	0.26	0.35	1	ISM2
				P IV	1247.113	1.400	22.36	0.26	0.42	1	PHOT
				Fe IV	1247.119	1.400	20.91	0.26	0.42	1	PHOT
1247.481	0.619	8.986	0.356	C III	1247.383	1.400	23.55	0.15	0.37	1	PHOT
				N IV	1247.388	14.000	22.35	0.15	3.37	1	PHOT
1247.707	1.368	1.853	0.283	N III	1247.601	14.000	25.47	0.33	3.38	1	PHOT
1248.146	2.301	2.323	0.389	Ni V	1248.065	14.000	19.46	0.55	3.41	1	PHOT
1248.595	1.776	1.312	0.321	Ni V	1248.489	14.000	25.45	0.43	3.39	1	PHOT
				Ni V	1248.499	14.000	23.05	0.43	3.39	1	PHOT
1249.631	0.493	5.285	0.315	Ni V	1249.522	14.000	26.15	0.12	3.36	1	PHOT
1250.146	0.936	3.776	0.213	Ni VI	1250.039	14.000	25.66	0.22	3.36	1	PHOT
				Fe IV	1250.045	1.400	24.22	0.22	0.40	1	PHOT
				Ni V	1250.047	14.000	23.74	0.22	3.36	1	PHOT
1250.449	6.656	2.219	0.645	Ni V	1250.344	14.000	25.18	1.60	3.72	1	PHOT
1250.498	0.415	10.370	0.514	Ni V	1250.388	14.000	26.37	0.10	3.36	1	PHOT
				Ni V	1250.403	14.000	22.78	0.10	3.36	1	PHOT

Table A.1: Continued.

$\lambda_{\rm obs}$	$\delta\lambda_{\rm obs}$	W_λ	δW_λ	Ion	$\lambda_{\rm lab}$	$\delta\lambda_{\rm lab}$	v	δv	$\delta v_{\rm tot}$	List	Origin
1250.621	1.051	1.762	0.277	S II	1250.578	0.000	10.31	0.25	0.25	4	ISM2
				N III	1250.519	14.000	24.45	0.25	3.37	1	PHOT
1250.661	0.759	2.294	0.268	S II	1250.578	0.000	19.90	0.18	0.18	4	ISM1
				Ni VI	1250.572	14.000	21.34	0.18	3.36	1	PHOT
1250.833	1.132	3.307	0.348	Fe V	1250.736	8.800	23.25	0.27	2.13	1	PHOT
1250.834	0.909	2.939	0.282	Fe V	1250.736	8.800	23.49	0.22	2.12	1	PHOT
1251.130	1.796	1.276	0.268	Fe V	1251.035	8.900	22.77	0.43	2.18	1	PHOT
				Ni V	1251.038	0.000	22.05	0.43	0.43	2	PHOT
1251.934	0.375	7.668	0.309	Fe V	1251.845	13.000	21.31	0.09	3.11	1	PHOT
1252.269	0.443	5.779	0.321	Ni V	1252.183	14.000	20.59	0.11	3.35	1	PHOT
1252.376	1.221	1.601	0.297	Ni V	1252.267	14.000	26.09	0.29	3.36	1	PHOT
				Ni IV	1252.271	14.000	25.14	0.29	3.36	1	PHOT
1252.874	0.434	12.285	0.250	Ni V	1252.765	14.000	26.08	0.10	3.35	1	PHOT
				Fe VI	1252.769	14.000	25.13	0.10	3.35	1	PHOT
1253.108	2.600	1.482	0.363	Ni V	1252.999	0.000	26.08	0.62	0.62	2	PHOT
				Ni V	1253.012	14.000	22.97	0.62	3.41	1	PHOT
1253.307	1.189	2.559	0.336	Ni IV	1253.196	14.000	26.55	0.28	3.36	1	PHOT
				Ni V	1253.196	14.000	26.55	0.28	3.36	1	PHOT
				Al V	1253.197	14.000	26.31	0.28	3.36	1	PHOT
				Ni V	1253.205	0.000	24.40	0.28	0.28	2	PHOT
				P IV	1253.218	1.400	21.29	0.28	0.44	1	PHOT
1253.601	1.230	2.436	0.334	Ni V	1253.489	14.000	26.79	0.29	3.36	1	PHOT
				Ni V	1253.511	14.000	21.52	0.29	3.36	1	PHOT
1253.767	0.497	4.174	0.291	Fe VI	1253.675	14.000	22.00	0.12	3.35	1	PHOT
				Fe IV	1253.677	1.400	21.52	0.12	0.36	1	PHOT
1253.843	0.585	2.195	0.236	S II	1253.805	0.000	9.09	0.14	0.14	4	ISM2
				Ni VI	1253.739	14.000	24.87	0.14	3.35	1	PHOT
1253.895	0.422	3.155	0.238	S II	1253.805	0.000	21.52	0.10	0.10	4	ISM1
				Fe IV	1253.808	0.000	20.80	0.10	0.10	2	PHOT
1253.965	0.768	2.072	0.248	Fe V	1253.870	13.000	22.71	0.18	3.11	1	PHOT
1254.095	0.553	7.984	0.337	N III	1254.000	100.000	22.71	0.13	23.91	1	PHOT
				Ni IV	1254.000	14.000	22.71	0.13	3.35	1	PHOT
				Fe V	1254.005	13.000	21.52	0.13	3.11	1	PHOT
1254.300	1.221	1.905	0.278	Ni V	1254.191	14.000	26.05	0.29	3.36	1	PHOT
				O III	1254.195	1.400	25.10	0.29	0.44	1	PHOT
1254.526	1.338	5.220	0.254	Ni V	1254.417	14.000	26.05	0.32	3.36	1	PHOT
				Ni V	1254.419	14.000	25.57	0.32	3.36	1	PHOT
				Ni V	1254.422	14.000	24.85	0.32	3.36	1	PHOT
1254.860	1.991	1.347	0.186	Fe V	1254.752	13.000	25.80	0.48	3.14	1	PHOT
1255.838	1.933	1.478	0.337	Ni IV	1255.737	14.000	24.11	0.46	3.37	1	PHOT
				Fe IV	1255.740	1.400	23.40	0.46	0.57	1	PHOT
				Ni V	1255.743	14.000	22.68	0.46	3.37	1	PHOT
1255.906	2.557	1.235	0.366	Ni V	1255.799	14.000	25.54	0.61	3.40	1	PHOT
				Ni V	1255.814	0.000	21.96	0.61	0.61	2	PHOT
1256.134	2.146	1.070	0.313	Fe IV	1256.025	1.400	26.02	0.51	0.61	1	PHOT

Table A.1: Continued.

λ_{obs}	$\delta\lambda_{obs}$	W_λ	δW_λ	Ion	λ_{lab}	$\delta\lambda_{lab}$	v	δv	δv_{tot}	List	Origin
1257.014	1.635	2.267	0.229	Ni V	1256.905	14.000	26.00	0.39	3.36	1	PHOT
				O IV	1256.910	140.000	24.81	0.39	33.39	1	PHOT
				P III	1256.922	1.400	21.94	0.39	0.51	1	PHOT
1257.735	0.242	11.102	0.278	Al IV	1257.624	14.000	26.46	0.06	3.34	1	PHOT
				Ni V	1257.626	14.000	25.98	0.06	3.34	1	PHOT
1258.117	1.022	2.494	0.277	Fe VI	1258.021	14.000	22.88	0.24	3.34	1	PHOT
1258.645	1.602	0.798	0.219	Ni V	1258.539	14.000	25.25	0.38	3.36	1	PHOT
1258.899	0.785	2.490	0.251	Fe V	1258.791	9.000	25.72	0.19	2.15	1	PHOT
1259.232	1.236	1.441	0.253	N III	1259.130	14.000	24.29	0.29	3.35	1	PHOT
1259.551	0.455	4.395	0.296	S II	1259.518	0.000	7.85	0.11	0.11	4	ISM2
				Fe V	1259.457	13.000	22.38	0.11	3.10	1	PHOT
1259.597	0.361	3.416	0.250	S II	1259.518	0.000	18.80	0.09	0.09	4	ISM1
1259.681	1.474	1.401	0.303	Ni VI	1259.582	14.000	23.56	0.35	3.35	1	PHOT
				Ni V	1259.587	14.000	22.37	0.35	3.35	1	PHOT
1259.830	1.163	2.373	0.333	Ni V	1259.722	14.000	25.70	0.28	3.34	1	PHOT
				Ni VI	1259.725	14.000	24.99	0.28	3.34	1	PHOT
				O IV	1259.730	140.000	23.80	0.28	33.32	1	PHOT
1260.456	0.136	56.915	0.428	Si II	1260.422	1.000	8.09	0.03	0.24	1	ISM2
1260.503	0.117	34.968	0.386	Si II	1260.422	1.000	19.27	0.03	0.24	1	ISM1
1261.444	0.477	3.642	0.253	Ni IV	1261.354	14.000	21.39	0.11	3.33	1	PHOT
1261.545	1.280	2.042	0.286	Ni V	1261.449	14.000	22.82	0.30	3.34	1	PHOT
1261.859	0.305	7.080	0.255	Ni VI	1261.756	0.000	24.47	0.07	0.07	2	PHOT
				Ni V	1261.760	14.000	23.52	0.07	3.33	1	PHOT
				Fe V	1261.761	13.000	23.28	0.07	3.09	1	PHOT
				O VI	1261.766	0.000	22.10	0.07	0.07	2	PHOT
1262.650	1.788	0.932	0.242	Ni V	1262.539	14.000	26.36	0.42	3.35	1	PHOT
				Al IV	1262.543	14.000	25.41	0.42	3.35	1	PHOT
				Ni V	1262.550	14.000	23.74	0.42	3.35	1	PHOT
1263.448	1.549	1.554	0.316	Fe V	1263.336	13.000	26.58	0.37	3.11	1	PHOT
				Fe V	1263.346	13.000	24.20	0.37	3.11	1	PHOT
1264.531	2.232	1.574	0.364	S IV	1264.418	14.000	26.79	0.53	3.36	1	PHOT
1264.635	0.201	15.447	0.313	Ni V	1264.529	14.000	25.13	0.05	3.32	1	PHOT
1265.036	1.454	1.126	0.272	O III	1264.929	1.400	25.36	0.34	0.48	1	PHOT
				Ni V	1264.931	14.000	24.89	0.34	3.34	1	PHOT
				Ni V	1264.937	14.000	23.46	0.34	3.34	1	PHOT
				Fe V	1264.945	13.000	21.57	0.34	3.10	1	PHOT
1265.769	0.442	2.862	0.221	N IV	1265.664	14.000	24.87	0.10	3.32	1	PHOT
				Ni V	1265.671	14.000	23.21	0.10	3.32	1	PHOT
				O IV	1265.677	14.000	21.79	0.10	3.32	1	PHOT
				Ni VI	1265.679	14.000	21.32	0.10	3.32	1	PHOT
1265.826	0.465	2.684	0.220	Ni V	1265.725	14.000	23.92	0.11	3.32	1	PHOT
				Ni IV	1265.728	14.000	23.21	0.11	3.32	1	PHOT
1266.193	1.645	1.523	0.274	Ni IV	1266.094	14.000	23.44	0.39	3.34	1	PHOT
				Fe VI	1266.103	14.000	21.31	0.39	3.34	1	PHOT
1266.506	0.272	9.608	0.265	Ni V	1266.408	14.000	23.20	0.06	3.31	1	PHOT

Table A.1: Continued.

$\lambda_{\rm obs}$	$\delta\lambda_{\rm obs}$	W_λ	δW_λ	Ion	$\lambda_{\rm lab}$	$\delta\lambda_{\rm lab}$	v	δv	$\delta v_{\rm tot}$	List	Origin
				Fe V	1266.418	13.000	20.83	0.06	3.08	1	PHOT
1266.969	0.709	3.182	0.282	Fe IV	1266.865	1.400	24.61	0.17	0.37	1	PHOT
				Ni V	1266.876	14.000	22.01	0.17	3.32	1	PHOT
1267.402	0.590	6.276	0.356	Fe V	1267.289	13.000	26.73	0.14	3.08	1	PHOT
				Ni V	1267.291	14.000	26.26	0.14	3.31	1	PHOT
				Ni V	1267.307	14.000	22.47	0.14	3.31	1	PHOT
1267.910	0.602	4.551	0.316	Ni V	1267.802	14.000	25.54	0.14	3.31	1	PHOT
1267.973	1.360	1.272	0.276	Ni V	1267.875	0.000	23.17	0.32	0.32	2	PHOT
1268.990	1.522	2.397	0.334	Ni V	1268.873	14.000	27.64	0.36	3.33	2	PHOT
1269.481	1.117	2.237	0.278	Fe V	1269.374	13.000	25.27	0.26	3.08	1	PHOT
				Fe V	1269.380	9.100	23.85	0.26	2.17	1	PHOT
				Ni V	1269.387	14.000	22.20	0.26	3.32	1	PHOT
				S V	1269.392	14.000	21.02	0.26	3.32	1	PHOT
1270.320	2.027	2.611	0.354	Fe IV	1270.210	1.400	25.96	0.48	0.58	1	PHOT
				N III	1270.214	14.000	25.02	0.48	3.34	1	PHOT
				O III	1270.231	1.400	21.01	0.48	0.58	1	PHOT
1270.564	1.433	1.153	0.236	Fe V	1270.472	9.100	21.71	0.34	2.17	1	PHOT
1270.791	0.295	8.832	0.281	Ni V	1270.677	14.000	26.90	0.07	3.30	1	PHOT
1271.362	1.624	1.390	0.197	Ni V	1271.275	14.000	20.52	0.38	3.32	1	PHOT
1272.156	0.814	6.891	0.400	Fe VI	1272.066	14.000	21.21	0.19	3.30	1	PHOT
1272.294	1.576	2.099	0.221	O IV	1272.210	100.000	19.79	0.37	23.57	1	PHOT
1273.070	0.677	3.189	0.262	N III	1272.961	14.000	25.67	0.16	3.30	1	PHOT
				N IV	1272.963	14.000	25.20	0.16	3.30	1	PHOT
1273.310	0.309	9.912	0.281	Ni V	1273.204	14.000	24.96	0.07	3.30	1	PHOT
				Fe IV	1273.211	1.400	23.31	0.07	0.34	1	PHOT
1273.923	0.563	3.732	0.252	Ni V	1273.827	14.000	22.59	0.13	3.30	1	PHOT
1274.366	0.920	2.699	0.173	Ni V	1274.264	14.000	24.00	0.22	3.30	1	PHOT
				Fe V	1274.265	13.000	23.76	0.22	3.07	1	PHOT
1276.533	0.500	4.468	0.293	Ni V	1276.428	15.000	24.66	0.12	3.52	1	PHOT
				P IV	1276.441	1.500	21.61	0.12	0.37	1	PHOT
1276.977	1.730	1.769	0.319	Fe VI	1276.877	15.000	23.48	0.41	3.54	1	PHOT
1277.052	0.208	10.931	0.254	Ni V	1276.958	15.000	22.07	0.05	3.52	1	PHOT
1277.224	1.500	1.343	0.255	Fe V	1277.139	13.000	19.95	0.35	3.07	1	PHOT
1277.281	1.458	1.211	0.159	C I	1277.245	1.500	8.45	0.34	0.49	1	ISM2
				Ni V	1277.170	15.000	26.06	0.34	3.54	1	PHOT
				O III	1277.170	100.000	26.06	0.34	23.47	1	PHOT
				Si VI	1277.190	150.000	21.36	0.34	35.21	1	PHOT
1278.285	3.432	2.226	0.261	Ni VI	1278.195	15.000	21.11	0.80	3.61	1	PHOT
1278.387	2.135	0.931	0.254	Fe VI	1278.292	15.000	22.28	0.50	3.55	1	PHOT
1279.431	0.556	7.960	0.236	O IV	1279.314	15.000	27.42	0.13	3.52	1	PHOT
1279.692	1.969	2.233	0.374	Fe V	1279.592	9.300	23.43	0.46	2.23	1	PHOT
1279.819	0.427	5.668	0.299	Ni V	1279.720	15.000	23.19	0.10	3.52	1	PHOT
1280.213	0.888	5.529	0.247	C I	1280.135	1.500	18.27	0.21	0.41	1	ISM1
				Ni V	1280.115	15.000	22.95	0.21	3.52	1	PHOT
1280.569	0.518	8.912	0.236	Fe V	1280.470	9.300	23.18	0.12	2.18	1	PHOT

Table A.1: Continued.

$\lambda_{\rm obs}$	$\delta\lambda_{\rm obs}$	W_λ	δW_λ	Ion	$\lambda_{\rm lab}$	$\delta\lambda_{\rm lab}$	v	δv	$\delta v_{\rm tot}$	List	Origin
1281.468	1.403	4.421	0.237	Fe IV	1281.364	1.500	24.33	0.33	0.48	1	PHOT
				Fe V	1281.368	9.300	23.40	0.33	2.20	1	PHOT
1282.155	1.299	1.108	0.231	Fe V	1282.060	9.300	22.21	0.30	2.20	1	PHOT
1282.306	0.915	2.705	0.274	Al V	1282.200	150.000	24.78	0.21	35.07	1	PHOT
				Ni V	1282.201	15.000	24.55	0.21	3.51	1	PHOT
				N III	1282.210	100.000	22.45	0.21	23.38	1	PHOT
1282.381	0.805	2.264	0.247	Ni V	1282.270	15.000	25.95	0.19	3.51	1	PHOT
1282.556	1.881	1.830	0.357	Ni IV	1282.443	15.000	26.42	0.44	3.53	1	PHOT
				Fe VI	1282.452	15.000	24.31	0.44	3.53	1	PHOT
				O III	1282.458	1.500	22.91	0.44	0.56	1	PHOT
				N IV	1282.460	100.000	22.44	0.44	23.38	1	PHOT
1282.836	1.071	4.585	0.392	Ni V	1282.724	15.000	26.18	0.25	3.51	1	PHOT
				O IV	1282.740	150.000	22.44	0.25	35.06	1	PHOT
				Ni V	1282.742	15.000	21.97	0.25	3.51	1	PHOT
1283.291	1.563	3.461	0.439	Ni V	1283.185	15.000	24.76	0.37	3.52	1	PHOT
				Ni V	1283.201	15.000	21.03	0.37	3.52	1	PHOT
1284.209	1.618	1.792	0.324	Fe V	1284.111	9.300	22.88	0.38	2.20	1	PHOT
1284.575	0.656	3.399	0.271	N III	1284.472	15.000	24.04	0.15	3.50	1	PHOT
				Ni V	1284.475	15.000	23.34	0.15	3.50	1	PHOT
1284.665	1.477	1.620	0.276	Ni V	1284.566	15.000	23.10	0.34	3.52	1	PHOT
1285.461	0.735	3.036	0.260	Fe VI	1285.362	15.000	23.09	0.17	3.50	1	PHOT
1285.892	1.384	1.407	0.247	Fe V	1285.787	13.000	24.48	0.32	3.05	1	PHOT
				Ni V	1285.793	15.000	23.08	0.32	3.51	1	PHOT
				Fe IV	1285.796	1.500	22.38	0.32	0.48	1	PHOT
1286.012	1.003	4.044	0.202	Fe V	1285.916	9.400	22.38	0.23	2.20	1	PHOT
1286.216	1.640	1.973	0.296	Ni IV	1286.124	0.000	21.44	0.38	0.38	2	PHOT
1287.137	0.860	2.749	0.303	Fe VI	1287.028	15.000	25.39	0.20	3.50	1	PHOT
				Ni V	1287.028	15.000	25.39	0.20	3.50	1	PHOT
				Fe V	1287.046	9.400	21.20	0.20	2.20	1	PHOT
1287.214	1.280	2.427	0.340	Fe V	1287.107	9.400	24.92	0.30	2.21	1	PHOT
1287.356	2.064	1.002	0.285	Ni V	1287.243	15.000	26.32	0.48	3.53	1	PHOT
1287.670	1.112	1.417	0.261	Ni V	1287.553	15.000	27.24	0.26	3.50	1	PHOT
1287.915	1.393	0.873	0.242	Ni V	1287.808	15.000	24.91	0.32	3.51	1	PHOT
1288.264	0.673	3.638	0.299	Fe V	1288.172	9.400	21.41	0.16	2.19	1	PHOT
1289.634	3.167	3.482	0.478	Fe V	1289.536	9.400	22.78	0.74	2.31	1	PHOT
1290.141	1.273	2.754	0.300	Si III	1290.040	100.000	23.47	0.30	23.24	1	PHOT
1290.261	1.394	1.190	0.156	O IV	1290.170	150.000	21.15	0.32	34.85	1	PHOT
1290.503	1.374	1.123	0.263	Ni V	1290.398	15.000	24.39	0.32	3.50	1	PHOT
				N VI	1290.400	620.000	23.93	0.32	144.03	1	PHOT
1290.684	1.940	0.791	0.179	P IV	1290.593	11.000	21.14	0.45	2.59	1	PHOT
1291.291	0.833	4.296	0.341	S VI	1291.176	15.000	26.70	0.19	3.49	1	PHOT
				Fe V	1291.187	9.400	24.15	0.19	2.19	1	PHOT
1293.403	0.889	3.110	0.279	C V	1293.300	350.000	23.88	0.21	81.13	1	PHOT
				Fe V	1293.306	9.500	22.48	0.21	2.21	1	PHOT
1293.482	0.615	4.932	0.184	N V	1293.380	110.000	23.64	0.14	25.50	1	PHOT

Table A.1: Continued.

$\lambda_{\rm obs}$	$\delta\lambda_{\rm obs}$	W_λ	δW_λ	Ion	$\lambda_{\rm lab}$	$\delta\lambda_{\rm lab}$	v	δv	$\delta v_{\rm tot}$	List	Origin
				Fe V	1293.382	9.500	23.18	0.14	2.21	1	PHOT
1294.651	1.431	1.969	0.328	Ni V	1294.539	15.000	25.94	0.33	3.49	1	PHOT
				Si III	1294.545	1.500	24.55	0.33	0.48	1	PHOT
				Fe VI	1294.549	15.000	23.62	0.33	3.49	1	PHOT
1295.387	0.999	2.539	0.305	Ni IV	1295.298	15.000	20.60	0.23	3.48	1	PHOT
1295.911	1.386	1.798	0.304	Ni V	1295.797	0.000	26.37	0.32	0.32	2	PHOT
				Ni V	1295.813	0.000	22.67	0.32	0.32	2	PHOT
				Fe VI	1295.817	15.000	21.75	0.32	3.48	1	PHOT
				O IV	1295.820	110.000	21.05	0.32	25.45	1	PHOT
1296.715	1.183	1.965	0.175	Ni IV	1296.608	15.000	24.74	0.27	3.48	1	PHOT
1296.826	0.841	3.763	0.300	Si III	1296.726	1.500	23.12	0.19	0.40	1	PHOT
				Fe V	1296.728	14.000	22.66	0.19	3.24	1	PHOT
				Fe VI	1296.734	15.000	21.27	0.19	3.47	1	PHOT
1296.970	1.388	4.497	0.238	Fe VI	1296.872	15.000	22.65	0.32	3.48	1	PHOT
1297.644	0.573	4.621	0.269	Fe V	1297.549	9.500	21.95	0.13	2.20	1	PHOT
				O IV	1297.554	15.000	20.79	0.13	3.47	1	PHOT
1298.830	1.029	2.977	0.331	Ni V	1298.738	15.000	21.24	0.24	3.47	1	PHOT
1298.924	2.681	1.076	0.338	Ni V	1298.808	15.000	26.78	0.62	3.52	1	PHOT
				Ni VI	1298.824	15.000	23.08	0.62	3.52	1	PHOT
1299.050	2.054	7.095	0.580	Si III	1298.946	1.500	24.00	0.47	0.59	1	PHOT
				Ni V	1298.949	15.000	23.31	0.47	3.49	1	PHOT
				Ni V	1298.954	15.000	22.16	0.47	3.49	1	PHOT
1300.327	2.146	1.050	0.302	O III	1300.218	1.500	25.13	0.49	0.60	1	PHOT
				Ni V	1300.228	15.000	22.83	0.49	3.49	1	PHOT
1300.710	0.512	4.819	0.270	Fe IV	1300.594	11.000	26.74	0.12	2.54	1	PHOT
				Fe V	1300.608	9.600	23.51	0.12	2.22	1	PHOT
1300.948	2.061	1.191	0.176	N IV	1300.842	15.000	24.43	0.48	3.49	1	PHOT
				Fe V	1300.843	9.600	24.20	0.48	2.26	1	PHOT
				Fe IV	1300.856	1.500	21.20	0.48	0.59	1	PHOT
				O III	1300.856	11.000	21.20	0.48	2.58	1	PHOT
1301.085	0.379	6.278	0.262	Ni V	1300.979	15.000	24.43	0.09	3.46	1	PHOT
1301.288	2.003	4.541	0.444	Fe VI	1301.174	15.000	26.27	0.46	3.49	1	PHOT
1301.904	1.213	2.225	0.276	P II	1301.874	1.500	6.91	0.28	0.44	1	ISM2
				Fe VI	1301.800	15.000	23.95	0.28	3.47	1	PHOT
1302.201	0.151	48.377	0.441	O I	1302.168	0.150	7.60	0.03	0.05	1	ISM2
1302.250	0.149	50.356	0.468	O I	1302.168	0.150	18.88	0.03	0.05	1	ISM1
1302.491	1.310	7.304	0.312	Ni V	1302.387	0.000	23.94	0.30	0.30	2	PHOT
				O VI	1302.400	480.000	20.95	0.30	110.48	1	PHOT
1303.426	1.541	3.058	0.445	N III	1303.319	15.000	24.61	0.35	3.47	1	PHOT
				Si III	1303.323	1.500	23.69	0.35	0.49	1	PHOT
				Ni V	1303.326	15.000	23.00	0.35	3.47	1	PHOT
1303.585	0.741	2.690	0.327	Fe V	1303.487	9.600	22.54	0.17	2.21	1	PHOT
				N IV	1303.490	110.000	21.85	0.17	25.30	1	PHOT
1303.637	1.069	2.556	0.351	Fe V	1303.523	9.600	26.22	0.25	2.22	1	PHOT
				O III	1303.538	1.500	22.77	0.25	0.42	1	PHOT

Table A.1: Continued.

$\lambda_{\rm obs}$	$\delta\lambda_{\rm obs}$	W_λ	δW_λ	Ion	$\lambda_{\rm lab}$	$\delta\lambda_{\rm lab}$	v	δv	$\delta v_{\rm tot}$	List	Origin
1304.408	0.103	23.330	0.293	Si II	1304.370	1.100	8.73	0.02	0.25	1	ISM2
1304.454	0.159	11.274	0.266	Si II	1304.370	1.100	19.31	0.04	0.26	1	ISM1
1304.914	0.939	1.444	0.231	Ni V	1304.798	15.000	26.65	0.22	3.45	1	PHOT
				O III	1304.811	1.500	23.67	0.22	0.41	1	PHOT
				Fe V	1304.814	9.600	22.98	0.22	2.22	1	PHOT
1304.987	0.715	3.103	0.295	Fe V	1304.873	9.600	26.19	0.16	2.21	1	PHOT
				N III	1304.877	15.000	25.27	0.16	3.45	1	PHOT
1305.806	0.490	3.174	0.231	O III	1305.692	11.000	26.17	0.11	2.53	1	PHOT
				Ni V	1305.693	15.000	25.95	0.11	3.45	1	PHOT
				Ni V	1305.696	15.000	25.26	0.11	3.45	1	PHOT
1305.913	0.158	5.384	0.179	N IV	1305.812	15.000	23.19	0.04	3.44	1	PHOT
				N IV	1305.821	15.000	21.12	0.04	3.44	1	PHOT
1306.035	1.469	2.634	0.318	Ni VI	1305.942	15.000	21.35	0.34	3.46	1	PHOT
1306.139	0.140	4.356	0.170	Ni V	1306.035	15.000	23.87	0.03	3.44	1	PHOT
1306.184	0.409	7.790	0.319	Ni V	1306.068	15.000	26.63	0.09	3.44	1	PHOT
				C III	1306.080	110.000	23.87	0.09	25.25	1	PHOT
				Fe V	1306.080	9.600	23.87	0.09	2.21	1	PHOT
1306.344	0.490	7.749	0.215	Ni V	1306.228	15.000	26.62	0.11	3.44	1	PHOT
				Ni V	1306.233	15.000	25.48	0.11	3.44	1	PHOT
				Ni V	1306.238	15.000	24.33	0.11	3.44	1	PHOT
1306.729	0.353	17.762	0.413	Ni V	1306.624	15.000	24.09	0.08	3.44	1	PHOT
1307.527	0.493	6.266	0.325	Fe V	1307.424	9.700	23.62	0.11	2.23	1	PHOT
1307.702	0.350	10.334	0.332	Ni V	1307.603	15.000	22.70	0.08	3.44	1	PHOT
1308.756	0.840	3.341	0.189	Fe VI	1308.644	15.000	25.66	0.19	3.44	1	PHOT
1309.624	1.192	2.065	0.272	O III	1309.510	1.500	26.10	0.27	0.44	1	PHOT
				Fe V	1309.519	9.700	24.04	0.27	2.24	1	PHOT
1309.755	1.713	0.665	0.211	Ni V	1309.653	15.000	23.35	0.39	3.46	1	PHOT
1309.805	1.658	1.605	0.300	Ni V	1309.689	15.000	26.55	0.38	3.45	1	PHOT
1310.178	0.682	2.263	0.235	O III	1310.064	11.000	26.09	0.16	2.52	1	PHOT
				O III	1310.072	1.500	24.26	0.16	0.38	1	PHOT
				Ni VI	1310.085	15.000	21.28	0.16	3.44	1	PHOT
1310.357	1.145	1.938	0.286	S V	1310.250	15.000	24.48	0.26	3.44	1	PHOT
				Ni V	1310.252	15.000	24.02	0.26	3.44	1	PHOT
				S V	1310.259	15.000	22.42	0.26	3.44	1	PHOT
				Ni VI	1310.261	15.000	21.97	0.26	3.44	1	PHOT
1311.214	0.374	6.459	0.305	Ni IV	1311.099	15.000	26.30	0.09	3.43	1	PHOT
				Ni IV	1311.101	15.000	25.84	0.09	3.43	1	PHOT
				Ni V	1311.106	15.000	24.69	0.09	3.43	1	PHOT
1311.347	1.009	2.140	0.295	Fe V	1311.238	9.700	24.92	0.23	2.23	1	PHOT
				Fe V	1311.252	14.000	21.72	0.23	3.21	1	PHOT
1311.662	1.835	6.273	0.334	Fe IV	1311.550	1.500	25.60	0.42	0.54	1	PHOT
				Ni IV	1311.553	15.000	24.92	0.42	3.45	1	PHOT
				Ni V	1311.560	15.000	23.31	0.42	3.45	1	PHOT
				O III	1311.568	11.000	21.49	0.42	2.55	1	PHOT
1311.933	0.483	5.854	0.316	Ni V	1311.819	15.000	26.05	0.11	3.43	1	PHOT

Table A.1: Continued.

λ_{obs}	$\delta\lambda_{obs}$	W_λ	δW_λ	Ion	λ_{lab}	$\delta\lambda_{lab}$	v	δv	δv_{tot}	List	Origin
				Fe V	1311.828	9.700	24.00	0.11	2.22	1	PHOT
				Fe V	1311.830	14.000	23.54	0.11	3.20	1	PHOT
1312.140	1.819	6.528	0.339	O III	1312.033	1.500	24.45	0.42	0.54	1	PHOT
				Ni IV	1312.040	15.000	22.85	0.42	3.45	1	PHOT
1312.755	0.794	2.287	0.265	Ni V	1312.646	15.000	24.89	0.18	3.43	1	PHOT
1312.837	0.566	6.098	0.315	Ni IV	1312.739	15.000	22.38	0.13	3.43	1	PHOT
				N IV	1312.740	110.000	22.15	0.13	25.12	1	PHOT
1313.285	2.568	2.861	0.407	Ni V	1313.194	15.000	20.77	0.59	3.47	1	PHOT
1313.412	0.391	5.919	0.266	Ni V	1313.296	15.000	26.48	0.09	3.42	1	PHOT
				P IV	1313.319	1.500	21.23	0.09	0.35	1	PHOT
1313.686	2.648	2.714	0.405	Fe V	1313.582	9.800	23.74	0.60	2.32	1	PHOT
1314.437	0.372	9.428	0.321	Ni V	1314.330	15.000	24.41	0.08	3.42	1	PHOT
1314.630	0.833	7.030	0.267	Fe V	1314.527	9.800	23.49	0.19	2.24	1	PHOT
1314.789	0.886	5.806	0.405	Ni V	1314.682	15.000	24.40	0.20	3.43	1	PHOT
				Ni VI	1314.691	0.000	22.35	0.20	0.20	2	PHOT
1315.020	2.387	1.168	0.343	P I	1314.994	1.500	5.93	0.54	0.64	1	ISM2
				Ni V	1314.909	15.000	25.31	0.54	3.46	1	PHOT
1315.098	2.335	1.018	0.314	Ni VI	1314.990	15.000	24.62	0.53	3.46	1	PHOT
				Ni V	1314.992	15.000	24.17	0.53	3.46	1	PHOT
				Ge IV	1315.000	1100.000	22.34	0.53	250.76	1	PHOT
1315.771	1.363	1.301	0.279	Ni V	1315.653	15.000	26.89	0.31	3.43	1	PHOT
1316.998	1.252	2.716	0.309	Ni V	1316.890	15.000	24.59	0.29	3.43	1	PHOT
				Fe IV	1316.892	15.000	24.13	0.29	3.43	1	PHOT
				Ni V	1316.892	15.000	24.13	0.29	3.43	1	PHOT
1317.547	0.343	6.558	0.257	Ni V	1317.447	15.000	22.76	0.08	3.41	1	PHOT
				Fe V	1317.452	14.000	21.62	0.08	3.19	1	PHOT
1317.842	1.738	0.847	0.229	Fe VI	1317.731	15.000	25.25	0.40	3.44	1	PHOT
				Ni IV	1317.742	15.000	22.75	0.40	3.44	1	PHOT
1317.961	0.460	6.948	0.292	Fe V	1317.860	9.800	22.98	0.10	2.23	1	PHOT
				Fe IV	1317.868	1.500	21.16	0.10	0.36	1	PHOT
1318.251	0.764	3.511	0.277	N V	1318.145	15.000	24.11	0.17	3.42	1	PHOT
				Ni V	1318.145	0.000	24.11	0.17	0.17	2	PHOT
				N IV	1318.148	15.000	23.43	0.17	3.42	1	PHOT
				Ni VI	1318.153	15.000	22.29	0.17	3.42	1	PHOT
1318.453	0.330	15.913	0.216	Fe V	1318.355	9.800	22.29	0.08	2.23	1	PHOT
				Fe IV	1318.359	1.500	21.38	0.08	0.35	1	PHOT
1318.615	0.252	10.987	0.292	Fe IV	1318.500	11.000	26.15	0.06	2.50	1	PHOT
				Ni VI	1318.506	15.000	24.78	0.06	3.41	1	PHOT
				N IV	1318.508	15.000	24.33	0.06	3.41	1	PHOT
				Ni V	1318.515	15.000	22.74	0.06	3.41	1	PHOT
				N V	1318.520	110.000	21.60	0.06	25.01	1	PHOT
1319.268	1.982	1.543	0.326	Fe V	1319.159	14.000	24.77	0.45	3.21	1	PHOT
				Ni V	1319.164	0.000	23.63	0.45	0.45	2	PHOT
1319.442	1.115	1.644	0.176	Fe V	1319.326	9.800	26.36	0.25	2.24	1	PHOT
1320.405	1.918	1.810	0.344	Fe V	1320.298	9.900	24.30	0.44	2.29	1	PHOT

Table A.1: *Continued.*

$\lambda_{\rm obs}$	$\delta\lambda_{\rm obs}$	W_λ	δW_λ	Ion	$\lambda_{\rm lab}$	$\delta\lambda_{\rm lab}$	v	δv	$\delta v_{\rm tot}$	List	Origin
				Fe V	1320.313	9.900	20.89	0.44	2.29	1	PHOT
1320.514	0.267	11.823	0.312	Fe V	1320.409	9.900	23.84	0.06	2.25	1	PHOT
				N III	1320.414	16.000	22.70	0.06	3.63	1	PHOT
1320.819	0.406	6.236	0.292	Ni IV	1320.706	0.000	25.65	0.09	0.09	2	PHOT
				Ni V	1320.727	16.000	20.88	0.09	3.63	1	PHOT
1320.995	2.244	1.757	0.332	Fe V	1320.878	14.000	26.55	0.51	3.22	1	PHOT
				Ni V	1320.889	0.000	24.06	0.51	0.51	2	PHOT
1321.445	0.349	6.550	0.257	Fe V	1321.341	9.900	23.60	0.08	2.25	1	PHOT
				Fe IV	1321.349	1.600	21.78	0.08	0.37	1	PHOT
1321.593	0.275	11.065	0.279	Fe V	1321.489	9.900	23.59	0.06	2.25	1	PHOT
1321.956	0.816	3.673	0.288	Fe V	1321.849	9.900	24.27	0.19	2.25	1	PHOT
				Si V	1321.860	160.000	21.77	0.19	36.29	1	PHOT
1322.519	0.749	2.503	0.252	O IV	1322.430	110.000	20.18	0.17	24.94	1	PHOT
1323.373	0.270	14.240	0.345	Fe IV	1323.262	11.000	25.15	0.06	2.49	1	PHOT
				Fe V	1323.271	9.900	23.11	0.06	2.24	1	PHOT
1323.656	1.137	5.405	0.269	Ni V	1323.553	16.000	23.33	0.26	3.63	1	PHOT
				Ni V	1323.562	16.000	21.29	0.26	3.63	1	PHOT
1324.092	0.647	8.566	0.390	Ni V	1323.977	16.000	26.04	0.15	3.63	1	PHOT
				Ni V	1324.000	16.000	20.83	0.15	3.63	1	PHOT
1324.579	2.293	1.553	0.353	Ni V	1324.466	16.000	25.58	0.52	3.66	1	PHOT
				Ni V	1324.470	16.000	24.67	0.52	3.66	1	PHOT
1324.990	1.842	1.642	0.332	Ni IV	1324.865	16.000	28.29	0.42	3.64	1	PHOT
1325.882	0.815	3.484	0.182	Fe IV	1325.778	1.600	23.52	0.18	0.41	1	PHOT
				Fe V	1325.782	9.900	22.61	0.18	2.25	1	PHOT
				P IV	1325.785	1.600	21.93	0.18	0.41	1	PHOT
1327.210	1.551	2.496	0.361	Fe V	1327.101	10.000	24.62	0.35	2.29	1	PHOT
1328.126	1.768	1.793	0.342	Si III	1328.016	1.600	24.83	0.40	0.54	1	PHOT
				P IV	1328.017	11.000	24.61	0.40	2.51	1	PHOT
				Ni V	1328.025	16.000	22.80	0.40	3.63	1	PHOT
1329.476	0.406	6.114	0.287	Ni V	1329.358	16.000	26.61	0.09	3.61	1	PHOT
1330.508	0.211	13.499	0.287	Fe V	1330.405	10.000	23.21	0.05	2.25	1	PHOT
1331.288	1.530	2.821	0.425	O III	1331.180	110.000	24.32	0.34	24.77	1	PHOT
				Fe V	1331.189	10.000	22.30	0.34	2.28	1	PHOT
				Fe VI	1331.195	16.000	20.94	0.34	3.62	1	PHOT
1331.744	0.511	8.064	0.407	Fe V	1331.639	10.000	23.64	0.12	2.25	1	PHOT
1334.062	0.829	3.576	0.233	Ni V	1333.958	16.000	23.37	0.19	3.60	1	PHOT
1334.287	1.492	2.688	0.397	Fe IV	1334.168	1.600	26.74	0.34	0.49	1	PHOT
				Ni V	1334.169	16.000	26.52	0.34	3.61	1	PHOT
				Fe IV	1334.170	1.600	26.29	0.34	0.49	1	PHOT
1334.552	0.186	68.786	0.591	Fe IV	1334.435	0.000	26.29	0.04	0.04	2	PHOT
				Fe IV	1334.438	1.600	25.61	0.04	0.36	1	PHOT
1334.617	0.182	67.057	0.588	C II	1334.532	1.600	19.09	0.04	0.36	1	ISM1
				Fe IV	1334.507	1.600	24.71	0.04	0.36	1	PHOT
				S IV	1334.513	16.000	23.36	0.04	3.59	1	PHOT
1335.087	1.485	2.958	0.441	Fe V	1334.994	14.000	20.88	0.33	3.16	1	PHOT

Table A.1: Continued.

$\lambda_{\rm obs}$	$\delta\lambda_{\rm obs}$	W_λ	δW_λ	Ion	$\lambda_{\rm lab}$	$\delta\lambda_{\rm lab}$	v	δv	$\delta v_{\rm tot}$	List	Origin
1335.735	0.261	15.147	0.501	Ni IV	1335.623	0.000	25.14	0.06	0.06	2	PHOT
				N III	1335.640	110.000	21.32	0.06	24.69	1	PHOT
1335.786	1.045	2.340	0.477	Fe V	1335.682	14.000	23.34	0.23	3.15	1	PHOT
1336.264	0.564	8.696	0.542	Fe IV	1336.106	1.600	35.45	0.13	0.38	1	PHOT
				Ni V	1336.136	16.000	28.72	0.13	3.59	1	PHOT
1338.734	0.543	17.134	0.581	O IV	1338.615	16.000	26.65	0.12	3.59	1	PHOT
1338.913	1.515	3.532	0.497	Fe V	1338.808	10.000	23.51	0.34	2.26	1	PHOT
1339.790	1.021	4.774	0.558	Ni IV	1339.674	16.000	25.96	0.23	3.59	1	PHOT
				Fe V	1339.691	10.000	22.15	0.23	2.25	1	PHOT
1341.185	1.702	2.329	0.512	Ni V	1341.074	16.000	24.81	0.38	3.60	1	PHOT
1342.289	0.704	5.834	0.462	Ni V	1342.176	16.000	25.24	0.16	3.58	1	PHOT
1343.104	1.619	4.531	0.585	O IV	1342.990	16.000	25.45	0.36	3.59	1	PHOT
1343.626	0.459	22.783	0.651	O IV	1343.514	16.000	24.99	0.10	3.57	1	PHOT
1345.708	0.800	4.988	0.515	Ni V	1345.591	16.000	26.07	0.18	3.57	1	PHOT
				Fe V	1345.603	10.000	23.39	0.18	2.23	1	PHOT
1345.768	1.668	4.558	0.792	Fe V	1345.656	10.000	24.95	0.37	2.26	1	PHOT
1345.833	1.668	3.587	0.635	Ni IV	1345.723	16.000	24.51	0.37	3.58	1	PHOT
1347.847	1.458	4.836	0.619	O III	1347.745	1.600	22.69	0.32	0.48	1	PHOT
				Ni V	1347.749	16.000	21.80	0.32	3.57	1	PHOT
1348.066	1.312	4.125	0.601	C III	1347.947	1.600	26.47	0.29	0.46	1	PHOT
				Fe V	1347.949	15.000	26.02	0.29	3.35	1	PHOT
				Si VI	1347.950	160.000	25.80	0.29	35.58	1	PHOT
				Fe V	1347.965	15.000	22.46	0.29	3.35	1	PHOT
1350.327	2.080	1.955	0.556	Ni IV	1350.218	16.000	24.20	0.46	3.58	1	PHOT
1350.635	0.842	6.407	0.545	Fe V	1350.515	15.000	26.64	0.19	3.33	1	PHOT
				Al V	1350.519	16.000	25.75	0.19	3.56	1	PHOT
				Ni IV	1350.521	16.000	25.31	0.19	3.56	1	PHOT
				Ni V	1350.525	0.000	24.42	0.19	0.19	2	PHOT
				Fe IV	1350.531	1.600	23.09	0.19	0.40	1	PHOT
				Al V	1350.532	16.000	22.86	0.19	3.56	1	PHOT
				Fe V	1350.537	10.000	21.75	0.19	2.23	1	PHOT
1351.523	1.105	5.338	0.532	Ni V	1351.412	16.000	24.62	0.25	3.56	1	PHOT
				Ni IV	1351.419	16.000	23.07	0.25	3.56	1	PHOT
1351.860	1.478	4.257	0.541	Fe V	1351.757	10.000	22.84	0.33	2.24	1	PHOT
1352.702	1.141	4.873	0.611	Fe V	1352.602	10.000	22.16	0.25	2.23	1	PHOT
1352.968	1.383	1.650	0.451	Al III	1352.858	1.600	24.38	0.31	0.47	1	PHOT
				Al V	1352.870	120.000	21.72	0.31	26.59	1	PHOT
				Ni V	1352.871	16.000	21.49	0.31	3.56	1	PHOT
1353.010	1.313	3.379	0.590	Ni IV	1352.904	16.000	23.49	0.29	3.56	1	PHOT
1353.863	0.929	5.390	0.559	Al IV	1353.755	16.000	23.92	0.21	3.55	1	PHOT
1354.951	0.574	9.322	0.523	Fe V	1354.846	10.000	23.23	0.13	2.22	1	PHOT
1356.186	1.620	2.228	0.450	Ni V	1356.068	16.000	26.09	0.36	3.55	1	PHOT
				Ni IV	1356.076	16.000	24.32	0.36	3.55	1	PHOT
				Ni IV	1356.079	16.000	23.65	0.36	3.55	1	PHOT
				P IV	1356.085	1.600	22.33	0.36	0.50	1	PHOT

Table A.1: *Continued.*

$\lambda_{\rm obs}$	$\delta\lambda_{\rm obs}$	W_λ	δW_λ	Ion	$\lambda_{\rm lab}$	$\delta\lambda_{\rm lab}$	v	δv	$\delta v_{\rm tot}$	List	Origin
1356.189	1.599	2.080	0.439	Ni V	1356.068	16.000	26.75	0.35	3.55	1	PHOT
				Ni IV	1356.076	16.000	24.98	0.35	3.55	1	PHOT
				Ni IV	1356.079	16.000	24.32	0.35	3.55	1	PHOT
				P IV	1356.085	1.600	22.99	0.35	0.50	1	PHOT
1357.175	1.455	5.426	0.741	Ni IV	1357.064	16.000	24.52	0.32	3.55	1	PHOT
1357.219	2.635	3.154	0.763	Fe V	1357.112	10.000	23.64	0.58	2.28	1	PHOT
				O III	1357.119	1.600	22.09	0.58	0.68	1	PHOT
1357.777	0.691	6.065	0.520	Ni V	1357.663	16.000	25.17	0.15	3.54	1	PHOT
				N IV	1357.668	16.000	24.07	0.15	3.54	1	PHOT
				Fe V	1357.679	10.000	21.64	0.15	2.21	1	PHOT
1358.674	1.483	2.658	0.516	Fe V	1358.565	10.000	24.05	0.33	2.23	1	PHOT
1359.112	0.801	12.367	0.439	Fe IV	1358.996	1.600	25.59	0.18	0.39	1	PHOT
				Fe V	1359.006	10.000	23.38	0.18	2.21	1	PHOT
1359.347	1.828	2.793	0.547	Ni IV	1359.237	16.000	24.26	0.40	3.55	1	PHOT
				O III	1359.237	1.600	24.26	0.40	0.54	1	PHOT
1359.508	0.953	6.146	0.530	Fe IV	1359.391	1.600	25.80	0.21	0.41	1	PHOT
				Ni IV	1359.394	16.000	25.14	0.21	3.53	1	PHOT
				Fe V	1359.405	10.000	22.71	0.21	2.22	1	PHOT
1361.380	0.530	18.311	0.432	Ni IV	1361.268	0.000	24.67	0.12	0.12	2	PHOT
				Fe V	1361.274	10.000	23.34	0.12	2.21	1	PHOT
				Fe V	1361.278	10.000	22.46	0.12	2.21	1	PHOT
1361.550	0.680	10.164	0.615	Fe V	1361.446	10.000	22.90	0.15	2.21	1	PHOT
1361.787	1.948	6.818	0.793	N IV	1361.672	17.000	25.32	0.43	3.77	1	PHOT
				Fe V	1361.691	10.000	21.14	0.43	2.24	1	PHOT
1361.930	0.478	11.809	0.563	Fe VI	1361.817	17.000	24.88	0.11	3.74	1	PHOT
				Fe V	1361.826	10.000	22.89	0.11	2.20	1	PHOT
1362.970	0.720	8.095	0.577	Fe V	1362.864	11.000	23.32	0.16	2.42	1	PHOT
				P IV	1362.872	12.000	21.56	0.16	2.64	1	PHOT
1363.182	0.476	12.489	0.564	Fe V	1363.076	11.000	23.31	0.10	2.42	1	PHOT
1363.749	0.536	14.930	0.377	Ni IV	1363.637	17.000	24.62	0.12	3.74	1	PHOT
				Fe V	1363.643	15.000	23.30	0.12	3.30	1	PHOT
				Fe V	1363.644	11.000	23.08	0.12	2.42	1	PHOT
1364.040	0.953	4.078	0.457	Fe IV	1363.927	1.700	24.84	0.21	0.43	1	PHOT
				Ni V	1363.929	17.000	24.40	0.21	3.74	1	PHOT
1364.923	0.768	6.706	0.492	Fe IV	1364.818	1.700	23.06	0.17	0.41	1	PHOT
				Fe V	1364.821	11.000	22.41	0.17	2.42	1	PHOT
1365.088	0.740	6.746	0.484	Fe V	1364.977	11.000	24.38	0.16	2.42	1	PHOT
				Fe V	1364.985	11.000	22.62	0.16	2.42	1	PHOT
1365.224	0.744	7.522	0.526	Fe V	1365.115	11.000	23.94	0.16	2.42	1	PHOT
1365.366	3.297	2.429	0.410	Si III	1365.253	1.700	24.81	0.72	0.81	1	PHOT
1365.672	0.638	11.322	0.623	Ni IV	1365.551	17.000	26.56	0.14	3.73	1	PHOT
				Fe V	1365.575	11.000	21.29	0.14	2.42	1	PHOT
1369.615	0.899	8.104	0.359	Fe IV	1369.493	1.700	26.71	0.20	0.42	1	PHOT
				Fe V	1369.507	15.000	23.64	0.20	3.29	1	PHOT
1370.413	1.626	5.540	0.714	Fe V	1370.302	11.000	24.28	0.36	2.43	1	PHOT

Table A.1: Continued.

$\lambda_{\rm obs}$	$\delta\lambda_{\rm obs}$	W_λ	δW_λ	Ion	$\lambda_{\rm lab}$	$\delta\lambda_{\rm lab}$	v	δv	$\delta v_{\rm tot}$	List	Origin
1371.045	0.815	6.001	0.554	Fe V	1370.943	11.000	22.30	0.18	2.41	1	PHOT
1371.343	2.030	1.804	0.530	Ni V	1371.229	17.000	24.92	0.44	3.74	1	PHOT
1371.409	1.003	11.864	0.818	O V	1371.296	17.000	24.70	0.22	3.72	1	PHOT
1371.787	1.893	3.603	0.629	Ni IV	1371.680	17.000	23.39	0.41	3.74	1	PHOT
1371.876	2.318	2.461	0.609	Ni V	1371.757	0.000	26.01	0.51	0.51	2	PHOT
				P IV	1371.767	1.700	23.82	0.51	0.63	1	PHOT
				Ni IV	1371.778	17.000	21.42	0.51	3.75	1	PHOT
1372.096	0.974	4.615	0.542	Fe V	1371.983	11.000	24.69	0.21	2.41	1	PHOT
1373.695	0.313	18.399	0.509	O III	1373.586	12.000	23.79	0.07	2.62	1	PHOT
				Fe V	1373.589	11.000	23.14	0.07	2.40	1	PHOT
				Ni VI	1373.598	17.000	21.17	0.07	3.71	1	PHOT
1373.781	0.332	16.014	0.498	Fe IV	1373.669	1.700	24.44	0.07	0.38	1	PHOT
				Al V	1373.670	17.000	24.22	0.07	3.71	1	PHOT
				Fe V	1373.679	11.000	22.26	0.07	2.40	1	PHOT
1374.075	0.589	7.126	0.463	Fe V	1373.964	11.000	24.22	0.13	2.40	1	PHOT
				N III	1373.970	120.000	22.91	0.13	26.18	1	PHOT
				Ni VI	1373.970	17.000	22.91	0.13	3.71	1	PHOT
				Fe V	1373.976	15.000	21.60	0.13	3.28	1	PHOT
1374.224	0.501	9.490	0.521	Ni IV	1374.113	0.000	24.22	0.11	0.11	2	PHOT
				Fe V	1374.119	11.000	22.91	0.11	2.40	1	PHOT
1374.714	2.986	3.678	0.759	Ni IV	1374.616	17.000	21.37	0.65	3.76	1	PHOT
1374.900	1.095	7.422	0.686	Fe V	1374.788	11.000	24.42	0.24	2.41	1	PHOT
				O V	1374.800	170.000	21.81	0.24	37.07	1	PHOT
1375.425	1.832	2.215	0.529	Fe V	1375.304	15.000	26.38	0.40	3.29	1	PHOT
1376.445	0.323	18.855	0.569	Ni V	1376.330	17.000	25.05	0.07	3.70	1	PHOT
				Fe V	1376.337	11.000	23.52	0.07	2.40	1	PHOT
				Ni V	1376.337	17.000	23.52	0.07	3.70	1	PHOT
1376.560	0.458	15.134	0.608	Ni V	1376.442	17.000	25.70	0.10	3.70	1	PHOT
				Fe V	1376.451	11.000	23.74	0.10	2.40	1	PHOT
				Ni VI	1376.455	17.000	22.87	0.10	3.70	1	PHOT
1377.739	0.828	4.851	0.461	Ni VI	1377.623	17.000	25.24	0.18	3.70	1	PHOT
				Ni IV	1377.642	17.000	21.11	0.18	3.70	1	PHOT
1378.200	1.261	2.946	0.458	Fe V	1378.088	11.000	24.36	0.27	2.41	1	PHOT
				O III	1378.094	1.700	23.06	0.27	0.46	1	PHOT
1378.668	0.350	19.157	0.544	O III	1378.556	12.000	24.36	0.08	2.61	1	PHOT
				Fe V	1378.561	11.000	23.27	0.08	2.39	1	PHOT
1378.813	3.540	2.604	0.692	Al VI	1378.700	1700.000	24.57	0.77	369.63	1	PHOT
				Ni IV	1378.708	17.000	22.83	0.77	3.78	1	PHOT
1379.169	0.802	12.400	0.467	S V	1379.057	17.000	24.35	0.17	3.70	1	PHOT
1380.218	0.564	8.342	0.550	Fe V	1380.112	11.000	23.03	0.12	2.39	1	PHOT
1384.156	1.742	5.930	0.786	Fe V	1384.058	11.000	21.23	0.38	2.41	1	PHOT
1384.303	2.249	1.814	0.361	Fe V	1384.200	11.000	22.31	0.49	2.43	1	PHOT
1384.801	1.921	3.193	0.399	Fe V	1384.685	11.000	25.11	0.42	2.42	1	PHOT
1385.422	0.869	6.555	0.595	Fe V	1385.312	11.000	23.80	0.19	2.39	1	PHOT
1385.794	0.710	11.935	0.676	Fe V	1385.684	11.000	23.80	0.15	2.38	1	PHOT

Table A.1: Continued.

$\lambda_{\rm obs}$	$\delta\lambda_{\rm obs}$	W_λ	δW_λ	Ion	$\lambda_{\rm lab}$	$\delta\lambda_{\rm lab}$	v	δv	$\delta v_{\rm tot}$	List	Origin
				Fe V	1385.694	11.000	21.63	0.15	2.38	1	PHOT
1386.813	1.106	2.006	0.393	Ni IV	1386.691	17.000	26.38	0.24	3.68	1	PHOT
				O IV	1386.710	170.000	22.27	0.24	36.75	1	PHOT
1387.201	0.443	13.993	0.529	Fe V	1387.095	11.000	22.91	0.10	2.38	1	PHOT
				Fe V	1387.100	2900.000	21.83	0.10	626.73	1	PHOT
				Ni IV	1387.101	0.000	21.61	0.10	0.10	2	PHOT
1387.821	2.334	1.922	0.543	O III	1387.707	1.700	24.63	0.50	0.62	1	PHOT
1388.046	0.393	17.440	0.619	Al III	1387.930	170.000	25.06	0.08	36.72	1	PHOT
				Fe V	1387.937	11.000	23.54	0.08	2.38	1	PHOT
				Fe VI	1387.946	17.000	21.60	0.08	3.67	1	PHOT
				Si III	1387.948	1.700	21.17	0.08	0.38	1	PHOT
1388.295	1.637	8.238	0.542	O III	1388.180	1.700	24.84	0.35	0.51	1	PHOT
				Fe V	1388.183	16.000	24.19	0.35	3.47	1	PHOT
				O III	1388.190	120.000	22.68	0.35	25.92	1	PHOT
				Fe V	1388.195	11.000	21.60	0.35	2.40	1	PHOT
1388.435	0.764	6.535	0.593	Fe V	1388.324	11.000	23.97	0.17	2.38	1	PHOT
1389.111	0.933	17.861	0.541	Ni V	1388.991	0.000	25.90	0.20	0.20	2	PHOT
				Ni V	1388.993	17.000	25.47	0.20	3.67	1	PHOT
				Fe V	1388.999	16.000	24.17	0.20	3.46	1	PHOT
1393.179	1.019	6.867	0.630	Fe V	1393.072	11.000	23.03	0.22	2.38	1	PHOT
1393.864	0.250	95.489	0.771	Ni VI	1393.753	17.000	23.88	0.05	3.66	1	PHOT
				Si IV	1393.755	1.700	23.45	0.05	0.37	1	PHOT
1394.380	0.632	7.767	0.540	Fe V	1394.270	11.000	23.65	0.14	2.37	1	PHOT
1394.776	0.723	13.898	0.437	Fe V	1394.671	11.000	22.57	0.16	2.37	1	PHOT
1396.661	1.396	3.968	0.548	S III	1396.552	17.000	23.40	0.30	3.66	1	PHOT
1397.219	1.493	6.280	0.448	Al VI	1397.100	1200.000	25.54	0.32	257.48	1	PHOT
				Fe V	1397.110	11.000	23.39	0.32	2.38	1	PHOT
				N III	1397.110	17.000	23.39	0.32	3.66	1	PHOT
1397.473	2.551	3.674	0.477	Fe V	1397.372	16.000	21.67	0.55	3.48	1	PHOT
				Ni IV	1397.374	17.000	21.24	0.55	3.69	1	PHOT
1397.862	2.103	2.278	0.574	Fe V	1397.751	11.000	23.81	0.45	2.40	1	PHOT
				Fe V	1397.757	16.000	22.52	0.45	3.46	1	PHOT
				S IV	1397.759	17.000	22.09	0.45	3.67	1	PHOT
1397.865	2.143	3.181	0.658	Fe V	1397.751	11.000	24.45	0.46	2.40	1	PHOT
				Fe V	1397.757	16.000	23.16	0.46	3.46	1	PHOT
				S IV	1397.759	17.000	22.73	0.46	3.67	1	PHOT
1398.079	0.922	8.584	0.658	S IV	1398.050	12.000	6.22	0.20	2.58	1	ISM2
				Fe V	1397.958	21.000	25.95	0.20	4.51	1	PHOT
				Fe V	1397.974	11.000	22.52	0.20	2.37	1	PHOT
1398.306	0.470	16.435	0.397	Ni IV	1398.193	17.000	24.23	0.10	3.65	1	PHOT
1398.942	1.422	4.175	0.383	Si V	1398.820	170.000	26.15	0.30	36.43	1	PHOT
1400.053	0.957	4.214	0.517	Ni IV	1399.947	17.000	22.70	0.20	3.65	1	PHOT
				Fe IV	1399.951	12.000	21.84	0.20	2.58	1	PHOT
1400.354	0.434	12.092	0.511	Fe V	1400.237	11.000	25.05	0.09	2.36	1	PHOT
				Ni V	1400.256	0.000	20.98	0.09	0.09	2	PHOT

Table A.1: Continued.

$\lambda_{\rm obs}$	$\delta\lambda_{\rm obs}$	W_λ	δW_λ	Ion	$\lambda_{\rm lab}$	$\delta\lambda_{\rm lab}$	v	δv	$\delta v_{\rm tot}$	List	Origin
1400.777	1.219	5.274	0.560	Ni IV	1400.682	17.000	20.33	0.26	3.65	1	PHOT
1402.494	0.400	22.898	0.671	Fe V	1402.385	11.000	23.30	0.09	2.35	1	PHOT
				Ni IV	1402.389	18.000	22.45	0.09	3.85	1	PHOT
				Fe V	1402.391	11.000	22.02	0.09	2.35	1	PHOT
1402.878	0.258	79.568	0.777	Fe V	1402.769	16.000	23.29	0.06	3.42	1	PHOT
				Si IV	1402.770	1.800	23.08	0.06	0.39	1	PHOT
				Al IV	1402.776	18.000	21.80	0.06	3.85	1	PHOT
1403.479	0.827	6.157	0.566	Fe V	1403.369	11.000	23.50	0.18	2.36	1	PHOT
				Fe V	1403.377	11.000	21.79	0.18	2.36	1	PHOT
1404.374	2.881	3.445	0.729	Fe V	1404.260	11.000	24.34	0.61	2.43	1	PHOT
1406.780	0.462	19.532	0.694	Ni VI	1406.662	18.000	25.15	0.10	3.84	1	PHOT
				Fe V	1406.668	11.000	23.87	0.10	2.35	1	PHOT
1406.937	0.575	16.160	0.703	Fe V	1406.824	11.000	24.08	0.12	2.35	1	PHOT
1407.113	2.234	3.869	0.779	N III	1406.990	130.000	26.21	0.48	27.70	1	PHOT
				Fe V	1407.010	11.000	21.95	0.48	2.39	1	PHOT
1407.357	0.426	16.469	0.620	Ni IV	1407.232	0.000	26.63	0.09	0.09	2	PHOT
				Fe V	1407.248	11.000	23.22	0.09	2.34	1	PHOT
				Ni V	1407.250	18.000	22.79	0.09	3.84	1	PHOT
				Fe V	1407.256	16.000	21.52	0.09	3.41	1	PHOT
1408.230	0.673	7.931	0.576	Fe V	1408.118	11.000	23.85	0.14	2.35	1	PHOT
1408.813	0.938	6.250	0.389	Ni IV	1408.715	18.000	20.86	0.20	3.84	1	PHOT
1408.896	1.500	5.036	0.698	Fe V	1408.800	11.000	20.43	0.32	2.36	1	PHOT
1409.141	0.522	15.610	0.657	Fe IV	1409.021	1.800	25.53	0.11	0.40	1	PHOT
				Fe V	1409.026	11.000	24.47	0.11	2.34	1	PHOT
1409.335	0.429	18.704	0.652	N III	1409.210	130.000	26.59	0.09	27.65	1	PHOT
				N IV	1409.211	18.000	26.38	0.09	3.83	1	PHOT
				Fe V	1409.225	11.000	23.40	0.09	2.34	1	PHOT
				Ni VI	1409.235	18.000	21.27	0.09	3.83	1	PHOT
				Ni V	1409.237	18.000	20.85	0.09	3.83	1	PHOT
1409.566	0.365	29.576	0.653	Fe V	1409.453	11.000	24.04	0.08	2.34	1	PHOT
1409.957	0.672	7.841	0.527	Ni IV	1409.841	18.000	24.67	0.14	3.83	1	PHOT
				Ni IV	1409.845	18.000	23.82	0.14	3.83	1	PHOT
				Fe V	1409.851	11.000	22.54	0.14	2.34	1	PHOT
1411.564	0.630	8.797	0.603	Ni IV	1411.451	18.000	24.00	0.13	3.83	1	PHOT
1411.678	0.835	10.154	0.697	Fe V	1411.566	11.000	23.79	0.18	2.34	1	PHOT
				Fe IV	1411.577	1.800	21.45	0.18	0.42	1	PHOT
1414.365	3.014	2.470	0.657	Fe IV	1414.251	1.800	24.17	0.64	0.74	1	PHOT
1414.708	1.021	4.335	0.335	Ni IV	1414.597	18.000	23.52	0.22	3.82	1	PHOT
1414.946	1.118	2.835	0.471	Fe V	1414.831	11.000	24.37	0.24	2.34	1	PHOT
1415.245	1.453	3.380	0.582	Fe V	1415.140	11.000	22.24	0.31	2.35	1	PHOT
1415.304	0.524	14.097	0.669	Fe V	1415.200	11.000	22.03	0.11	2.33	1	PHOT
				Si VI	1415.200	1300.000	22.03	0.11	275.37	1	PHOT
				Ni VI	1415.204	18.000	21.18	0.11	3.81	1	PHOT
1416.334	0.885	8.451	0.785	Fe V	1416.222	11.000	23.71	0.19	2.34	1	PHOT
1416.639	1.432	1.908	0.496	Ni IV	1416.531	18.000	22.86	0.30	3.82	1	PHOT

Table A.1: Continued.

$\lambda_{\rm obs}$	$\delta\lambda_{\rm obs}$	W_λ	δW_λ	Ion	$\lambda_{\rm lab}$	$\delta\lambda_{\rm lab}$	v	δv	$\delta v_{\rm tot}$	List	Origin
1417.075	1.686	5.354	0.466	Ni IV	1416.958	18.000	24.75	0.36	3.82	1	PHOT
				S IV	1416.975	0.000	21.16	0.36	0.36	2	PHOT
1417.673	4.885	3.613	0.930	Al IV	1417.555	18.000	24.96	1.03	3.94	1	PHOT
1418.235	0.591	12.359	0.659	Fe V	1418.124	11.000	23.47	0.12	2.33	1	PHOT
1419.234	2.601	2.447	0.594	Ni IV	1419.126	18.000	22.82	0.55	3.84	1	PHOT
1419.405	0.666	7.893	0.530	Fe V	1419.295	11.000	23.23	0.14	2.33	1	PHOT
1419.557	2.125	1.413	0.447	Ni IV	1419.450	18.000	22.60	0.45	3.83	1	PHOT
				Ni IV	1419.452	0.000	22.18	0.45	0.45	2	PHOT
1419.683	1.387	1.503	0.396	Ni IV	1419.569	0.000	24.08	0.29	0.29	2	PHOT
				Ni IV	1419.577	18.000	22.39	0.29	3.81	1	PHOT
1420.236	0.780	7.690	0.543	P IV	1420.111	1.800	26.39	0.16	0.41	1	PHOT
				O III	1420.117	13.000	25.12	0.16	2.75	1	PHOT
				Fe V	1420.118	11.000	24.91	0.16	2.33	1	PHOT
				Ni IV	1420.126	18.000	23.22	0.16	3.80	1	PHOT
				Fe IV	1420.131	1.800	22.17	0.16	0.41	1	PHOT
1420.530	1.120	3.347	0.514	Fe V	1420.424	11.000	22.37	0.24	2.33	1	PHOT
1420.587	0.998	4.989	0.598	Fe VI	1420.463	18.000	26.17	0.21	3.80	1	PHOT
				Fe V	1420.477	11.000	23.22	0.21	2.33	1	PHOT
1420.713	0.570	12.067	0.635	Fe V	1420.606	11.000	22.58	0.12	2.32	1	PHOT
1421.131	1.809	4.015	0.698	Fe V	1421.014	11.000	24.68	0.38	2.35	1	PHOT
				O III	1421.021	1.800	23.21	0.38	0.54	1	PHOT
1421.332	1.015	5.381	0.626	Ni IV	1421.216	18.000	24.47	0.21	3.80	1	PHOT
				Ni IV	1421.226	18.000	22.36	0.21	3.80	1	PHOT
1422.595	1.089	5.092	0.607	O III	1422.471	1.800	26.13	0.23	0.44	1	PHOT
				Fe V	1422.479	11.000	24.45	0.23	2.33	1	PHOT
				O III	1422.495	13.000	21.08	0.23	2.75	1	PHOT
1425.206	1.523	4.273	0.622	Fe V	1425.086	11.000	25.24	0.32	2.34	1	PHOT
				Al VI	1425.100	1800.000	22.30	0.32	378.63	1	PHOT
1425.839	2.236	4.493	0.811	Fe IV	1425.729	1.800	23.13	0.47	0.60	1	PHOT
1426.483	2.333	3.890	0.753	Ni IV	1426.371	18.000	23.54	0.49	3.81	1	PHOT
1426.911	2.439	2.028	0.600	C III	1426.796	1.800	24.16	0.51	0.64	1	PHOT
				Fe V	1426.798	16.000	23.74	0.51	3.40	1	PHOT
				Al IV	1426.800	1300.000	23.32	0.51	273.13	1	PHOT
				O IV	1426.810	18.000	21.22	0.51	3.82	1	PHOT
1427.557	1.004	2.941	0.499	Si V	1427.450	180.000	22.47	0.21	37.80	1	PHOT
				Ni IV	1427.452	18.000	22.05	0.21	3.79	1	PHOT
1428.208	1.176	1.451	0.254	Al III	1428.083	1.800	26.24	0.25	0.45	1	PHOT
				Fe V	1428.094	12.000	23.93	0.25	2.53	1	PHOT
1429.043	2.086	3.586	0.648	Ni IV	1428.933	18.000	23.08	0.44	3.80	1	PHOT
1429.119	0.771	8.662	0.364	Fe V	1429.006	12.000	23.71	0.16	2.52	1	PHOT
1429.587	0.529	14.295	0.574	Fe V	1429.470	12.000	24.54	0.11	2.52	1	PHOT
1430.295	1.240	2.743	0.495	N III	1430.190	130.000	22.01	0.26	27.25	1	PHOT
				Ni IV	1430.190	18.000	22.01	0.26	3.78	1	PHOT
1430.422	1.270	5.578	0.642	N IV	1430.298	18.000	25.99	0.27	3.78	1	PHOT
				Fe V	1430.312	12.000	23.06	0.27	2.53	1	PHOT

Table A.1: Continued.

$\lambda_{\rm obs}$	$\delta\lambda_{\rm obs}$	W_λ	δW_λ	Ion	$\lambda_{\rm lab}$	$\delta\lambda_{\rm lab}$	v	δv	$\delta v_{\rm tot}$	List	Origin
1430.533	1.721	2.322	0.581	P III	1430.410	1.800	25.78	0.36	0.52	1	PHOT
				Ni IV	1430.429	18.000	21.80	0.36	3.79	1	PHOT
1430.688	0.362	26.325	0.674	N III	1430.568	18.000	25.15	0.08	3.77	1	PHOT
				Fe V	1430.572	12.000	24.31	0.08	2.52	1	PHOT
1430.859	1.218	3.790	0.571	Si V	1430.740	180.000	24.93	0.26	37.71	1	PHOT
				Fe V	1430.748	17.000	23.26	0.26	3.57	1	PHOT
				Fe V	1430.754	12.000	22.00	0.26	2.53	1	PHOT
1431.117	2.604	1.950	0.587	Ni IV	1431.012	18.000	22.00	0.55	3.81	1	PHOT
1432.562	2.313	7.798	0.562	Ni IV	1432.449	18.000	23.65	0.48	3.80	1	PHOT
1433.199	1.254	5.744	0.643	Ni VI	1433.077	18.000	25.52	0.26	3.77	1	PHOT
				Fe V	1433.092	12.000	22.38	0.26	2.52	1	PHOT
1435.150	0.941	8.057	0.631	Ge V	1435.030	180.000	25.07	0.20	37.60	1	PHOT
				Si V	1435.030	180.000	25.07	0.20	37.60	1	PHOT
				Fe V	1435.048	12.000	21.31	0.20	2.51	1	PHOT
1435.345	1.653	3.683	0.629	N III	1435.220	130.000	26.11	0.35	27.15	1	PHOT
				Fe V	1435.235	17.000	22.98	0.35	3.57	1	PHOT
				Ni IV	1435.243	18.000	21.31	0.35	3.78	1	PHOT
1438.061	1.694	3.423	0.630	Ni IV	1437.937	18.000	25.85	0.35	3.77	1	PHOT
1438.920	1.099	12.516	0.461	Ni IV	1438.814	18.000	22.09	0.23	3.76	1	PHOT
1439.162	0.956	8.925	0.392	Ni IV	1439.039	0.000	25.62	0.20	0.20	2	PHOT
				Fe V	1439.050	12.000	23.33	0.20	2.51	1	PHOT
				Ni IV	1439.052	18.000	22.92	0.20	3.75	1	PHOT
1439.689	0.944	2.513	0.252	Ni IV	1439.584	18.000	21.87	0.20	3.75	1	PHOT
1440.640	0.405	22.949	0.698	Fe V	1440.528	12.000	23.31	0.08	2.50	1	PHOT
1440.904	1.026	6.417	0.654	Fe V	1440.793	12.000	23.10	0.21	2.51	1	PHOT
				Ni IV	1440.798	18.000	22.06	0.21	3.75	1	PHOT
1441.161	0.507	12.134	0.613	Fe V	1441.049	12.000	23.30	0.11	2.50	1	PHOT
1442.243	1.214	1.967	0.457	Ni IV	1442.130	19.000	23.49	0.25	3.96	1	PHOT
1442.334	0.505	15.544	0.655	Fe V	1442.215	12.000	24.74	0.10	2.50	1	PHOT
1444.537	1.725	4.520	0.612	Ni IV	1444.417	19.000	24.91	0.36	3.96	1	PHOT
				Ni IV	1444.431	0.000	22.00	0.36	0.36	2	PHOT
				Ni V	1444.435	0.000	21.17	0.36	0.36	2	PHOT
1445.010	1.763	7.572	0.842	N IV	1444.886	19.000	25.73	0.37	3.96	1	PHOT
				Fe IV	1444.903	1.900	22.20	0.37	0.54	1	PHOT
1446.727	0.471	16.294	0.654	Fe V	1446.617	12.000	22.80	0.10	2.49	1	PHOT
1448.603	0.585	11.320	0.578	Fe V	1448.488	12.000	23.80	0.12	2.49	1	PHOT
				Fe IV	1448.489	1.900	23.59	0.12	0.41	1	PHOT
1448.958	0.350	19.916	0.552	Fe IV	1448.832	1.900	26.07	0.07	0.40	1	PHOT
				Fe V	1448.847	12.000	22.97	0.07	2.48	1	PHOT
1449.125	1.102	8.381	0.643	Fe V	1449.000	3200.000	25.86	0.23	662.01	1	PHOT
				Ni IV	1449.021	19.000	21.52	0.23	3.94	1	PHOT
1449.884	2.021	4.684	0.706	Ni VI	1449.757	0.000	26.26	0.42	0.42	2	PHOT
				Fe V	1449.761	12.000	25.43	0.42	2.52	1	PHOT
				N IV	1449.767	19.000	24.19	0.42	3.95	1	PHOT
				Fe IV	1449.772	1.900	23.16	0.42	0.57	1	PHOT

Table A.1: Continued.

$\lambda_{\rm obs}$	$\delta\lambda_{\rm obs}$	W_λ	δW_λ	Ion	$\lambda_{\rm lab}$	$\delta\lambda_{\rm lab}$	v	δv	$\delta v_{\rm tot}$	List	Origin
				Ni IV	1449.778	19.000	21.92	0.42	3.95	1	PHOT
1450.035	0.720	9.690	0.658	Ni II	1449.997	1.900	7.86	0.15	0.42	1	ISM2
				Fe V	1449.929	12.000	21.92	0.15	2.49	1	PHOT
1451.214	1.868	1.988	0.551	Ni VI	1451.097	19.000	24.17	0.39	3.94	1	PHOT
				Fe V	1451.101	12.000	23.35	0.39	2.51	1	PHOT
1452.333	0.835	9.724	0.682	Ni IV	1452.220	19.000	23.33	0.17	3.93	1	PHOT
1452.595	1.852	6.180	0.834	Fe IV	1452.477	1.900	24.36	0.38	0.55	1	PHOT
				Fe V	1452.483	17.000	23.12	0.38	3.53	1	PHOT
1453.605	2.749	2.249	0.596	Ni IV	1453.495	19.000	22.69	0.57	3.96	1	PHOT
				Fe IV	1453.502	1.900	21.24	0.57	0.69	1	PHOT
1453.732	0.498	13.558	0.579	Fe IV	1453.606	1.900	25.99	0.10	0.41	1	PHOT
				Fe V	1453.617	12.000	23.72	0.10	2.48	1	PHOT
1454.811	0.610	8.834	0.551	Fe V	1454.683	12.000	26.38	0.13	2.48	1	PHOT
				Fe V	1454.700	12.000	22.88	0.13	2.48	1	PHOT
1455.532	1.745	2.906	0.409	Ni V	1455.420	19.000	23.07	0.36	3.93	1	PHOT
				Ni IV	1455.422	19.000	22.66	0.36	3.93	1	PHOT
1455.674	0.491	17.099	0.705	Fe V	1455.555	12.000	24.51	0.10	2.47	1	PHOT
1456.280	0.501	13.867	0.661	Fe V	1456.162	12.000	24.29	0.10	2.47	1	PHOT
1456.395	1.095	9.375	0.778	Fe V	1456.289	12.000	21.82	0.23	2.48	1	PHOT
1457.841	0.971	9.400	0.762	Fe V	1457.732	12.000	22.42	0.20	2.48	1	PHOT
1459.366	0.941	7.185	0.590	Fe V	1459.253	12.000	23.21	0.19	2.47	1	PHOT
				Fe IV	1459.257	1.900	22.39	0.19	0.44	1	PHOT
				Si V	1459.260	190.000	21.78	0.19	39.03	1	PHOT
1459.911	2.315	13.189	1.396	Fe V	1459.769	12.000	29.16	0.48	2.51	1	PHOT
1459.959	1.370	13.581	1.330	Fe V	1459.828	12.000	26.90	0.28	2.48	1	PHOT
1460.840	0.776	12.956	0.758	Fe V	1460.722	17.000	24.22	0.16	3.49	1	PHOT
				Fe V	1460.730	12.000	22.58	0.16	2.47	1	PHOT
1462.746	0.547	15.364	0.694	Fe V	1462.636	12.000	22.55	0.11	2.46	1	PHOT
1464.798	0.340	19.901	0.547	Fe V	1464.686	12.000	22.92	0.07	2.46	1	PHOT
				Fe IV	1464.695	1.900	21.08	0.07	0.40	1	PHOT
1464.992	1.048	5.367	0.556	Fe V	1464.873	12.000	24.35	0.21	2.47	1	PHOT
				Ni V	1464.875	19.000	23.94	0.21	3.89	1	PHOT
1465.498	0.467	16.625	0.660	Fe V	1465.380	12.000	24.14	0.10	2.46	1	PHOT
				Al V	1465.393	19.000	21.48	0.10	3.89	1	PHOT
1466.762	0.561	14.555	0.654	Fe V	1466.650	12.000	22.89	0.11	2.46	1	PHOT
1468.149	2.505	3.569	0.461	Ni V	1468.019	19.000	26.55	0.51	3.91	1	PHOT
				Ni IV	1468.041	0.000	22.05	0.51	0.51	2	PHOT
1468.271	2.065	1.746	0.342	Fe V	1468.153	23.000	24.10	0.42	4.72	1	PHOT
				Ni IV	1468.161	19.000	22.46	0.42	3.90	1	PHOT
1469.021	0.766	7.493	0.542	Fe V	1468.908	12.000	23.06	0.16	2.45	1	PHOT
				O III	1468.915	1.900	21.63	0.16	0.42	1	PHOT
1469.115	0.401	13.234	0.507	Fe V	1468.998	12.000	23.88	0.08	2.45	1	PHOT
1472.214	0.517	13.441	0.612	Fe V	1472.095	12.000	24.23	0.11	2.45	1	PHOT
				Fe V	1472.106	17.000	21.99	0.11	3.46	1	PHOT
1472.628	0.588	9.018	0.576	Ni IV	1472.502	0.000	25.65	0.12	0.12	2	PHOT

Table A.1: Continued.

$\lambda_{\rm obs}$	$\delta\lambda_{\rm obs}$	W_λ	δW_λ	Ion	$\lambda_{\rm lab}$	$\delta\lambda_{\rm lab}$	v	δv	$\delta v_{\rm tot}$	List	Origin
				Fe V	1472.511	12.000	23.82	0.12	2.45	1	PHOT
				Ni VI	1472.513	19.000	23.41	0.12	3.87	1	PHOT
1472.745	1.170	6.977	0.679	N III	1472.620	19.000	25.45	0.24	3.87	1	PHOT
				Ni IV	1472.626	19.000	24.23	0.24	3.87	1	PHOT
1475.718	1.075	9.931	0.781	Al V	1475.600	1400.000	23.97	0.22	284.41	1	PHOT
				Fe V	1475.605	12.000	22.96	0.22	2.45	1	PHOT
1476.340	1.913	1.599	0.522	Ni IV	1476.233	19.000	21.73	0.39	3.88	1	PHOT
1476.925	1.523	2.762	0.566	Fe IV	1476.815	14.000	22.33	0.31	2.86	1	PHOT
				Ni IV	1476.815	19.000	22.33	0.31	3.87	1	PHOT
1477.411	4.197	3.853	1.004	Ni IV	1477.284	19.000	25.77	0.85	3.95	1	PHOT
1477.926	1.957	2.801	0.659	Fe V	1477.797	12.000	26.17	0.40	2.47	1	PHOT
				Al V	1477.800	1400.000	25.56	0.40	283.99	1	PHOT
				Al VI	1477.800	1900.000	25.56	0.40	385.41	1	PHOT
1478.896	1.739	5.686	0.483	Fe V	1478.785	12.000	22.50	0.35	2.46	1	PHOT
1479.590	0.530	13.176	0.580	Fe V	1479.476	12.000	23.10	0.11	2.43	1	PHOT
				P III	1479.479	2.000	22.49	0.11	0.42	1	PHOT
1482.364	1.370	3.400	0.589	Fe IV	1482.241	2.000	24.88	0.28	0.49	1	PHOT
				Ni IV	1482.248	20.000	23.46	0.28	4.05	1	PHOT
1482.778	2.532	2.093	0.402	S IV	1482.663	20.000	23.25	0.51	4.08	1	PHOT
				Ni IV	1482.665	20.000	22.85	0.51	4.08	1	PHOT
1483.279	1.394	3.018	0.379	Fe IV	1483.158	2.000	24.46	0.28	0.49	1	PHOT
1483.375	1.278	4.847	0.676	Fe V	1483.259	12.000	23.45	0.26	2.44	1	PHOT
1485.129	1.403	1.491	0.407	Fe V	1485.017	12.000	22.61	0.28	2.44	1	PHOT
1485.567	1.278	5.823	0.636	N III	1485.440	20.000	25.63	0.26	4.04	1	PHOT
				Fe V	1485.451	12.000	23.41	0.26	2.44	1	PHOT
1489.356	1.031	4.803	0.538	Fe V	1489.225	24.000	26.37	0.21	4.84	1	PHOT
				Fe V	1489.243	13.000	22.75	0.21	2.62	1	PHOT
				Ni V	1489.248	20.000	21.74	0.21	4.03	1	PHOT
1489.646	0.979	8.120	0.385	Fe IV	1489.528	2.000	23.75	0.20	0.45	1	PHOT
				Ni IV	1489.529	20.000	23.55	0.20	4.03	1	PHOT
				Fe IV	1489.540	2.000	21.33	0.20	0.45	1	PHOT
1489.948	1.011	4.553	0.467	Ni IV	1489.836	20.000	22.54	0.20	4.03	1	PHOT
1490.193	0.948	1.085	0.246	Ni IV	1490.082	0.000	22.33	0.19	0.19	2	PHOT
1492.757	1.832	2.997	0.516	Ni IV	1492.646	20.000	22.29	0.37	4.03	1	PHOT
1493.124	1.117	6.182	0.351	N IV	1493.010	140.000	22.89	0.22	28.11	1	PHOT
				Ni IV	1493.019	0.000	21.08	0.22	0.22	2	PHOT
1493.799	1.037	4.048	0.474	Ni IV	1493.672	20.000	25.49	0.21	4.02	1	PHOT
				Fe V	1493.679	18.000	24.08	0.21	3.62	1	PHOT
1495.289	1.627	1.548	0.353	Si III	1495.171	2.000	23.66	0.33	0.52	1	PHOT
				Fe IV	1495.178	2.000	22.26	0.33	0.52	1	PHOT
1495.913	1.782	2.128	0.425	Ni IV	1495.797	20.000	23.25	0.36	4.02	1	PHOT
				C V	1495.800	69.000	22.65	0.36	13.83	1	PHOT
				Fe IV	1495.808	2.000	21.04	0.36	0.54	1	PHOT
1496.385	0.648	8.029	0.494	Fe V	1496.265	13.000	24.04	0.13	2.61	1	PHOT
				P V	1496.276	14.000	21.84	0.13	2.81	1	PHOT

Table A.1: Continued.

$\lambda_{\rm obs}$	$\delta\lambda_{\rm obs}$	W_λ	δW_λ	Ion	$\lambda_{\rm lab}$	$\delta\lambda_{\rm lab}$	v	δv	$\delta v_{\rm tot}$	List	Origin
1498.890	1.427	2.379	0.430	Ni IV	1498.763	20.000	25.40	0.29	4.01	1	PHOT
1499.010	1.088	2.517	0.400	Ni IV	1498.893	20.000	23.40	0.22	4.01	1	PHOT
				Fe V	1498.902	18.000	21.60	0.22	3.61	1	PHOT
1499.357	1.473	2.662	0.453	N IV	1499.230	20.000	25.40	0.29	4.01	1	PHOT
				Fe V	1499.232	13.000	25.00	0.29	2.62	1	PHOT
1499.573	2.091	1.368	0.409	Fe IV	1499.442	2.000	26.19	0.42	0.58	1	PHOT
1501.907	0.331	25.631	0.567	Si III	1501.780	2.000	25.35	0.07	0.40	1	PHOT
1504.452	1.742	1.087	0.362	Fe V	1504.329	13.000	24.51	0.35	2.61	1	PHOT
1507.170	2.252	1.849	0.489	Ni IV	1507.061	20.000	21.68	0.45	4.00	1	PHOT
1509.214	1.472	1.499	0.393	Ni IV	1509.101	20.000	22.45	0.29	3.98	1	PHOT
1512.840	1.615	2.229	0.477	Fe IV	1512.725	2.000	22.79	0.32	0.51	1	PHOT
1512.897	1.332	1.332	0.232	Ni IV	1512.772	0.000	24.77	0.26	0.26	2	PHOT
1516.789	0.988	3.458	0.407	Ni IV	1516.668	20.000	23.92	0.20	3.96	1	PHOT
1517.902	1.944	4.521	0.419	Fe IV	1517.783	2.100	23.50	0.38	0.57	1	PHOT
				Fe V	1517.787	13.000	22.71	0.38	2.60	1	PHOT
1519.140	2.199	5.088	0.729	O IV	1519.020	210.000	23.68	0.43	41.44	1	PHOT
				P III	1519.025	2.100	22.70	0.43	0.60	1	PHOT
1519.722	3.270	3.175	0.726	Fe IV	1519.602	2.100	23.67	0.65	0.77	1	PHOT
				Ni IV	1519.604	21.000	23.28	0.65	4.19	1	PHOT
1520.754	0.801	5.271	0.498	Ni IV	1520.621	21.000	26.22	0.16	4.14	1	PHOT
1524.044	1.617	3.266	0.569	O III	1523.911	2.100	26.16	0.32	0.52	1	PHOT
				Fe IV	1523.923	2.100	23.80	0.32	0.52	1	PHOT
1525.432	0.653	6.109	0.489	O IV	1525.300	150.000	25.94	0.13	29.48	1	PHOT
				Ni IV	1525.306	21.000	24.76	0.13	4.13	1	PHOT
				N III	1525.311	21.000	23.78	0.13	4.13	1	PHOT
				Fe IV	1525.312	2.100	23.59	0.13	0.43	1	PHOT
1526.190	0.916	10.612	0.422	Fe IV	1526.066	2.100	24.36	0.18	0.45	1	PHOT
1526.749	0.127	38.986	0.470	Si II	1526.707	1.500	8.25	0.02	0.30	1	ISM2
1526.805	0.159	16.781	0.396	Si II	1526.707	1.500	19.24	0.03	0.30	1	ISM1
				Ni VI	1526.687	21.000	23.17	0.03	4.12	1	PHOT
				N IV	1526.699	21.000	20.81	0.03	4.12	1	PHOT
1527.810	1.383	2.483	0.426	Ni IV	1527.685	21.000	24.53	0.27	4.13	1	PHOT
1527.911	0.918	3.963	0.431	Ni IV	1527.793	21.000	23.15	0.18	4.12	1	PHOT
1530.380	1.043	5.953	0.578	Fe IV	1530.256	2.100	24.29	0.20	0.46	1	PHOT
1530.572	1.786	4.825	0.681	Fe V	1530.440	13.000	25.86	0.35	2.57	1	PHOT
1531.349	1.510	4.395	0.613	Fe IV	1531.223	2.100	24.67	0.30	0.51	1	PHOT
				Ge VI	1531.227	21.000	23.89	0.30	4.12	1	PHOT
1532.609	1.906	1.669	0.496	Fe IV	1532.490	2.100	23.28	0.37	0.55	1	PHOT
1532.757	0.726	12.313	0.395	N IV	1532.621	21.000	26.60	0.14	4.11	1	PHOT
				Fe IV	1532.630	2.100	24.84	0.14	0.43	1	PHOT
				Fe V	1532.647	13.000	21.52	0.14	2.55	1	PHOT
1533.028	0.732	7.239	0.506	Fe IV	1532.903	2.100	24.45	0.14	0.43	1	PHOT
1533.383	1.516	6.395	0.399	Fe IV	1533.267	2.100	22.68	0.30	0.51	1	PHOT
1533.506	2.301	1.908	0.482	Fe V	1533.387	13.000	23.27	0.45	2.58	1	PHOT
				O III	1533.387	2.100	23.27	0.45	0.61	1	PHOT

Table A.1: Continued.

$\lambda_{\rm obs}$	$\delta\lambda_{\rm obs}$	W_λ	δW_λ	Ion	$\lambda_{\rm lab}$	$\delta\lambda_{\rm lab}$	v	δv	$\delta v_{\rm tot}$	List	Origin
1533.704	3.264	1.497	0.490	N III	1533.575	21.000	25.22	0.64	4.15	1	PHOT
				Fe IV	1533.578	2.100	24.63	0.64	0.76	1	PHOT
				P IV	1533.581	15.000	24.04	0.64	3.00	1	PHOT
				Fe V	1533.594	25.000	21.50	0.64	4.93	1	PHOT
1533.990	0.871	7.809	0.601	Fe IV	1533.869	2.100	23.65	0.17	0.44	1	PHOT
1534.067	1.372	4.011	0.587	Fe IV	1533.949	2.100	23.06	0.27	0.49	1	PHOT
1534.838	0.592	9.093	0.564	Ni IV	1534.710	21.000	25.00	0.12	4.10	1	PHOT
1535.033	4.258	2.288	0.739	Ni IV	1534.931	21.000	19.92	0.83	4.18	1	PHOT
1535.862	6.041	4.474	1.131	Fe IV	1535.734	2.100	24.99	1.18	1.25	1	PHOT
1536.700	1.352	6.477	0.655	Fe IV	1536.577	2.100	24.00	0.26	0.49	1	PHOT
1537.204	2.987	2.693	0.729	O III	1537.080	2.100	24.18	0.58	0.71	1	PHOT
				Fe V	1537.081	19.000	23.99	0.58	3.75	1	PHOT
1537.373	1.377	3.742	0.565	Fe IV	1537.237	2.100	26.52	0.27	0.49	1	PHOT
				Ni IV	1537.248	21.000	24.38	0.27	4.10	1	PHOT
1538.245	2.079	3.616	0.682	N III	1538.111	21.000	26.12	0.41	4.11	1	PHOT
				Fe IV	1538.122	2.100	23.97	0.41	0.58	1	PHOT
1538.411	1.416	7.306	0.426	Fe IV	1538.286	2.100	24.36	0.28	0.49	1	PHOT
1539.051	0.915	6.562	0.523	Ni IV	1538.923	21.000	24.94	0.18	4.09	1	PHOT
				Fe IV	1538.926	2.100	24.35	0.18	0.45	1	PHOT
1542.277	0.703	6.442	0.531	Fe IV	1542.155	2.100	23.72	0.14	0.43	1	PHOT
1542.825	0.524	13.299	0.605	Fe IV	1542.698	2.100	24.68	0.10	0.42	1	PHOT
				N III	1542.705	21.000	23.32	0.10	4.08	1	PHOT
1543.362	0.964	5.081	0.565	Fe V	1543.236	13.000	24.48	0.19	2.53	1	PHOT
1543.540	3.093	4.550	0.823	Ni IV	1543.422	21.000	22.92	0.60	4.12	1	PHOT
				N IV	1543.429	21.000	21.56	0.60	4.12	1	PHOT
1544.033	1.765	0.944	0.197	Ni IV	1543.898	21.000	26.21	0.34	4.09	1	PHOT
				Ni V	1543.915	21.000	22.91	0.34	4.09	1	PHOT
1544.208	2.368	1.885	0.511	Ni IV	1544.075	21.000	25.82	0.46	4.10	1	PHOT
1544.355	1.787	2.255	0.488	N III	1544.227	21.000	24.85	0.35	4.09	1	PHOT
				Fe V	1544.232	13.000	23.88	0.35	2.55	1	PHOT
1544.613	0.714	8.282	0.527	Fe IV	1544.486	2.100	24.65	0.14	0.43	1	PHOT
1545.521	1.711	2.081	0.504	Ni IV	1545.394	21.000	24.64	0.33	4.09	1	PHOT
1546.355	1.354	2.998	0.538	Ni IV	1546.233	21.000	23.65	0.26	4.08	1	PHOT
				N III	1546.240	21.000	22.30	0.26	4.08	1	PHOT
1546.526	1.420	9.349	0.505	Fe IV	1546.404	2.100	23.65	0.28	0.49	1	PHOT
				O III	1546.407	2.100	23.07	0.28	0.49	1	PHOT
1547.732	6.013	9.757	0.841	Fe IV	1547.615	2.100	22.66	1.16	1.23	1	PHOT
1548.238	0.325	87.436	1.469	C IV	1548.195	27.000	8.33	0.06	5.23	1	ISM2
1548.345	1.064	86.416	1.737	C IV	1548.195	27.000	29.05	0.21	5.23	1	PHOT
1548.813	3.068	1.867	0.605	Ni IV	1548.680	21.000	25.75	0.59	4.11	1	PHOT
1550.815	0.158	54.423	1.420	C IV	1550.772	27.000	8.31	0.03	5.22	1	ISM2
1550.907	1.202	99.303	1.872	C IV	1550.772	27.000	26.10	0.23	5.22	1	PHOT
1551.031	1.161	4.329	0.609	Fe V	1550.907	14.000	23.97	0.22	2.72	1	PHOT
1552.328	2.151	2.359	0.603	Fe IV	1552.208	2.100	23.18	0.42	0.58	1	PHOT
				Si VI	1552.220	210.000	20.86	0.42	40.56	1	PHOT

Table A.1: Continued.

λ_{obs}	$\delta\lambda_{obs}$	W_λ	δW_λ	Ion	λ_{lab}	$\delta\lambda_{lab}$	v	δv	δv_{tot}	List	Origin
1552.474	1.789	5.273	0.755	Fe IV	1552.349	2.100	24.14	0.35	0.53	1	PHOT
1552.825	1.833	8.241	0.548	Fe IV	1552.705	2.100	23.17	0.35	0.54	1	PHOT
1553.287	1.909	4.662	0.772	Fe IV	1553.171	2.100	22.39	0.37	0.55	1	PHOT
1553.414	0.637	1.547	0.457	Fe IV	1553.296	2.100	22.77	0.12	0.42	1	PHOT
1554.345	0.624	12.668	0.662	Si I	1554.296	1.500	9.45	0.12	0.31	1	ISM2
				Fe V	1554.219	14.000	24.30	0.12	2.70	1	PHOT
1557.301	2.716	2.010	0.422	Ni VI	1557.176	22.000	24.07	0.52	4.27	1	PHOT
				Fe IV	1557.182	2.200	22.91	0.52	0.67	1	PHOT
1557.412	3.179	2.171	0.722	Ni IV	1557.281	22.000	25.22	0.61	4.28	1	PHOT
				N IV	1557.288	22.000	23.87	0.61	4.28	1	PHOT
1557.576	1.240	1.530	0.446	Fe IV	1557.456	2.200	23.10	0.24	0.49	1	PHOT
1560.396	1.008	7.131	0.685	C I	1560.309	2.200	16.72	0.19	0.46	1	ISM1
				Fe IV	1560.269	2.200	24.40	0.19	0.46	1	PHOT
				Fe V	1560.279	26.000	22.48	0.19	5.00	1	PHOT
1561.316	2.371	5.735	0.522	Fe IV	1561.197	2.200	22.85	0.46	0.62	1	PHOT
				Fe V	1561.205	14.000	21.31	0.46	2.73	1	PHOT
1562.385	1.579	2.255	0.518	Fe IV	1562.261	0.000	23.80	0.30	0.30	2	PHOT
1562.582	1.019	5.788	0.632	Fe IV	1562.460	2.200	23.41	0.20	0.47	1	PHOT
				Fe V	1562.461	14.000	23.22	0.20	2.69	1	PHOT
1562.871	1.158	11.844	0.541	N III	1562.732	22.000	26.67	0.22	4.23	1	PHOT
				Fe IV	1562.751	2.200	23.02	0.22	0.48	1	PHOT
1563.257	3.057	3.632	0.899	Ni VI	1563.118	22.000	26.66	0.59	4.26	1	PHOT
				Fe IV	1563.137	2.200	23.01	0.59	0.72	1	PHOT
1563.358	2.107	3.306	0.723	Fe IV	1563.231	2.200	24.36	0.40	0.58	1	PHOT
1563.713	1.896	4.227	0.754	Fe IV	1563.576	0.000	26.27	0.36	0.36	2	PHOT
				Fe IV	1563.583	2.200	24.93	0.36	0.56	1	PHOT
				N III	1563.602	22.000	21.28	0.36	4.23	1	PHOT
1566.374	1.604	6.715	0.807	N III	1566.247	22.000	24.31	0.31	4.22	1	PHOT
				Fe IV	1566.257	2.200	22.39	0.31	0.52	1	PHOT
1566.691	1.071	4.685	0.402	O III	1566.557	16.000	25.64	0.20	3.07	1	PHOT
				Fe IV	1566.568	2.200	23.54	0.20	0.47	1	PHOT
1568.084	1.603	6.077	0.438	Fe IV	1567.956	2.200	24.47	0.31	0.52	1	PHOT
				O V	1567.960	220.000	23.71	0.31	42.06	1	PHOT
1568.397	0.718	13.757	0.743	Fe IV	1568.259	2.200	26.38	0.14	0.44	1	PHOT
				Fe IV	1568.276	2.200	23.13	0.14	0.44	1	PHOT
1568.832	2.044	3.326	0.747	Ni V	1568.704	0.000	24.46	0.39	0.39	2	PHOT
				Fe IV	1568.716	2.200	22.17	0.39	0.57	1	PHOT
1569.348	1.146	5.008	0.657	Fe IV	1569.222	2.200	24.07	0.22	0.47	1	PHOT
				Fe V	1569.231	20.000	22.35	0.22	3.83	1	PHOT
1570.108	2.995	2.310	0.693	Fe V	1569.977	14.000	25.01	0.57	2.73	1	PHOT
1570.305	1.295	4.510	0.649	Fe IV	1570.178	2.200	24.25	0.25	0.49	1	PHOT
1570.539	1.244	4.711	0.646	Fe IV	1570.416	2.200	23.48	0.24	0.48	1	PHOT
				Ni V	1570.421	0.000	22.53	0.24	0.24	2	PHOT
1571.371	1.470	2.866	0.593	Fe IV	1571.244	2.200	24.23	0.28	0.50	1	PHOT
1574.733	2.829	4.654	0.948	Fe IV	1574.606	2.200	24.18	0.54	0.68	1	PHOT

Table A.1: Continued.

$\lambda_{\rm obs}$	$\delta\lambda_{\rm obs}$	W_λ	δW_λ	Ion	$\lambda_{\rm lab}$	$\delta\lambda_{\rm lab}$	v	δv	$\delta v_{\rm tot}$	List	Origin
1575.736	1.675	3.013	0.668	Al IV	1575.619	22.000	22.26	0.32	4.20	1	PHOT
				Fe IV	1575.620	2.200	22.07	0.32	0.53	1	PHOT
1578.865	1.819	2.237	0.646	Fe IV	1578.740	2.200	23.74	0.35	0.54	1	PHOT
1584.243	1.605	4.827	0.495	Fe IV	1584.116	2.200	24.03	0.30	0.52	1	PHOT
				Fe IV	1584.125	2.200	22.33	0.30	0.52	1	PHOT
				O IV	1584.130	160.000	21.38	0.30	30.28	1	PHOT
1584.666	2.127	4.593	0.890	Fe V	1584.535	14.000	24.79	0.40	2.68	1	PHOT
				Fe V	1584.545	27.000	22.89	0.40	5.12	1	PHOT
1585.965	1.364	3.816	0.627	Fe IV	1585.838	2.200	24.01	0.26	0.49	1	PHOT
1588.243	1.435	1.560	0.513	Fe IV	1588.128	2.200	21.71	0.27	0.50	1	PHOT
1591.614	2.795	4.354	0.985	Ni IV	1591.475	23.000	26.18	0.53	4.36	1	PHOT
				Ni VI	1591.498	23.000	21.85	0.53	4.36	1	PHOT
1592.176	0.994	11.684	0.896	Fe IV	1592.050	2.300	23.73	0.19	0.47	1	PHOT
1598.132	2.027	3.770	0.866	Fe IV	1598.011	2.300	22.70	0.38	0.58	1	PHOT
1598.948	2.545	3.067	0.880	N III	1598.820	160.000	24.00	0.48	30.00	1	PHOT
				O IV	1598.820	160.000	24.00	0.48	30.00	1	PHOT
				Fe V	1598.823	14.000	23.44	0.48	2.67	1	PHOT
1601.792	1.397	8.252	0.937	Fe IV	1601.652	2.300	26.20	0.26	0.50	1	PHOT
				Fe IV	1601.670	2.300	22.84	0.26	0.50	1	PHOT
				Si V	1601.670	230.000	22.84	0.26	43.05	1	PHOT
1602.179	2.035	5.453	0.962	Fe IV	1602.061	2.300	22.08	0.38	0.57	1	PHOT
1603.302	1.056	7.921	0.770	O III	1603.169	16.000	24.87	0.20	3.00	1	PHOT
				Fe IV	1603.177	2.300	23.37	0.20	0.47	1	PHOT
1603.851	1.323	6.454	0.756	Fe IV	1603.731	2.300	22.43	0.25	0.50	1	PHOT
1605.893	1.898	5.091	0.949	Al III	1605.766	2.300	23.71	0.35	0.56	1	PHOT
1606.089	1.253	9.329	0.941	Si V	1605.960	230.000	24.08	0.23	42.93	1	PHOT
				Fe IV	1605.970	2.300	22.21	0.23	0.49	1	PHOT
1607.959	1.532	6.413	0.922	Fe V	1607.833	15.000	23.49	0.29	2.81	1	PHOT
1608.501	0.784	10.902	0.905	Fe II	1608.451	0.230	9.32	0.15	0.15	1	ISM2
				Ni V	1608.389	23.000	20.88	0.15	4.29	1	PHOT
1608.552	0.962	3.267	0.631	Fe II	1608.451	0.230	18.82	0.18	0.18	1	ISM1
				Al V	1608.420	230.000	24.60	0.18	42.87	1	PHOT
1609.133	1.351	5.988	0.891	Fe V	1609.003	21.000	24.22	0.25	3.92	1	PHOT
				Fe IV	1609.004	2.300	24.04	0.25	0.50	1	PHOT
1609.221	0.926	11.646	0.970	Ni IV	1609.088	23.000	24.78	0.17	4.29	1	PHOT
				Fe IV	1609.100	2.300	22.54	0.17	0.46	1	PHOT
1609.967	1.438	8.012	0.856	Fe IV	1609.835	2.300	24.58	0.27	0.51	1	PHOT
1610.048	1.876	3.542	0.765	Fe IV	1609.924	2.300	23.09	0.35	0.55	1	PHOT
1610.155	1.816	3.654	0.704	Fe V	1610.018	15.000	25.51	0.34	2.81	1	PHOT
				O III	1610.023	2.300	24.58	0.34	0.55	1	PHOT
				Fe IV	1610.035	2.300	22.34	0.34	0.55	1	PHOT
1610.595	1.633	3.334	0.763	N III	1610.462	23.000	24.76	0.30	4.29	1	PHOT
				Ni IV	1610.464	23.000	24.39	0.30	4.29	1	PHOT
				Fe IV	1610.467	2.300	23.83	0.30	0.53	1	PHOT
1611.327	1.996	4.865	0.605	Al V	1611.190	230.000	25.49	0.37	42.79	1	PHOT

Table A.1: Continued.

λ_{obs}	$\delta\lambda_{\text{obs}}$	W_λ	δW_λ	Ion	λ_{lab}	$\delta\lambda_{\text{lab}}$	v	δv	δv_{tot}	List	Origin
				Fe IV	1611.203	2.300	23.07	0.37	0.57	1	PHOT
1611.996	1.358	9.148	0.982	Al III	1611.873	2.300	22.88	0.25	0.50	1	PHOT
1614.155	2.762	12.859	1.533	Ni IV	1614.023	23.000	24.52	0.51	4.30	1	PHOT
				Fe IV	1614.038	16.000	21.73	0.51	3.02	1	PHOT
1614.774	2.276	8.822	0.767	Fe IV	1614.645	2.300	23.95	0.42	0.60	1	PHOT
1615.134	1.584	7.629	1.069	Fe IV	1615.004	2.300	24.13	0.29	0.52	1	PHOT
1615.731	1.649	6.562	0.906	P IV	1615.588	2.300	26.54	0.31	0.53	1	PHOT
				Fe IV	1615.605	2.300	23.38	0.31	0.53	1	PHOT
1616.811	0.891	18.794	0.682	Fe V	1616.674	21.000	25.40	0.17	3.90	1	PHOT
				Ni IV	1616.676	23.000	25.03	0.17	4.27	1	PHOT
				Fe IV	1616.681	2.300	24.11	0.17	0.46	1	PHOT
1617.166	4.184	3.604	0.752	Fe V	1617.037	21.000	23.92	0.78	3.97	1	PHOT
				Fe V	1617.040	15.000	23.36	0.78	2.89	1	PHOT
1617.811	1.574	7.401	0.993	Fe IV	1617.679	2.300	24.46	0.29	0.52	1	PHOT
				Fe IV	1617.685	2.300	23.35	0.29	0.52	1	PHOT
1618.708	1.669	1.491	0.457	Fe IV	1618.574	2.300	24.82	0.31	0.53	1	PHOT
				Ni VI	1618.579	23.000	23.89	0.31	4.27	1	PHOT
				Fe IV	1618.588	2.300	22.23	0.31	0.53	1	PHOT
1619.146	1.121	4.347	0.730	Fe IV	1619.022	2.300	22.96	0.21	0.47	1	PHOT
1620.228	2.210	2.715	0.519	Fe V	1620.086	15.000	26.28	0.41	2.81	1	PHOT
				Ni V	1620.102	23.000	23.32	0.41	4.28	1	PHOT
1621.047	1.911	6.738	0.671	Fe IV	1620.915	2.300	24.41	0.35	0.55	1	PHOT
				Al V	1620.930	230.000	21.64	0.35	42.54	1	PHOT
1621.277	3.110	6.837	1.285	Fe IV	1621.139	2.300	25.52	0.58	0.72	1	PHOT
1621.699	1.560	10.304	1.132	Fe IV	1621.569	2.300	24.03	0.29	0.51	1	PHOT
1623.531	2.449	6.026	1.157	Fe IV	1623.386	2.300	26.78	0.45	0.62	1	PHOT
				Ni V	1623.403	23.000	23.64	0.45	4.27	1	PHOT
1623.652	1.418	5.237	0.907	Fe IV	1623.515	2.300	25.30	0.26	0.50	1	PHOT
				Fe IV	1623.532	2.300	22.16	0.26	0.50	1	PHOT
1624.383	1.595	2.598	0.474	Fe V	1624.255	15.000	23.63	0.29	2.78	1	PHOT
1625.401	1.191	9.045	0.617	Fe V	1625.271	15.000	23.98	0.22	2.78	1	PHOT
1626.402	2.126	6.190	0.689	Fe IV	1626.268	2.400	24.70	0.39	0.59	1	PHOT
				Fe IV	1626.279	2.400	22.67	0.39	0.59	1	PHOT
1626.606	1.238	7.157	0.939	Fe IV	1626.467	2.400	25.62	0.23	0.50	1	PHOT
1627.039	1.174	9.394	1.009	Fe V	1626.900	21.000	25.61	0.22	3.88	1	PHOT
				Fe IV	1626.904	2.400	24.88	0.22	0.49	1	PHOT
1628.674	1.690	4.492	0.787	Fe IV	1628.544	2.400	23.93	0.31	0.54	1	PHOT
				Ni IV	1628.550	24.000	22.83	0.31	4.43	1	PHOT
1630.808	1.738	5.984	0.643	Fe IV	1630.678	2.400	23.90	0.32	0.54	1	PHOT
				Fe V	1630.686	15.000	22.43	0.32	2.78	1	PHOT
				S IV	1630.688	24.000	22.06	0.32	4.42	1	PHOT
1631.208	0.919	16.023	1.082	Si I	1631.171	1.700	6.80	0.17	0.36	1	ISM2
				Fe IV	1631.077	2.400	24.08	0.17	0.47	1	PHOT
				Fe IV	1631.092	2.400	21.32	0.17	0.47	1	PHOT
1632.203	2.145	10.640	1.307	Fe IV	1632.082	2.400	22.23	0.39	0.59	1	PHOT

Table A.1: Continued.

$\lambda_{\rm obs}$	$\delta\lambda_{\rm obs}$	W_λ	δW_λ	Ion	$\lambda_{\rm lab}$	$\delta\lambda_{\rm lab}$	v	δv	$\delta v_{\rm tot}$	List	Origin
1632.508	5.979	22.948	7.223	O IV	1632.390	240.000	21.67	1.10	44.09	1	PHOT
1634.135	1.374	7.173	0.660	Al V	1634.000	1700.000	24.77	0.25	311.88	1	PHOT
				Fe IV	1634.004	2.400	24.03	0.25	0.51	1	PHOT
1639.527	1.576	9.782	1.161	N III	1639.390	24.000	25.05	0.29	4.40	1	PHOT
				Fe IV	1639.400	2.400	23.22	0.29	0.53	1	PHOT
1640.181	1.146	11.850	1.131	C IV	1640.040	38.000	25.77	0.21	6.95	1	PHOT
				Fe IV	1640.042	2.400	25.41	0.21	0.49	1	PHOT
1640.286	1.635	5.826	0.669	Fe IV	1640.155	2.400	23.94	0.30	0.53	1	PHOT
				Ni IV	1640.156	24.000	23.76	0.30	4.40	1	PHOT
1641.991	1.453	7.727	1.102	Fe IV	1641.864	2.400	23.19	0.27	0.51	1	PHOT
1647.224	1.192	9.571	0.728	Fe IV	1647.093	2.400	23.84	0.22	0.49	1	PHOT
1651.711	1.681	11.508	0.812	Fe IV	1651.577	2.400	24.32	0.31	0.53	1	PHOT
1653.032	2.707	10.490	1.557	Fe IV	1652.902	2.400	23.58	0.49	0.66	1	PHOT
1653.539	1.470	4.069	0.945	Al V	1653.400	1700.000	25.20	0.27	308.22	1	PHOT
				Ni VI	1653.401	24.000	25.02	0.27	4.36	1	PHOT
				Fe IV	1653.407	2.400	23.93	0.27	0.51	1	PHOT
1654.871	2.511	4.862	1.251	Fe V	1654.744	15.000	23.01	0.45	2.76	1	PHOT
1656.786	1.655	11.422	0.831	Fe IV	1656.652	2.400	24.25	0.30	0.53	1	PHOT
				C III	1656.665	27.000	21.90	0.30	4.89	1	PHOT
1658.565	2.339	4.888	1.134	Fe IV	1658.433	2.500	23.86	0.42	0.62	1	PHOT
1660.245	2.092	7.293	1.364	Fe IV	1660.103	2.500	25.64	0.38	0.59	1	PHOT
1661.724	2.070	6.975	0.871	Fe IV	1661.573	2.500	27.32	0.37	0.59	1	PHOT
1662.455	1.930	10.682	1.562	Fe IV	1662.319	2.500	24.53	0.35	0.57	1	PHOT
1662.654	1.772	5.328	1.141	Fe IV	1662.519	2.500	24.34	0.32	0.55	1	PHOT
				O V	1662.538	0.000	20.92	0.32	0.32	2	PHOT
1670.840	0.438	29.656	1.244	Al II	1670.787	2.500	9.51	0.08	0.46	1	ISM2
1670.893	0.673	11.358	1.035	Al II	1670.787	2.500	19.02	0.12	0.46	1	ISM1
1673.817	1.566	7.955	1.148	Fe IV	1673.670	2.500	26.33	0.28	0.53	1	PHOT
				Fe IV	1673.679	2.500	24.72	0.28	0.53	1	PHOT
1675.780	2.340	5.479	1.396	Fe IV	1675.661	2.500	21.29	0.42	0.61	1	PHOT
1676.562	1.135	2.372	0.758	Ni IV	1676.421	25.000	25.21	0.20	4.47	1	PHOT
				P IV	1676.426	2.500	24.32	0.20	0.49	1	PHOT
				Fe V	1676.429	16.000	23.78	0.20	2.87	1	PHOT
1687.810	4.486	20.544	2.669	Fe IV	1687.683	2.500	22.56	0.80	0.91	1	PHOT
1690.454	13.283	12.308	3.300	Fe IV	1690.305	2.500	26.43	2.36	2.40	1	PHOT
				Fe IV	1690.321	2.500	23.59	2.36	2.40	1	PHOT
1699.022	5.699	17.100	2.634	Fe IV	1698.884	2.600	24.35	1.01	1.11	1	PHOT
1718.036	3.232	12.373	2.973	Ni V	1717.885	26.000	26.35	0.56	4.57	1	PHOT
				Fe IV	1717.896	2.600	24.43	0.56	0.72	1	PHOT
				N III	1717.909	26.000	22.16	0.56	4.57	1	PHOT
1718.300	3.264	12.043	2.986	Fe IV	1718.163	2.600	23.90	0.57	0.73	1	PHOT
1718.686	2.929	34.752	4.110	N IV	1718.550	26.000	23.72	0.51	4.56	1	PHOT
				Fe IV	1718.562	2.600	21.63	0.51	0.68	1	PHOT
1722.684	2.494	15.779	2.559	O V	1722.530	260.000	26.80	0.43	45.25	1	PHOT
				Si IV	1722.562	2.600	21.23	0.43	0.63	1	PHOT

Table A.1: Continued.

$\lambda_{\rm obs}$	$\delta\lambda_{\rm obs}$	W_λ	δW_λ	Ion	$\lambda_{\rm lab}$	$\delta\lambda_{\rm lab}$	v	δv	$\delta v_{\rm tot}$	List	Origin
1722.846	3.336	11.964	3.028	Fe IV	1722.710	2.600	23.67	0.58	0.74	1	PHOT
1724.200	2.658	11.896	2.646	Fe IV	1724.055	2.600	25.21	0.46	0.65	1	PHOT
				Ni IV	1724.070	26.000	22.61	0.46	4.54	1	PHOT
1725.757	6.881	15.544	2.587	Fe IV	1725.627	2.700	22.58	1.20	1.28	1	PHOT
1727.523	6.895	14.536	4.576	Si IV	1727.376	2.700	25.51	1.20	1.29	1	PHOT
1828.124	6.460	6.599	1.366	Fe IV	1827.979	3.000	23.78	1.06	1.17	1	PHOT
1854.858	2.793	18.392	2.552	Al III	1854.716	3.100	22.95	0.45	0.67	1	PHOT
1860.571	4.581	7.297	2.077	C V	1860.420	84.000	24.33	0.74	13.55	1	PHOT
				Fe IV	1860.422	3.100	24.01	0.74	0.89	1	PHOT
1862.937	4.013	19.903	1.837	Al III	1862.790	3.100	23.66	0.65	0.82	1	PHOT
2205.032	10.314	6.880	2.234	Ni IV	2204.880	43.000	20.67	1.40	6.01	1	PHOT
2344.280	0.927	33.107	3.341	Fe II	2344.214	0.490	8.44	0.12	0.13	1	ISM2
2344.359	3.398	11.278	2.348	Fe II	2344.214	0.490	18.54	0.43	0.44	1	ISM1
2374.522	2.557	13.676	2.399	Fe II	2374.461	0.500	7.70	0.32	0.33	1	ISM2
2374.611	2.632	3.981	1.649	Fe II	2374.461	0.500	18.94	0.33	0.34	1	ISM1
2382.834	0.373	68.398	1.982	Fe II	2382.765	0.510	8.68	0.05	0.08	1	ISM2
2382.913	0.943	25.788	1.290	Fe II	2382.765	0.510	18.62	0.12	0.13	1	ISM1
2586.723	1.229	26.012	2.729	Fe II	2586.650	0.600	8.46	0.14	0.16	1	ISM2
2586.808	4.412	15.956	3.020	Fe II	2586.650	0.600	18.31	0.51	0.52	1	ISM1
2600.244	0.635	55.866	3.284	Fe II	2600.173	0.600	8.19	0.07	0.10	1	ISM2
2600.332	1.635	39.157	3.254	Fe II	2600.173	0.600	18.33	0.19	0.20	1	ISM1
2796.429	1.331	132.763	5.328	Mg II	2796.352	7.000	8.26	0.14	0.76	1	ISM2
2796.534	1.214	74.147	4.876	Mg II	2796.352	7.000	19.51	0.13	0.76	1	ISM1
2803.613	0.689	139.207	3.633	Mg II	2803.531	7.000	8.77	0.07	0.75	1	ISM2
2803.715	1.191	36.877	3.887	Mg II	2803.531	7.000	19.68	0.13	0.76	1	ISM1
2853.042	3.391	20.284	3.951	Mg I	2852.964	0.730	8.20	0.36	0.36	1	ISM2

Bibliography

Aller L. H., 1959, PASP, 71, 324

Anderson L. S., 1989, ApJ, 339, 558

Arnaud K. A., 1996, in Jacoby G. H., Barnes J., eds, Astronomical Data Analysis Software and Systems V Vol. 101 of Astronomical Society of the Pacific Conference Series, XSPEC: The First Ten Years. p. 17

Asplund M., Grevesse N., Sauval A. J., Scott P., 2009, in Blandford ed., Annual Review of Astronomy and Astrophysics, Vol. 47, ANNUAL REVIEW OF ASTRONOMY AND ASTROPHYSICS, VOL 47. ANNUAL REVIEWS, 4139 EL CAMINO WAY, PO BOX 10139, PALO ALTO, CA 94303-0897 USA

Auer L. H., 1987, Acceleration of Convergence. p. 101

Auer L. H., Mihalas D., 1969, ApJ, 158, 641

Badnell N. R., 1986, Journal of Physics B: Atomic and Molecular Physics, 19, 3827

Badnell N. R., 1997, Journal of Physics B: Atomic, Molecular and Optical Physics, 30, 1

Badnell N. R., 2011, Computer Physics Communications, 182, 1528

Bagdonaite J., Salumbides E. J., Preval S. P., Barstow M. A., Barrow J. D., Murphy M. T., Ubachs W., 2014, Phys. Rev. Lett., 113, 123002

Bannister N. P., Barstow M. A., Holberg J. B., Bruhweiler F. C., 2003, MNRAS, 341, 477

Barrow J. D., Sandvik H. B., Magueijo J. a., 2002, Phys. Rev. D, 65, 063504

Barstow M. A., Barstow J. K., Casewell S. L., Holberg J. B., Hubeny I., 2014, MNRAS, 440, 1607

Barstow M. A., Boyce D. D., Welsh B. Y., Lallement R., Barstow J. K., Forbes A. E., Preval S., 2010, ApJ, 723, 1762

Barstow M. A., Cruddace R. G., Kowalski M. P., Bannister N. P., Yentis D., Lapington J. S., Tandy J. A., Hubeny I., Schuh S., Dreizler S., Barbee T. W., 2005, MNRAS, 362, 1273

Barstow M. A., Good S. A., Burleigh M. R., Hubeny I., Holberg J. B., Levan A. J., 2003, MNRAS, 344, 562

Barstow M. A., Good S. A., Holberg J. B., Hubeny I., Bannister N. P., Bruhweiler F. C., Burleigh M. R., Napiwotzki R., 2003, MNRAS, 341, 870

Barstow M. A., Holberg J. B., Hubeny I., Good S. A., Levan A. J., Meru F., 2001, MNRAS, 328, 211

Barstow M. A., Hubeny I., Holberg J. B., 1998, MNRAS, 299, 520

Barstow M. A., Hubeny I., Holberg J. B., 1999, MNRAS, 307, 884

Barstow M. A., Hubeny I., Lanz T., Holberg J. B., Sion E. M., 1996, in Bowyer S., Malina R. F., eds, IAU Colloq. 152: Astrophysics in the Extreme Ultraviolet The Composition and Structure of White Dwarf Atmospheres Revealed by Extreme Ultraviolet Spectroscopy. p. 203

Bautista M. A., Romano P., Pradhan A. K., 1998, ApJS, 118, 259

Berengut J. C., Flambaum V. V., Ong A., Webb J. K., Barrow J. D., Barstow M. A., Preval S. P., Holberg J. B., 2013, Physical Review Letters, 111, 010801

Bergeron P., Liebert J., Fulbright M. S., 1995, ApJ, 444, 810

Bergeron P., Wesemael F., Dufour P., Beauchamp A., Hunter C., Saffer R. A., Gianninas A., Ruiz M. T., Limoges M. M., Dufour P., Fontaine G., Liebert J., 2011, ApJ, 737, 28

Bessel F., 1844, MNRAS, 6, 136

Bohlin R. C., Gilliland R. L., 2004, AJ, 127, 3508

Bruhweiler F., Barstow M., Holberg J., Sahu M., 1999, in American Astronomical Society Meeting Abstracts Vol. 31 of Bulletin of the American Astronomical Society, The Unusual C IV Absorption in the Spectrum of the DA White Dwarf G191-B2B. p. 1419

Casewell S. L., Dobbie P. D., Napiwotzki R., Burleigh M. R., Barstow M. A., Jameson R. F., 2009, MNRAS, 395, 1795

Claver C. F., Liebert J., Bergeron P., Koester D., 2001, ApJ, 563, 987

Chayer P., LeBlanc F., Fontaine G., Wesemael F., Michaud G., Vennes S., 1994, ApJL, 436, L161

Chayer P., Fontaine G., Wesemael F., 1995a, ApJS, 99, 189

Chayer P., Vennes S., Pradhan A. K., Thejll P., Beauchamp A., Fontaine G., Wesemael F., 1995b, ApJ, 454, 429

Chayer P., Kruk J. W., Ake T. B., Dupree A. K., Malina R. F., Siegmund O. H. W., Sonneborn G., Ohl R. G., 2000, ApJL, 538, L91

Cowan R. D., 1981, The Theory of Atomic Structure and Spectra. Los Alamos Series in Basic and Applied Sciences, University of California Press

Craig N., Abbott M., Finley D., Jessop H., Howell S. B., Mathioudakis M., Sommers J., Vallerga J. V., Malina R. F., 1997, ApJS, 113, 131

Cruddace R., Paresce F., Bowyer S., Lampton M., 1974, ApJ, 187, 497

Cruddace R. G., Kowalski M. P., Yentis D., Brown C. M., Gursky H., Barstow M. A., Bannister N. P., Fraser G. W., Spragg J. E., Lapington J. S., Tandy J. A., Sanderson B., Culhane J. L., Barbee T. W., Kordas J. F., Goldstein W., Fritz G. G., 2002, ApJL, 565, L47

Dickinson N. J., Barstow M. A., Hubeny I., 2012, MNRAS, 421, 3222

Dickinson N. J., Barstow M. A., Welsh B. Y., 2012, MNRAS, 428, 1873

Dixon W. V., Sahnow D. J., Barrett P. E., Civeit T., Dupuis J., Fullerton A. W., Godard B., Hsu J. C., Kaiser M. E., Kruk J. W., Lacour S., Lindler D. J., Massa D., Robinson R. D., Romelfanger M. L., Sonnentrucker P., 2007, PASP, 119, 527

Dupuis J., Chayer P., Vennes S., Christian D. J., Kruk J. W., 2000, ApJ, 537, 977

Finley D. S., Basri G., Bowyer S., 1990, ApJ, 359, 483

Flambaum V. V., Shuryak E. V., 2008, in Danielewicz P., Piecuch P., Zelevinsky V., eds, Nuclei and Mesoscopic Physic - WNMP 2007 Vol. 995 of American Institute of Physics Conference Series, How changing physical constants and violation of local position invariance may occur?. pp 1–11

Flammarion C., 1877, Astronomical register, 15, 186

Hernandez S., 2012, Space Telescope Imaging Spectrograph Instrument Handbook for Cycle 21 v. 12.0

Herschel W., 1785, Royal Society of London Philosophical Transactions Series I, 75, 40

Holberg J. B., 2007, Sirius – Brightest Diamond in the Night Sky

Holberg J. B., Barstow M. A., Bruhweiler F. C., Cruise A. M., Penny A. J., 1998, ApJ, 497, 935

Holberg J. B., Barstow M. A., Hubeny I., Sahu M. S., Bruhweiler F. C., Landsman W. B., 2003 Vol. 291 of ASPCS, A Detailed View of the Photosphere of the Hot White Dwarf G191-B2B from STIS. p. 383

Holberg J. B., Basile J., Wesemael F., 1986, ApJ, 306, 629

Holberg J. B., Bergeron P., 2006, AJ, 132, 1221

Hubeny I., 1988, Computer Physics Communications, 52, 103

Hubeny I., Lanz T., 1995, ApJ, 439, 875

Hubeny I., 2003, in Hubeny I., Mihalas D., Werner K., eds, Astronomical Society of the Pacific Conference Series Vol. 288 of Astronomical Society of the Pacific Conference Series, Accelerated Lambda Iteration: An Overview. p. 17

Hubeny I., Lanz T., 2011, in Astrophysics Source Code Library, record ascl:1109.022 Synspec: General Spectrum Synthesis Program. p. 9022

Kahn S. M., Wesemael F., Liebert J., Raymond J. C., Steiner J. E., Shipman H. L., 1984, ApJ, 278, 255

Kowalski P. M., Saumon D., 2006, ApJL, 651, L137

Kramida A., Yu Reader J., Team N. A., , 2013, NIST reference, NIST Atomic Spectra Database (ver. 5.1), [Online]. Available: http://physics.nist.gov/asd [2014, August 21]. National Institute of Standards and Technology, Gaithersburg, MD.

Kurucz R. L., 1981, SAO Special Report, 390

Kurucz R. L., 1992, RMxAA, 23, 45

Kurucz R. L., 2011, Canadian Journal of Physics, 89, 417

Lajoie C. P., Bergeron P., 2007, ApJ, 667, 1126

Lanz T., Barstow M. A., Hubeny I., Holberg J. B., 1996, ApJ, 473, 1089

Lehner N., Jenkins E. B., Gry C., Moos H. W., Chayer P., Lacour S., 2003, ApJ, 595, 858

Lemke M., 1997, A&AS, 122, 285

Markwardt C. B., 2009, in Bohlender D. A., Durand D., Dowler P., eds, Astronomical Data Analysis Software and Systems XVIII Vol. 411 of Astronomical Society of the Pacific Conference Series, Non-linear Least-squares Fitting in IDL with MPFIT. p. 251

Marsh M. C., Barstow M. A., Buckley D. A., Burleigh M. R., Holberg J. B., Koester D., O'Donoghue D., Penny A. J., Sansom A. E., 1997, MNRAS, 286, 369

Mestel L., 1952, MNRAS, 112, 583

Napiwotzki R., Green P. J., Saffer R. A., 1999, in Solheim S. E., Meistas E. G., eds, 11th European Workshop on White Dwarfs Vol. 169 of Astronomical Society of the Pacific Conference Series, How accurately do we know the parameters of hot DA white dwarfs?. p. 492

Oke J. B., 1974, ApJS, 27, 21

Preval S. P., Barstow M. A., Holberg J. B., Dickinson N. J., 2013, MNRAS, 436, 659

Rauch T., Werner K., Bohlin R., Kruk J. W., 2013, A&A, 560

Rauch T., Werner K., Quinet P., Kruk J. W., 2014a, A&A, 564

Rauch T., Werner K., Quinet P., Kruk J. W., 2014b, A&A, 566

Redfield S., Linsky J. L., 2008, ApJ, 673, 283

Salaris M., Dom'ınguez I., Garc'ıa-Berro E., Hernanz M., Isern J., Mochkovitch R., 1997, ApJ, 486, 413

Sion E. M., Greenstein J. L., Landstreet J. D., Liebert J., Shipman H. L., Wegner G. A., 1983, ApJ, 269, 253

Tat H. H., Terzian Y., 1999, PASP, 111, 1258

Tremblay P. E., Bergeron P., 2009, ApJ, 696, 1755

Tremblay P. E., Bergeron P., Gianninas A., 2011, ApJ, 730, 128

van Maanen A., 1917, PASP, 29, 258

Vennes S., Chayer P., Dupuis J., 2005, ApJL, 622, L121

Vennes S., Chayer P., Dupuis J., Lanz T., 2006, ApJ, 652, 1554

Vennes S., Chayer P., Hurwitz M., Bowyer S., 1996, ApJ, 468, 898

Vennes S., Lanz T., 2001, ApJ, 553, 399

Vennes S., Polomski E. F., Lanz T., Thorstensen J. R., Chayer P., Gull T. R., 2000, ApJ, 544, 423

Verner D. A., Barthel P. D., Tytler D., 1994, A&A, 108, 287

Vidal C. R., Cooper J., Smith E. W., 1973, ApJS, 25, 37

Werner K., Dreizler S., 1999, Journal of Computational and Applied Mathematics, 109, 65

Werner K., Deetjen J. L., Dreizler S., Nagel T., Rauch T., Schuh S. L., 2003, in Hubeny I., Mihalas D., Werner K., eds, Stellar Atmosphere Modeling Vol. 288 of Astronomical Society of the Pacific Conference Series, Model Photospheres with Accelerated Lambda Iteration. p. 31